DEPOSITION AND PLANARIZATION OF EPITAXIAL OXIDE THIN FILMS FOR HIGH TEMPERATURE SUPERCONDUCTING DEVICE APPLICATIONS

by

BERTHA PI-JU CHANG

S.B., Materials Science and Engineering
Massachusetts Institute of Technology
(1988)

Submitted to the Department of Materials Science and Engineering
on May 5, 1995 in Partial Fulfillment of
the Requirements for the Degree of

Doctor of Philosophy
in Ceramics
at the

Massachusetts Institute of Technology

June, 1995

Signature of Author______________________________
Department of Materials Science and Engineering
May 5, 1995

Certified by______________________________
Michael J. Cima, Norton Associate Professor of Ceramics
Thesis Supervisor

Accepted by______________________________
Carl V. Thompson II, Professor of Electronic Materials
Chair, Departmental Committee on Graduate Students

DEPOSITION AND PLANARIZATION OF EPITAXIAL OXIDE THIN FILMS FOR HIGH TEMPERATURE SUPERCONDUCTING DEVICE APPLICATIONS

Bertha P. Chang

Submitted to the Department of Materials Science and Engineering
on May 5, 1995
in partial fulfillment of the requirements for the degree of
Doctor of Philosophy in Ceramics

ABSTRACT

Planarization processing of interlayer films is required in the fabrication of any multilayer device in order to achieve complete step coverage over patterned surfaces. This issue becomes more complex for multilayer epitaxial structures, however, since epitaxial growth and planarization need to take place simultaneously. A generally applicable epitaxial planarization process is important to fabrication of epitaxial device structures. Realization of such a process will permit complete step coverage as well as prevent growth of misoriented grains over underlying sharp steps.

The effects of both macroscopic and microscopic surface relief on epitaxial dielectric film growth and planarization processes were investigated in this thesis. It was found in the course of studying epitaxial planarization of ~1500 Å high steps that the presence of microscopic steps one to two unit cells high also affect epitaxial development of the dielectric film. Both the individual and combined effects of these two types of surface relief were examined specifically in the context of multilayer high temperature superconducting $Ba_2YCu_3O_{7-x}$ (BYC) device processing.

The three dielectric materials used in this thesis were yttria-stabilized ZrO_2, CeO_2, and MgO. All three are lattice-matched to BYC and possess materials properties appropriate to device fabrication and performance. Ion beam assisted deposition (IBAD) was used to investigate planarization processing of YSZ and CeO_2 while off-axis rf magnetron sputtering was used to study MgO film growth.

Homoepitaxial planarization of IBAD YSZ on patterned YSZ single crystal substrates was demonstrated. BYC films deposited subsequently on planarized YSZ exhibited high J_c values. A similar trend towards planarization was observed for heteroepitaxial planarization of IBAD CeO_2 films on patterned $LaAlO_3$. The presence of substrate microsteps in the substrate, however, disrupted epitaxial film growth due to the large lattice mismatch that existed between CeO_2 and $LaAlO_3$ in the [001] direction.

Oriented MgO films were found to grow differently on $SrTiO_3$ and $LaAlO_3$. MgO grew epitaxially on $SrTiO_3$ while film growth of MgO on $LaAlO_3$ was found to be affected by the presence of native substrate steps. These steps appeared to act as preferential nucleation sites and if properly oriented, helped to reinforce oriented film growth.

Thesis Supervisor: Michael J. Cima
Title: Norton Associate Professor of Ceramics

TABLE OF CONTENTS

LIST OF FIGURES

CHAPTER 1

CHAPTER 2

CHAPTER 3

CHAPTER 4

CHAPTER 5

CHAPTER 6

LIST OF TABLES

Table # Page #

CHAPTER 1

CHAPTER 4

CHAPTER 6

ACKNOWLEDGEMENTS

I would like to first extend my thanks to my advisor, Michael Cima. His willingness to take me into his group upon my return to MIT and his support and guidance throughout the past five years are greatly appreciated. I would also like to thank my committee members, Manny Oliveria, Uday Pal, and Carl Thompson, for their suggestions and comments on this thesis research.

Many, many thanks go to the staff at CPRL for making life and research so much easier. I would like to thank Lenny Rigione for substrates, filaments, spinning, photolithography, testing, and countless other small things. John Centorino is thanked for his help with my equipment problems. Barbara Layne and Eve Downing are also thanked for their help with papers, editing, and cheery hellos.

The technical staff in the CMSE are acknowledged for their assistance in many ways: Joe Adario and Peter Kloumann in the X-ray facility, Libby Shaw in the surface science lab, and Mike Frongillo in the TEM facility.

I was also very fortunate to have the support and friendship of numerous graduate students and postdocs at CPRL. Special thanks go especially to fellow thin film students Dr. Paul McIntyre, Jack Smith, and Man Fai Ng, with whom I have shared much of the past five years while working on spots, lines, and films. I'd also like to thank fellow IBAD'ers Dr. Neville Sonnenberg, Kevin Ressler, and Angela Longo for their help in the course of this research. Other students who have provided comradeship over the years are Dr. Yuying Tang, Dr. Simone Peterson, and Dr. Raymond Chiu.

I'd also like to acknowledge the assistance, technical expertise, and helpful discussions of many researchers at IBM, Yorktown Heights: Dr. William J. Gallagher, Dr. Ray Robertazzi, Dr. Lock See Yu-Jahnes, Dr. Jonathan Sun, Bob Sandstrom, Carol Jessen, Dr. Steve Rossnagel, Dr. Jim Harper, Dr. Ed Giess, and Dr. Eugene O'Sullivan.

I feel especially lucky for the many friends that have helped me make it through graduate school. Thanks go to Julie Tsai, Una Hwang, and CP Ma for nearly a decade of friendship, music, and late nights at MIT. I also thank Emi Ishida, Alice Chow, Wendy Lin, and Paohua Kuo of the MIT/Stanford group as well as the rest of the '88 McCormick gang (you know who you are!). I especially thank Deanna Kwan, Roxanne Pan, Grace May, and the "TPP" fellowship for their friendship, prayers, and support.

Most of all, I'd like to thank my family. My parents have always encouraged me in every endeavor, be it academic or musical. Their love and unflagging support have sustained me through college and especially through graduate school. I would also like to thank my sisters Janice, Iris, and Sharon for being there whenever I needed a listening ear, or to just talk about anything from "old times" to the New York Yankees.

CHAPTER 1

INTRODUCTION

Conduction lines are one potential application of high temperature superconducting (HTSC) thin films in microelectronics devices. Zero resistance at temperatures below the critical transition temperature (T_c) provides HTSC materials with an advantage over conventionally used metals or metal alloys: present day limitations on conduction line size and length can be overcome without incurring the increased line and/or rf resistance associated with metallic lines. This in turn allows for devices to be designed with increased functionality and performance. Epitaxial c-axis oriented thin films of $Ba_2YCu_3O_{7-x}$ (T_c = 93 K) grown on single crystal substrates have critical current densities in excess of 10^6 A/cm^2 at 77 K. This is sufficiently high to meet device specifications for applications such as transmission lines in microwave devices and interconnects in multichip modules (MCM's) and superconducting quantum interference devices (SQUIDs).[1-3] Optimizing the processing and hence electrical properties of $Ba_2YCu_3O_{7-x}$ (BYC) thin films has therefore been the focus of a great deal of research.

An equally important consideration, however, is the dielectric interlayer material used in multilayer HTSC devices. Both the materials properties and processing of suitable insulators also need to be carefully investigated in the context of HTSC devices. The schematics shown in Figure 1.1 illustrate the multilayer nature of these devices which consist of multiple layers of superconducting lines separated by dielectric interlayers and connected by vias. The points where the conduction paths transversely cross over one another are referred to as crossovers. It is clear that in order for epitaxial BYC growth to be sustained throughout the device structure during processing, epitaxially grown interlayers of a lattice matched dielectric material are needed. Additional processing

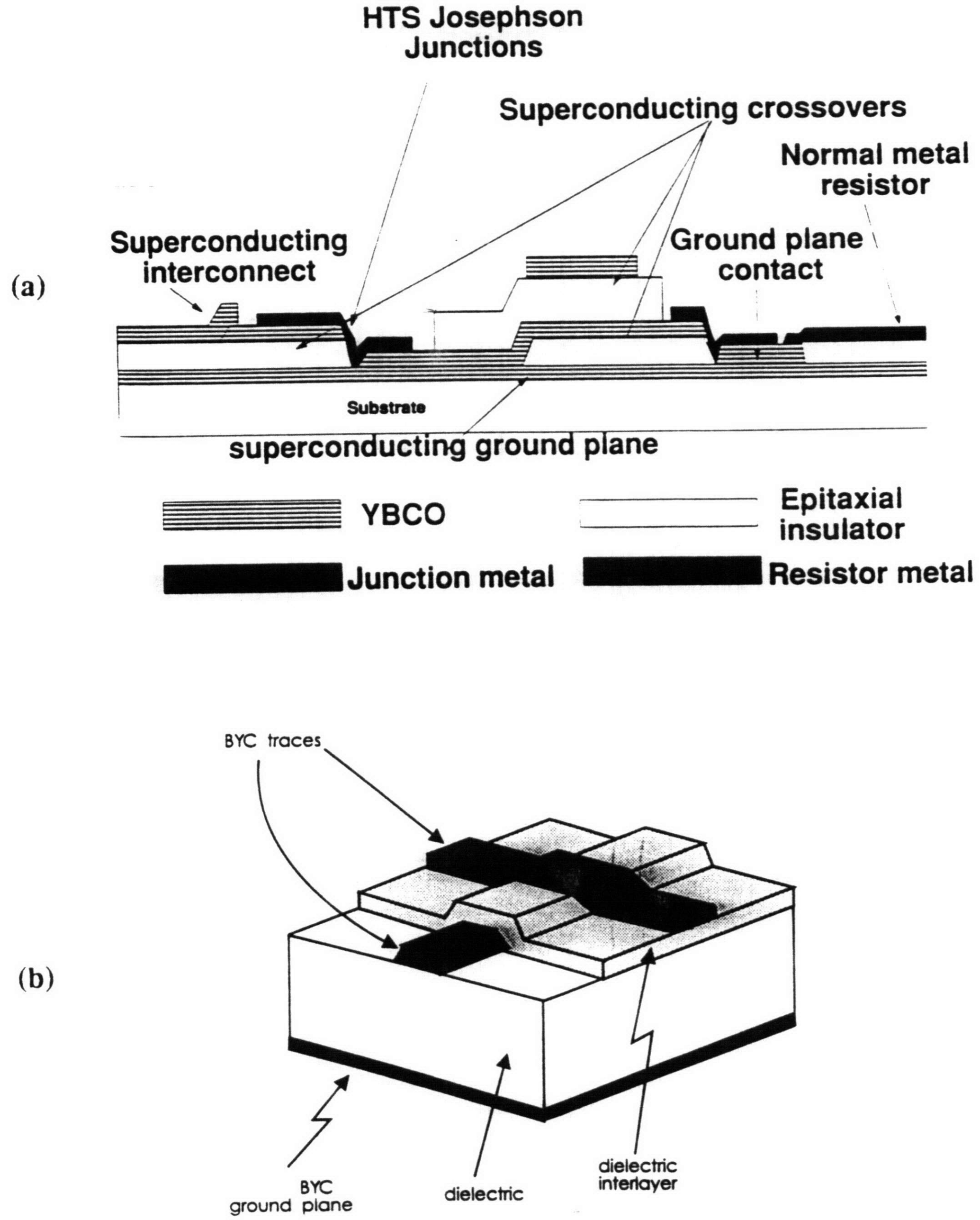

Figure 1.1 Schematics illustrating the multilayer nature of HTSC devices: (a) vertical schematic of a generic circuit involving HTSC junctions over a superconducting ground plane (from Reference 4), and (b) a basic crossover structure.

considerations require the dielectric material to have a good coefficient of thermal expansion (CTE) match with BYC and minimal chemical reactivity at processing temperatures. Constraints on the choice of dielectric material are also imposed by the electrical requirements for a given device. Both MCM's and microwave devices require low dielectric constant insulators in order to meet restrictions on signal line impedance and signal delay. Microwave devices also require insulators with low dielectric losses ($\tan \delta < 10^{-4}$) at high frequency in order to minimize signal loss.

An epitaxial dielectric planarization technology is also essential to the development of multilayer HTSC devices from a device processing perspective since actual device fabrication extends beyond merely depositing alternating layers of BYC and dielectric film. The patterning of each BYC film into a layer of conduction lines results in the formation of numerous sharp steps over which succeeding dielectric layers and BYC lines will need to be grown. Each crossover becomes susceptible to degraded electrical behavior if planarization processing is not utilized. Poor or incomplete step coverage of BYC lines by a dielectric interlayer can result in subsequent short-circuiting at crossovers while poor step coverage of underlying steps by a BYC film can result in open-circuit behavior. In addition, each crossover is also susceptible to weak-link behavior since deposition of BYC over sharp steps can lead to nucleation and growth of a-axis grains.[5,6] The resulting high angle grain boundaries lead to reduced current carrying capability[7] by the HTSC lines. Examination of the crossover population in multilayer devices underscores the seriousness of this issue. For example, preliminary calculations[8] show that for a 100 chip MCM with 500 logic gates per chip[9] and two conduction layers, the number of required signal connections results in ~9.7×10^6 crossovers (see Figure 1.2). MCM's with a greater number of logic gates per chip will have an even higher number of crossovers. It is essential, therefore, for the dielectric film deposition process to be able to planarize underlying steps while maintaining epitaxial growth.

One method by which attempts have been made to circumvent some of the problems that arise upon patterning BYC films into device structures is to taper off the edges of the patterned BYC lines. This is done through appropriate lithography and ion milling techniques to generate beveled edges with a slope angle of less than 45°. These

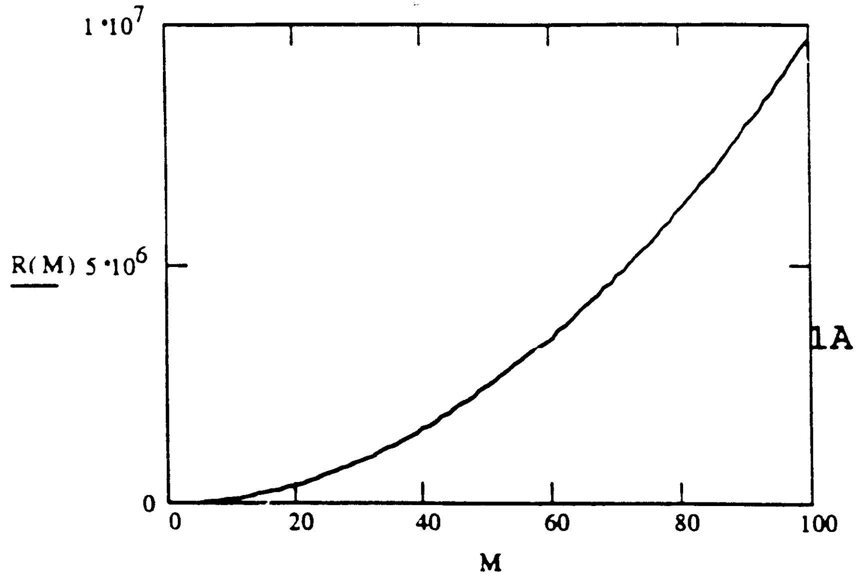

Figure 1.2 MCM crossover population R(M) as a function of chip number (M). Calculated for 500 logic gates per chip and two conduction layers.[8]

gently sloped edges permit good step coverage to be achieved by subsequently deposited films. In some cases, the use of beveled edges has also been a successful way of avoiding the growth of a-axis BYC grains. Jia *et al.*[5,6] examined this issue by carrying out a series of studies on BYC film growth over step edges patterned at a variety of angles in single crystal $SrTiO_3$ and $LaAlO_3$ substrates. Their results showed that a-axis growth was avoided for step angles of less than 40°. However, Wellstood *et al.*[3] found that BYC deposited using pulsed laser deposition (PLD) over a 20° $SrTiO_3$ step grew with the c-axis orientation parallel to the step. The different results obtained by the two groups are most likely a consequence of different deposition conditions which in turn can affect the relative rates of film growth and nucleation. McIntyre[10] compared BYC films deposited over stepped surfaces using metal-organic deposition and PLD, and showed that the relative rates of growth and nucleation can have a significant effect on the degree of a-axis material that develops.

These results demonstrate that although tapered BYC lines can give good step coverage, a-axis BYC film growth may not always be avoided. In addition, even if good step coverage and BYC c-axis film growth could be achieved, the surface still remains nonplanar. Thus the problem of providing good photolithographic resolution is unresolved with this method. In addition, this nonplanarity will worsen as the number of layers in the device increases. A planarization process that is able to address all of the problems associated with patterned surfaces is needed.

HTSC devices are only one example of a number of forthcoming devices that involve multilayer epitaxial structures.[11] Examples of other applications include ferroelectric, optoelectronic, and piezoelectric devices, all of which involve the use of various epitaxial oxides. Again, epitaxial growth is required in order to achieve the desired materials properties. It is clearly seen that all of these applications face similar scientific and technological issues: epitaxial growth must be achieved and an epitaxial planarization technology is needed for device fabrication.

Planarization techniques are currently used extensively in the fabrication of Si-based VLSI devices. Planar surfaces are required in order to provide for good step coverage, which prevents both open and short circuits in Al interconnects, and for adequate filling in of vias. In addition, planar surfaces allow photolithographic resolution and accuracy to be maintained throughout the device fabrication process. Techniques commonly used to achieve these ends include rf bias sputtering of Al[12,13] or SiO_2,[14,15] reflow methods which use spin-on glasses or polymers,[16] and etchback.[16] *Ex situ* techniques such as the damascene process,[17] which involves chemical-mechanical polishing, have also become increasingly prevalent. The key difference here is that there is usually no requirement to grow planarized layers with a specific crystallographic orientation.

Successful *in situ* epitaxial planarization has been reported in a number of compound semiconductor systems.[18] However, the mechanisms involved often rely on materials-specific properties, such as selective regrowth, and therefore are not generally extendable to other materials. A more general and accessible method of epitaxially planarizing a patterned surface is therefore required for multilayer epitaxial structures.

Thesis Motivation

Although both heteroepitaxial thin film growth and planarization have been studied extensively in the past, it is necessary to examine both issues in the context of multilayer HTSC device processing. In addition, a process needs to be developed by which dielectric heteroepitaxial film growth and planarization may occur simultaneously. The realization of such a process is crucial to the fabrication of HTSC and other devices involving epitaxial multilayers.

Scope of Thesis

The purpose of this thesis is to investigate different aspects of epitaxial growth and planarization of dielectric films as they pertain to HTSC devices. Three sets of studies were conducted towards this end. Candidate dielectric materials used in the course of this investigation were yttria-stabilized zirconia ($Y\text{-}ZrO_2$ or YSZ), ceria (CeO_2), and magnesia (MgO).

The first set of experiments explored homoepitaxial planarization of YSZ films grown on patterned YSZ single crystal substrates. Homoepitaxy provided the simplest system by which to study the feasibility of epitaxial planarization processing since lattice mismatch was not an issue. YSZ films were deposited using normal incidence ion beam assisted deposition (IBAD) onto YSZ substrates that had been patterned with a hill-and-valley structure. Both homoepitaxial film growth and planarization progress were studied as a function of deposition parameters using X-ray diffraction (XRD) and scanning electron microscopy (SEM). A correlation was made between IBAD planarization processing and existing planarization models based on rf bias sputtering. BYC films were subsequently deposited over planarized YSZ surfaces and their electrical properties measured as a way of further characterizing the homoepitaxial planarization process.

The second set of experiments studied heteroepitaxial planarization of IBAD CeO_2 films on patterned $LaAlO_3$ substrates. The lattice matching relationship between CeO_2 and $LaAlO_3$ is very similar to that between CeO_2 and BYC. The effects of ion beam energy and incidence angle on film orientation and planarization progress were examined using XRD and SEM. Cross-sectional transmission electron microscopy (TEM) was used to examine the microstructure and defects of IBAD CeO_2 films ion bombarded at normal incidence and the effect of lattice mismatch on heteroepitaxial planarization was analyzed.

The third set of experiments studied heteroepitaxial growth of MgO films. MgO has attractive dielectric properties but the relatively large 9% lattice mismatch with respect to BYC poses potential processing problems. Therefore, the growth of MgO on single crystal substrates with lattice constants similar to BYC was undertaken to better understand MgO growth in systems with large lattice mismatches and also to determine the feasibility of using MgO in HTSC devices. MgO was deposited using off-axis rf magnetron sputtering onto single crystal $SrTiO_3$ and $LaAlO_3$ substrates. The development of MgO film orientation and microstructure as a function of deposition temperature was examined by XRD and SEM. In addition, the effects of substrate surface features on MgO film growth were studied by modifying substrates surfaces through ion milling, and vicinal polishing. The modified surfaces were characterized by atomic force microscopy (AFM) prior to MgO film deposition. The relationships of deposition conditions and substrate surface features to the character and properties of sputtered MgO films were analyzed.

Thesis Organization

Chapter 2 first reviews the dielectric materials that most appropriately satisfy the requirements for interlayer materials in HTSC devices as described in the first part of this chapter. A review of rf bias sputtering, an *in situ* planarization technique used in semiconductor device processing, is then presented. Models for relevant planarization mechanisms are discussed and results from the literature are presented. Finally, epitaxial and graphoepitaxial mechanisms are briefly discussed. Chapter 3 covers the experimental techniques used for film deposition and film characterization in this thesis research. Chapter 4 presents the study on homoepitaxial planarization of YSZ films on patterned YSZ substrates along with the results of BYC deposition on planarized YSZ. Chapter 5 covers the study on heteroepitaxial planarization of patterned $LaAlO_3$ substrates by IBAD CeO_2 films. Chapter 6 presents the study of oriented film growth of MgO thin films on $SrTiO_3$ and $LaAlO_3$ substrates. A summary of the major conclusions from Chapters 4-6 is presented in Chapter 7 along with suggestions for future work.

CHAPTER 2
BACKGROUND

Background is provided in this chapter for the research presented in this thesis. In the first section, MgO, YSZ, and CeO_2 are identified as dielectric materials that are compatible with multilayer HTSC device processing and performance objectives. Each material is then reviewed in the specific context of BYC thin film processing as well as epitaxial growth in general. The use of rf bias sputtering as an *in situ* planarization technique is then presented and the relevant planarizing mechanisms discussed. The final section briefly reviews the basic concepts of epitaxy and epitaxial growth modes. Graphoepitaxy is also reviewed and in particular, the growth of films on single crystal substrates with natural surface relief is discussed.

2.1 DIELECTRIC INTERLAYER MATERIALS FOR HTSC DEVICES

The requirements that are placed on dielectric materials used in HTSC devices severely limits the number of available materials to choose from. As discussed in Chapter 1, these requirements include a good lattice and CTE match to BYC, no chemical reaction with BYC at processing temperatures, and a sufficiently low dielectric constant to meet device specifications. Single crystal substrates that are currently used for epitaxial BYC film growth meet the first three requirements to varying degrees.

Some of the more commonly used substrate materials are listed in Table 2.1[19,20] together with their relevant physical properties. Although all of these materials are lattice matched to BYC, the lattice matching conditions that are involved vary.[21] Epitaxial c-axis

Table 2.1 Lattice constants and dielectric properties of various insulators lattice-matched to $Ba_2YCu_3O_{7-x}$

	Lattice parameters			Mismatch			CTE
	a (Å)	*b* (Å)	*c* (Å)	ε_a (%)	ε_b (%)	ε_c[a] (%)	(ppm/°C)
$SrTiO_3$	3.905			2.0	0.7	0.1	10.3
$LaAlO_3$	3.793			-0.9	-2.2	-3.0	
MgO	4.213			9.2	8.0	7.4	12.6
$NdGaO_3$	3.837	3.889	3.853	0.3	0.3	-1.3	8.0
Y-ZrO_2	5.101			-6.1	-7.5	-8.2	9.2
CeO_2	5.411[d]			-0.04	-1.3	-2.0	8-11
BYC	3.827	3.877	11.709	---	---	---	12.0[b]

[a] Calculated with respect to c/3 for BYC

[b] Average value for ceramic

	(hkl)	ε	*tan* δ
$SrTiO_3$	(100)	277	0.0125
$SrTiO_3$	(110)	170	0.0130
$LaAlO_3$	(100)	23	0.007
MgO	(100)	9.62	0.0091
$NdGaO_3$	(001)	20.2	0.002
Y-ZrO_2	(100)	27.5	0.0054
CeO_2	(100)	26[d]	

[c] Dielectric constant, ε, and loss, tan δ, values at 1 MHz, measured at room temperature.

[d] From Ref. 20.

[e] All values (except for CeO_2) from Ref. 19.

BYC grows in a "cube-on-cube" fashion on $SrTiO_3$, $LaAlO_3$, $NdGaO_3$, and MgO, e.g. BYC (001) || $SrTiO_3$ (001) and BYC [100] || $SrTiO_3$ [100]. BYC is therefore also lattice-matched to these substrates in the [001] direction. The best lattice match on YSZ, however, is achieved with a 45° in-plane rotation of the film, e.g. BYC [110] || YSZ [100]. A substantial mismatch therefore exists in the [001] direction.

From the physical properties listed in Table 2.1, it is seen that MgO (ε~10) most favorably meets the low dielectric constant criterion while $SrTiO_3$ (ε~300) cannot be considered for device applications. The remaining materials all have similar dielectric constant values ranging from $\varepsilon = 20.2 - 27.5$. Of these materials, $LaAlO_3$ is not preferred as an interlayer material since it cannot be grown twin-free.[22] $NdGaO_3$, which can be grown twin-free, has been used successfully for growth of high J_c BYC films.[19,23] However, it has also been found that $NdGaO_3$ may be unsuitable for BYC deposition at elevated temperatures (T>900°C) due to possible film-substrate chemical reactions.[24] In addition, because both $LaAlO_3$ and $NdGaO_3$ are multication component oxides, processing can be more complex since stoichiometry needs to be maintained. Y-ZrO_2, however, has the advantage of being essentially a single cation material. Although some degree of chemical reactivity exists between BYC and YSZ to form $BaZrO_3$,[25] this can be remedied by using an appropriate buffer layer material such as CeO_2. CeO_2 itself has not been used as a substrate for BYC thin film deposition due to the limited availability of single crystal CeO_2 substrates, but instead has found wide use in thin film form.[26,27] Like YSZ, CeO_2 is lattice matched to BYC through a 45° rotation of the (001) plane about the [001] axis.[21] Therefore it is seen that of the materials listed in Table 2.1, MgO, YSZ, and CeO_2 are all acceptable dielectric materials based on the criteria listed above.

For each specific device application, the geometry of the superconducting lines and the dielectric interlayers will be governed by the electrical requirements of the device. A group at Conductus has recently demonstrated a functional HTSC MCM with two levels of BYC interconnects.[28] The BYC wiring consisted of 2500-3000 Å thick, 40 μm wide crossunders and a second level of 10-30 μm wide lines. The two levels were contacted by 40 μm square vias through a 5000 Å thick layer of $SrTiO_3$. The authors point out, however, that for practical applications, HTSC MCM's will require, among other things, 1-3 μm wide HTSC conduction lines separated by 1-2 μm thick layers of low dielectric constant insulator. The actual dielectric thickness will depend in part on the value of the dielectric constant of the interlayer material. It is important to keep this thickness range in mind when considering dielectric processing methods. Dielectric film epitaxy will need to be sustained throughout this entire thickness. The dielectric deposition method used will also need to be able to grow the films to these thicknesses within reasonable processing times.

2.1.1 MgO

The interest in MgO as a dielectric interlayer material stems primarily from the fact that it has the lowest dielectric constant of all lattice matched substrate materials currently in use for BYC. However, the 9.2% lattice mismatch between MgO and BYC is also the largest of all the materials listed in Table 2.1 although a coincident site lattice involving multiples of BYC [110] and MgO [100] spacings does exist. Several groups have reported that BYC deposition onto single crystal MgO yielded c-axis BYC films with multiple in-plane orientations.[29-32] The J_c's measured for these films were much lower than those found for BYC films grown on $SrTiO_3$ or $LaAlO_3$. This was attributed to the large BYC-MgO lattice mismatch. However, these J_c values were still higher than expected for polycrystalline films since high angle grain boundaries in BYC should act as weak links. Hwang *et al.*[33] found that several in-plane orientations for BYC grains on MgO are possible by using a near coincident site lattice (NCSL) theory. These theoretical results were consistent with the above studies in which BYC was found to grow with multiple in-plane orientations on MgO. The J_c was preserved, nonetheless, due to the low energy configurations that exist between BYC grains which allows a high connectivity of Cu-O-Cu chains.

It was also found that the growth of essentially single crystal BYC films on MgO with J_c's of 3.4-6 x 10^6 A/cm^2 at 77K[34-41] was achieved with proper preparation of the MgO single crystal substrates. Annealing or vicinal polishing of the substrate generated a high density of atomic surface steps which provided favored nucleation sites for BYC film growth. A graphoepitaxial mechanism was proposed to explain the improvement in BYC film orientation. A more detailed review of this work is presented later in Section 2.3.2.2.

A number of studies have been conducted on growing oriented MgO thin films. Although a great deal of the recent focus on MgO has been with respect to HTSC applications, epitaxial MgO has wide applicability. MgO can be used for epitaxial oxide growth on GaAs,[42] as buffer layers for ferroelectric films,[42,43] and as barrier layers for low temperature superconducting junction devices.[44-48] Methods that have been used to deposit epitaxial MgO thin films include electron beam (e-beam) evaporation, sputtering, and pulsed laser deposition (PLD).

2.1.2 CeO_2

CeO_2 is a dielectric material with the fluorite crystal structure. It is lattice matched to both Si and BYC as well as other BYC substrate materials. Epitaxial growth of CeO_2 on Si substrates was studied as part of an investigation into silicon-on-insulator (SOI) applications by Inoue *et al.*[20,49] who were able to use e-beam evaporation to grow epitaxial CeO_2 layers on Si as well as CeO_2 (110) on (100) Si. It was found that CeO_2 (111) || Si (111) epitaxy was easily obtained at low deposition temperatures below 200°C, while epitaxial growth on (100) and (110) Si substrates as well as CeO_2 (110) on Si (100) needed to be carried out at 800°C. CeO_2 has also found extensive use as a "magic" buffer layer for BYC films.[26,27] Wu *et al.*[26] were first able to grow epitaxial (100) CeO_2 on (100) $LaAlO_3$ and YSZ substrates, and also $(1\bar{1}02)$ r-plane sapphire substrates. Subsequent BYC deposition over the CeO_2 layers yielded films with J_c's in excess of 10^6 A/cm^2 on all substrates. CeO_2 has since become one of the most widely used buffer layer materials for BYC films.

2.1.3 YSZ

Yttria-stabilized zirconia also has the fluorite crystal structure and has been used as a template for BYC growth both as a single crystal substrate and in thin film form. Although YSZ reacts with BYC at high temperatures to form $BaZrO_3$,[25] BYC films have been grown successfully over YSZ using physical deposition methods at low deposition temperatures which suggests that adverse reaction may be avoided within certain processing windows.

The existence of multiple in-plane orientations of (001) BYC films on (001) YSZ single crystal substrates has been reported.[50,51] The two most commonly observed in-plane orientations are BYC [100] || YSZ [110] and BYC [100] || YSZ [100], which, following Fork *et al.*'s[50] convention, will be referred to as $\phi=45°$ and $\phi=0°$, respectively. Fork *et al.* also detected a third in-plane orientation rotated ~9° ($\phi=9°$) away from $\phi=0°$ material. All three orientations can be explained using a coincident site lattice (CSL) model.[50]

Garrison *et al.*[51] showed that growth of BYC films with more than 90 vol.% of either $\phi=0°$ or $\phi=45°$ material resulted in superconducting films with J_c's ~ 10^6 A/cm^2 at 77K. Films with a substantial degree of mixed in-plane orientations, however, had J_c's that were nearly four orders of magnitude lower at 2 x 10^2 A/cm^2. This was attributed to weak-link behavior resulting from the presence of the high angle grain boundaries.

Fork *et al.* carried out a systematic investigation of BYC film growth on YSZ substrates and found that the BYC in-plane orientation was affected by a number of factors. Changing the deposition temperature and partial pressure of oxygen as well as the Y_2O_3 content of the underlying YSZ was found to selectively enhance the growth of either $\phi=45°$ or $\phi=0°$ material, depending on the direction of the parameter change. The most dramatic effect, however, was found by depositing an initial buffer layer of at least 600 Å of either homoepitaxial YSZ or epitaxial CeO_2 over the YSZ substrate which greatly enhanced the amount of $\phi=45°$ material to over 98 vol% on YSZ and to over 99 vol% on CeO_2. The reasons behind this are not clear, but since a minimum buffer layer thickness was required to avoid mixed growth, it is possible that substrate surface features that enhanced either $\phi=0°$ or $\phi=9°$ growth were suppressed by the buffer layer.

Epitaxial YSZ films have also been grown over Si[52,53] and sapphire[54] substrates using PLD. The partial pressure of oxygen was found to be the most critical processing parameter in all cases in which too low of p_{O2} resulted in films with a mixed (111) and (100) orientation. Too high a p_{O2} for deposition on Si substrates also suppressed YSZ epitaxy due to the growth of silicon oxide. Optimal p_{O2} values for growth at 800°C were

50 mTorr and 4 x 10^{-4} Torr, for sapphire and Si substrates, respectively. Typical J_c values for subsequently deposited BYC films were greater than 10^6 A/cm^2. All BYC films grown over YSZ thin films exhibited 100% ϕ=45° in-plane orientation, unlike growth over single crystal YSZ substrates. A problem was observed with cracking of >500 Å thick BYC films deposited over buffered Si due to the large CTE mismatch between BYC and Si.

2.1.4 45° Grain Boundary Junctions

A dividend that arises from the 45° in-plane rotation of epitaxial BYC films grown over CeO_2 and YSZ surfaces is the ability to create so-called 45° grain boundaries *in situ* for devices such as superconducting quantum interference devices (SQUIDs).[21,27,55-57] This is accomplished in its simplest form by using a combination of three film layers designated as the base, seed, and buffer layers, as shown in Figure 2.1, in which the base and seed layers have a cube-on-cube epitaxial relationship while the buffer layer grows cube-on-cube over the seed layer and with a 45° in-plane rotation over the base layer. This type of grain boundary engineering has been demonstrated for materials sets such as $SrTiO_3$, MgO, and CeO_2. A thin seed layer of epitaxial MgO is deposited over a $SrTiO_3$ base layer and then photolithographically patterned and etched to expose half of the underlying $SrTiO_3$. A CeO_2 buffer layer is then deposited over both the MgO and $SrTiO_3$. The CeO_2 film grows with two different in-plane orientations separated by a 45° grain boundary since CeO_2 and MgO match in a cube-on-cube fashion while CeO_2 and $SrTiO_3$ are rotated 45° about the [001] direction. A subsequently deposited BYC film grows epitaxially over each of the two CeO_2 regions and thus also contains a 45° grain boundary. This method of artificially introducing a grain boundary takes advantage of the different lattice matching conditions that exist among HTSC-compatible materials.

2.2 PLANARIZATION USING rf BIAS SPUTTERING

In situ planarization using rf bias sputtering has been demonstrated for both

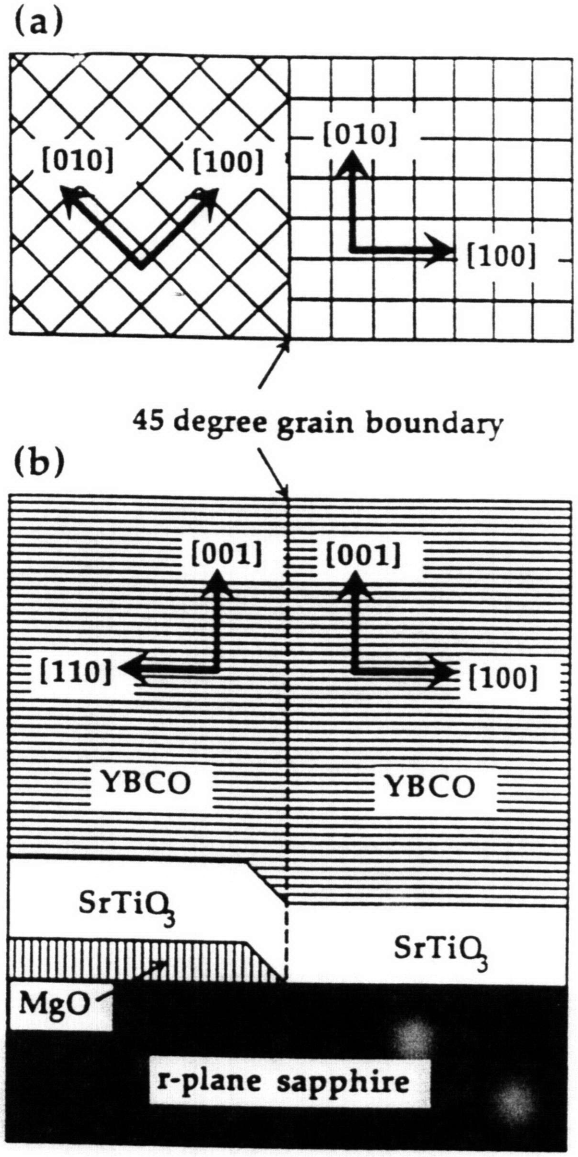

Figure 2.1 Schematics depicting the materials and crystallographic relationships involved in fabricating 45° grain boundaries in BYC films (from Reference 55).

insulating[14,5] and conducting[12,13] films. In this method, biasing the substrate holder allows film growth and ion bombardment to take place simultaneously on the substrate surface. Planarization can then occur as a result of the variation in sputtering yield of the film as a function of ion incidence angle as described by C.Y. Ting *et al.*[14]

The exact nature of the angular dependence of etch rate varies with material. However, etch rates for oblique incidence ion bombardment are generally higher than for normal ion incidence due to the greater ease with which primary forward scattered material can be ejected (see Figure 2.2). Thus, for normal incidence ion bombardment of a substrate surface, the highest degree of etching will occur for non-planar features such as the sloped sides of an interconnect line. A rough surface can therefore be made planar through etching alone.

The rf sputter deposition rate in rf bias sputtering is assumed to be dependent on cathode power alone and, to first order, independent of substrate surface topography.[14,15] Proper choice of cathode power and substrate bias gives a deposition rate that is balanced by an etch rate for a particular slope angle (i.e., the equilibrium angle), as shown in Figure 2.2. Under these types of processing conditions, a film is planarized as it grows. The lowest net deposition rates are obtained over non-planar surfaces where film growth tends toward the equilibrium angle as seen in Figure 2.3. Establishment of this equilibrium angle results in the eventual formation of a cone of film material as the angled surfaces come together. Once completed, the cone is a stable structure and neither grows nor shrinks. Meanwhile, the higher net deposition rate experienced by the flat areas of the substrate surface allow them to eventually bury the cone, resulting in a planar film. It is essential that the deposition and etch rates be chosen properly. Too high of a deposition rate overwhelms the etching rate and results in conformal film growth over the underlying structure with poor step coverage. If etch rates are too high, no film growth takes place and the patterned surface itself comes under attack. It can be seen that for a given set of processing conditions, the wider the interconnect line, the thicker the film required for planarization to take place. Decreasing the net deposition rate decreases the equilibrium angle which allows planarization to be achieved with a thinner film. However, the lower net deposition rates may lead to even longer processing times.

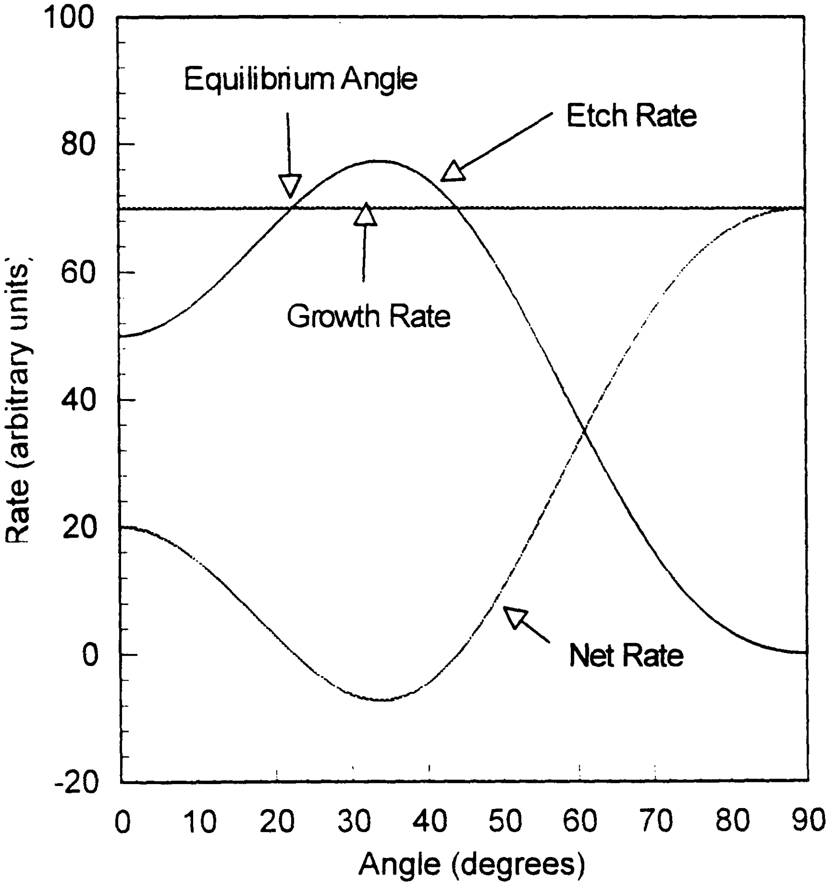

Figure 2.2 Simultaneous etch and growth rates plotted as a function of ion incidence angle.

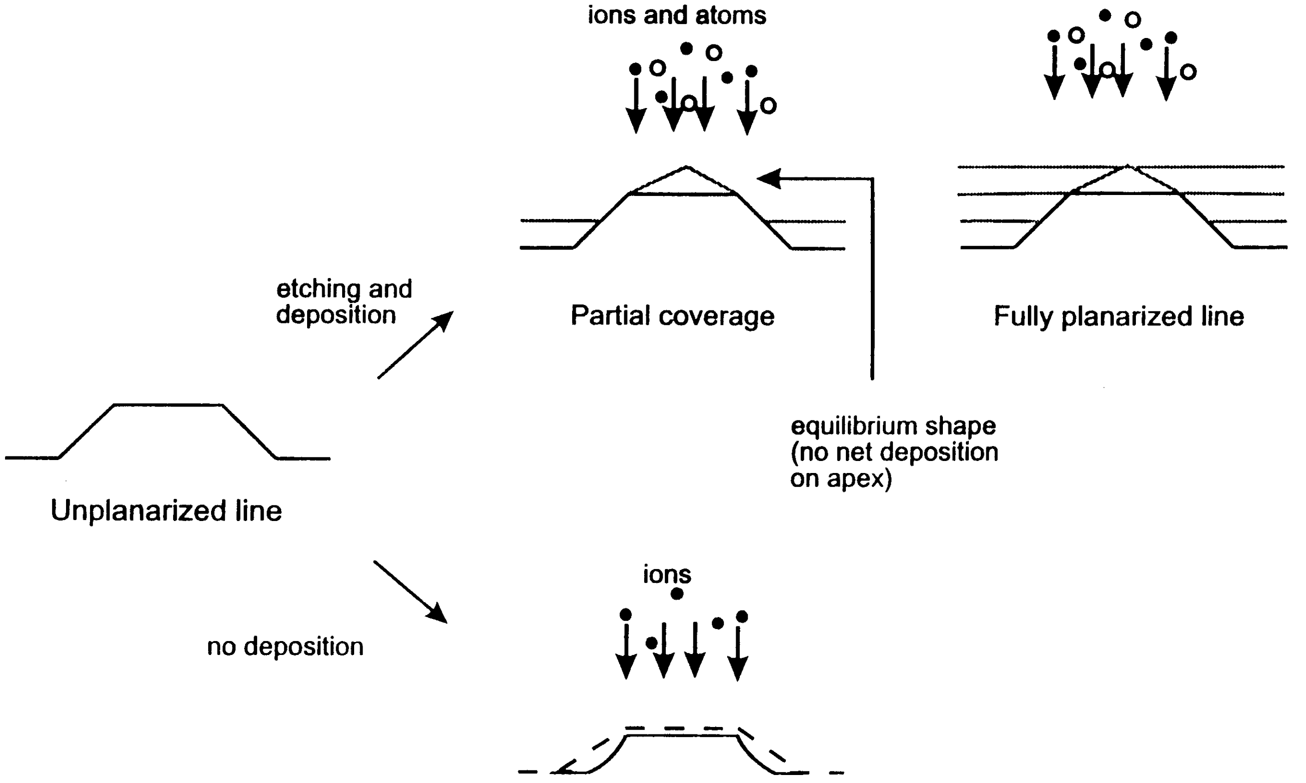

Figure 2.3 Schematic illustrating planarization process via angled surface formation and cone burial as described by C.Y. Ting *et al.*[14]

The above model was developed for planarization of isolated or widely spaced interconnects. This model is also valid for planarization of more closely spaced lines and is relevant for filling in of vias. However, additional parameters such as angular distribution of resputtered material and redeposition become more important and also need to be taken into account. Bader and Lardon[12] have shown through computer simulations that the redeposition of film material sputtered from the growing film has a substantial influence on planarization. Redeposition increases the efficiency of the burial process and also improves coverage of sidewalls. Their computer-simulated profiles agree well with their experimental results for planarizing Al films over a grooved surface.

Redeposition is a function of the angular distribution of material sputtered from a surface, which in turn is influenced by several factors including the energy of the bombarding ions, the angle of ion incidence, and the crystalline nature of the material being sputtered. For amorphous and polycrystalline materials, Vossen[58] describes a dependence on ion energy. A cosine distribution results from bombardment with incident ions of moderate energy (~1-10 keV), as shown in Figure 2.4. Increasing the ion incidence energy to greater than 10 keV causes most of the sputtered species to be emitted normal to the surface (i.e., over-cosine distribution), while lowering the ion incidence energy to below 1 keV modifies the angular distribution to one primarily of sideways emissions (i.e., under-cosine). For single crystal materials and polycrystalline materials with a preferred orientation, bombardment at any incidence angle results in material being ejected preferentially along close-packing directions[59,60] as shown in Figure 2.5, which depicts polar plots[12] based on the work of Tsuge and Esho.[60] Figure 2.5(a) shows that normal incidence bombardment results in a symmetric "butterfly" distribution in which sputtered material is emitted preferentially along the close-packed directions of the material. Increasing ejection along the surface normal for increasing energy of normal incidence ions is also observed,[60] which is consistent with Vossen's paper.[59] For off-normal incidence bombardment, material is ejected in the forward direction from the incident beam with increasingly oblique incidence.

The effects of these factors can be seen by examining evolution of the sample surface topography during planarization processing. C.Y. Ting *et al.*[14] point out that in

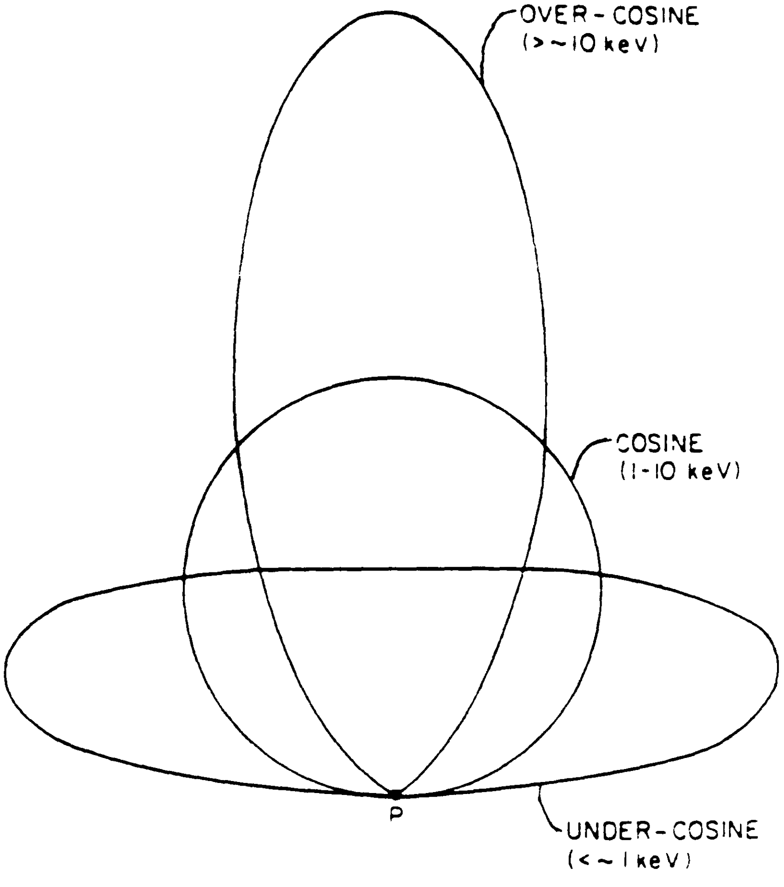

Figure 2.4 Sputter emission patterns as a function of ion incidence energy.

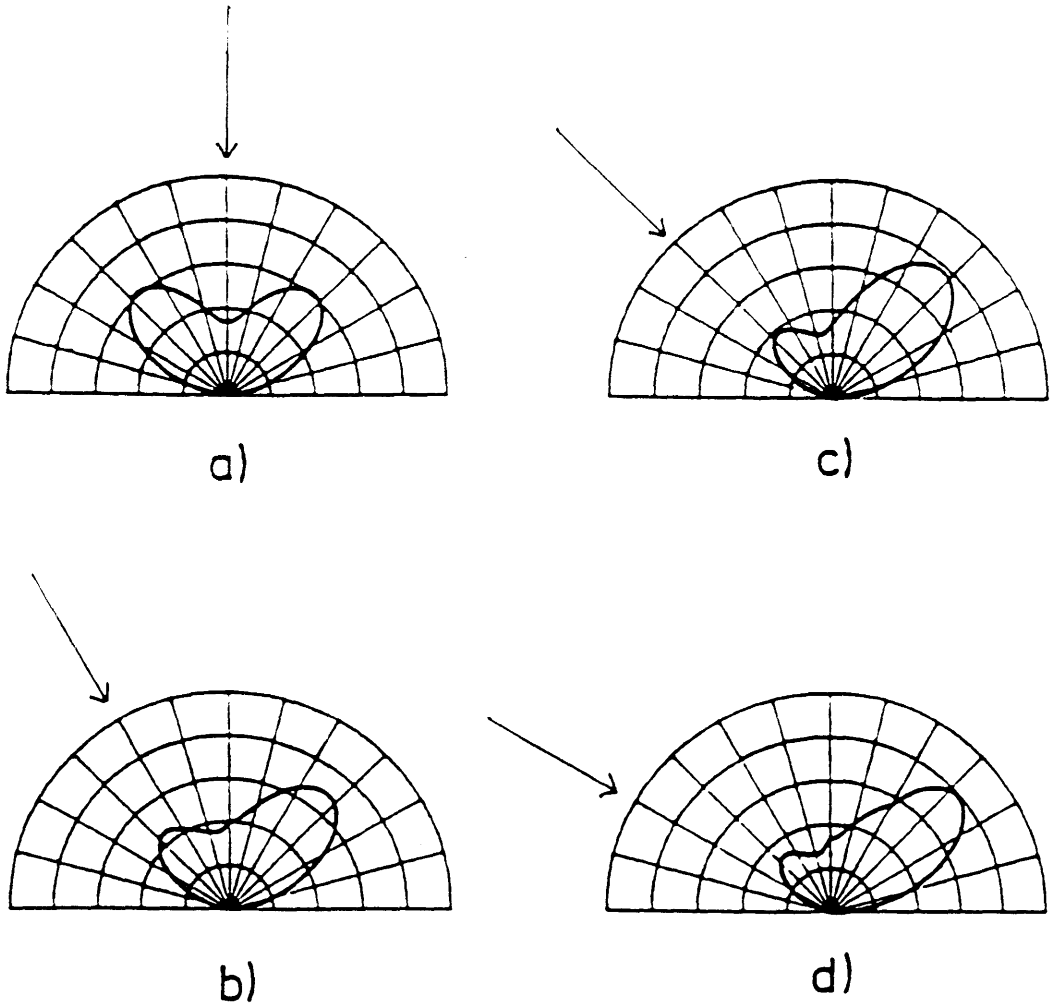

Figure 2.5 Angular dependence of sputtered atoms in plane of incidence. The angles of incidence are: (a) 0°, (b) 30°, (c) 45°, and (d) 60°.

their experimental results for rf bias sputtered SiO_2, an extension of the cone slope always intersects the top corner of the underlying interconnect structure as shown in the schematic in Figure 2.3. The authors maintain that this demonstrates that their planarization mechanism is wholly a burial process and not an edge-moving one. However, C.H. Ting *et al.*[15] observe that even when the underlying line is too wide for cone formation to proceed to completion, the deposited SiO_2 film is still able to smooth over protruding corners due to an increase in film thickness in the planar film near the step edge. This effect was observed both experimentally and in computer simulations of the planarization process (see Figure 2.6). It is clear that in this case, extension of the cone slope does not necessarily intersect the top corner of the underlying interconnect, but the angled surfaces extend beyond the lateral dimensions of the underlying interconnect line. This so called "edge-climbing" effect has similarities to observations made by Kennedy[61] in his studies of step coverage improvement through substrate biasing. Kennedy's model shows that ion bombardment of angled surfaces results in redeposition of forward sputtered material towards the bottom step edge (see Figure 2.7). This in turn is consistent with the work of Tsuge and Esho as described above where oblique incidence bombardment results in forward sputtering of material. This indicates that edge-climbing results from redeposition of forward sputtered material from the angled surfaces. C.H. Ting *et al.* note that the edge-climbing effect increases with decreasing sidewall slope, and is thus a strong function of the net deposition rate curve, and hence material. Therefore, the lower the slope angle, the greater the incidence angle of the incoming ions, and hence, the greater the degree of sputter yield and redeposition.

Although C.H. Ting *et al.* report that they observe only a slight global increase in deposition when redeposition is taken into account in their computer simulations, it is clear that redeposition plays a significant role on a local scale by improving both sidewall and step coverage. The fact that C.Y. Ting *et al.* did not observe the edge climbing effect may be a function of the angle of their interconnect sidewalls and/or their processing conditions. Since they do not report ion energies, it is not possible to estimate the angular distribution of resputtered material for their work. Given the large parameter space with which it is possible to carry planarization using rf bias sputtering, it may be

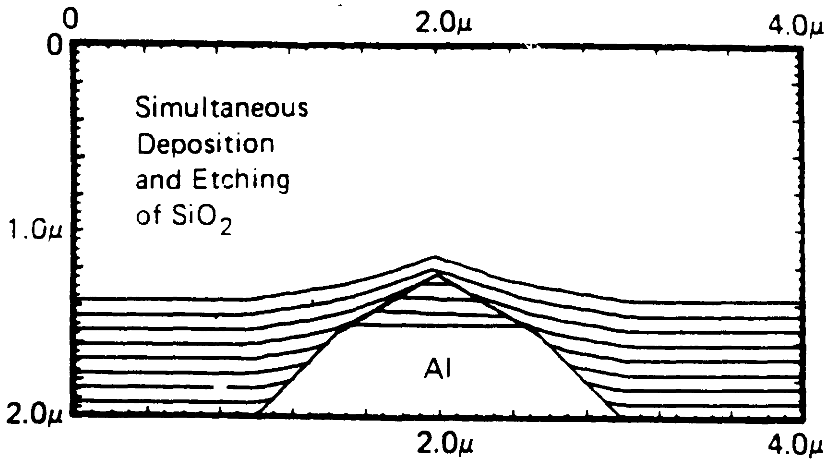

Figure 2.6 Simulated profile for SiO_2 rf-bias sputter planarization of Al interconnects illustrating effect of redeposition (from Reference 15).

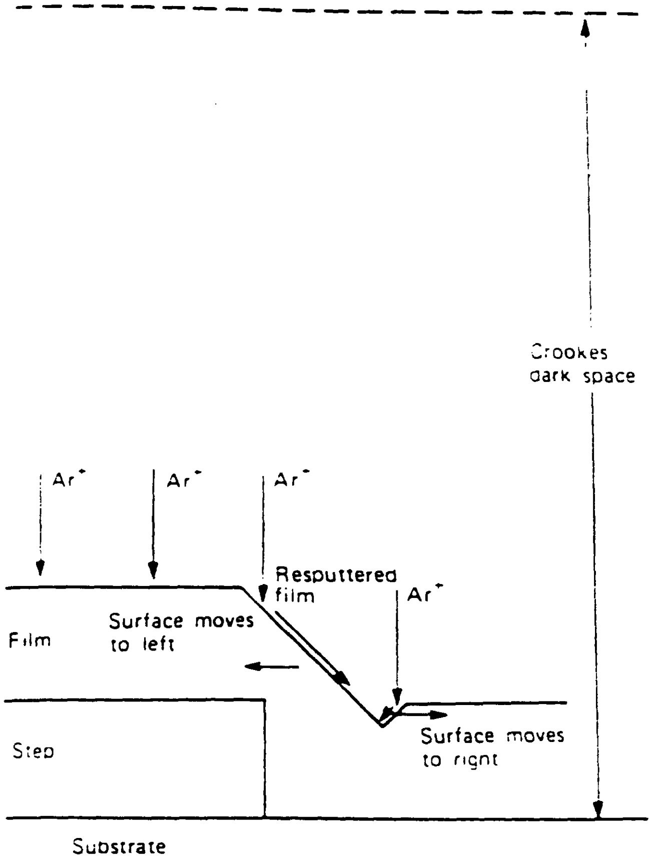

Figure 2.7 Schematic illustrating mechanism by which improved step coverage is obtained when using rf-bias sputtering (from Reference 61).

that their processing took place in a regime that was less dependent on redeposition.

2.3 ORIENTED THIN FILM GROWTH

2.3.1 Epitaxy

The orientation of an epitaxial thin film is determined by the orientation of an underlying single crystal substrate, resulting in the alignment of the two crystallographic lattices with one another. Lattice misfit in epitaxy is defined as $f = (a_f - a_s)/a_s$,[62] where a_f and a_s are the lattice constants of the film and substrate, respectively. Early theories used a strictly geometrical approach in predicting potential epitaxial systems. Royer[63] believed that the substrate and overgrowth needed to possess the same crystal structure and have a lattice misfit below 15% in order for epitaxy to occur. It has since been found that the requirement for identical crystal structures is not so stringent; as long as the film and substrate have a highly coincident atomic structure at the interface which is energetically favored over a random orientation, then epitaxy is probable.[64] It has also been shown that epitaxy can occur for a wide range of misfits. Pashley[62] points out in his review that misfits ranging from -39% to +90% have been measured for certain alkali halide systems. The geometrical approach, however, is still prevalent today, although for different reasons as mentioned below. The lattice misfit of ~4% between Si and Ge, for instance, is considered fairly large in semiconductor film growth.

Mismatch between the overgrowth and substrate can be accommodated in two ways. Pseudomorphism (forced zero misfit) occurs when the film is thin enough to be strained elastically to match the lattice constant of the substrate.[64] A corresponding distortion takes place in the vertical direction. The strain is relieved through the introduction of misfit dislocations beyond a critical strain which is a function of film thickness and lattice mismatch. Completely unstrained or relaxed material will, therefore, have a lattice constant equal to that of bulk material. Partially relaxed systems can also occur in which the film is strained with localized misfit dislocations occurring periodically. Misfit dislocations are of special concern in the semiconductor industry primarily because they adversely affect charge transport. This is the one of the main reasons lattice mismatch is used as the first epitaxial criterion in semiconductor film growth, for which the most desirable system would be truly pseudomorphic. Strained-layer coherent epitaxy at reasonable thicknesses generally requires lattice misfits below 2%.[65]

The major growth modes in epitaxy are Frank-van der Merwe (F-M), layer-by-layer growth; Volmer-Weber (V-M), three dimensional nucleation and growth on a bare substrate; and Stranski-Krastanov (S-K), initial layer-by-layer growth followed by cluster formation. The schematics in Figure 2.8 illustrate these three growth modes which can be classified according to surface energy[66] and lattice mismatch.[67]

F-M growth takes place for systems in which the substrate has a greater surface energy than the film or for which there is a zero misfit. V-M growth occurs if the film has a higher surface energy than the substrate, and also for systems with too large of a lattice mismatch, regardless of the surface energies involved. Systems with strong substrate-film interfacial energies develop in the S-K mode. Excessive strain causes the growth to revert to three-dimensional nucleation and growth after the initial layers have formed.

Recent calculations[67,68] have shown that layer-by-layer growth is never energetically favored for non-zero misfit systems due to the strain energies involved. F-M growth can occur if the nucleation barrier is large, but it will be metastable. Competition between V-M and S-K modes is then determined by the relative strengths of the substrate-film and film-film interfacial energies.

2.3.2 Graphoepitaxy

In graphoepitaxial film growth, film orientation is influenced by the surface relief of the underlying substrate rather than by a crystallographic lattice match.[69] This permits oriented film growth even on amorphous substrates without having to rely on conventional epitaxial growth mechanisms. Graphoepitaxy may be achieved in a number of ways and comprises a number of mechanisms through which orientation may be achieved.[69,70] The most commonly used approach is to create an artificial relief pattern,

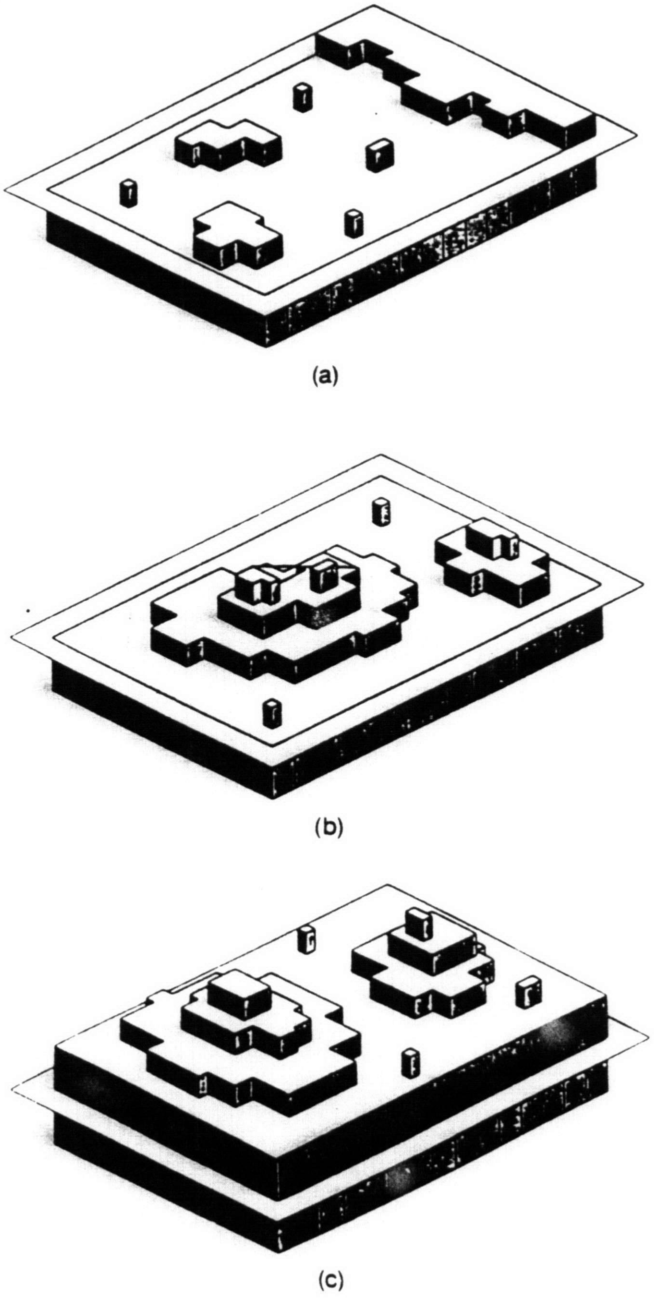

Figure 2.8 Various thin film growth modes: (a) Frank-van der Merwe, (b) Volmer-Weber, and (c) Stranski-Krastanov.

usually on the substrate surface or sometimes in the film itself. In some cases graphoepitaxy on substrates with "naturally-occurring" relief structures has also been reported.

2.3.2.1 Graphoepitaxial Mechanisms

It has been shown thermodynamically how graphoepitaxy can occur on amorphous substrates.[71,72] If the interfacial energy between a given film material and a flat amorphous substrate is minimized for a particular film crystallographic orientation, then the equilibrium film orientation will be similar to a wire texture. For a substrate with the appropriate relief geometry, the interfacial energy is then minimized for a unique in-plane orientation, or essentially a single crystal film. For example, a substrate with a square-wave relief pattern would promote an (001) oriented film with the <100> directions parallel to the square-wave grating for a cubic material whose lowest energy faces are {100}. It has also been shown how the driving force for graphoepitaxy is a function of the relief dimensions. For a surface relief grating with period, *p*, and height, *h*, the driving force increases with (*h/p*).

Several attempts have been made to classify graphoepitaxial mechanisms.[69,70] However, these classifications have been open to debate,[70,73] indicating that the mechanisms involved are still not fully understood. This portion of the literature review will focus on mechanisms described by Smith *et al.*[69] as those that "operate on material in which crystalline grains cannot move as rigid bodies relative to the substrate." In this category, film orientation occurs either directly at the outset with oriented nuclei forming on the patterned surfaces, during film growth, or following deposition through various processing approaches. The period, *p*, of the surface relief in these cases should be smaller than the diameter of grains of the same film grown on a flat substrate.

Smith *et al.* point out the low likelihood of oriented nucleation due to the large difference between the dimensions of critical nuclei (~10 Å) and radii of curvature of artificially created surface steps (~50 Å) on amorphous substrates. Graphoepitaxy during film growth is more likely and comprises several orientation mechanisms, including reorientation during coalescence and preferential growth of grains that are aligned with artificial relief.

Post-deposition techniques that have been used most often involve melting and resolidification or solid-state recrystallization to yield an oriented film.[69] For example, scanning a laser or a strip heater over amorphous Si films grown over gratings etched into SiO_2 substrates causes partial melting to occur. Grains with a (100) texture and <100> parallel to the grating sidewalls remain solid and serve as seeds for resolidification of the molten material with a preferred crystallographic orientation. A refinement of these techniques is zone-melting recrystallization (ZMR), which depends primarily on patterning the film instead of the underlying substrate and embodies additional advantages such as entraining of dislocations.

Graphoepitaxial solid-state recrystallization is a method of converting an amorphous or polycrystalline film deposited over a surface relief grating to one with a single in-plane orientation by annealing at temperatures below the film material melting point and utilizing the phenomenon known as surface-energy-driven secondary grain growth (SEDSGG).[69,74] SEDSGG is driven by the reduction of surface energy, which is highly dependent on crystallographic orientation, as opposed to normal grain growth, in which the driving force is the reduction of grain boundary energy.[75] Grains with the lowest surface energies grow by consuming those with higher surface energies. The result is a film with a single out-of-plane crystallographic orientation and in-plane wire texture. The driving force for SEDSGG is inversely proportional to film thickness and grain sizes tend to be much greater than the film thickness while normal grain growth usually produces grains with sizes on the order of the film thickness. As with the thermodynamic model discussed above, the presence of a surface grating acts to align the grains during SEDSGG, producing a film with a single in-plane orientation. The first demonstration of this type of graphoepitaxy was for Ge films.[74]

2.3.2.2 Graphoepitaxy on Single-crystal Substrates

It has long been observed that preferential nucleation occurs at monatomic surface steps on single-crystal substrates.[76] Although the possibility of oriented nucleation taking place at artificially created steps appears unlikely, the dimensions of natural surface relief on single crystal substrates suggest that these types of steps may indeed support graphoepitaxial growth.[73]

Osaka and co-workers have studied Sn vapor deposited at room temperature on single-crystal (100) KCl[77] and NaCl[78] substrates which were cleaved in an ultra-high vacuum (UHV). Slow cleavage of these alkali halides produced surfaces with six different zones, each of which had its own step density and characteristics. Step heights as low as 1.0 and 0.5 nm were observed on KCl and NaCl, respectively. It was found that in the absence of steps, Sn grew epitaxially on KCl with (010) Sn $\|$ (001) KCl, and [100] Sn $\|$ [100] or [010] KCl, which correspond to lattice misfits of -1.1% and 7.3%, respectively. When steps were present, however, the Sn particles would be aligned with the steps, even when the steps were not parallel to the substrate <100>. Reorientation of islands upon coalescence was also observed. If the step period was less than a critical width, w_c, coalescence between an island located at a step and an epitaxial island would result in a larger island oriented parallel to the step. For spatial periods greater than w_c, however, the epitaxial islands were able to grow to a larger size before coalescence occurred and thus were able to dominate the step-oriented islands. This emphasized the importance of small spatial periods. Osaka *et al.* concluded that a stronger influence on the orientation of Sn particles was exerted by the KCl surface relief than by epitaxial forces as a result of a greater extent of minimization of surface and interfacial energies. Complete epitaxy was thus obtained when the steps ran parallel to the substrate <100> directions. Osaka *et al.* also point out, however, that the extent of graphoepitaxy for a given system will depend on the extent to which the interfacial energies can be minimized. Therefore, graphoepitaxy may not always occur.

Osaka *et al.* also examined Sn growth on NaCl. Over non-stepped areas, Sn particles grew with a completely random orientation. This was most likely due to the larger misfit between Sn and NaCl as compared to Sn and KCl (13.6% and 3.5% for the above-mentioned orientations). In the presence of steps, however, Sn grew with its <100> directions parallel to the steps, regardless of the underlying substrate crystallographic orientation, demonstrating that Sn does grow graphoepitaxially on NaCl. The authors point out that previous work describing epitaxial Sn growth on NaCl did not take into account the effects of surface topography and that it may actually have been graphoepitaxy instead of true epitaxy that was occurring in these instances.

Work carried out at Cornell University on the growth of BYC superconducting thin films on MgO substrates[34-40] also demonstrated how surface steps can influence oriented thin film growth. Single crystal MgO substrates were prepared in one of two ways prior to film deposition to generate surface relief. In one series of studies,[34,35] (001) oriented MgO substrates were optically polished and then heated in air or oxygen to 1100-1200°C for 12-24 hours. At these annealing temperatures, the atomic mobility was high enough to permit surface step formation which lowered the total free energy of the system. In another study,[36,39] MgO single crystal substrates were vicinally polished 3° to 10° from the (001) normal and annealed in the same manner as before. Vicinal surfaces have a high Miller index which upon annealing, will reconstruct so that it consists of a series of low index terraces and steps.[79] Again, the formation of surface steps lowers the overall surface energy. BYC was then deposited on both types of treated substrates using pulsed laser deposition. Previous work using MgO substrates had showed that BYC films nucleated preferentially at steps and grew via an island mechanism.

X-ray and pole figure analysis showed that BYC films deposited on the annealed substrates were c-axis oriented with a single in-plane orientation. These films had critical current densities of 3.4-6 x 10^6 A/cm^2 which were comparable to high quality films grown on $SrTiO_3$ and $LaAlO_3$ substrates. In contrast, BYC grown on substrates which either had not been annealed or were chemically etched to generate an atomically smooth surface had more than one in-plane orientation and substantially lower J_c's. The authors concluded that the presence of atomic-scale surface steps provided preferential nucleation sites for BYC and acted to align the nuclei, which resulted in increased alignment between the grains as they grew. The absence of in-plane rotations between BYC grains resulted in the avoidance of the high angle tilt boundaries that are often observed in BYC films grown on MgO.

c-axis BYC also grew with a single in-plane orientation on vicinally polished

MgO. It was found, however, that the BYC [001] was parallel to the substrate surface normal rather than the MgO [001]. In addition, the BYC grains had a much larger aspect ratio than typically observed. These results indicated that it was indeed graphoepitaxy and not conventional epitaxy that was taking place. The presence of parallel steps caused aligned nucleation and growth of BYC grains, which coalesced to form elongated grains. The rotation between the film and substrate [001] directions, which was also reported by Streiffer *et al.*,[41] can be interpreted in terms of a more favorable lattice match between the film and the substrate. In addition, Streiffer *et al.* observed that the quality of the BYC in-plane orientation also improved with greater substrate vicinal angles, which would be consistent with the improvement of lattice match with increasing rotational angle. However, BYC grown on vicinal $SrTiO_3$ does not exhibit the same trend, which indicates that the degree of lattice mismatch may play a large role in determining whether or not graphoepitaxy occurs.

It is seen from the results obtained by both Osaka *et al.* and at Cornell that graphoepitaxy can also take place on single crystal surfaces with the appropriate topographical features and, therefore, is not a phenomenon restricted to artificially altered surfaces alone.

CHAPTER 3

THIN FILM DEPOSITION AND CHARACTERIZATION TECHNIQUES

Details of some of the experimental techniques used throughout the research covered in this thesis are provided in this chapter. This in turn allows the experimental approach in each chapter to focus on aspects unique to that study. The items covered in this chapter are substrate preparation, thin film deposition, and film characterization. In all cases, the technique is described and the experimental procedures are outlined. Any departure from the conditions detailed here will be mentioned explicitly as needed in succeeding chapters.

3.1 SUBSTRATES

3.1.1 Substrate Preparation

The substrates used in this thesis research were commercially available single crystal YSZ (9.5 mol% yttria),[80] $LaAlO_3$,[81] and $SrTiO_3$[82] which had been polished to an optical finish by the vendor. Substrates used for thin film growth were typically 1/4" x 1/4" x 0.020" in size. Larger as-purchased substrates were diced in-house to the desired size using a diamond-impregnated wire saw.[83] All substrates were cleaned by ultrasonication in successive baths of chloroform, acetone, and methyl alcohol for ~15 minutes each. Immediately prior to use, the substrates were carefully wiped with Kimwipes®[84] and methyl alcohol and examined under an optical microscope to confirm that all lint had been removed from the surface.

3.1.2 Substrate Heater Block Mounting

Substrates were mounted on stainless steel blocks that were in turn attached to heater assemblies for both IBAD and sputter deposition. (Details of the heaters are given in Sections 3.2.2 and 3.3.2.) Silver paste was used to ensure good thermal contact between the substrates and the stainless steel block. A slow bakeout procedure was first used to remove solvents from the silver paste before loading the block inside the vacuum chamber. This procedure minimized dewetting that could occur between the silver paste and the substrates due to binder removal upon heating.[85]

The stainless steel blocks were first polished clean and rinsed with solvents. A thin layer of silver paste[86] was spread on the block and the substrates were pressed down over the paste. The block was then heated for 2-4 hours at 80°C in an oven before being transferred to a Neytech furnace. There it was heated to 220°C at 1°/min, held for 4 hours, heated to 400°C at 1°/min, and held for another 4 hours before furnace cooling to room temperature. The entire bakeout procedure was carried out in air. The block was then transferred to the proper vacuum deposition chamber.

3.1.3 Substrate Patterning

Patterned (001) oriented YSZ and $LaAlO_3$ substrates were used for the planarization work described in Chapters 4 and 5. In all cases, the substrates were patterned with 2-3 μm wide lines spaced 2-3 μm apart using standard photolithographic procedures and ion milling.

After substrate cleaning, Shipley 1813 photoresist[87] was spun onto each substrate at 4000 rpm for 30 seconds using a Headway Research spin coater.[88] The specimens were then subjected to a 25 minute soft bake at 90°C. A chrome mask consisting of 3 μm lines spaced 3 μm apart was used to pattern the photoresist. Exposure was carried out with a Karl Suss model MJB3 contact aligner[89] for 8-10 seconds at a setting of 195 watts. The mask and substrates were aligned such that the lines ran parallel to the substrate edges. The photoresist was then developed in CD-30[90] for 20 seconds, rinsed in deionized water for 10 seconds, and hard-baked at 90°C for another 25 minutes.

Ion milling was used to etch ~1500 Å deep trenches in the substrate surfaces using an Oxford ion mill[91] equipped with a 6" Kaufman ion source. The ion source was operated with an Ar ion beam at a beam voltage of 500 V and an ion beam fluence of ~300 μA/cm^2. The individual substrates were held down with thermal grease[92] on a rotating substrate table. No active cooling was employed but the substrates were milled in 5 minute segments to prevent excessive ion bombardment-induced heating and subsequent degradation of the photoresist from occurring. The ion beam was turned off for a 5 minute cooling period following each 5 minute milling segment. Total ion milling time was typically 30 minutes.

After milling, the substrates were first ultrasonicated in either xylene or isopropyl alcohol for 5 minutes to remove the thermal grease before being ultrasonicated in acetone for another 5 minutes to strip off the photoresist. A scanning electron micrograph of a patterned $LaAlO_3$ substrate is shown in Figure 3.1. At this point, the patterned substrates were sometimes fractured in half in order to maximize the number of substrates available for experiments. Each substrate was then cleaned using successive ultrasonicating baths of acetone and methyl alcohol of 15 minutes each and wiped with methyl alcohol and Kimwipes®. The substrates were then mounted on stainless steel blocks with silver paste and baked out using the procedure described in Section 3.1.2.

3.2 ION BEAM ASSISTED DEPOSITION

3.2.1 Background

IBAD is a technique that involves electron beam (e-beam) evaporation of a film and simultaneous bombardment of the growing film with an ion beam. Variations on this technique include dual ion beam sputtering (DIBS)[93] and ion-assisted pulsed laser deposition.[94] IBAD has been used to successfully grow dielectric films with improved properties by favorably affecting the microstructure, density, adhesion, stress, and stoichiometry of the films.[95] More recently, IBAD has been used to grow biaxially aligned films on amorphous[96-99] and polycrystalline[98-101] substrates. The ion bombardment influences the alignment of the growing films by affecting nucleation and also by enhancing the growth of grains of certain orientations. The biaxial alignment can be

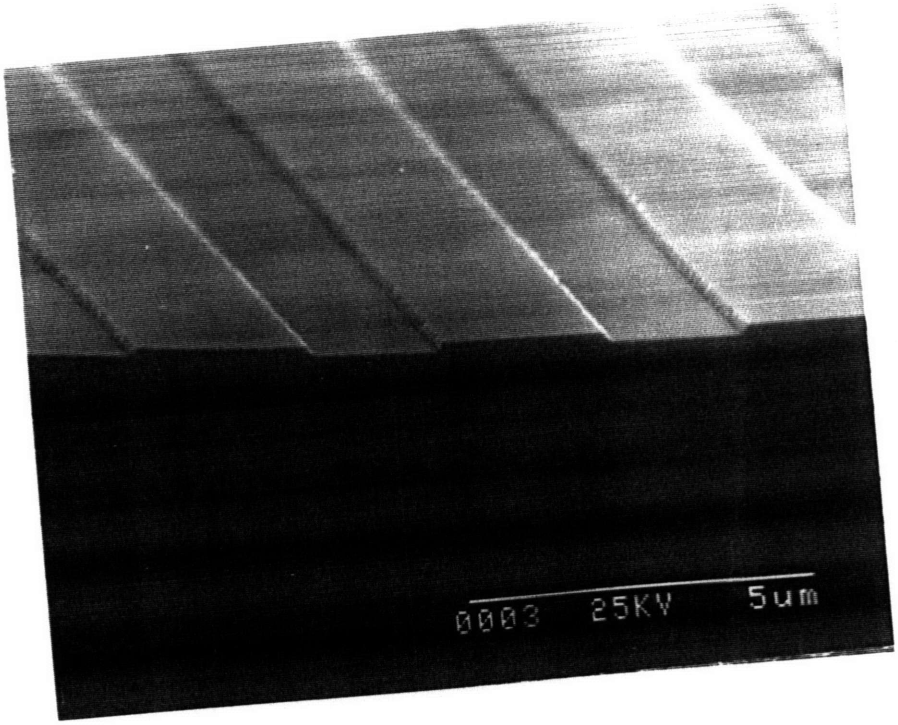

Figure 3.1 SEM micrograph of (001) $LaAlO_3$ substrate patterned with parallel groove structure using standard photolithographic procedures and ion milling as described in Section 3.1.3.

changed by adjusting the angle of ion bombardment. This effect is related to the different ion channeling directions and etching rates of grains of different orientations.

3.2.2 System Description

Figure 3.2 is a schematic of the ion beam assisted electron beam deposition system used in this thesis work. Base pressures of 2×10^{-7} Torr were obtained using a diffusion pump with a liquid nitrogen trap. Evaporation was carried out using a Temescal 14 kW electron gun[102] with specimen sweep capability and a 4-hearth, water-cooled, copper crucible. An Ion Tech rf ion source[103] with a 3 cm diameter beam was used to provide the ion assist during deposition. An Ar - 8% O_2 gas mixture (by volume) was flowed through the ion source while pure Ar was used for the plasma bridge neutralizer. Substrates were located on a heated substrate stage located above the ion source. A swivel assembly allowed variation of the angle of ion incidence.

Deposition rates and film thicknesses were monitored during deposition with a quartz crystal thickness monitor[104] located at the top of the chamber. It should be noted that the measured IBAD deposition rates are probably different from the actual values for evaporation alone since it has been observed that the ion beam affects the thickness monitor. All deposition rates reported in this thesis are the monitor detected rates unless otherwise noted.

The stainless steel substrate block was attached to a Boroelectric heater[105] on the substrate stage. Control of the heater was carried out using an Omega 2010 SSR temperature controller.[106] Block temperatures were monitored using two independent Inconel sheathed Type K thermocouples inserted inside the block. Silver paste was used to ensure intimate contact between the block and the thermocouples. It is expected that the measured block temperatures were higher than the actual substrate surface temperatures due to poor thermal conductivity in vacuum. All deposition temperatures reported in this thesis are the measured block temperatures.

Both YSZ and CeO_2 films were deposited in this system. The YSZ evaporation source was sintered yttria-stabilized (8 wt.%) ZrO_2[107] pellets that had been crushed into 3 mm sized pieces. CeO_2 was evaporated from pieces of fused CeO_2[108] 3-6 mm in size.

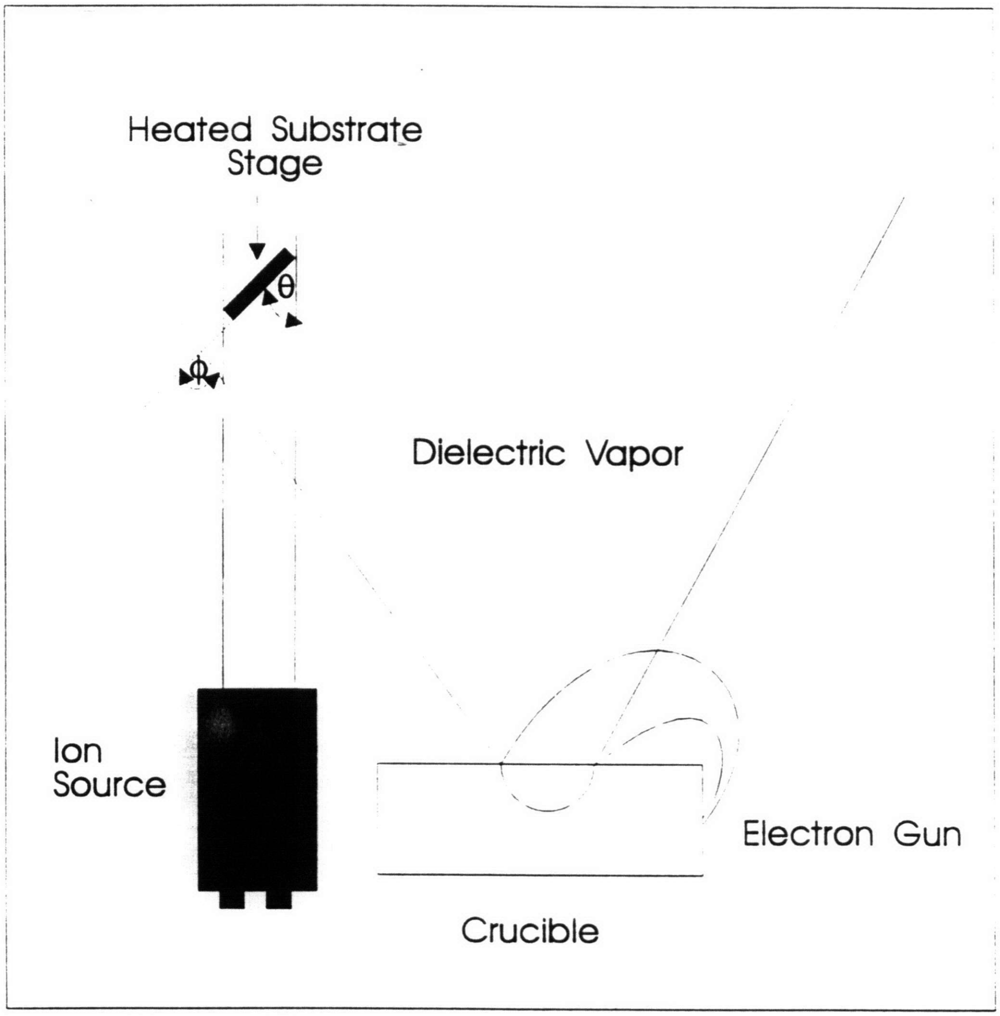

Figure 3.2 Schematic of ion beam assisted deposition system.

3.2.3 Deposition Procedure

The angle of ion incidence (θ in Figure 3.2) is defined as the angle between the incoming ion source and the plane of the substrates. This was varied between 90° (normal incidence ion beam bombardment) and 45°. It should be noted that at 90° ion incidence, the evaporated species arrive at an acute angle, ϕ, to the substrate block, while at 45° ion incidence, the evaporated species arrive at approximately 90° (see Figure 3.2).

The following procedure was used for evaporating both YSZ and CeO_2 films. After loading the substrate block, the system was allowed to pump down to a vacuum of $<5\times10^{-7}$ Torr before starting the Boroelectric heater. The block was first heated to 100°C in 30 minutes and then to 400°C or 600°C over a 2 hour period. The evaporation source was meanwhile slowly heated to the desired e-beam power level and allowed to equilibrate. A shutter located over the crucible protected the substrates from exposure to the evaporated species during conditioning of the evaporation source. Once the desired block temperature and e-beam power level had been reached and equilibrated, the shutter was opened to allow film deposition to begin. Deposition to the desired film thickness was then carried out, after which power to the e-beam was shut off and the substrate block cooled to room temperature over a period of 3 hours, unless an IBAD deposition run immediately followed the evaporation run. The pressure during evaporation was typically $\sim10^{-6}$ Torr.

The heater and evaporation source warm-up procedure for IBAD was identical to that described for evaporation alone unless IBAD was immediately preceded by an evaporation run. In the latter case, the evaporation source was maintained at its elevated e-beam power setting after evaporation had been completed with the shutter closed to protect the specimens. Gas flows to the ion source and the plasma bridge neutralizer were initiated and stabilized once both the desired settings for the heater and evaporation source had been reached. The ion source was then ignited and allowed to warm up for 2 minutes before turning on the ion beam and opening the crucible shutter at the same time. Adjustments were made to achieve the desired IBAD deposition rate at this point. After depositing to the target film thickness, both the ion source and the e-beam powers were shut off and the substrates cooled to room temperature in 3 hours. Chamber pressures during IBAD were typically ~2×10^{-4} Torr.

3.3 RF MAGNETRON SPUTTERING

3.3.1 Background

The MgO films investigated in Chapter 6 were grown using off-axis rf-magnetron sputtering. Sputtering is a momentum transfer process in which energetic particles incident on a target cause atoms to be ejected from the surface. Deposition occurs wherever the ejected atoms come to rest. In practice, ions are used as the sputtering species since they can be accelerated through an electric field to impinge upon a specified target. One way of providing ions for sputtering is by generating a plasma through electron-gas atom collisions. Most plasma-based sputter deposition systems are variations on the basic dc technique in which a high voltage established between a negatively charged source target and an electrically grounded substrate is sufficient to sustain the plasma and thus the sputtering process. Charge buildup on insulating targets, however, eventually leads to termination of sputtering due to both the repelling of ions and the lack of secondary electrons to supply to the plasma. Using an rf power source permits sputtering of insulating targets since the alternating voltage prevents charge buildup from occurring. Sputtering efficiency is also increased since ionization occurs in front of the target due to electrons oscillating in the rf field and therefore does not rely on electrons being supplied from a conductive target. Sputtering efficiency can be further increased by placing magnets behind the target, as is done in magnetron systems. The resulting magnetic field confines the electrons to the target area and also increases the path length travelled by electrons which in turn increases the number of electron-gas atom collisions. This allows sustaining of the plasma at lower deposition pressures.

In a "standard" on-axis sputtering system, the target and substrate are situated parallel to and facing each other. Problems arise, however, when sputtering multi-cation compounds consisting of elements with large electronegativity differences, such as

$Ba_2YCu_3O_{7-\delta}$, or any other complex oxide, in which negative ions are formed that are accelerated towards the substrate. This results in selective resputtering of the film due to the different native etch rates of materials, and can cause severe non-stoichiometry problems.[109] By locating the target and substrates at a 90° angle to each other, the substrates are located within the plasma but outside the region of direct negative ion impact. Stoichiometric complex oxides, such as BYC[110,111] and $LaAlO_{3}$[112] have been successfully fabricated with this technique. One major drawback with this type of sputtering configuration, however, are lower deposition rates. Typical deposition rates are several hundred angstroms per hour.[3]

3.3.2 System Description

The off-axis sputter system used in this work in housed in a ~50 *l* stainless steel vacuum chamber. A schematic of the system is shown in Figure 3.3. The vacuum chamber is pumped by a Balzers[113] TPU270 turbopump with a pumping speed of 270 *l*/s. Base pressures of ~2×10^{-7} Torr were achieved without bakeout.

An US Gun II[114] planar magnetron source was used in the rf mode as the sputter source with rf power supplied by an Advanced Energy[115] 600W 13.56 MHz rf generator. The sputter gas consisted of an Ar - O_2 mixture. Separate MKS[116] mass flow controllers allowed independent control of the two gas flows. The gases were then mixed and introduced through a single injection inlet located at the side of the anode (ground shield). This permits lower overall chamber pressures while allowing the plasma to be maintained at higher pressures. Chamber sputtering pressure during deposition was adjusted using an MKS throttle valve and monitored by a MKS Baratron capacitance manometer.

A 2" diameter 1/4" thick stoichiometric MgO target[117] was used for MgO film deposition. The target was attached directly to the target support using silver paste and baked out for 55 min using an IR lamp. In addition, an aluminum guard ring was fitted to the ground shield to mask the gun backing from the plasma.[118]

The substrate to target distance was about 5 cm. Deposition rates and film thicknesses were monitored using an Inficon quartz crystal rate monitor[119] installed in an off-axis configuration at approximately the same distance away from the target as the

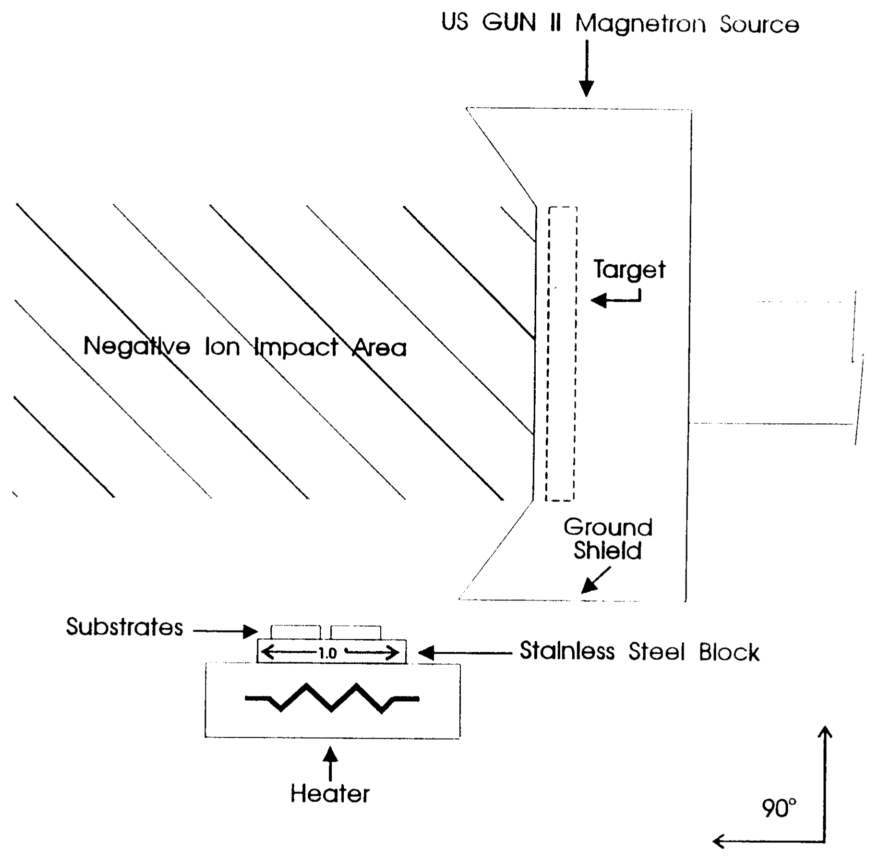

Figure 3.3 Schematic of off-axis rf magnetron sputter deposition system.

substrates.

The stainless steel substrate block was attached to a resistive heater that was fabricated from Kanthal[120] wire and controlled using an Omega[106] temperature controller. The block itself was heated through radiative heating. Deposition temperature was monitored using two independent Inconel sheathed type K thermocouples inserted into the block. Silver paste was also used to ensure intimate contact of the thermocouples with the block. Again, the measured block temperatures were presumably higher than the actual substrate surface temperatures. All reported deposition temperatures are the measured block temperatures.

3.3.3 Deposition Procedure

The following procedure was used to deposit MgO films. After loading the substrate block, the chamber was pumped on until a base pressure of at least ~2 x 10^{-7} Torr was achieved. The heater was then ramped at a rate of 10°C/min to the desired deposition temperature, which was varied between 200°C and 700°C. Upon reaching temperature, the system was allowed to outgas until the chamber pressure was below 1 x 10^{-6} Torr. This usually took about one hour after which the Ar-O_2 sputter gas flow mixture was initiated. O_2 flow was varied between 10-20% out of a total gas flow of 10 sccm. The sputter gas pressure was stabilized at ~5.5 mTorr before igniting the plasma. For deposition at pressures below 5.5 mTorr, the plasma was ignited and stabilized at 5.5 mTorr before lowering the deposition pressure. Unless otherwise stated, all runs were carried out at 100 W of power which yielded a dc self-bias of ~-30 to -50 V and a deposition rate of ~18 Å/min.

The MgO target was presputtered for 30 minutes before beginning deposition on the substrates. This step ensured the removal of any contaminants or surface hydroxide that might have formed while the chamber was exposed to air. A shutter located in front of the heater block protected the substrates during this step.

At the end of the presputter step, the shutter was removed and the thickness monitor rezeroed. Sputter deposition was then continued until the desired film thickness had been reached. The plasma was then terminated and the heater temperature brought to 400°C for deposition temperatures above 400°C, or held at temperature for deposition runs below 400°C. The chamber was then flooded with ~500 Torr of oxygen and the films annealed for 30 minutes. The heater was then shut off and the samples cooled to room temperature before the chamber was vented with oxygen and the samples removed.

3.4 X-RAY DIFFRACTION

A number of X-ray diffraction (XRD) techniques were used to characterize the orientation of the deposited films. θ/2θ and rocking curve measurements were used to determine the out-of-plane films orientations while four-circle diffractometry and X-ray pole figures were used to measure the in-plane orientation. All of these techniques utilize radiation of a fixed wavelength while varying the angle of incidence.

3.4.1 Out-of-plane Texture

θ/2θ XRD, also referred to as powder diffractometry, probes (*hkl*) planes parallel to the sample surface. When used in the symmetric, or Bragg-Brentano mode, the detector position (2θ) is set at twice the angle of incidence, θ, in order to maintain parafocusing. A completely random polycrystalline sample will exhibit diffraction peaks from all allowed (*hkl*) planes, in which peak intensities are governed by a number of factors including atomic position and scattering. At the other extreme, a single crystal that is properly oriented in the diffractometer will diffract only from one set of parallel (*hkl*) planes (e.g. only (*h00*) peaks detected for a (100) oriented single crystal). The peak intensities of textured samples is a measure of the number of planes diffracting for each (*hkl*), and therefore the degree of texture in a film can be determined by comparing the XRD trace against the theoretical powder peak intensities.

A rocking curve measurement of a given peak gives a measure of the degree of alignment of the diffraction vector of the corresponding (*hkl*) plane with the surface normal. The measurement is carried out by fixing the detector position at the proper 2θ value while varying θ from 0° to 2θ. A film that is highly oriented will have a narrow rocking curve. If the preferred orientation is aligned with the surface normal, the rocking curve should have a maximum value at 1/2(2θ). If the maximum occurs at $\theta \neq 1/2(2\theta)$, this is an indication of the preferred orientation being tilted away from the plane of the surface. Rocking measurements should be carried out on a double crystal diffractometer for true quantitative analysis. However, rocking curve measurements obtained using a powder diffractometer can still provide a qualitative assessment of the film texturing.

Although both θ/2θ and rocking curve scans yield useful information regarding the out-of-plane texturing of a film, no information is obtained concerning the in-plane alignment and hence the degree of epitaxy in the film.

3.4.2 In-plane Alignment

3.4.2.1 Four-circle Diffractometry

The goniometer of a four-circle diffractometer has more degrees of freedom than a powder diffractometer. This permits the sample to be adjusted so that planes that are not parallel to the surface may be probed. By examining the relationship of the positions of these planes with respect to the out-of-plane texture, it is then possible to determine the in-plane orientation, if any, that exists within the film.

Figure 3.4 is a schematic of the four-circle diffractometer geometry. In addition to the θ and 2θ axes, the χ and ϕ axes can be used to adjust the tilt of the sample out of the plane used for θ/2θ scans and the in-plane rotation, respectively. An additional parameter, ω, is defined as $\omega = 2\theta - 2(\theta)$. A standard θ/2θ scan on a four-circle diffractometer would be carried out by setting $\omega = 0$ and $\chi = 90°$.

To illustrate the manner in which the in-plane orientations of films were determined, the procedure used to measure the in-plane texturing of MgO films deposited on (100) oriented single crystal substrates is described. The sample was first aligned to the substrate (002) peak at $\chi = 90°$ by adjusting ω to maximize the peak intensity. The goniometer was then moved to $\chi \sim 45°$ and ϕ rotated until one of the four substrate {101} peaks was located. The intensity of this peak was then maximized in both χ and ϕ. Any discrepancy in χ and ω from theoretical values of 45° and 0° were probably due

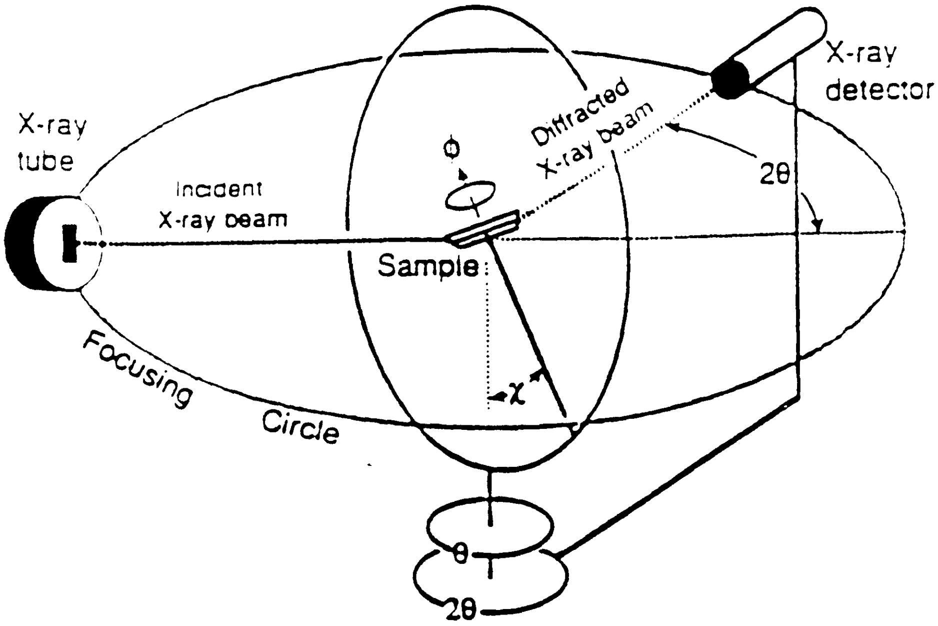

Figure 3.4 Schematic of four-circle X-ray diffraction geometry.

to slight misalignments of the sample on the sample holder. Once the conditions were maximized for the substrate peak, the detector was then moved to the appropriate 2θ position and a ϕ-scan performed to determine the in-plane texturing of the MgO films. For films that were preferentially oriented (001) out-of-plane, the {202} peak was probed at χ~45°, while for films that were preferentially (110) oriented the {001} peak was probed at χ~45°. For these positions, single crystal-like films should exhibit 4-fold and 2-fold symmetry in ϕ, respectively. Results other than these would indicate either multiple or no in-plane texturing.

3.4.2.2 X-ray pole figure Measurements

The pole figure goniometer is similar to that of the four-circle diffractometer in that it allows *(hkl)* planes that are not parallel to the sample surface to be probed. A pole figure plot is a contour map that gives a stereographic representation of the texture of the sample by showing the location and intensities of the poles of the plane being probed. The α′ and β axes of the pole figure goniometer correspond to the χ and ϕ axes, respectively, on the four-circle goniometer. To carry out a pole figure measurement, the detector is set at the 2θ value for the plane of interest and α′ is varied. At each setting of α′, β is swept through 360°. A pole figure can therefore be considered as a series of ϕ scans taken at different χ settings and compiled together to give an overall picture of the texture of a sample.

3.4.3 Experimental Conditions

All θ/2θ and rocking curve measurements were carried out on a Rigaku[122] RU300 diffractometer with a rotating anode source. CuK_α radiation was used at an accelerating voltage of 50 kV and a current of 200 mA. The divergence and scatter slits used were 1° while the receiving slit was 0.15 mm. In addition, a 0.30 mm RSM slit was used to filter out unwanted K_β radiation. All samples were scanned from $2\theta = 10\text{-}100°$ at 10°/min and a sampling interval of 0.05°. Four-circle diffractometry was conducted on a Huber four-circle diffractometer with CuK_α radiation provided by a Rigaku RU300 rotating anode source at an accelerating voltage of 50 kV and a current of 160 mA.

Pole figure measurements were carried out using a Rigaku RU200 rotating anode source at an accelerating voltage of 50 kV and a current of 180 mA. All pole figures were measured from $\alpha'=15°$ to 90° with an α' step of 5° and a β step of 5°. Individual β-scans were measured with a β step of 1°.

3.5 FILM MICROSTRUCTURE

Film microstructure was examined using both scanning electron microscopy (SEM) and atomic force microscopy (AFM). SEM work was carried out on a Hitachi[123] S-530 microscope using an accelerating voltage of 25 kV. All SEM samples were sputter-coated with gold prior to SEM observation. AFM work was conducted on a Digital[124] Nanoscope III with a Si tip in the non-destructive tapping mode.

Substrate surfaces were also examined in some cases prior to film deposition using both AFM and optical microscopy. An Olympus[125] BH2 microscope equipped with polarizers and Nomarksi optics was used for the optical microscopy.

CHAPTER 4
HOMOEPITAXIAL PLANARIZATION OF IBAD YSZ

4.1 INTRODUCTION

Development of an epitaxial planarization technology is necessary for successful fabrication of any device involving multilayer epitaxial structures. As is the case with VLSI device processing, planar surfaces are required for good step coverage and for maintaining photolithographic resolution and accuracy. Planar surfaces are also needed to maintain epitaxial quality since the possibility exists for growth of non-epitaxial film as well as formation of other undesirable defects over stepped surfaces. This is an area of special concern for high temperature superconductors (HTSC) such as $Ba_2YCu_3O_{7-x}$ (BYC). In this chapter, the feasibility of an epitaxial planarization process appropriate for multilayer epitaxial devices is studied. Patterned yttria-stabilized ZrO_2 (YSZ) single crystal substrates are planarized with (YSZ) films grown by ion beam assisted deposition (IBAD). A homoepitaxial system such as this provides a model system for studying epitaxial planarization since lattice mismatch is not present. As described in Chapter 3, IBAD involves simultaneous deposition and ion bombardment of a growing film. It therefore embodies essentially the same processing parameters as rf bias sputtering, the *in situ* planarization technique reviewed in Chapter 2.

The results of YSZ homoepitaxial planarization using IBAD are presented in this chapter. YSZ substrates were patterned with a parallel groove structure in order to simulate a layer of conduction lines. The effects of deposition conditions on planarization progress as well as film orientation were determined. The effectiveness of the planarization process was subsequently evaluated by measuring the electrical properties of superconducting BYC films deposited over planarized YSZ surfaces. In the second half of this chapter, the mechanism by which planarization takes places is compared to those reported in the literature. A model was then developed to account for observations unique to this study.

4.2 EXPERIMENTAL PROCEDURE

4.2.1 YSZ Deposition

(001) YSZ single crystal substrates were patterned and mounted on stainless steel heater blocks using the procedures described in Chapter 3. The angle of ion incidence was fixed at 90° throughout this study. It should be noted that at this ion incidence angle, the evaporated species arrive at an acute angle to the substrate block. The substrates were therefore positioned with the groove direction running parallel to the incoming evaporated species in order to minimize shadowing at the steps (see Figure 4.1).

All YSZ depositions were carried out at 600°C. Unless otherwise specified, the following conditions were used for IBAD deposition. All IBAD YSZ films were preceded by an initial 1000 Å thick layer of YSZ evaporated at 0.2 Å/s. IBAD deposition rates were varied between monitor-detected rates of 0.2 Å/s and 1.0 Å/s. Ion beam parameters used were 500 V beam voltage, 180 $\mu A/cm^2$ ion fluence, 600 V accelerating voltage, and 100 mA (i.e., 200%) neutralizing current. An Ar-8%O_2 gas flow of ~7.00 sccm was used for the ion source while an Ar flow of 3.8 sccm was used for the plasma bridge neutralizer. Typical deposition pressures were ~10^{-6} Torr for evaporation alone and ~$2x10^{-4}$ Torr for IBAD.

4.2.2 BYC Deposition and Electrical Characterization

500 Å thick layers each of YSZ and CeO_2 were evaporated at 0.2 Å/s and 600°C after completion of the IBAD layer for planarized samples continuing on for BYC deposition. The CeO_2 was deposited as a buffer layer in order to prevent any reaction from occurring between the BYC and YSZ films. Two types of control specimens were

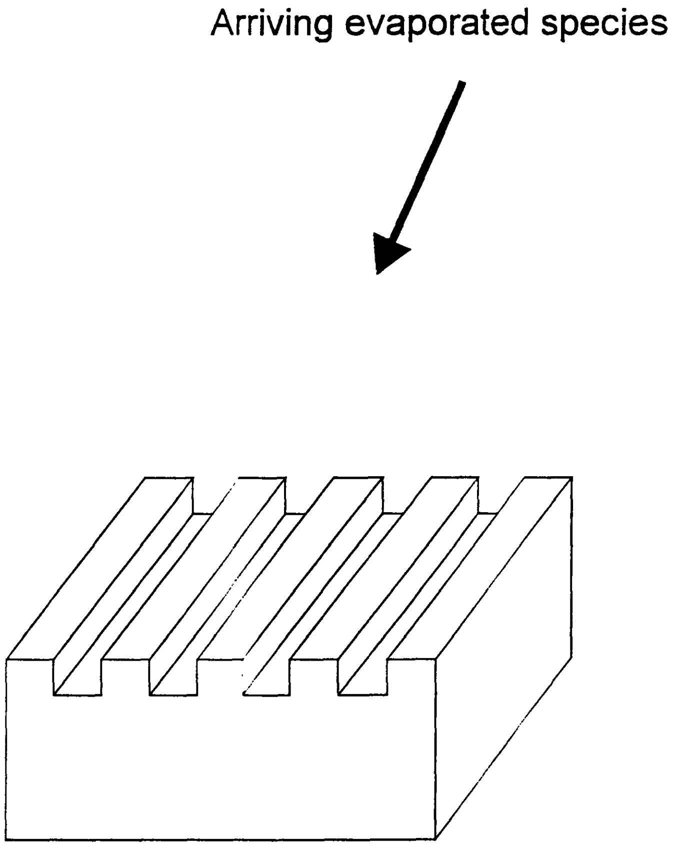

Figure 4.1 Schematic illustrating direction of arriving evaporated species with respect to patterned substrate groove direction.

included with the IBAD-planarized patterned YSZ substrates for BYC deposition. These consisted of as-received (i.e., unpatterned) YSZ substrates taken through the entire IBAD planarization process and patterned YSZ substrates simply coated with a 500 Å thick buffer CeO_2 buffer layer evaporated at 0.2 Å/s and 600°C.

BYC films were deposited using pulsed laser deposition (PLD).[126] Samples for BYC deposition were mounted on a Haynes alloy substrate block using silver paste and heated to 800°C in 300 mTorr of oxygen prior to deposition of BYC. A Nd-YAG laser was used in its frequency-tripled mode to provide UV pulses at 355 nm wavelength. The laser energy density during deposition was 3 J/cm^2/pulse and the repetition rate was 10 Hz. The typical deposition rate at a substrate-to-target distance of 5 cm was ~0.1 nm/pulse. Total deposition time was 3 min 26 sec. The samples were subsequently vented to 600 Torr of oxygen and then cooled to room temperature over a 1 hour period.

BYC films were also deposited using off-axis dc magnetron sputtering[127] and inverted cylindrical magnetron sputtering.[128] Deposition conditions for off-axis dc magnetron sputtering were as follows. Deposition was carried out at a substrate temperature of ~700°C. A stoichiometric BYC target was sputtered at 0.55 A and 130 V using an 80% Ar-20% O_2 gas mixture at a sputtering pressure of 100 mTorr to yield a film deposition rate of ~5 Å/min. A stoichiometric BYC target was also used for inverted cylindrical magnetron sputtering. Deposition rates of ~60 Å/min were obtained at dc target sputtering conditions of 0.35 A and ~150 V in a 400 mTorr 50% Ar-50% O_2 atmosphere. Deposition temperatures were ~750°C-780°C.

Electrical properties of the BYC films were determined using four-point dc current-voltage measurements. A 200 x 1650 μm line was patterned in each BYC film using photolithography and subsequent ion milling to generate test structures for critical current density (J_c) measurements. The line was positioned to run orthogonally to the underlying substrate grooves in each sample and thus passed over ~275 lines, or equivalently, ~550 edges (see Figure 4.2). Silver contacts were evaporated over the films and subsequently annealed at 450°C in flowing oxygen for 30 minutes to ensure adhesion of the silver to the film. The sample was then mounted in a chip carrier attached to a temperature probe. Wire bonding[129] was used to contact the silver pads to the chip carrier

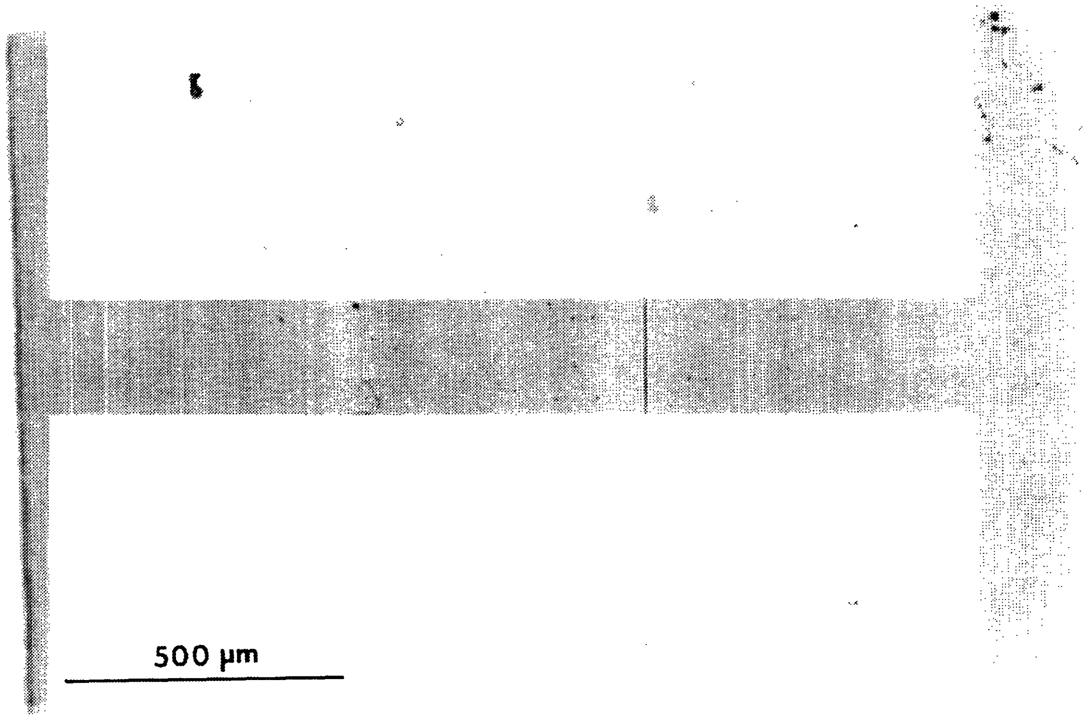

Figure 4.2 Optical micrograph of 200 x 1650 μm patterned BYC test structure used for critical current density (J_c) measurements.

with 0.025 mm diameter aluminum wire. Multiple wires were used for each pad to ensure sufficient current-carrying capability. The temperature probe was lowered into a liquid helium dewar for T_c measurements. J_c measurements were carried out at 77 K using a 10^{-6} V/cm criterion.

4.2.3 Film Characterization

Film orientation was studied using X-ray diffraction (XRD), four-circle diffractometry, and X-ray pole figures, as described in Chapter 3. Planarization progress and film microstructure were examined with profilometry[130] and scanning electron microscopy (SEM). The profilometer was operated at a force of 12 mg and the lowest scanning speed setting on the instrument. Typical scan lengths were 50 μm.

4.3 RESULTS AND DISCUSSION: DIELECTRIC FILM PROPERTIES

4.3.1 Deposition and Etch Rates

The three different rates that will be discussed in this section are the monitor-detected deposition rate, the net IBAD deposition rate, and the IBAD etch rate. The monitor-detected rate refers to the deposition rate that was measured *in situ* by the quartz crystal thickness monitor during film growth and is related to the total evaporative flux. The net IBAD deposition rate for each film was experimentally determined by dividing the film thickness measured from cross-sectional SEM micrographs by the total time it took to grow the film. The IBAD etch rate refers to the sputter etch rate of IBAD YSZ films as measured in separate ion etching experiments described below. Attempts were made to ascertain the net IBAD deposition rates as well as the IBAD etch rates since the monitor-detected deposition rates were used primarily to provide guidelines during film processing and did not necessarily reflect the true growth rate of the film.

The monitor-detected and measured net deposition rates for several IBAD deposition runs are shown in Table 4.1 and Figure 4.3(a) along with relevant processing conditions. No numbers were obtained for a monitor-detected rate of 0.2 Å/s. SEM

Table 4.1 Deposition rates and molecular fluxes for various IBAD YSZ planarization runs

Run ID	Monitor-detected Deposition Rate (Å/s)	Measured Net IBAD Deposition Rate (Å/s)	IBAD Gas Flow (sccm)	Neutralizer Emission Current Value
111993	1.0	1.4	7.5	150%
112293	0.5	0.7	7.5	150%
112393	0.2	----	7.0	200%
120893	0.3	0.14	7.0	200%
120993	0.3	0.15	7.0	200%
ARPA2	0.3	0.3	5.0	200%

Run ID	Monitor-detected Deposition Rate (Å/s)	Monitor-based Molecular Flux (molecules/cm^2 sec)[a]	Measured Net IBAD Deposition Rate (Å/s)	Net IBAD Molecular Flux (molecules/cm^2 sec)[b]
111993	1.0	2.73 x 10^{14}	1.4	2.55 x 10^{14}
112293	0.5	1.37 x 10^{14}	0.7	1.28 x 10^{14}
112393	0.2	----	----	----
120893	0.3	8.21 x 10^{13}	0.14	2.55 x 10^{13}
120993	0.3	8.21 x 10^{13}	0.15	2.73 x 10^{13}
ARPA2	0.3	8.21 x 10^{13}	0.3	5.47 x 10^{13}

[a] Monitor-based molecular flux calculated using theoretical density of zirconia (5.6 g/cc).

[b] Net IBAD molecular flux calculated using estimated film density of 3.73 g/cc and measured net IBAD deposition rates.

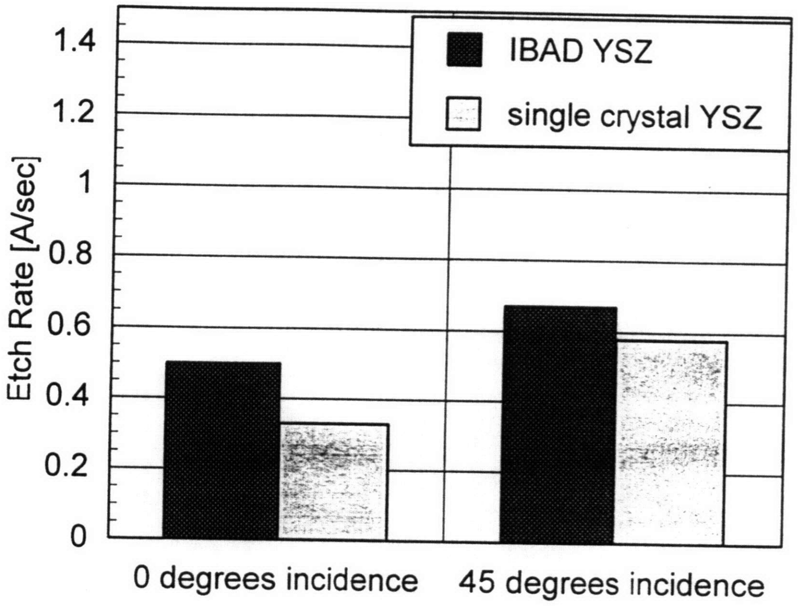

Figure 4.4 Bar graph summarizing etch rates measured for IBAD YSZ deposited at 0.15 Å/s and (001) single crystal YSZ substrates. Ion beam conditions used were 500 eV and 180 μA/cm².

analysis of this sample revealed the absence of any film, indicating that the etch rate was greater than the total deposition rate. Two different net rates were measured for a monitor-detected rate of 0.3 Å/s as a result of system equipment changes that had taken place between the two deposition runs.

The IBAD etch rate was estimated by ion beam etching an IBAD film that had been previously grown at a net IBAD deposition rate of 0.15 Å/s on an as-received YSZ substrate. After completion of the IBAD deposition, the film was removed from the chamber and half of the sample was masked off using colloidal silver paste.[131] The sample was then remounted and loaded into the IBAD chamber where it was ion etched for 10 minutes at 600°C using the same ion beam parameters normally used for IBAD film growth. After cooling, the sample was removed and the silver mask dissolved in nitric acid. Profilometry was used to measure the resulting step height of the film. The etch rate was then calculated from the step height and the total etch time. An etching experiment was also carried out at an ion incidence angle of 45° using the same procedure. For comparison, both etching runs also included bare as-received single crystal YSZ substrates.

Results from the two etching studies are summarized in Figure 4.4. It is seen that etching at a 45° ion incidence angle results in higher etch rates for both IBAD and single-crystal YSZ. This is consistent with the etching behavior of most materials. Ion bombardment at more oblique angles usually results in an increased sputtering yield as a result of the longer path the ions traverse close to the target surface and the greater ease with which forward scattered material can leave the target surface.

It is also seen that single crystal YSZ etches at lower rates for both ion incidence angles. In general, etch rate differences can result from differences in material density (or porosity), degree of material crystallinity, degree of preferred orientation, and material composition. If it is assumed here that the only difference between single crystal YSZ substrates and IBAD YSZ films is material density, then the density of the IBAD film can be estimated as being two-thirds that of the single crystal (i.e., theoretical) density of 5.6 g/cc, or, 3.73 g/cc, since the etch rate for single crystal YSZ at normal incidence was found to be two-thirds that of the IBAD YSZ film. Factors that can influence film

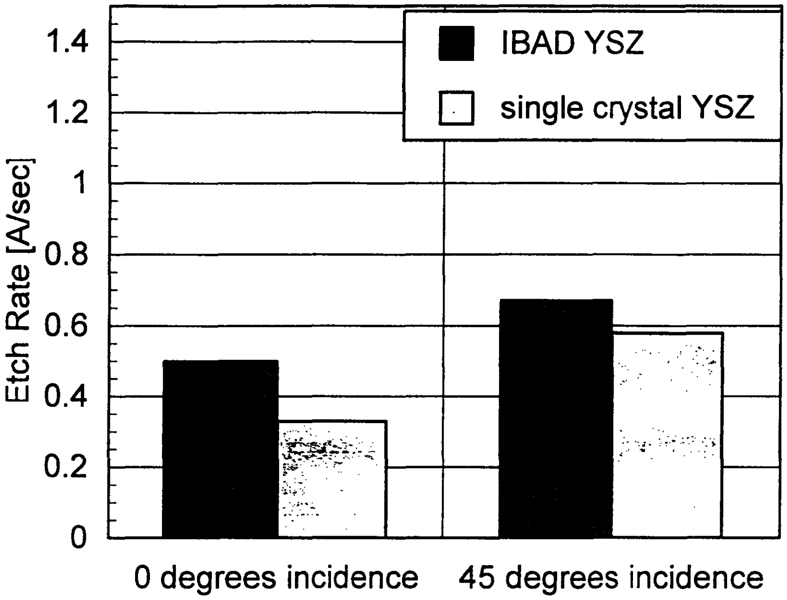

Figure 4.4 Bar graph summarizing etch rates measured for IBAD YSZ deposited at 0.15 Å/s and (001) single crystal YSZ substrates. Ion beam conditions used were 500 eV and 180 μA/cm^2.

density include parameters such as deposition rate, deposition pressure, deposition temperature, sticking coefficient, as well as the ion source parameters used during IBAD. The surface over which film growth is taking place can also influence the microstructure, and hence, density of the film.

The discrepancies in Table 4.1 between the monitor-detected and measured net IBAD deposition rates are due in part to the fact that the deposited IBAD films are not fully dense. The method used to estimate the net IBAD deposition rates listed in Table 4.1 is not completely accurate since what is being measured is the thickness of the IBAD film and not the actual amount of deposited material. The quartz crystal thickness monitor, on the other hand, monitors the deposition rate by sensing the mass of material that is being deposited and converting it to an average deposition rate using the theoretical density of 5.6 g/cc for zirconia.

A more meaningful quantitative comparison of the arriving molecular fluxes based on the monitor-detected and measured net IBAD deposition rates can be made, however, by using the estimated IBAD YSZ film density determined above. Molecular fluxes were calculated using the theoretical density of zirconia for the monitor-detected rates and the estimated density of 3.73 g/cc for the net IBAD rates. These values are listed in Table 4.1 and are also depicted graphically in Figure 4.3(b). Comparison of the two molecular fluxes show that the net fluxes are always lower than the fluxes calculated from the monitor-detected rates. This is expected since ion etching is taking place at the film. Although it is also expected that the density of the IBAD films will vary somewhat as the relative amounts of deposition and etching are changed, it is seen that use of the above estimated density for all of the films does provide quantitative insight into the actual amount of material arriving at the substrate.

Examination of the data in Table 4.1 and Figure 4.3 also shows how changes in IBAD deposition parameters, specifically the neutralizer emission current, can affect the amount of material that is deposited on the substrate. When the value of the neutralizer emission current is kept constant, changes in monitor-detected rates result in changes in the net IBAD molecular flux that scale in the same manner. For example, at 150% neutralizer emission current, a 50% reduction in the monitor-detected rate from 1.0 to 0.5

Å/s also results in a 50% decrease in the measured molecular flux from 2.55 x 10^{14} to 1.28 x 10^{14} molecules/cm^{2}sec. Comparison of deposition runs carried out at different neutralizer emission currents, however, show that changes in net IBAD molecular flux do not scale linearly with changes in monitor-detected deposition rates. A 70% reduction in the monitor-detected rate from 1.0 to 0.3 Å/s results in an order of magnitude reduction in the measured molecular flux from 2.55 x 10^{14} to 2.55 x 10^{13} molecules/cm^{2}sec. This non-linear decrease is consistent with the increase in the neutralizer emission current from 150% to 200% between the two runs. A greater degree of substrate charging is likely to occur for IBAD carried out at lower emission currents which in turn reduces the effectiveness of the ion etching process. When the neutralizer emission current is increased to 200% of the beam current, the higher degree of ion etching in conjunction with a lower evaporation rate results in less material being deposited.

It was also observed that the deposition rates detected by the thickness monitor can be affected by hardware changes in the IBAD vacuum chamber. This is seen by the two different measured molecular fluxes obtained for a monitor-detected rate of 0.3 Å/s as shown for the last two samples listed in Table 4.1. It is therefore important to be able to determine the actual density of deposited films in order to verify the actual deposition conditions.

The measured net IBAD deposition rates will be used throughout the rest of the chapter, except as specifically noted, in order to facilitate discussion of the different IBAD processing conditions that were used. The main exception will be for the sample that was processed at a monitor-detected rate of 0.2 Å/s in which no net deposition took place.

4.3.2 Dielectric Topography

Details of the various YSZ film topographies obtained in the course of this research are presented and described in this section. A summary of these results in given in Table 4.2.

Evaporation of YSZ without ion beam assist at 0.2 Å/s over a patterned YSZ substrate results in largely conformal coverage of the underlying steps in which the

Table 4.2 Summary of step coverage and film topography for YSZ deposited over patterned YSZ single crystal substrates.

Deposition Method	Rate (Å/s)	Step coverage/film topography
Evaporation	0.2	Conformal coverage; crevices in film over steps
IBAD	1.4[a]	Conformal coverage; sharply defined steps in film
IBAD	0.7, 0.3[a]	Complete step coverage; shallower step angles in film that in substrate, but overall topography still non-planar
IBAD	0.15[a]	Cone formation and burial observed; decreasing step height with increasing IBAD processing time
IBAD	0.2[b]	No film deposited; etching of substrate observed

[a] Net IBAD rate

[b] Monitor detected IBAD rate

substrate topography is reproduced in the overlying film. The SEM micrograph in Figure 4.5 also indicates that optimal step coverage was not achieved since crevices appear to be present in the film over the steps.

Deposition and etch rates need to be properly balanced in order for planarization to occur as described by C.Y. Ting's model.[14] If the deposition rate is too low, no net deposition occurs, and instead, the patterned surface itself comes under attack. On the other hand, conformal film coverage of the patterned surface results when the deposition rate is too high and overwhelms the etch rate. Both types of extreme results were observed in the course of this study.

No film deposition resulted for a monitor-detected IBAD deposition rate of 0.2 Å/s (see Figure 4.6). Instead, the net etching rate was sufficiently high to remove the initial evaporated layer of YSZ as well as etch at the underlying substrate. This specimen is, therefore, an example, of how uneven surfaces can be rendered planar through etching alone.

A net IBAD YSZ deposition rate of 1.4 Å/s results in conformal coverage of the patterned YSZ substrate as shown in Figure 4.7. This result is similar to the one obtained for evaporation of YSZ over a patterned substrate. The steps are sharply defined in both the film and the substrate as seen in Figure 4.7.

A trend towards improved step coverage and planarization is observed as the net IBAD deposition rate is decreased from 1.4 Å/s. Figures 4.8 and 4.9 are SEM micrographs for films deposited at net rates of 0.7 Å/s and 0.3 Å/s, respectively. (The 0.7 Å/s film has an evaporated YSZ capping layer while the 0.3 Å/s film has both evaporated YSZ and CeO_2 capping layers.) The sharp step edges present in the substrate are not reflected in the overlying films. Instead, the films exhibit a shallower step angle. These results are consistent with those reported in the literature.[61,132-134] As described by Kennedy,[61] resputtering of the film causes redeposition over areas that are otherwise shadowed from deposition. This is most clearly manifested in Figure 4.8(b). In this micrograph, the initial evaporated YSZ layer can be clearly distinguished from both the substrate and the 0.7 Å/s IBAD film. It can be seen that this initial evaporated layer does not provide good step coverage over the patterned features of the substrate. The patterned

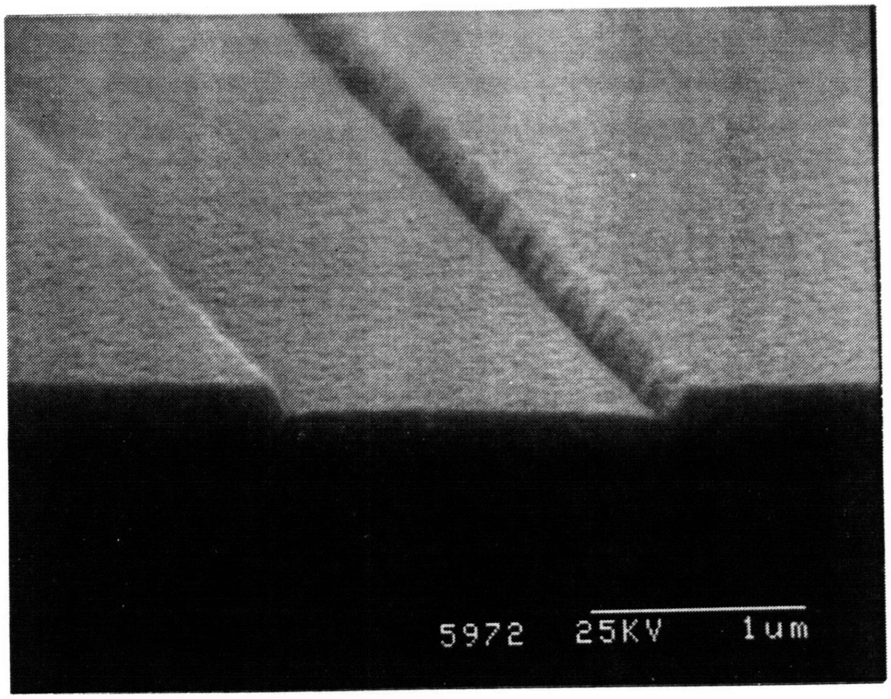

Figure 4.5 SEM micrograph showing conformal coverage of a patterned YSZ substrate by YSZ evaporated at 0.2 Å/s and 600°C.

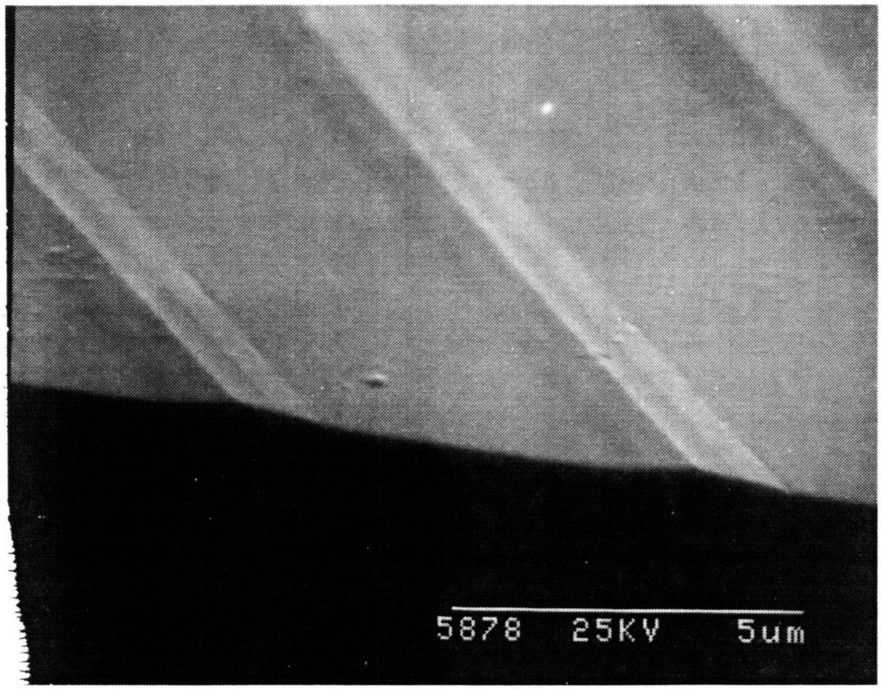

Figure 4.6 SEM micrograph of an etched substrate resulting from IBAD deposition at a monitor-detected rate of 0.2 Å/s at 600°C.

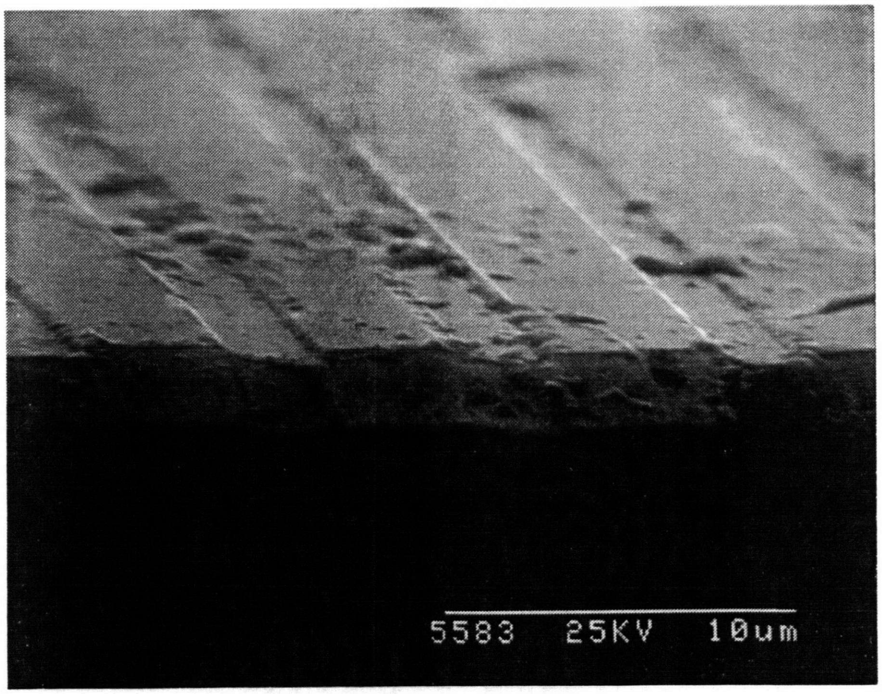

Figure 4.7 SEM micrograph of an IBAD YSZ film deposited over a patterned YSZ substrate at a net IBAD rate of 1.4 Å/s and 600°C.

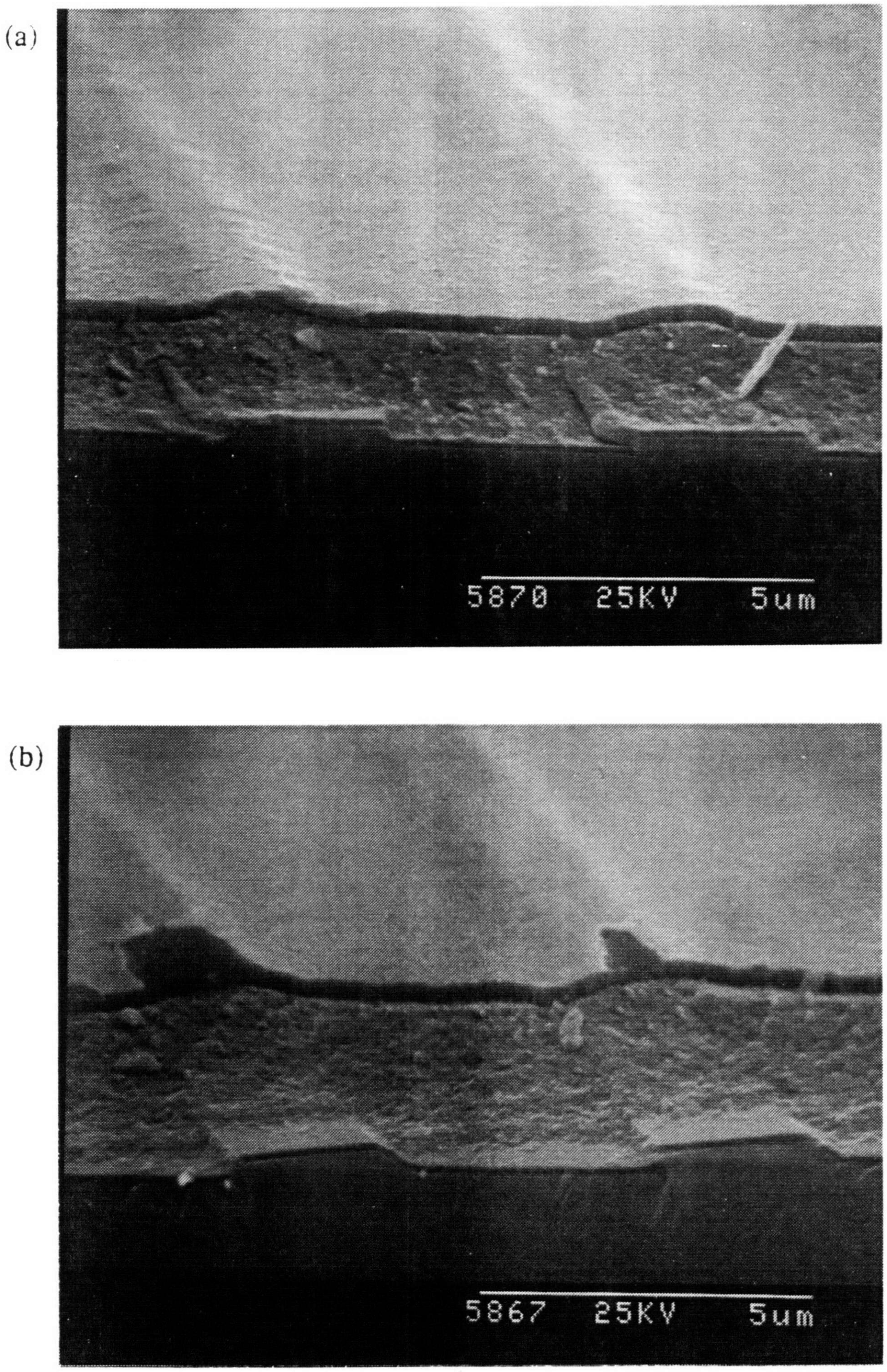

Figure 4.8 SEM micrograph of an IBAD YSZ film deposited at a net IBAD rate of 0.7 Å/s over: (a) symmetric, and (b) asymmetric substrate steps. An evaporated YSZ capping layer was subsequently deposited over the IBAD YSZ film.

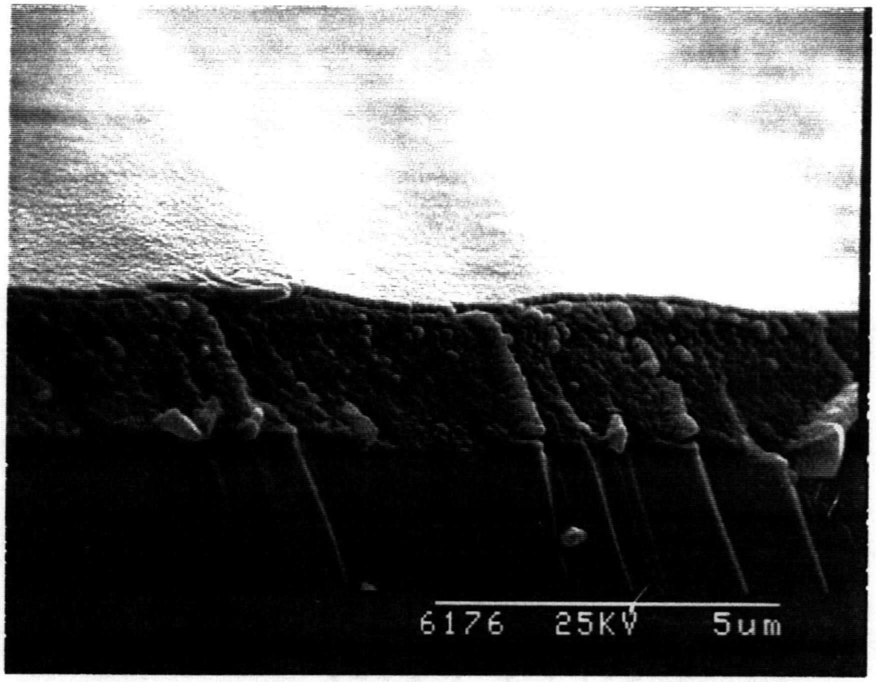

Figure 4.9 SEM micrograph of an IBAD YSZ film deposited at a net IBAD rate of 0.3 Å/s. Capping layers of YSZ and CeO_2 were subsequently evaporated over the IBAD YSZ film.

substrates hills in this region of the sample are asymmetric with respect to step sidewall slope; the right hand side of each step has a shallower slope than the left hand side. Evaporated YSZ step coverage is obtained only on the shallow right hand sidewall of each step. Good IBAD film coverage is obtained over all steps, however, including those which were not fully covered by the initial evaporated layer. The surface topography is smoothed out sufficiently after IBAD processing such that a continuous capping layer can be evaporated across the sample surface. The overall surface profile, however, is still nonplanar.

A progression towards cone formation and planarization is observed when the net deposition rate is further decreased to ~0.15 Å/s. Figures 4.10(a) and 4.11(a) are SEM micrographs of films processed for 165 minutes and 555 minutes of IBAD deposition time, respectively. Clearly defined angled surfaces are found over each step edge. These surfaces approach one another as the film grows and eventually meet to form a cone. Figures 4.10(b) and 4.11(b) are higher magnification images for these two specimens. The YSZ film in the valley adjacent to each step is found to be thicker than that of film grown over either the step or the valley.

Figures 4.12(a)-(d) are a series of SEM micrographs of a sample after ~720 minutes of IBAD at ~0.15 Å/s and ~4000 Å of BYC deposition using off-axis dc magnetron sputtering. The sharply defined substrate topography has given way to a more gently undulating surface that is similar to the samples that were IBAD-planarized for shorter intervals. The BYC appears to have been deposited over the underlying dielectric layers in a conformal manner.

Profilometry traces taken at different stages of processing for this sample are shown in Figure 4.13. The trace of the bare patterned substrate surface shows a square-wave type profile with a peak-to-peak amplitude of ~1750 Å. After IBAD and capping layer processing, the contour of the surface has changed to a sinusoidal shape with a reduced amplitude of ~1300 Å as seen in Figure 4.13(b). Figure 4.13(c) shows a third profilometry trace taken after BYC deposition. Both the shape of the trace and the amplitude are similar to those observed in Figure 4.13(b). These results are consistent with the topographical evolution observed by SEM.

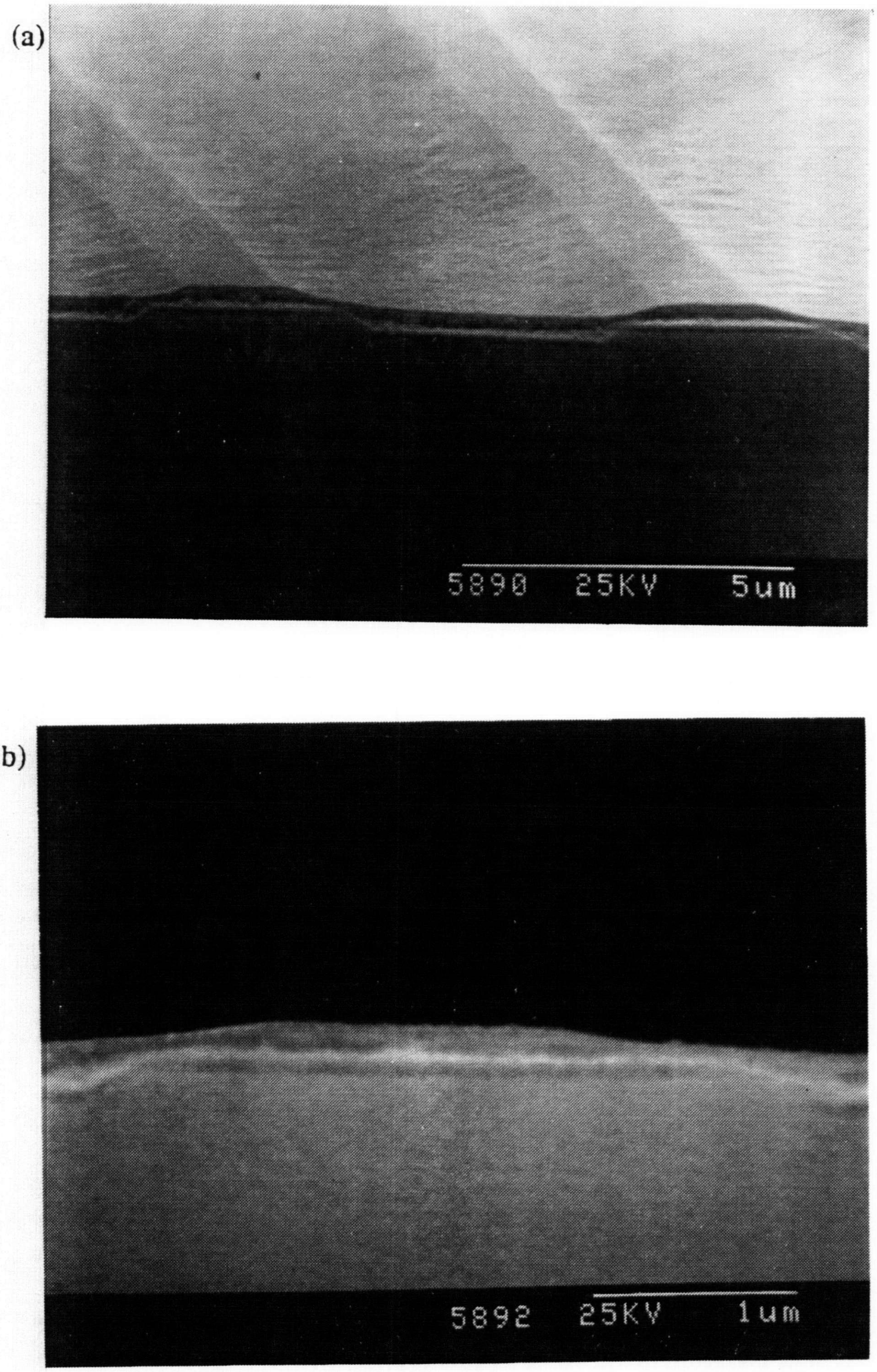

Figure 4.10 SEM micrographs of an IBAD YSZ film deposited at a net IBAD rate of ~0.15 Å/s for 165 minutes: (a) 75° tilt, and (b) 90° tilt.

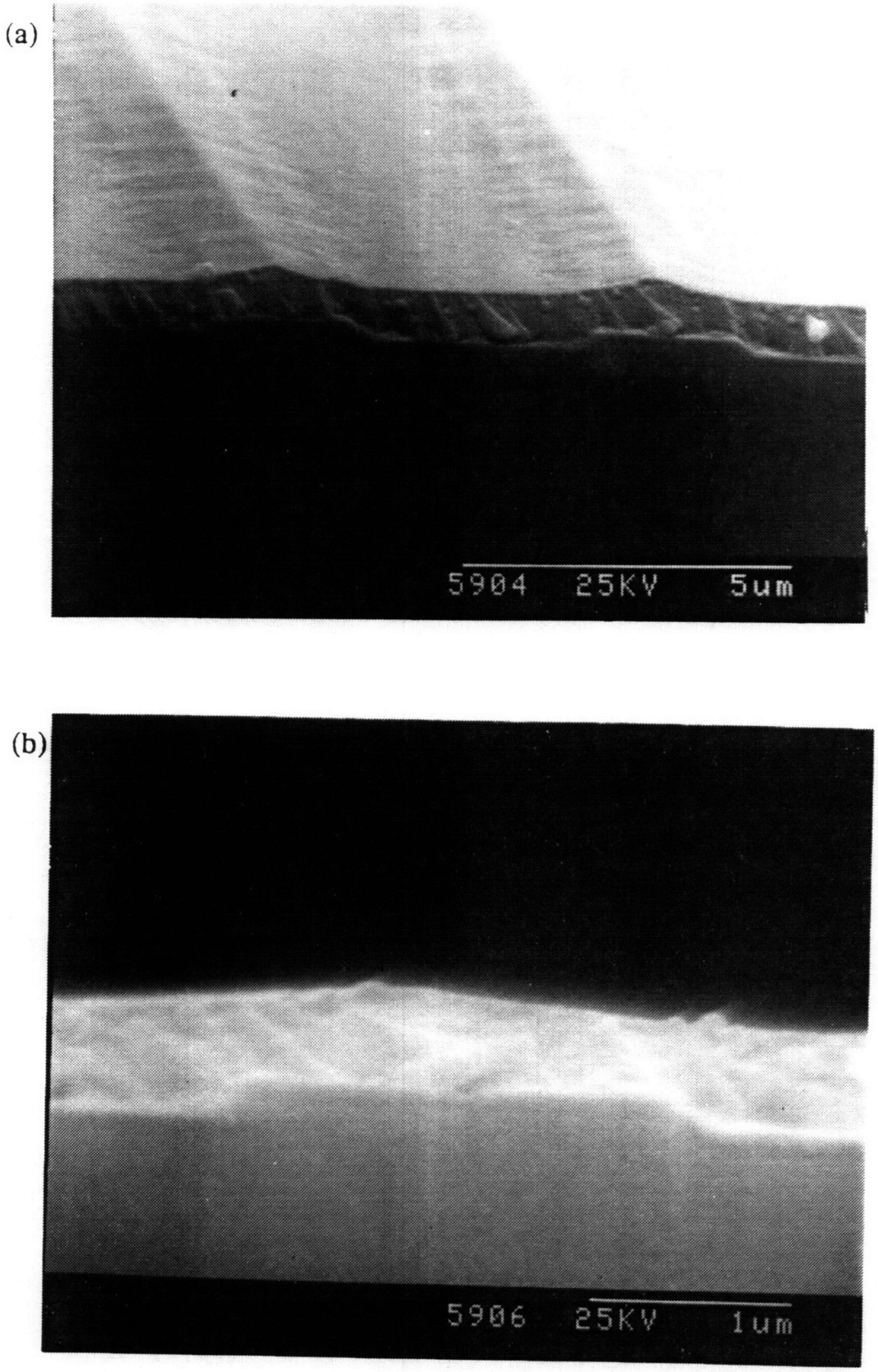

Figure 4.11 SEM micrographs of an IBAD YSZ film deposited at a net IBAD rate of ~0.15 Å/s for 555 minutes: (a) 75° tilt, and (b) 90° tilt.

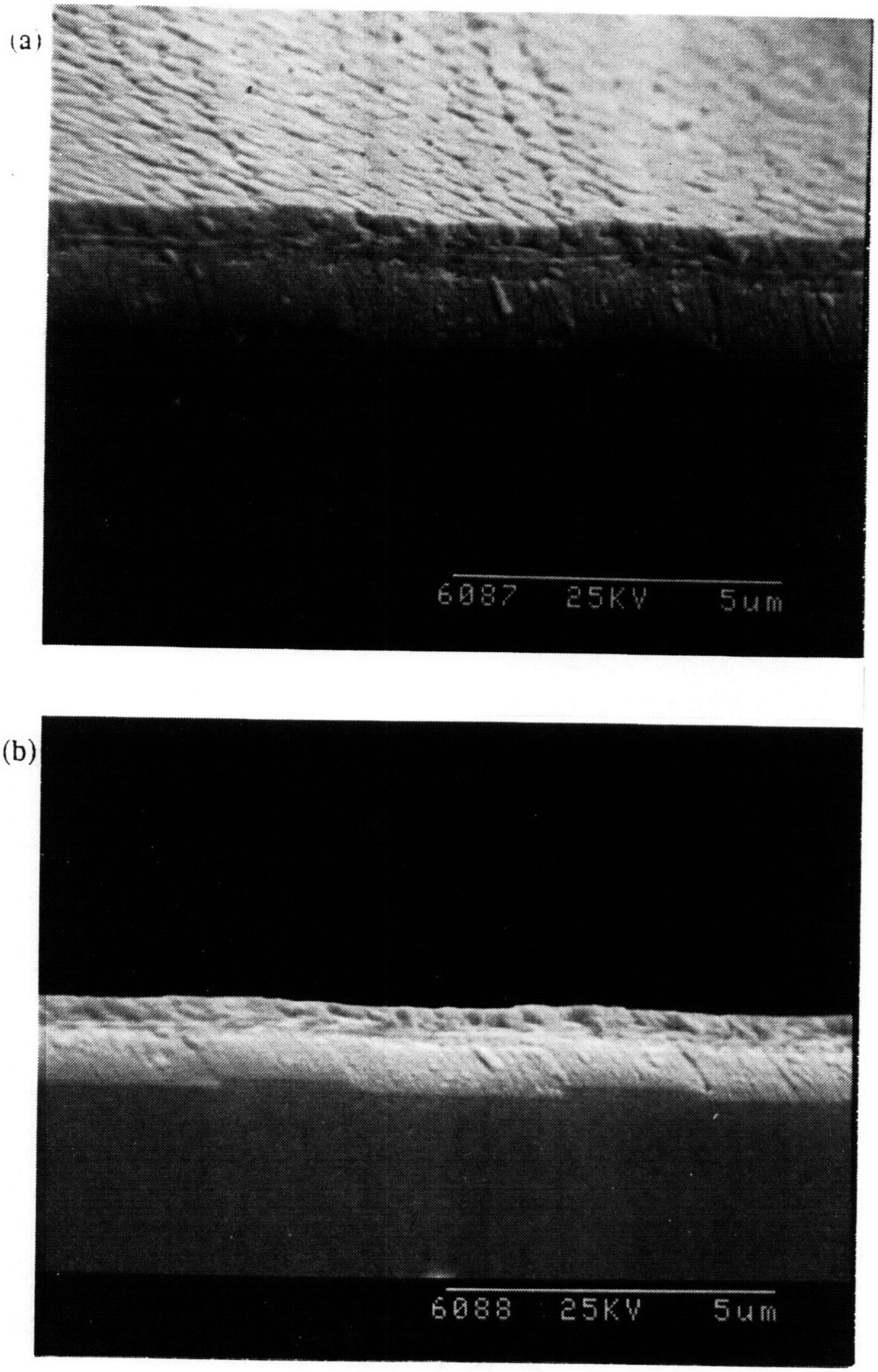

Figure 4.12 SEM micrographs of an IBAD YSZ film deposited at a net IBAD rate of ~0.15 Å/s for 720 minutes; BYC was subsequently deposited on top using off-axis dc magnetron sputtering: (a) 75° tilt, and (b)-(d) 90° tilt.

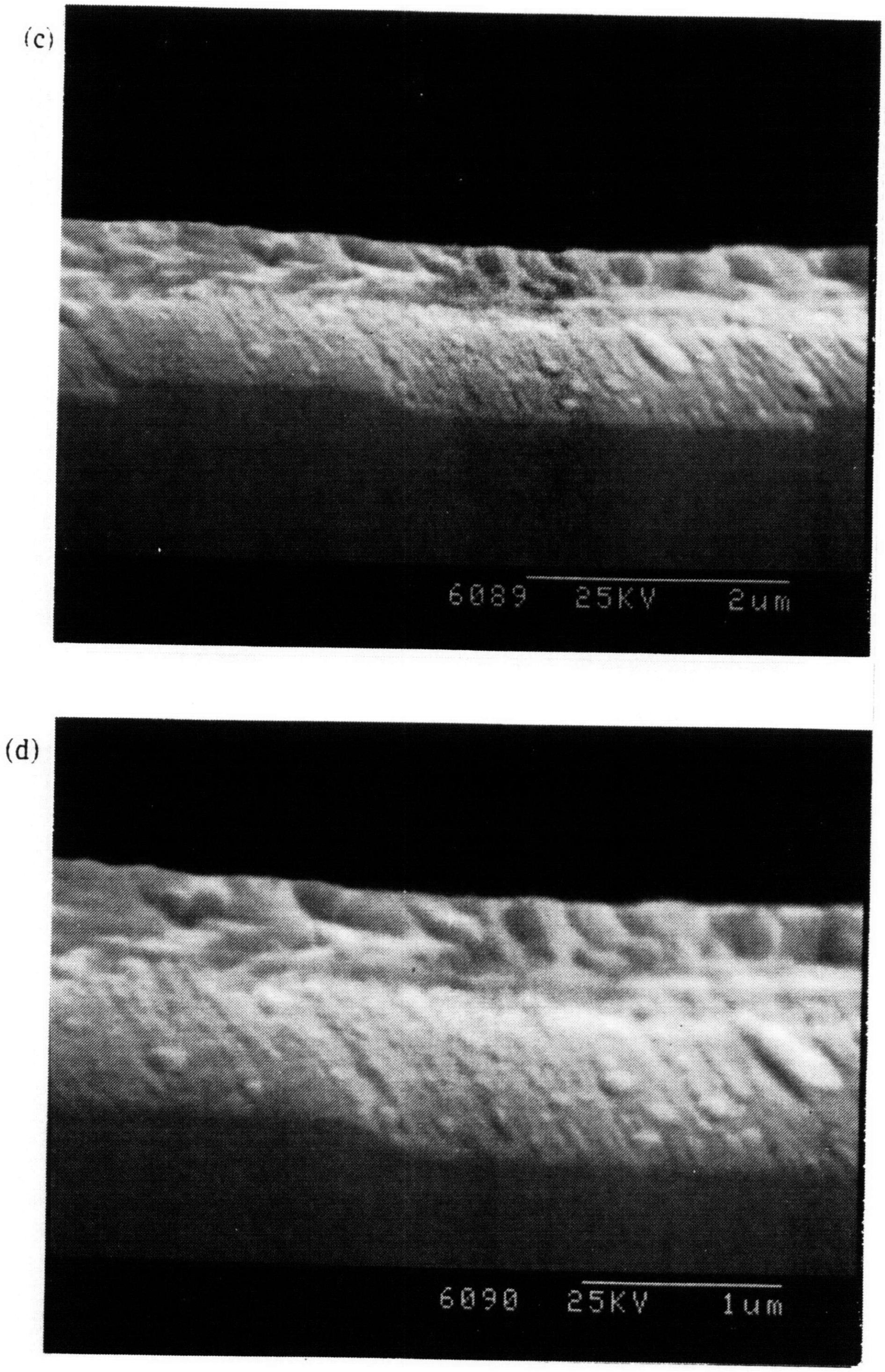

Figure 4.12 (continued).

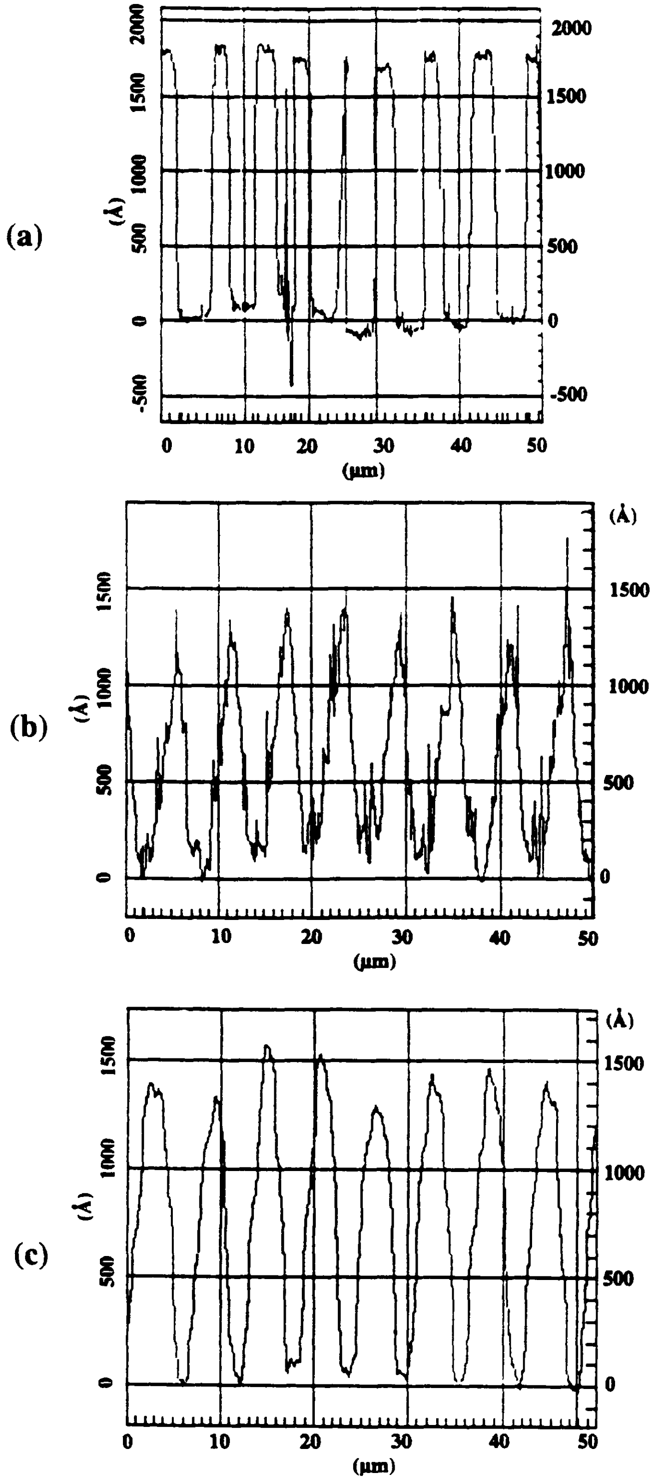

Figure 4.13 Profilometry scans of sample shown in Figure 4.12: (a) before any film deposition, (b) after 720 minutes of IBAD YSZ, and (c) after sputtered BYC film growth.

These results for IBAD YSZ deposited at ~0.15 Å/s are similar to the predictions of C.Y. Ting *et al.*'s planarization model. The series of SEM micrographs in Figures 4.10-4.12 show how angled YSZ films develop over each step edge and grow towards one another with increasing deposition time to form cones. The step height becomes reduced with increasing deposition time as shown by profilometry measurements. A more quantitative analysis of the IBAD planarization results, including comparison to C.Y. Ting's model, will be presented in Section 4.5.

4.3.3 YSZ Film Microstructure

YSZ films evaporated over YSZ substrates at 0.2 Å/s and 600°C have an extremely dense columnar microstructure as shown in Figure 4.5. Examination of the IBAD YSZ sample in Figure 4.14 reveals that a different microstructure is found for both YSZ films evaporated at high pressures and YSZ films deposited with IBAD. The deposition sequence for this particular sample was as follows. ~700 Å of YSZ was first evaporated at low pressures (labeled region "1") before depositing ~8000 Å of IBAD YSZ (region "2") at a monitor-detected rate of 0.5 Å/s. At this point, the ion source was turned off but the source gases were left flowing as another 2150 Å of YSZ (region "3") was evaporated at the same nominal rate. The nominal deposition thickness for both evaporated layers was 1000 Å. A columnar microstructure is also observed for the evaporated capping layer (region "3") which was grown at higher pressures, but the columnar grains are larger. This layer also appears more porous than either the initial evaporated YSZ film or capping layers grown at low pressures (see, for example, Figure 4.9). The columnar microstructure is not observed in the IBAD YSZ film.

Columnar microstructures are commonly observed in evaporated films where the microstructure is a function of substrate temperature as described by the structure zone models of Movchan and Demchishin.[135] At low substrate temperatures ($<0.3\ T/T_m$ (K)), adatom mobilities are low. This causes the formation of a porous film consisting of a highly voided columnar microstructure due to shadowing effects from atoms that have already been deposited. A more strongly bonded columnar microstructure emerges with increasing substrate temperature due to higher adatom mobility. Thornton[136] modified the

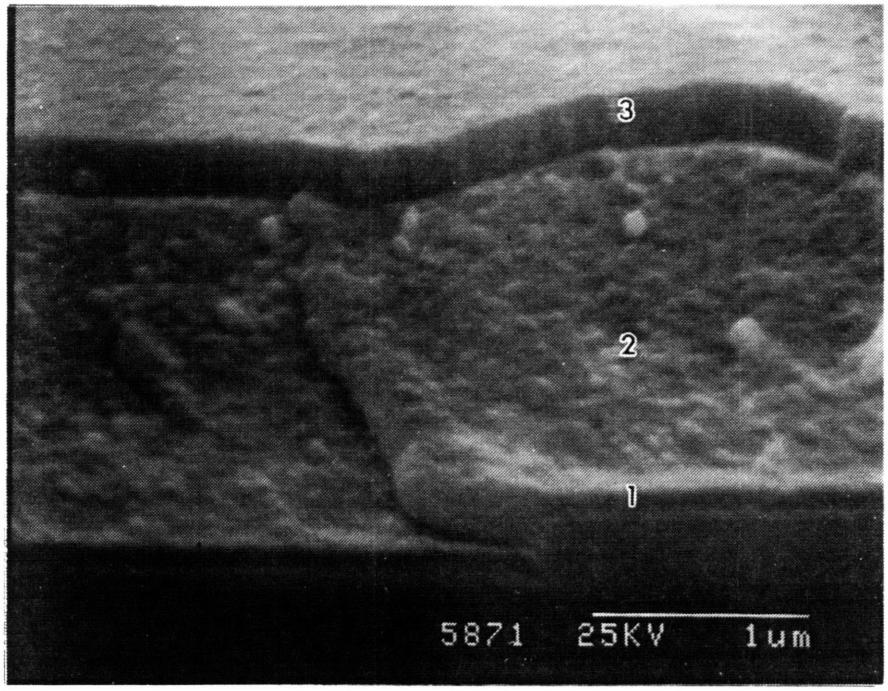

Figure 4.14 SEM micrograph of same sample as in Figure 4.8, showing: (1) initial evaporated YSZ film grown at 0.2 Å/s and low pressures, (2) IBAD YSZ grown at a net IBAD rate of 0.7 Å/s, and (3) evaporated capping YSZ grown at high pressures.

structure zone diagram for sputter deposition by also taking the sputtering pressure into account. At higher gas pressures adatom surface mobility is again limited, this time due to adsorbed argon. This has the same effect as low substrate temperatures and again leads to the development of a porous columnar microstructure.

It is clear from Figures 4.5 and 4.8 that deposition pressure and/or deposition rate affect the microstructure and density of evaporated YSZ films. Examination of the initial and capping YSZ layers in Figure 4.8 reveals a three-fold difference in film thickness although the same amount of film material was deposited for both layers as registered by the thickness monitor. This suggests that the capping layer is only one-third as dense as the initial layer. In this case, the capping layer was grown at both higher deposition pressures (2×10^{-4} Torr vs. 10^{-6} Torr) and higher deposition rates (0.5 Å/s vs. 0.2 Å/s as detected by the monitor). Both conditions can contribute to a lower quality film due to lower adatom mobilities as described above. It is also well known that evaporation at higher background pressures can lead to a more porous film due to entrapment of contaminant gases.[137]

On the other hand, a columnar microstructure is not observed in the IBAD YSZ film. This is consistent with results reported in the literature where ion bombardment was found to modify the microstructure and produce a finer-grained film.[138] The action of the ion beam causes sputtering, redeposition, and redistribution of film atoms to occur. This leads to bridging of voids between grains and interrupts columnar growth. Film densification will occur up to certain values of ion energy and ion-to-atom ratios as atoms become "downward packed" during deposition.[139] These results have been demonstrated through computer modelling based on a variety of approaches and have been confirmed experimentally. (No generalization regarding the effect of ion bombardment on film density can be made however, without knowing the absolute ion energy, ion-to-atom ratio, and film density, since decreases in film density caused by ion bombardment have also been observed.)

4.3.4 YSZ and CeO_2 Film Orientations

XRD measurements of IBAD YSZ films show only the YSZ (00*l*) peaks, but these results are inconclusive since it is not possible to distinguish the film peaks from the substrate peaks. An XRD scan of CeO_2 evaporated over the IBAD YSZ can be used, however, to qualitatively evaluate the orientation of the underlying YSZ since CeO_2 grows epitaxially on YSZ.[21] Evaporated CeO_2 overlayers, therefore, served a dual role as a buffer layer and as a film orientation probe. A 500 Å layer of YSZ was first evaporated over the IBAD YSZ layer before evaporating 500 Å of CeO_2. Both layers were deposited at 0.2 Å/s.

Figures 4.15(a) and (b) show XRD traces for CeO_2 evaporated over IBAD YSZ films processed for 90 and 720 minutes, respectively, at ~0.15 Å/s on patterned substrates. Only the CeO_2 (00*l*) peaks are detected for both samples. The full width at half maximum value (FWHM) of the CeO_2 (002) rocking curve is 1.87° for 90 minutes of IBAD YSZ and 3.70° for 720 minutes of IBAD YSZ. Four-circle diffractometry phi scans of the CeO_2 films show the existence of a single in-plane orientation that is consistent with underlying homoepitaxial YSZ (see Figure 4.16).

CeO_2 (002) rocking curve measurements for CeO_2 grown over the control substrates used in this study show narrower peaks. CeO_2 films evaporated directly over either patterned or as-received YSZ single crystal substrates have FWHM values of 0.72° and 0.81°, respectively. Rocking curves for CeO_2 grown over IBAD-processed as-received substrates are broader. These peaks, however, are still not as wide as those measured for planarized patterned substrates although the exact peak widths do vary with IBAD processing time and conditions. FWHM values for various substrates processed at one set of conditions are shown in Table 4.3.

It was also found that homoepitaxial development of the IBAD YSZ layer can be maintained without depositing the initial layer of evaporated YSZ. CeO_2 films evaporated over IBAD YSZ films that were grown directly on a (001) YSZ single crystal substrate are (001) oriented with the correct in-plane orientation.

Anomalous CeO_2 (002) rocking curves were detected for one set of IBAD planarized samples processed for ~833 minutes at 0.3 Å/s when the XRD measurement was taken across, or "rocked" orthogonally, to the patterned groove direction, as shown in Figure 4.17(a). Two broad low intensity peaks were found, one on each side of the

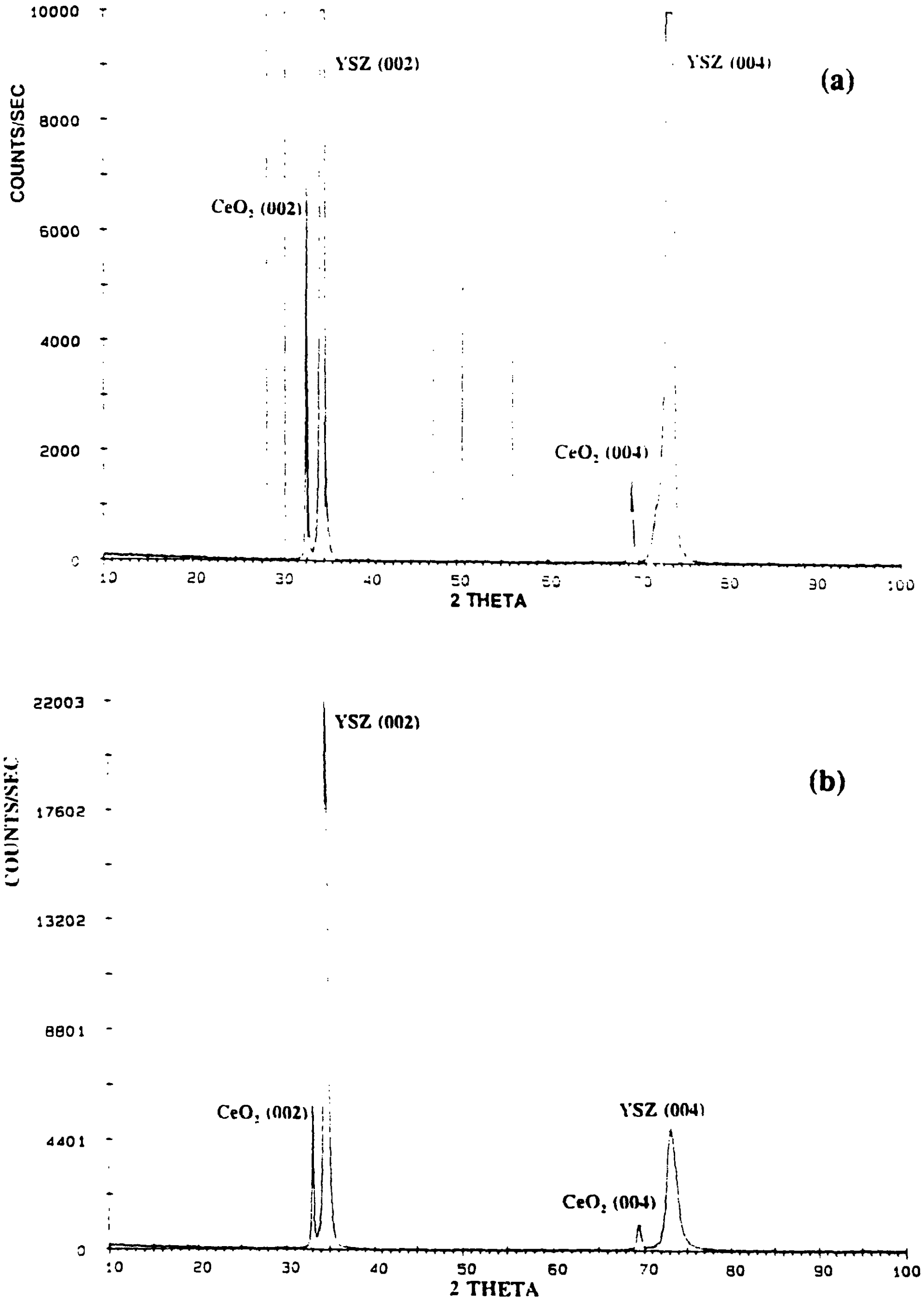

Figure 4.15 θ/2θ XRD scans of CeO_2 films evaporated over IBAD YSZ films that were grown at a net IBAD rate of ~0.15 Å/s for (a) 90 minutes, and (b) 720 minutes.

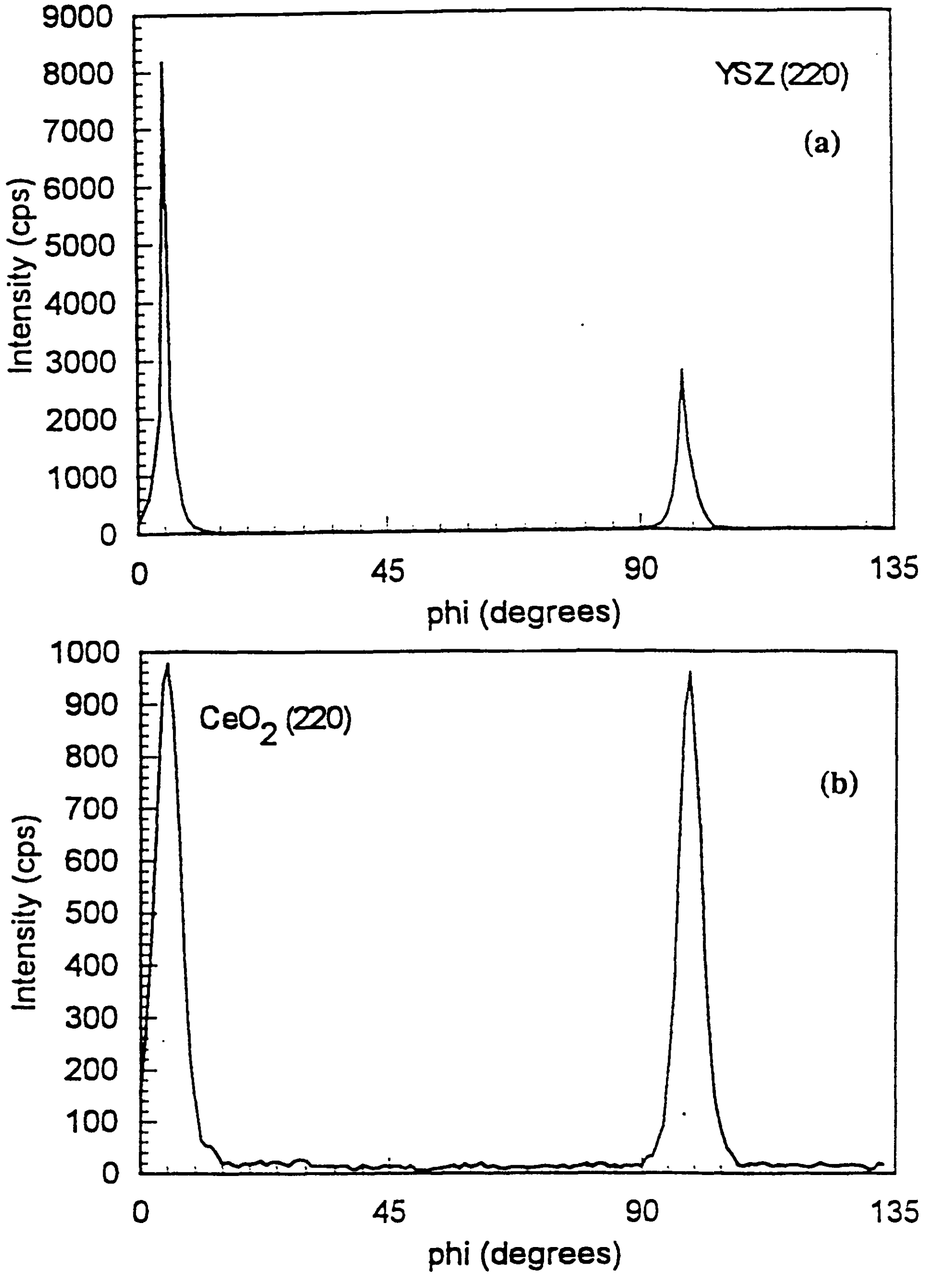

Figure 4.16 Four-circle diffractometry ϕ-scans at $\chi = 45°$ for an IBAD YSZ film deposited at a net IBAD rate of ~0.15 Å/s for 90 minutes: (a) YSZ {220} planes, and (b) CeO_2 {220} planes.

Table 4.3 CeO_2 (002) rocking curves for CeO_2 films deposited on various YSZ surfaces

Sample Number and Substrate Description	FWHM CeO_2 (002)
(A) IBAD-processed as-received YSZ substrate	2.34°
(B) unplanarized patterned YSZ substrate	0.73°
(C) IBAD-planarized YSZ substrate	2.94°
(D) IBAD-planarized YSZ substrate	3.02°

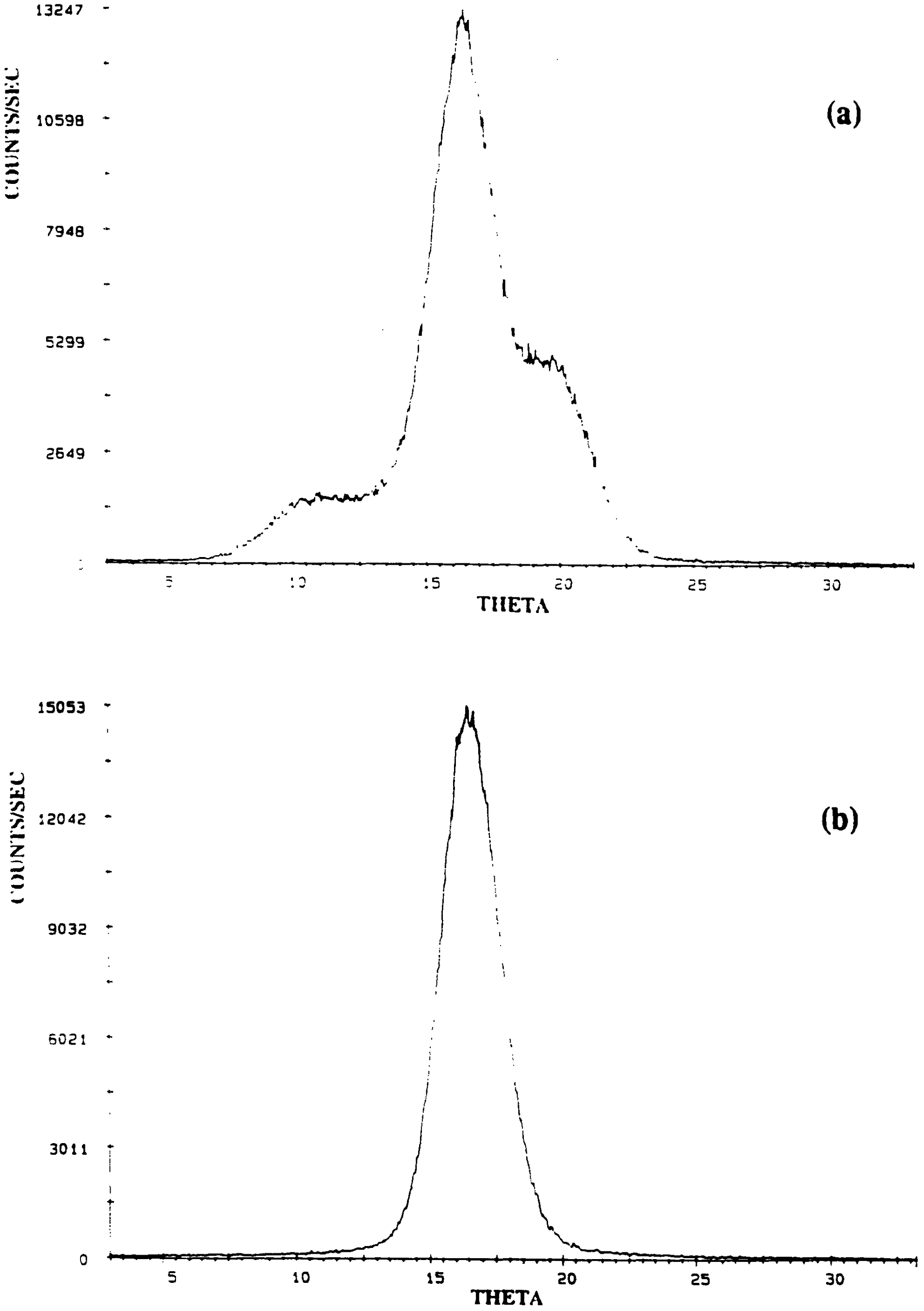

Figure 4.17 CeO_2 (002) rocking curves for sample shown in Figure 4.9. Rocking curves measured: (a) orthogonally, and (b) parallel, to underlying substrate groove direction.

main peak. The anomalous peaks were not detected when the rocking curve measurement was taken parallel to the groove direction (see Figure 4.17(b)). CeO_2 rocking curve measurements for the as-received YSZ substrate that had been IBAD-processed together with these specimens did not reveal the presence of any anomalous peaks.

The ion beam parameters used in this study do not prevent epitaxial development from occurring, since XRD scans of CeO_2 overlayers evaporated on IBAD YSZ films indicate that the IBAD YSZ layers grow homoepitaxially over (001) YSZ single crystal substrates, both with and without an initial evaporated YSZ layer. However, the epitaxial quality of the IBAD film does appear to be affected by ion bombardment. XRD rocking curves for CeO_2 deposited on IBAD YSZ surfaces are always broader than for CeO_2 grown over single crystal YSZ. In addition, the observed trend for broadening of CeO_2 rocking curves with longer IBAD processing times indicates that the epitaxial quality of the IBAD layer becomes somewhat worse with increased IBAD. For example, for deposition at 0.15 Å/s, the FWHM of the CeO_2 (002) rocking curve increases from 1.87° for 90 minutes of IBAD YSZ to 3.70° for 720 minutes of IBAD YSZ. On the other hand, 833 minutes of IBAD YSZ at a net rate of 0.3 Å/s results in CeO_2 (002) rocking curve widths that vary between 3° to 3.5°. This also suggests that the absolute value of the ion-to-atom ratio may affect the degree of epitaxial quality.

It is not altogether surprising that ion bombardment may cause some epitaxial deterioration since it is expected that ion bombardment will introduce some degree of disorder into the growing film. As discussed above with respect to microstructural changes, reordering takes place during ion bombardment. The energy of the ions is an important parameter. For example, it has been found that for simultaneous film deposition and ion bombardment, improved film properties can be achieved with ion beam energies of 200-300 eV.[140] It was also found that although higher ion beam energies led to similar improvements, it was obtained at the expense of incurring deeper film damage. Ion bombardment can heal out, or "anneal" film structure over a distance of several atomic layers, but ions of higher energies penetrate more deeply into the film which results in damage that cannot be annealed. The ion beam energies used in this study (500 eV) are probably sufficiently high to introduce a small degree of crystallographic disorder into the growing IBAD film. The disorder appears to be cumulative, resulting in an increasing amount of epitaxial degradation with increasing IBAD deposition time. Harper *et al.*[132] point out that lower ion energies can be used in ion-assisted deposition to achieve the same desired film modifications as long as a sufficiently high current density is maintained. This allows the required amount of resputtering to take place while minimizing film damage. Harper *et al.* also note that the total ion beam energy/atom is a critical parameter as well. This is consistent with the smaller degree of epitaxial disorder observed with IBAD at higher deposition rates.

For each particular set of IBAD parameters examined, the FWHM values of films grown on the unpatterned as-received substrates are also lower than counterpart films grown on patterned substrates. This suggests that there are two contributions to the increase in rocking curve widths. One comes from the decreased epitaxial quality of the IBAD film as described above. The other arises from the presence of the patterned substrate surface. In the case of the series of IBAD films deposited at 0.3 Å/s for 833 minutes, a third component of misorientation is observed in the anomalous peaks detected during rocking curve measurements. Since these peaks are observed only when the rocking curve measurement is taken orthogonally to the step direction on patterned substrates, it is clear that this additional misorientation arises from the underlying steps.

4.4 DEPOSITION OF BYC FILMS OVER PLANARIZED YSZ FILMS

BYC films were deposited over both planarized and control YSZ substrates in order to ascertain the effectiveness of the planarization process. BYC deposition methods used were pulsed laser deposition (PLD) and sputtering. XRD and electrical measurements were used to characterize the properties of the BYC films.

4.4.1 Results

4.4.1.1 PLD BYC Films

PLD BYC films were deposited on substrates that had been IBAD processed for 833 minutes at ~0.3 Å/s. XRD θ/2θ scans of the PLD films show only the BYC (00*l*) peaks (see Figure 4.18). BYC deposited on the unplanarized substrate (i.e. no IBAD layer) exhibits the narrowest CeO_2 (002) and BYC (005) rocking curves. BYC grown over IBAD-processed surfaces exhibit wider curves (see Table 4.4), in which the broadest curves are found for growth over patterned substrates. The anomalous rocking curves described in Section 4.3.4 are detected in both CeO_2 (002) and BYC (005) rocking curve measurements for deposition over IBAD-planarized patterned YSZ samples (see Figures 4.17 and 4.19). They are not observed in films grown over either the as-received YSZ substrate or the CeO_2 coated unplanarized substrate. X-ray pole figure measurements confirm BYC epitaxy with BYC [100] || CeO_2 [110] || YSZ [110].

The electrical properties of these films are also summarized in Table 4.4. BYC deposited on the as-received IBAD-processed control substrate exhibited a T_c (0) of ~91 K and a J_c of 1.86×10^6 A/cm^2 at 77 K. BYC grown over the unplanarized patterned surface exhibited a T_c onset of ~92.6 K but did not become fully superconducting for measurements down to 25 K. In contrast, BYC grown over planarized patterned substrates became fully superconducting at 85.3 K and 88.7 K, respectively. Cross-sectional SEM analysis of these films revealed some variation in BYC film thickness across the test structure. J_c ranges of 5.2-7.0 x 10^5 A/cm^2 and 4.4-5.6 x 10^5 A/cm^2 were calculated for these two samples, respectively, based on the range of film thicknesses obtained.

Figures 4.20(a)-(d) are planview SEM micrographs for these four samples. An extremely dense BYC film is obtained for growth over the CeO_2-coated unplanarized substrate. The BYC films obtained over IBAD processed surfaces are less dense. Cross-sectional SEM micrographs of the edge of the patterned test structure for BYC grown over the patterned substrates are shown in Figures 4.21(a)-(c). Figure 4.21(a) suggests poor BYC step coverage for the unplanarized sample. A significant improvement in the degree of surface planarity and BYC step coverage is obtained for BYC deposited over

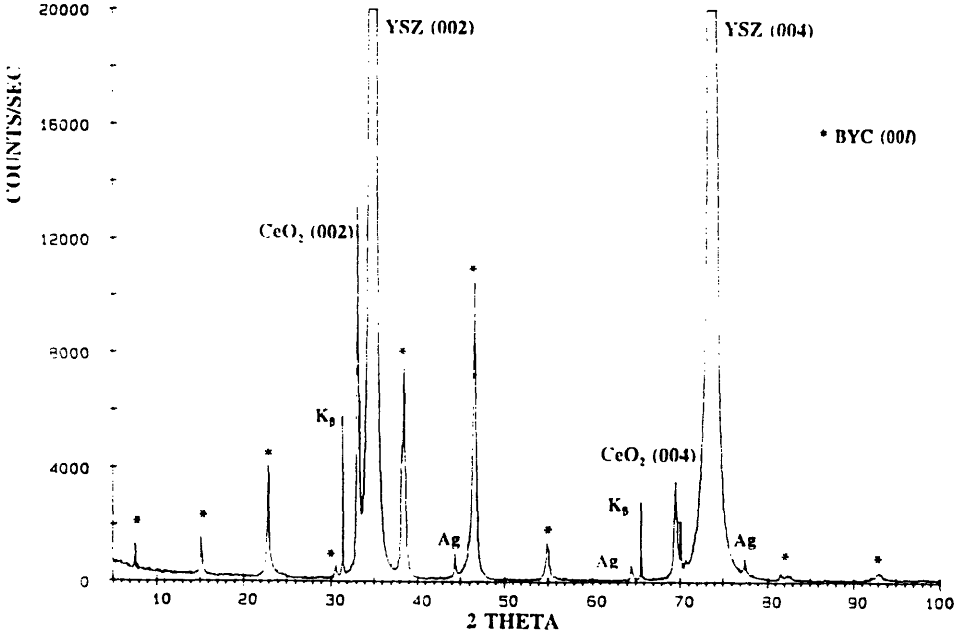

Figure 4.18 θ/2θ XRD scan of PLD BYC film deposited over CeO$_2$-buffered, IBAD YSZ planarized patterned substrates. IBAD YSZ layer was deposited at a net IBAD rate of 0.3 Å/s.

TABLE 4.4: Electrical and XRD properties of PLD BYC films deposited on various (001) YSZ substrates

Sample Number and Substrate Description	T_c(onset) (K)	Tc(0) (K)	J_c (A/cm^2)	ρ_{300} ($\mu\Omega$-cm)	ρ_{300}/ρ_{100}	FWHM BYC(005)	FWHM CeO_2 (002)
(A) IBAD-processed as received YSZ	93	91	1.86×10^6	495	3.10	1.82°	2.34°
(B) unplanarized patterned YSZ	92.6	---	---	3.90×10^4	1.42	0.66°	0.73°
(C) IBAD-planarized patterned YSZ	91	85.3	$5.2\text{-}7.0 \times 10^5$ [a]	411-560 [a]	2.55	2.49°	2.94°
(D) IBAD-planarized patterned YSZ	92	88.7	$4.4\text{-}5.6 \times 10^5$ [a]	329-416 [a]	2.77	2.68°	3.02°

[a] J_c and ρ_{300} ranges for samples C and D calculated from range of BYC film thickness measured.

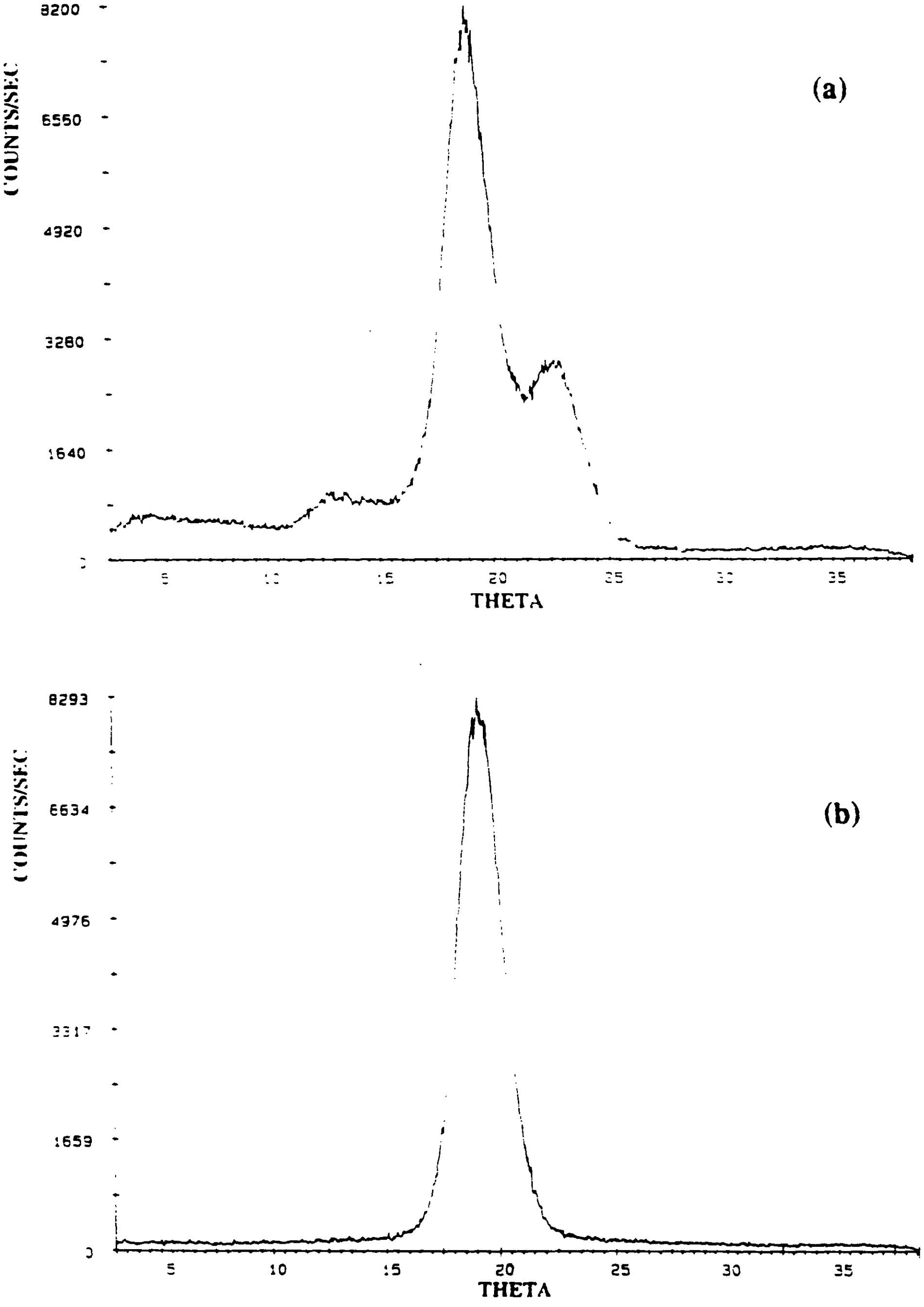

Figure 4.19 BYC (005) rocking curves for same sample as in Figure 4.18. Rocking curves measured: (a) orthogonally, and (b) parallel, to underlying substrate groove direction.

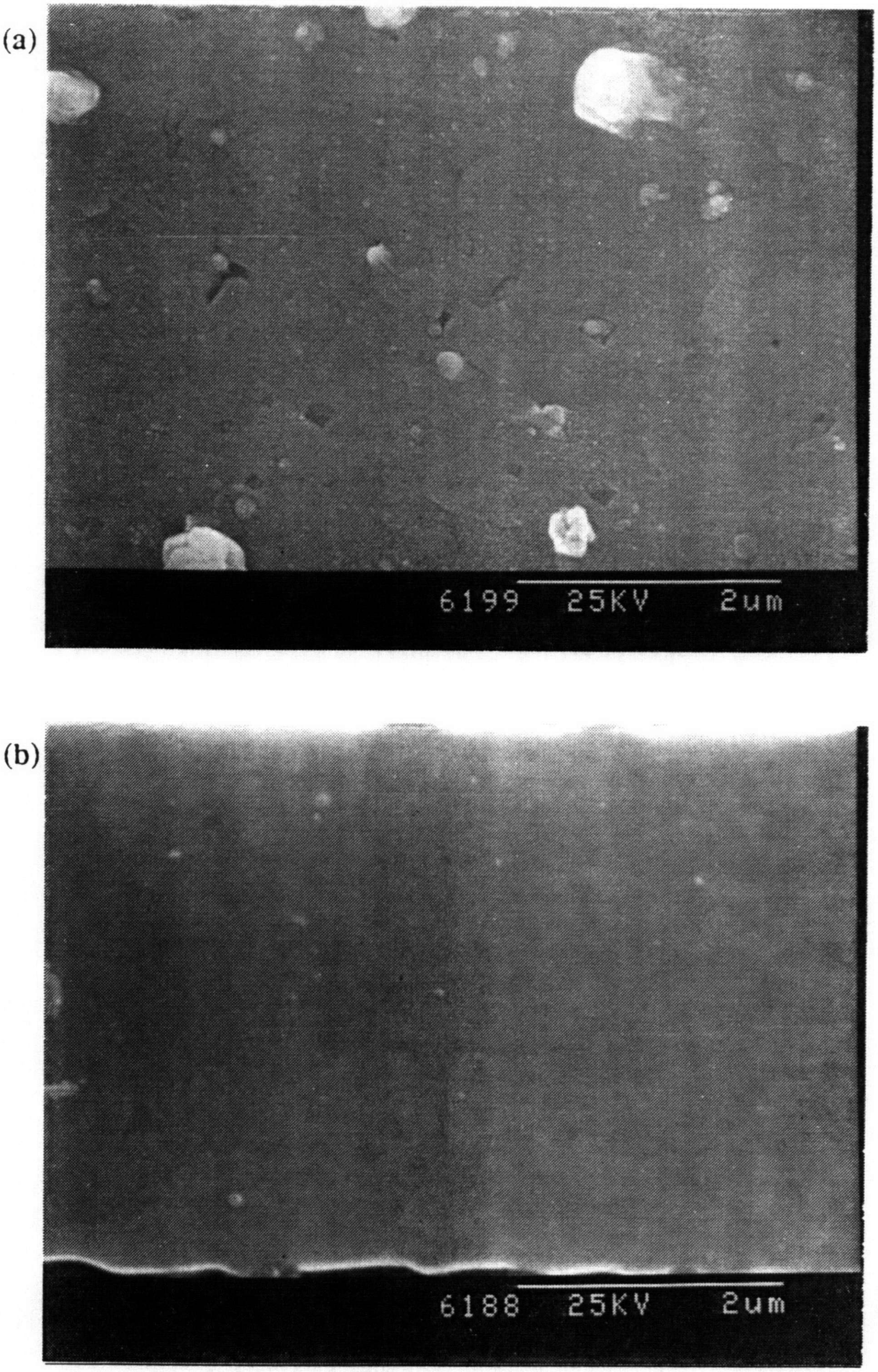

Figure 4.20 Planview SEM micrographs for PLD BYC films deposited on: (a) sample A - IBAD processed, as-received YSZ substrate; (b) sample B - unplanarized, patterned YSZ substrate; (c) and (d) samples C and D - IBAD-planarized, patterned YSZ substrates.

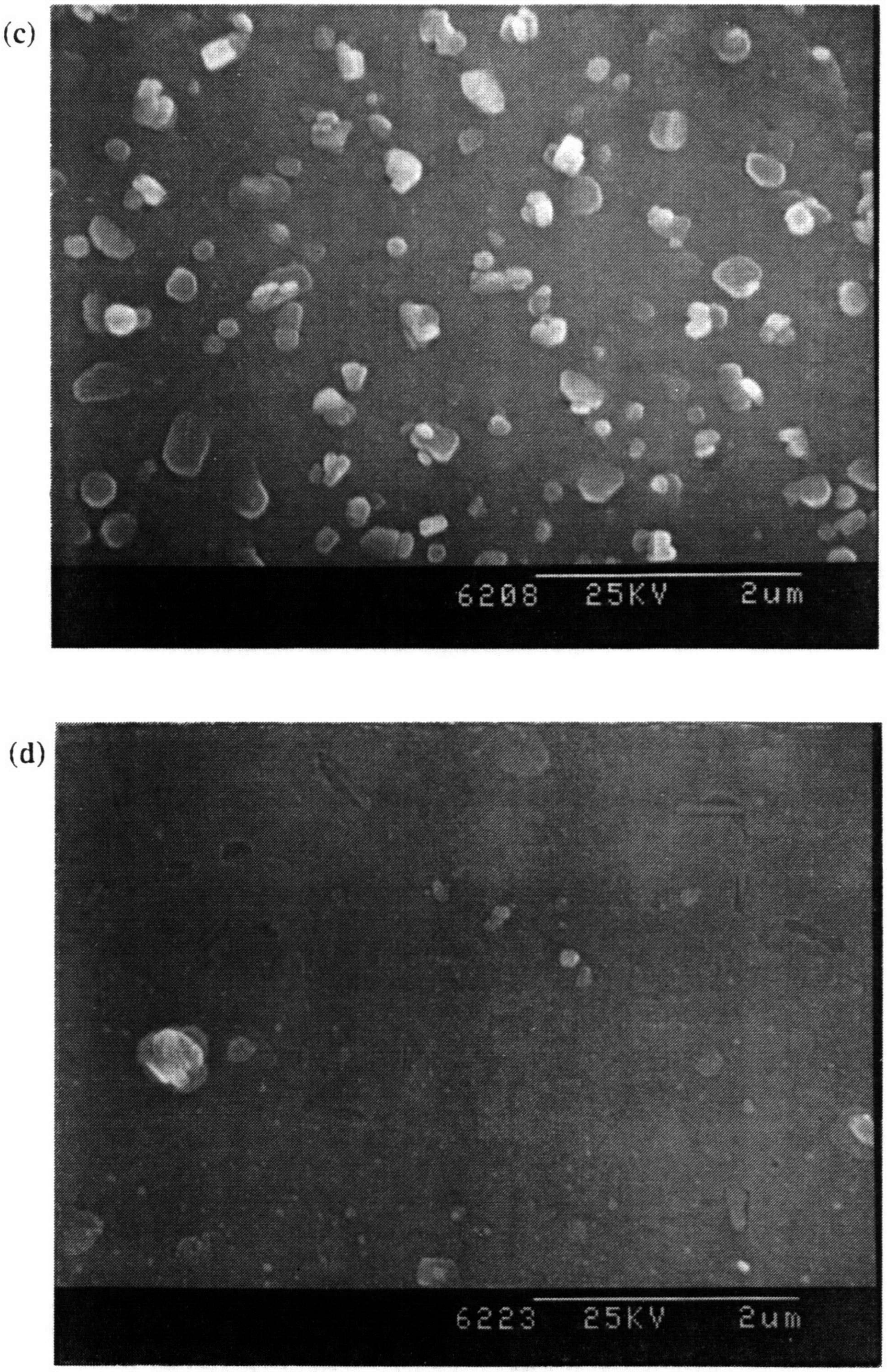

Figure 4.20 (continued).

(a)

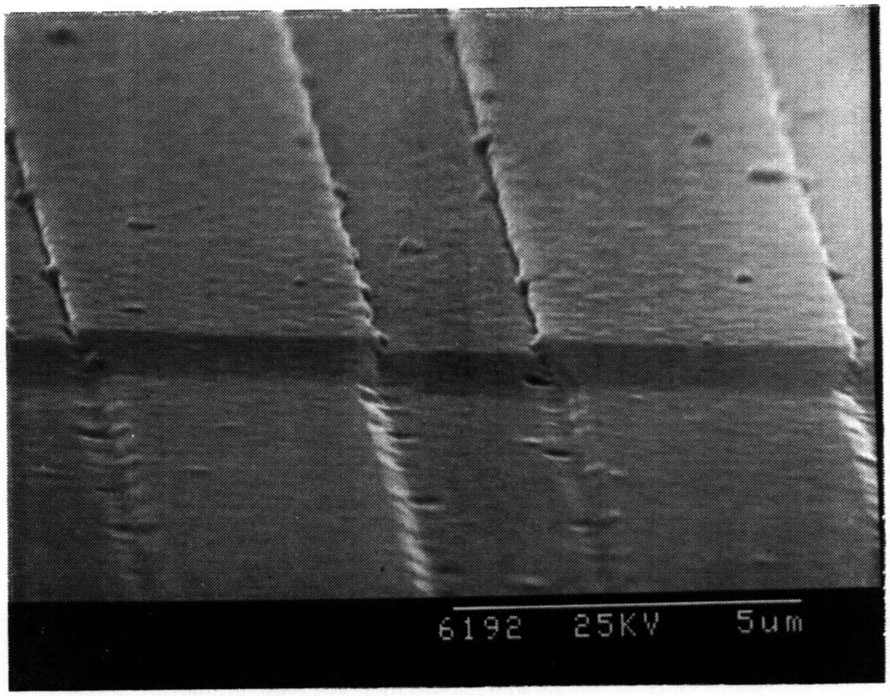

Figure 4.21 SEM micrographs of patterned PLD BYC test structure on: (a) sample B - unplanarized, patterned YSZ substrate; (b) and (c) samples C and D, respectively, - IBAD-planarized patterned YSZ substrates.

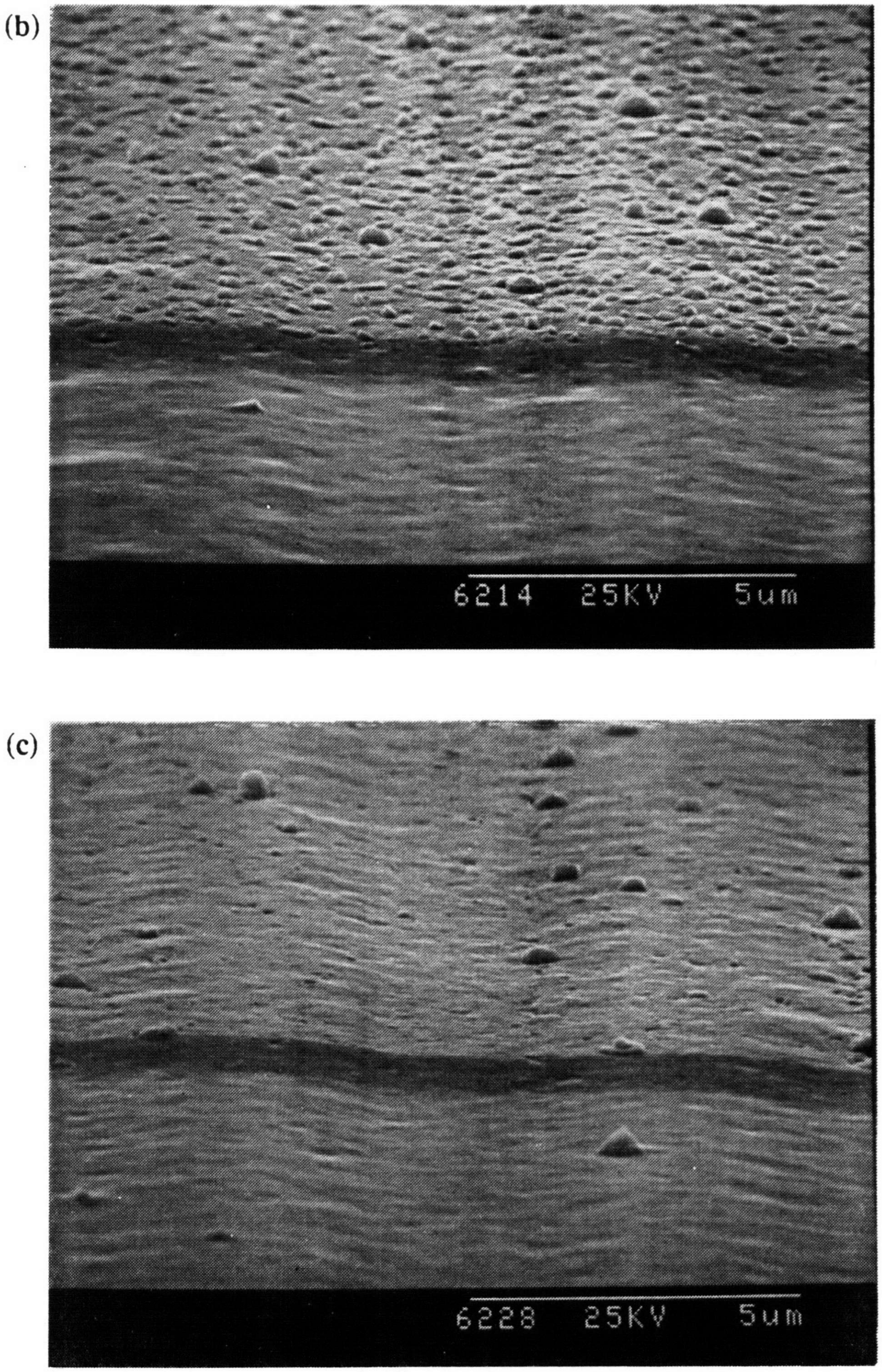

Figure 4.21 (continued).

IBAD-planarized surfaces. Sample C appears to have been planarized to a greater extent that sample D.

4.4.1.2 Sputtered BYC Films

BYC films were deposited using two different sputtering methods on substrates that had been IBAD processed for 720 minutes at ~0.15 Å/s. Table 4.5 is a summary of the properties of these films. Only BYC (00*l*) peaks (i.e. c-axis orientation) are detected in $\theta/2\theta$ XRD scans on all samples. Rocking curve measurements show that FWHM values for both the BYC (005) and CeO_2 (002) peaks are the greatest for samples that had undergone IBAD processing, regardless of the initial substrate topography. The narrowest rocking curves are measured for the unplanarized control substrate which had only an evaporated CeO_2 buffer layer deposited prior to BYC film growth.

Four-circle diffractometry ϕ-scans show that both the CeO_2 and BYC films are singly in-plane oriented for all samples (see Figure 4.22). The measured in-plane relationships with respect to the substrate indicates that heteroepitaxial growth was sustained through the entire film deposition, or BYC [100] $\|$ CeO_2 [110] $\|$ YSZ [110]. χ-scans of the BYC (012) plane reveal the absence of a-axis grains for all samples to the detection limit of the diffractometer.

Electrical properties of the BYC films are summarized in Table 4.5. BYC deposited on the as received IBAD-processed substrate became superconducting at 88.5 K with a J_c of 8.4 x 10^5 A/cm^2 at 77 K. In contrast, BYC grown over the CeO_2-coated unplanarized substrate exhibited semiconducting properties. A superconducting onset was detected at 89.5 K but zero resistance was not achieved for measurements down to 75 K. BYC deposited over IBAD-planarized substrates also manifested contrasting properties. Sample #4 had a T_c (0) of 88.9 K and a J_c of ~1.25 x 10^4 A/cm^2, while Sample #3 exhibited semiconducting properties similar to the unplanarized control sample.

Planview SEM micrographs for all BYC films deposited over IBAD surfaces show a porous microstructure (see Figure 4.23). Square-shaped BYC grains oriented ~45° with respect to the substrate edges and patterned line directions are seen in all cases. BYC grown over evaporated CeO_2, however, appears much denser as seen in Figure 4.23(b).

TABLE 4.5 Electrical and XRD properties of sputtered BYC films deposited on various (001) YSZ substrates

Sample Number and Substrate Description	T_c(onset) (K)	Tc(0) (K)	J_c (A/cm^2)	ρ_{300} ($\mu\Omega$-cm)	ρ_{300}/ρ_{100}	FWHM BYC(005)	FWHM CeO_2 (002)
#1 - IBAD processed as-received[a]	91	88.5	8.4 x 10^5	445	2.56	2.65°	3.77°
#2 - unplanarized patterned YSZ[a]	----	---	---	1.6 x 10^5	----	0.83°	0.92°
#3 - IBAD-planarized patterned YSZ[b]	----	----	----	6.4 x 10^4	----	1.78°	2.66°
#4 - IBAD-planarized patterned YSZ[a]	90.1	88.9	1.25 x 10^4	----	1.86	2.70°	3.68°

[a] BYC deposited by off-axis dc magnetron sputtering
[b] BYC deposited by inverted cylindrical magnetron sputtering

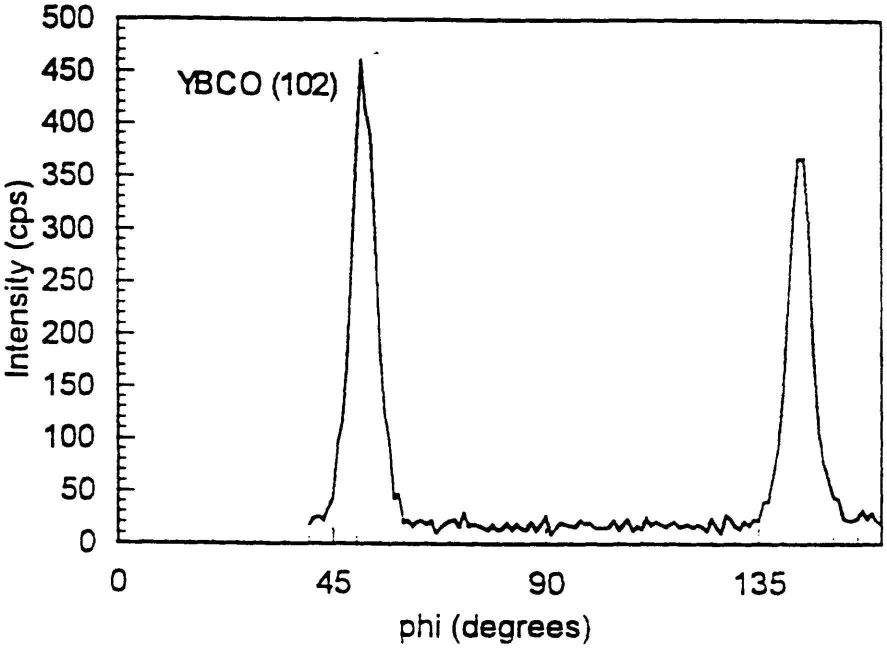

Figure 4.22 Four-circle diffractometry φ-scan of BYC (012) plane for sputtered BYC film deposited over IBAD YSZ planarized patterned substrate. IBAD YSZ was deposited at a net rate of 0.15 Å/s.

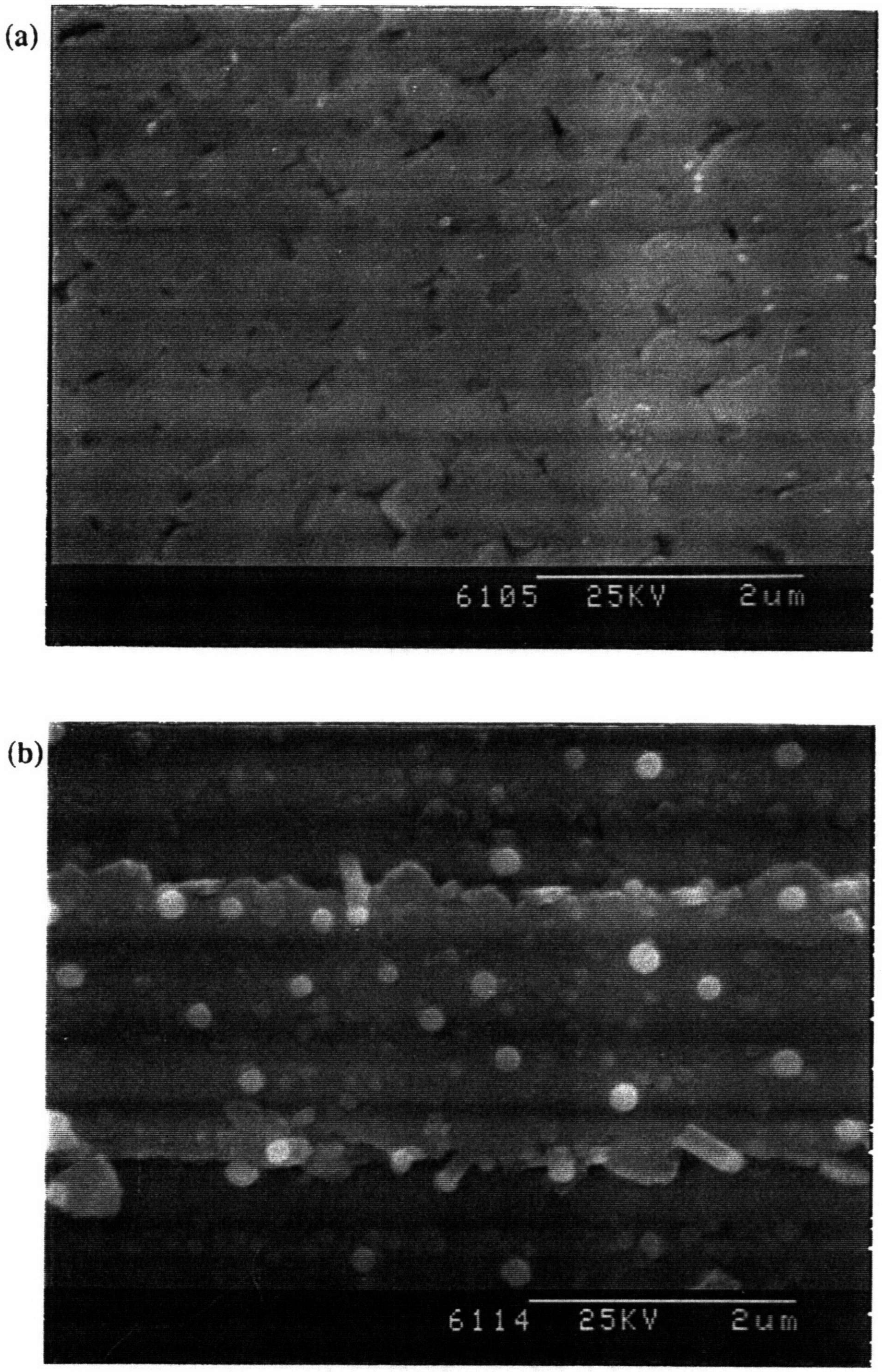

Figure 4.23 Planview SEM's for BYC films sputtered on: (a) sample #1 - IBAD-processed, as-received YSZ substrate; (b) sample #2 - unplanarized, patterned YSZ substrate; (c) sample #3 - planarized patterned substrate; and (d) sample #4 - planarized patterned substrate (BYC grown by inverted cylindrical magnetron sputtering).

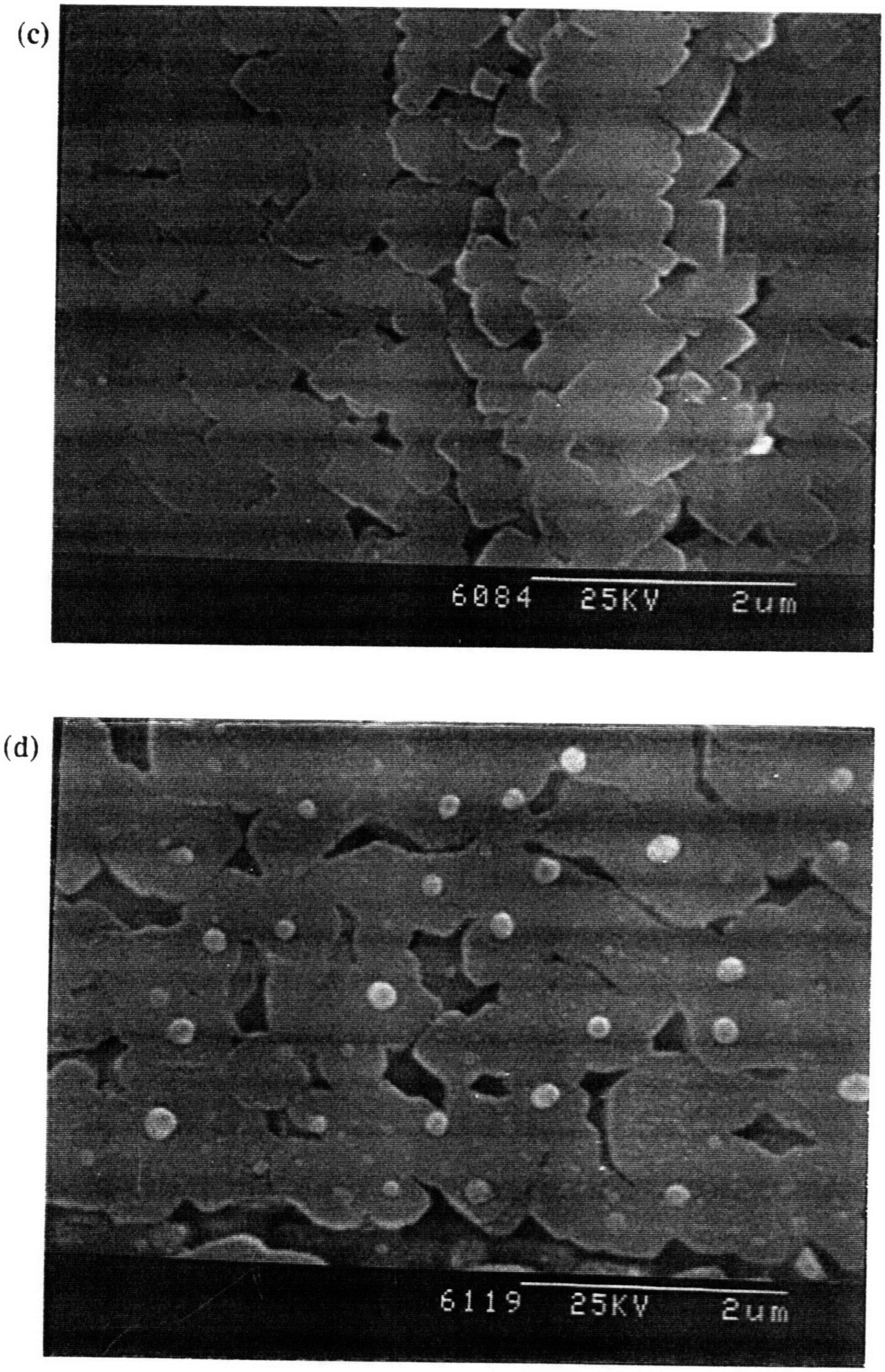

Figure 4.23 (continued)

Cross-sectional SEM analysis shows that BYC deposited over an unplanarized substrate retains the profile of the underlying substrate (see Figure 4.24(a)). In addition, the higher magnification micrograph in Figure 4.24(b) indicates poor BYC step coverage; the BYC film is much thinner on the sidewalls than over the planar regions. For BYC deposited using off-axis sputtering over a largely planarized surface (previously discussed in Section 4.3.2), the BYC film microstructure is fairly uniform across the surface but a significant degree of film porosity and disorder appears to be concentrated over the step edges (see Figure 4.25). Figures 4.26(a) and (b) are micrographs of the BYC film deposited by inverted cylindrical sputtering over a planarized surface. Although the film appears planar on a global scale, wide fissures in the BYC exist over the step edges.

4.4.2 Discussion

4.4.2.1 PLD BYC Films

The XRD and SEM results for PLD BYC deposited on the as-received IBAD-processed control substrate reflect the nature of the underlying IBAD YSZ film. Epitaxial c-axis oriented growth of BYC is achieved, but X-ray rocking curves for this film are broader than for BYC grown directly over CeO_2-buffered YSZ single crystal substrates. SEM micrographs in Figure 4.20(a) also show that the film microstructure is not as dense as for BYC grown over more ideal surfaces. Nevertheless, the measured electrical properties demonstrate that the homoepitaxial planarization process is capable of supporting high J_c epitaxial BYC film growth in spite of the slight degradation caused by IBAD in YSZ epitaxy.

An extremely dense BYC film microstructure, excellent XRD results, and narrow rocking curves are obtained for the PLD BYC film deposited on the CeO_2-buffered unplanarized control substrate. The BYC film is continuous since a T_c measurement could be made. The high T_c onset temperature of 92.6K also confirms that the BYC film is of good quality. However, otherwise poor electrical properties are measured for this sample which can be correlated directly with poor BYC step coverage. The fact that the film never became fully superconducting is consistent with topographical results as shown by SEM. The BYC film over the steps is thin enough so that even when the lowest

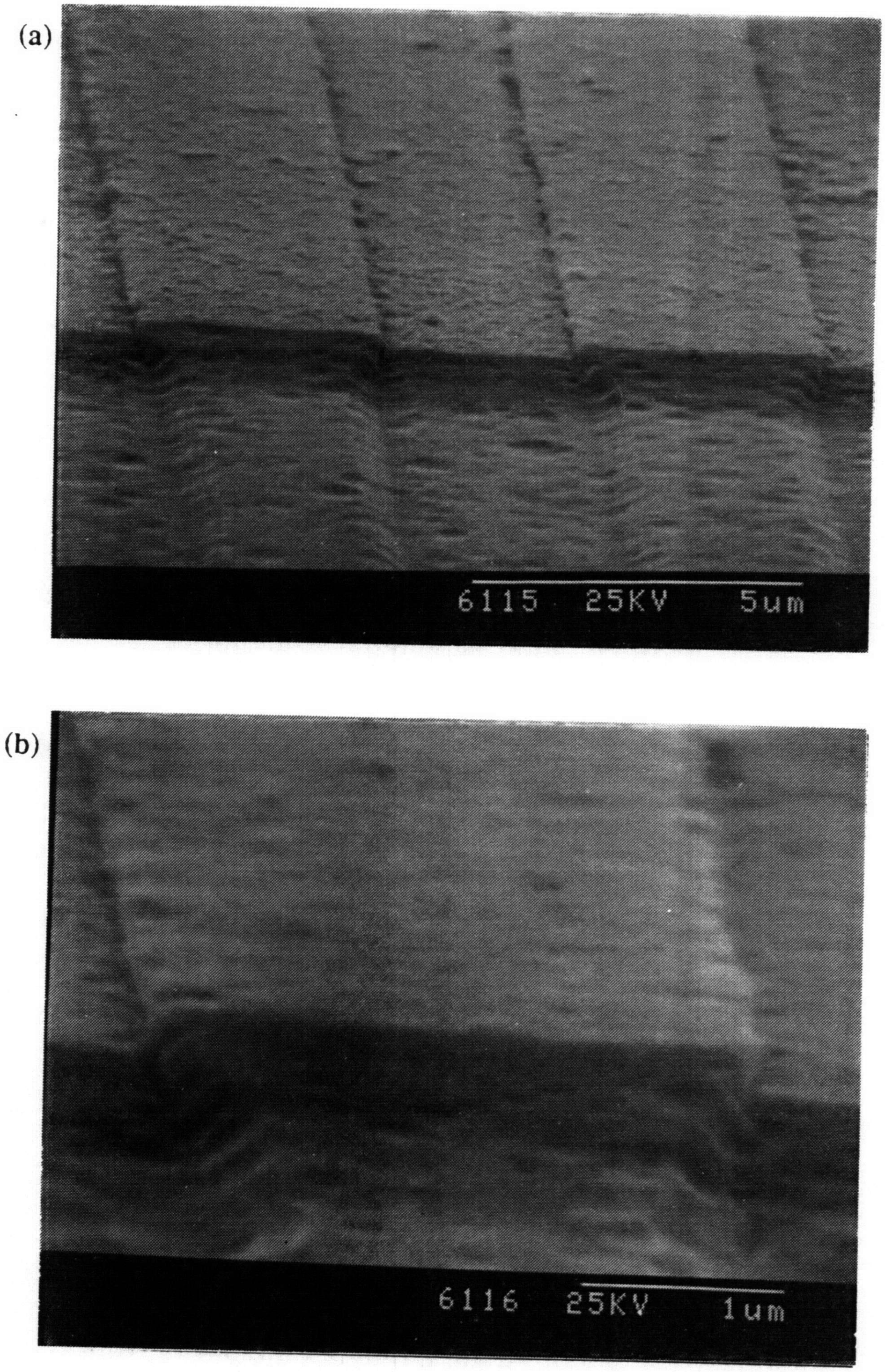

Figure 4.24 SEM micrographs of patterned sputtered BYC test structure for sample #2 on an unplanarized patterned YSZ substrate at: (a) 10K, and (b) 30K magnification.

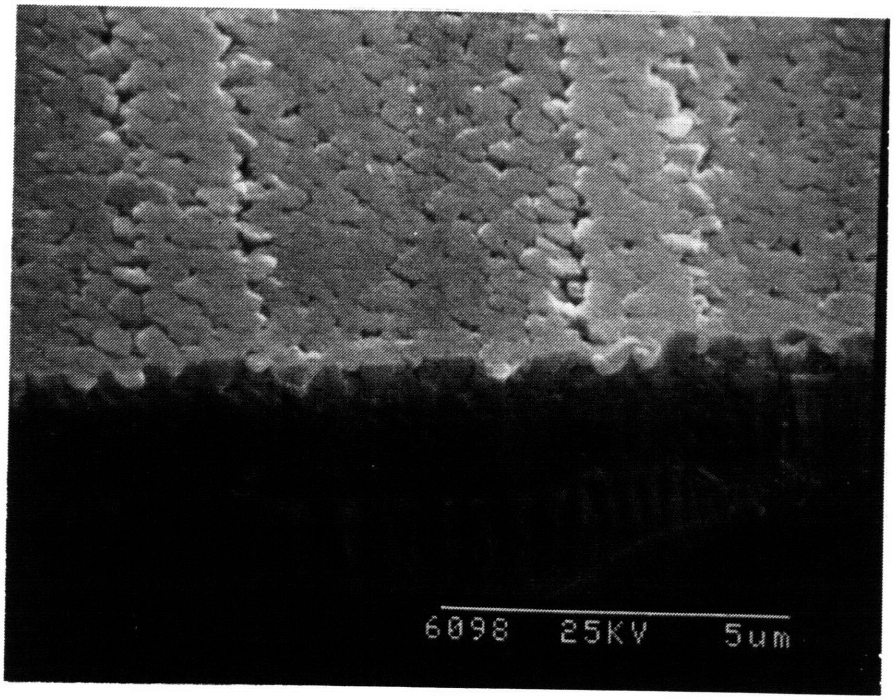

Figure 4.25 SEM micrograph for sample #3 of sputtered BYC grown over an IBAD-planarized patterned YSZ substrate.

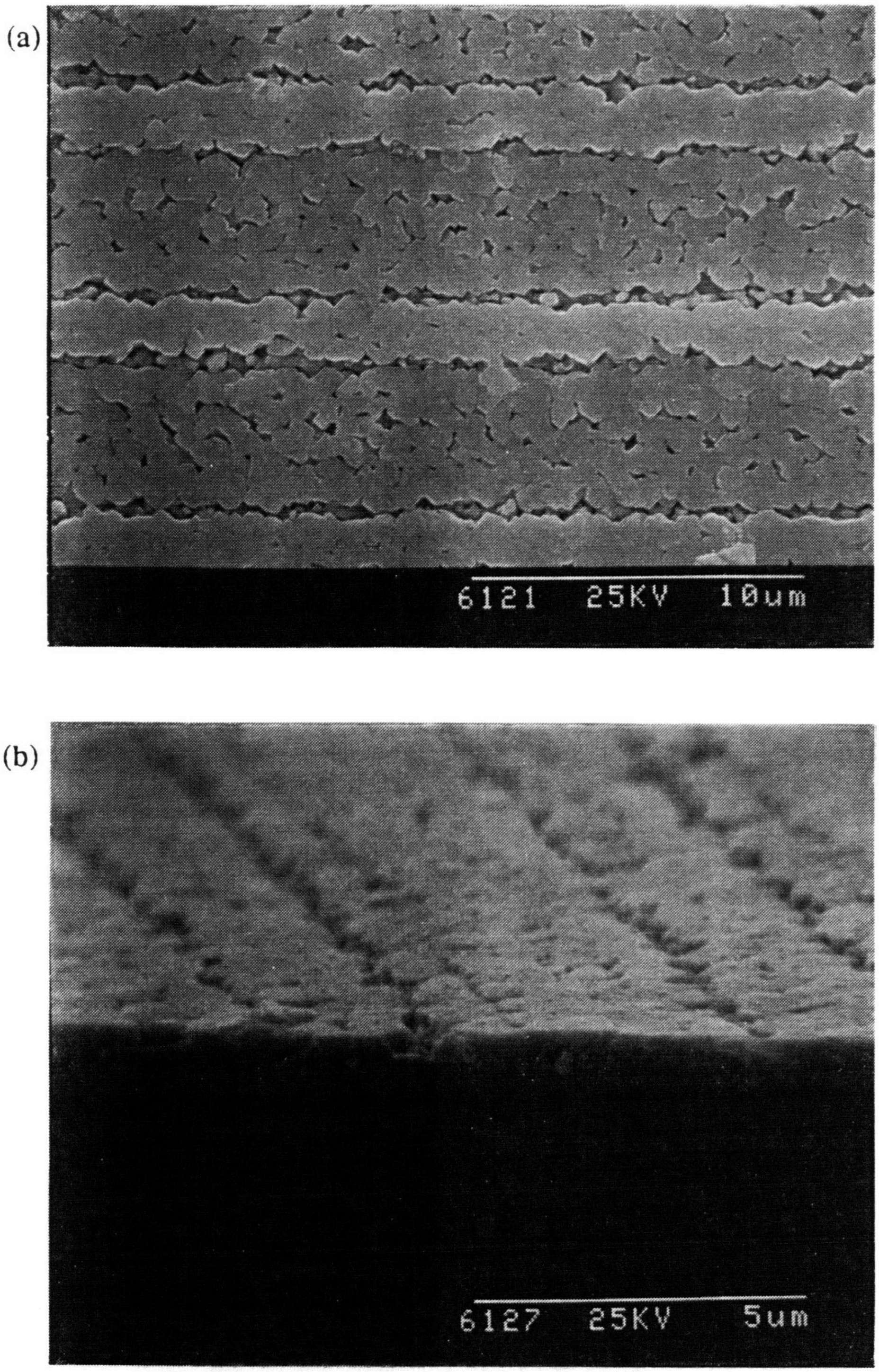

Figure 4.26 SEM micrographs of sample #4 of BYC deposited by inverted cylindrical magnetron sputtering over an IBAD-planarized YSZ substrate: (a) planview, and (b) 75° tilt.

available test current was used (5 nA) in measuring the T_c, the critical current in these regions was always exceeded, preventing the film from becoming fully superconducting. A similar type of T_c result was reported by Oh *et al.*[1], in which a small degree of finite resistance was detected in T_c measurements of interconnects in a HTSC flux transformer. This was attributed to regions of weakened BYC connectivity over unplanarized steps in the device.

A substantial improvement in surface planarity and BYC electrical properties is obtained for IBAD planarization processing. Continuous BYC films with complete step coverage were grown over both planarized samples C and D. As seen in Table 4.4, both specimens became fully superconducting at reasonable temperatures and supported a significant amount of current at 77K, demonstrating the efficacy of the planarization process. However, the J_c values for these two specimens are not as high as that obtained for the as-received control sample. Comparison of the J_c values, surface topography, and XRD properties of these three samples reveal a consistent trend. Samples with higher J_c's have a higher degree of surface planarity and narrower BYC (005) rocking curves as seen both in Figure 4.21 and Table 4.4. Furthermore, both samples C and D exhibited the previously mentioned anomalous peaks in both CeO_2 and BYC rocking curve measurements. This additional degree of misorientation might also account for the decreased J_c values.

4.4.2.2 Sputtered BYC Films

Sputtered BYC films grown over IBAD surfaces are of lower quality than their PLD BYC counterparts in all aspects. These films are epitaxial but have broader rocking curves than the PLD films. SEM micrographs in Figure 4.23 reveal a much more porous microstructure as well. The best electrical results were obtained for the film grown on the as-received IBAD processed control substrate which was also the case with the PLD BYC films. However, only one of the BYC films grown on planarized surfaces had a measurable $T_c(0)$ and J_c. The critical current densities for both of these samples, however, were up to an order of magnitude lower than their PLD counterparts. Examination of the BYC step coverage for the latter sample (see Figures 4.23(c) and 4.25) shows a greater degree of BYC film porosity and disorder over the step edges. This defective microstructure probably contributed to the low J_c value measured for this film.

BYC deposited over a planarized surface using inverted magnetron sputtering exhibited poor electrical properties similar to those obtained for BYC grown over the unplanarized control substrate. In both cases, SEM shows that the BYC film did not grow uniformly over the dielectric surface (see Figures 4.26 and 4.24). The film grown using inverted cylindrical magnetron sputtering contains large gaps located over the substrate step edges despite the fact that the underlying surface had been planarized to a large extent. The BYC film grown over the unplanarized control sample exhibits the best XRD characteristics and film microstructure of all the sputtered films, but also possesses the expected poor step coverage.

It is also interesting to note that for all of these samples, the square-shaped BYC grains observed by SEM are oriented at a 45° angle with respect to the trenches, which were patterned to run parallel to the substrate <100> directions. This is consistent with the in-plane orientation relationship detected by four-circle diffractometry ϕ-scans which found BYC [100] $\parallel$ CeO_2 [110] $\parallel$ [110].

4.4.2.3 General Discussion of BYC Results

Based on the results obtained for these films, as discussed above, it appears that BYC film growth is very sensitive to both the nature of the IBAD-planarized surfaces and the deposition technique being used. While XRD results showed that the BYC films largely reflected the crystallographic quality of the underlying dielectric layer, the microstructural development of the films varied depending on the deposition technique. This appeared to be a function of both the nature of the dielectric surface and the nonplanar topography. The effect of the former on BYC growth can be discerned by examining BYC films grown over the as-received IBAD-processed substrates (i.e., no substrate steps). A dense film was obtained only with PLD while porous BYC was grown using sputtering. In the added presence of an undulating surface, a continuous BYC film was achieved using PLD. Both sputtering methods, on the other hand, produced films with defective regions concentrated over underlying step edges despite planarization processing.

In all cases, the deposition conditions used for BYC film growth had been previously optimized for deposition on single crystal substrates. The results from this study, however, suggest that the BYC deposition technique and/or deposition conditions need to be specifically chosen or tailored for growth over IBAD-processed or planarized dielectric film surfaces.

Although the results of this study are promising, the slight degradation in epitaxy is still of concern. This misorientation needs to be avoided in order to optimize BYC electrical properties. Since some of the degradation is probably caused by ion bombardment, one solution may be to use lower energy ions and a sufficiently high ion fluence during IBAD so that planarization can still be achieved with reasonable processing times. The CeO_2 rocking curve results also indicate that the presence of substrate steps somehow contribute to misorientation. This is especially evident in the anomalous peaks detected in rocking curve measurements for certain samples, and warrants additional investigation.

The actual degree of planarity required for high J_c BYC film growth has not been established, as seen by conflicting results in the literature.[3,5-6] This ambiguity is probably due in part to the variety of BYC deposition techniques and processing conditions that have been used. For the results obtained in this study, it may be possible that in addition to reflecting the crystallographic nature of the underlying dielectric film, the BYC films possess an additional component of misorientation as a result of growth over a gently undulating rather than a flat surface. If this is true, then additional planarization processing is required to achieve a greater degree of planarity.

One point should be mentioned regarding the IBAD films over which the PLD BYC films were grown. Several "mishaps" were encountered during the course of dielectric evaporation and IBAD for these samples. The first was a building-wide power failure which interrupted evaporation of the initial evaporated YSZ layer. A heater malfunction also occurred near the end of the IBAD run which caused the substrate temperature to drop briefly to ~400°C before the problem was rectified. Figure 4.27 shows a cross-sectional SEM image of one of these films. Variations in film

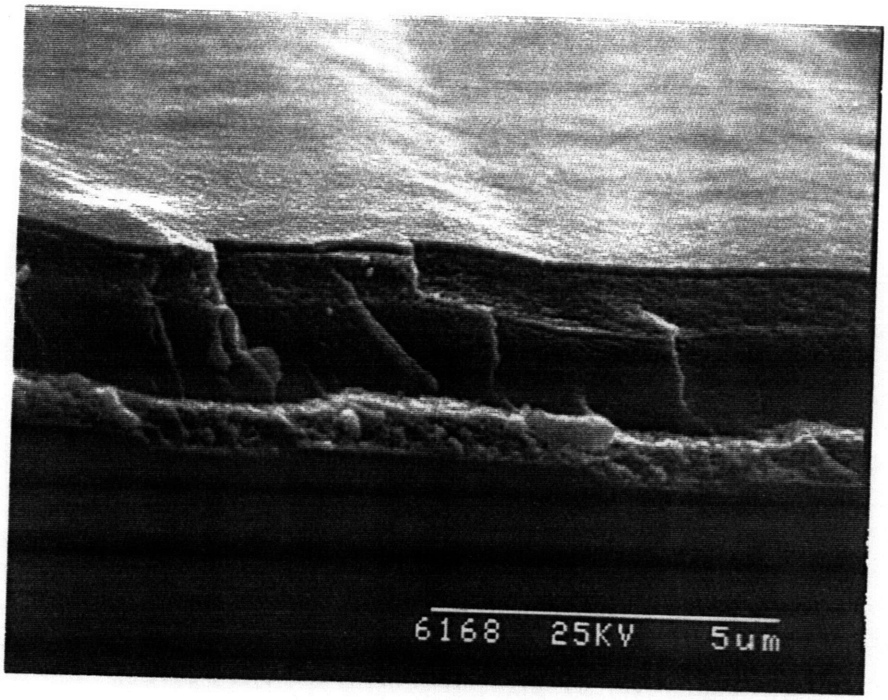

Figure 4.27 Cross-sectional SEM micrograph of IBAD YSZ grown at a net IBAD rate of 0.3 Å/s showing the variation in appearance of different layers as a result of changes in processing parameters during film growth (see text).

microstructure corresponding with the different dielectric processing conditions can be seen. The fact that reasonable electrical properties were measured for subsequently deposited PLD BYC films indicates that the dielectric deposition process is a fairly robust one. This is an especially important consideration for device manufacturing.

4.5 TIME DEPENDENCE AND MECHANISM OF PLANARIZATION

4.5.1 Time Dependence of Growth and Etching

One way of examining the time dependence of planarization is to look at the time dependence of θ, since the initial sample surface has features with non-zero values of θ, whereas θ will be zero everywhere for a planar surface. (Again, θ is defined as the angle between the incoming evaporated or ion flux and the normal to the substrate surface.) The two primary processes that are taking place during IBAD processing are bulk deposition and pure etching. The time dependence of θ and hence, surface profile evolution, for these two processes will therefore first be examined separately before considering simultaneous deposition and etching.

The rate of bulk deposition, or film growth, will be a function of the substrate topography. This dependence on the angle of the underlying step can be seen in the varying degrees of step coverage achieved by the initial evaporated layer in Figure 4.8(b), as discussed earlier. Steps with shallower slopes receive good film coverage while nearly vertical steps experience almost no deposition since they "see" less of the incoming evaporated flux. Figure 4.28 shows two deposition rates measured for YSZ evaporated on two different step angles. These two points can be fitted to a cosine curve which is consistent with observations in the literature[141] where evaporative growth has been modelled using a cosine growth law, i.e.,

$$R(\theta) = R_{\perp}\cos\theta \qquad (4\text{-}1)$$

where $R_{\perp}$ is the film growth rate over planar regions and θ is the angle between the substrate normal and the incoming vapor stream. This growth law assumes that θ remains constant with time, i.e., conformal film growth.

For the case of pure etching only, Carter *et al.*[142,143] have analytically examined the topographical evolution of ion beam etched non-planar amorphous surfaces in two dimensions. In their treatment, it was assumed that all topographical evolution occurs only as a result of sputtering which is a function of the angle of ion incidence, θ. For the etching of any surface with a contour given by $y = f(x)$ using a beam of Φ ions/sec, the

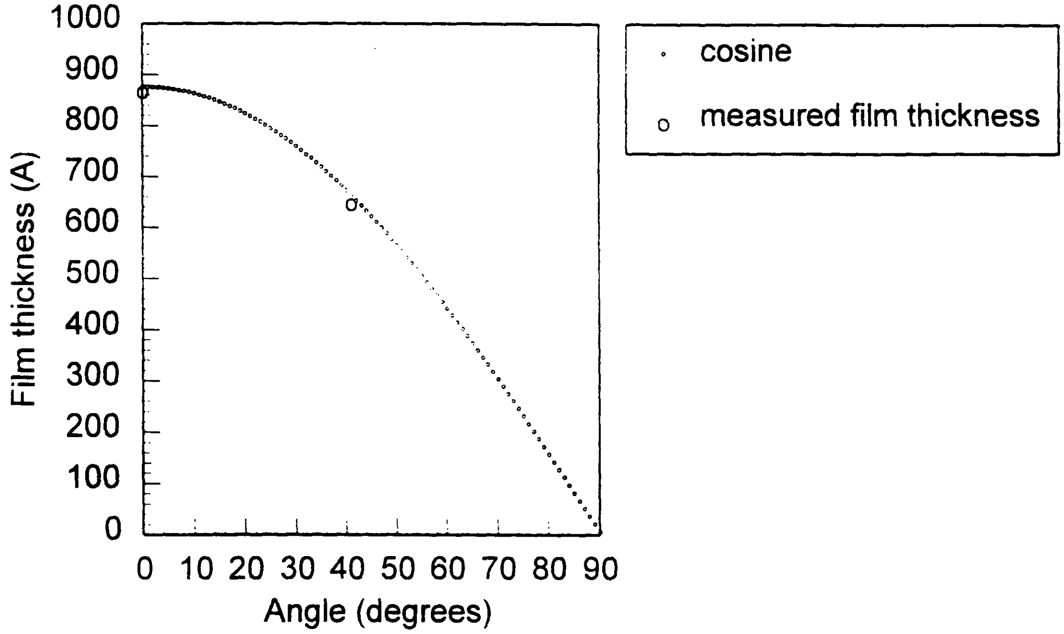

Figure 4.28 Evaporated YSZ film thicknesses measured for growth over two different substrate step angles. A cosine growth dependence is observed.

time dependence of the angle, θ, is given by

$$\frac{\partial\theta}{\partial t} = -\frac{\Phi}{n}\frac{\partial S}{\partial\theta}\cos^2\theta\frac{\partial\theta}{\partial x} \tag{4-2}$$

where S(θ) is the sputtering yield and n is the atomic density of the material. It is not generally possible to solve for the time-dependent variation of the surface profile.

The steady state condition for Equation 4-2 can be determined, however, and is

$$\frac{\partial\theta}{\partial t} = 0, \frac{\partial\theta}{\partial x} = 0$$

i.e., θ is constant with time and there is no lateral movement of the surface topography. The only change will be in the -y direction, i.e., erosion of the surface without a change in contour. It is seen that steady state occurs when θ = 0 or θ = π/2, which gives a surface composed of horizontal and/or vertical planes.

Several studies[144,145] have been carried out using numerical methods based on Equation 4-2 to predict topographical evolution of sinusoidal surfaces of the form y = asin(x). Knowledge of S(θ) is needed, however, to obtain actual time dependence of the profile evolution. In actuality, S(θ) must be determined experimentally since it is a function of material as well as processing conditions. The parameter that can be most easily measured is usually the material etch rate, V(θ). Examples of experimentally determined etch rate data are shown in Figure 4.29. Etch rate is defined as being proportional to the sputter yield, S(θ),[146] or

$$V(\theta) \propto \frac{S(\theta)}{n}\cos\theta \tag{4-3}$$

where the cos θ term takes into account reduced ion current density at non-normal angles of incidence.

A cosine sum was used by the authors in the above studies to empirically model experimentally determined etch rate data. Carter *et al.* used an equation of the following form for the sputter yield

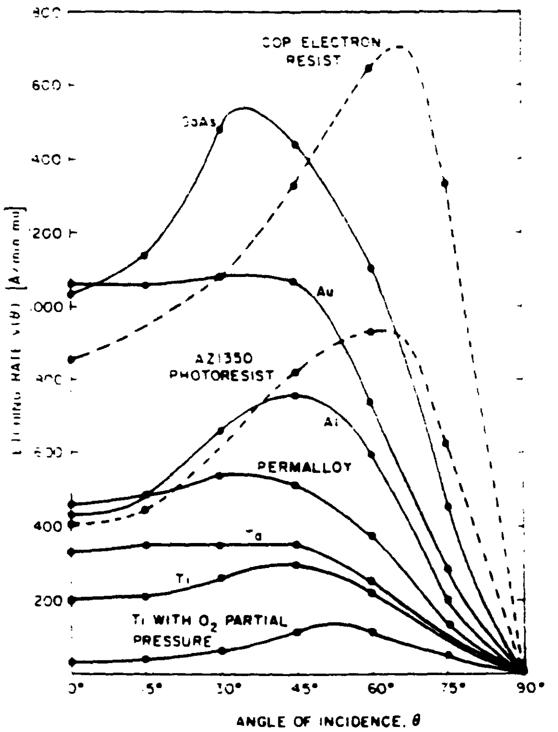

Figure 4.29 Experimentally measured etch rates as a function of the angle of ion incidence for a variety of materials. Rate are normalized to 1 mA/cm^2 for an ion beam energy of 500 eV (from Reference 146).

$$S(\theta)=A\cos\theta+B\cos^2\theta+C\cos^4\theta \qquad (4\text{-}4a)$$

to generate the hypothetical sputter yield curve shown in Figure 4.30. Rangelow[145] modelled etch rates using an equation of the form

$$V(\theta)=A_1\cos\theta+A_2\cos^2\theta+A_3\cos^3\theta+A_4\cos^4\theta \qquad (4\text{-}4b)$$

The constants A_i were chosen to approximate the experimental etch rate curves of various materials. Rangelow emphasizes that great care is required in determining the $V(\theta)$ curves for use in numerical calculations of profile evolution. Inaccurate assumptions as to the shape of $V(\theta)$ can have the effect of greatly distorting the predicted profiles.

In all of the above-mentioned studies, computer simulations showed that etching of a sinusoidal surface results in first the formation of intermediate triangular surfaces by the positive half-cycles and planar surfaces by the negative half-cycles (see Figure 4.31). The final contours are planar, as expected. The angles developed by the triangles tend to θ_m, the angle at which maximum etching occurs, if the initial angle of incidence is greater than θ_m.

The net effects of simultaneous deposition and etching can now be examined by combining Equations 4-1 and 4-4b and by ignoring any possible interaction terms to yield

$$R(\theta)-V(\theta)=(R_\perp-A_1)\cos\theta-A_2\cos^2\theta-A_3\cos^3\theta-A_4\cos^4\theta \qquad (4\text{-}5)$$

The actual dependence of net growth/etching will therefore depend on the relative magnitudes of the constants $R_\perp$ and A_i and will be functions of the material that is being used and the processing parameters. It is clear that in order to establish the time dependence of planarization, knowledge of the time dependence of θ for simultaneous deposition and etching is required, which in turn requires detailed knowledge of $R(\theta)$ and $V(\theta)$. Therefore, experimental values of growth and etch rates are needed for all angles in order to analyze contour evolution.

Although detailed knowledge of $R(\theta)$ and $V(\theta)$ are not available for IBAD YSZ, curves for these two rates can be approximated using the experimentally determined values presented in Section 4.3. In Figure 4.32, an etch curve for IBAD YSZ is plotted

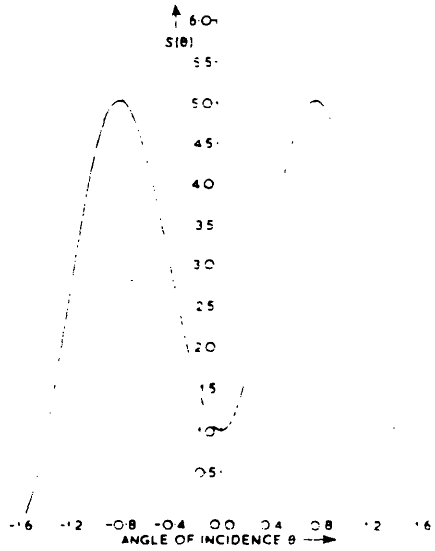

Figure 4.30 Hypothetical S(θ) curve obtained by Carter *et al.*[143] using a cosine equation of the form shown in Equation 4.4a with constants A=3.2696, B=13.1059, and C=-15.3755.

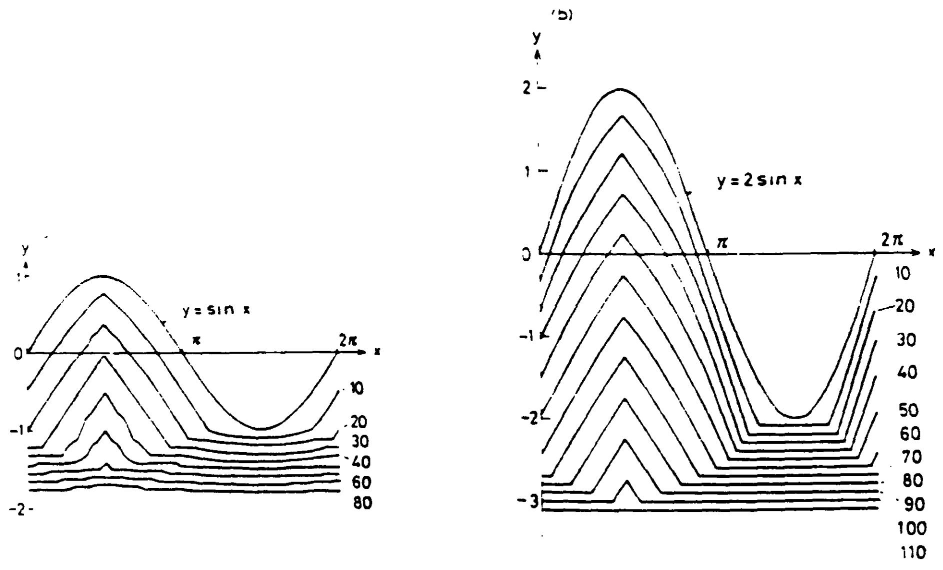

Figure 4.31 Computer simulations showing topographical evolution towards a planar surface of ion-etched sinusoidal surfaces of the form y=a sin(x) (from Reference 144).

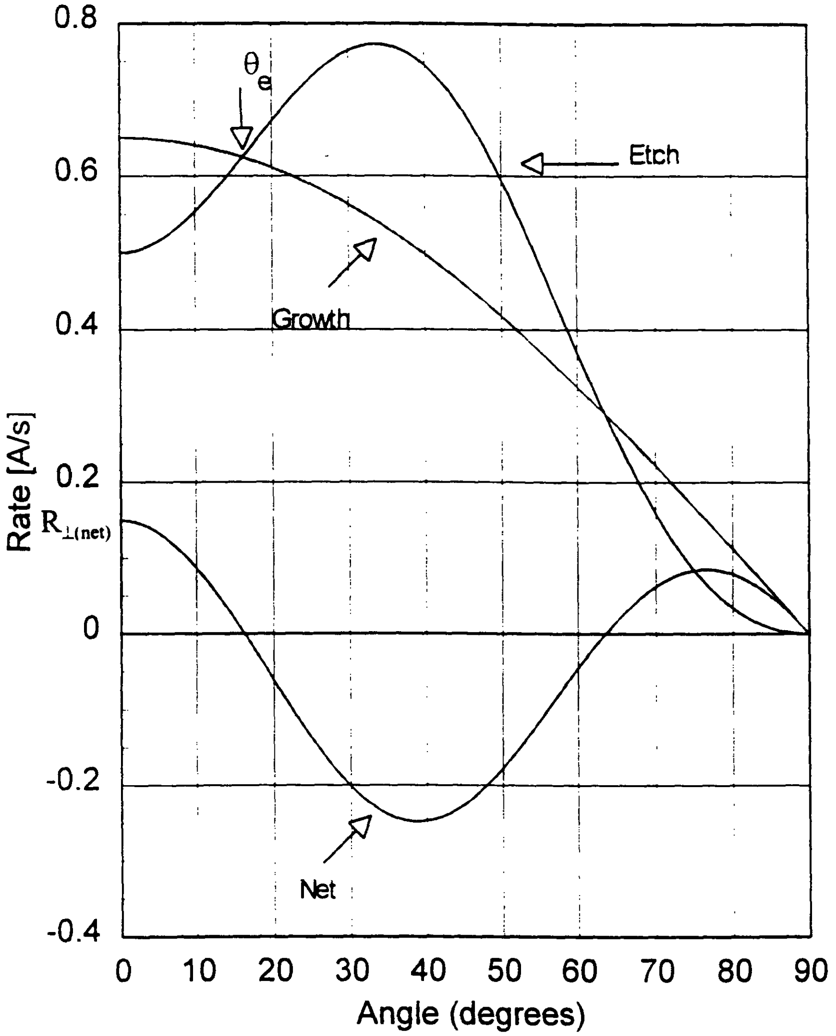

Figure 4.32 Growth rate, etch rate, and net deposition rate curves plotted as a function of step angle using experimentally measured data for IBAD YSZ.

using a cosine sum equation and roughly fitting it to the two etch rate values of 0.5 Å/s and 0.67 Å/s that were obtained for angles of 0° and 45°, respectively (see Section 4.3.1). (It must be noted that although these two values imply the presence of a maximum, θ_m, in the etch rate curve for IBAD YSZ, the actual value of θ_m is not known, and hence it is possible for it to lie on either side of θ=45°.) A growth curve is also plotted using the cosine growth law and a $R_\perp$ value of 0.65 Å/s. A net deposition curve based on the bulk deposition and bulk etching rates is calculated and plotted. The point where the growth and etch rate curves coincide is termed the equilibrium angle, θ_e, and corresponds to the point where the net deposition rate curve crosses zero. The maximum net growth rate, $R_{\perp(net)}$, occurs at 0°.

This graph is similar to the one used by C.Y. Ting *et al.*[14] to model planarization carried out by rf-bias sputtering, and likewise predicts a linear planarization rate. Cone formation will occur at the equilibrium angle, θ_e, for film deposited on non-planar surfaces. Since θ_e is where the net deposition rate is zero, no net growth or etching will take place on these film surfaces. Again, since the maximum growth rate will occur over planar surfaces at the rate $R_{\perp(net)}$, the rate of cone burial and hence, planarization, will therefore proceed at this rate.

Time required for planarization as a function of underlying step geometry

The total time needed to achieve full planarization for C.Y. Ting's model can be calculated by examining the geometrical relationships of this model, as shown in Figure 4.33. The final height of the completed cone structure, h_c, is given by

$$h_c=\frac{1}{2}w_s\tan\theta_e \qquad (4-6)$$

where w_s is the width of the underlying step and θ_e is the equilibrium angle where deposition and etching balance each other. In order for planarization to occur, the thickness of the film deposited over surrounding planar regions needs to equal the combined heights of the cone and the underlying step, h_s, or,

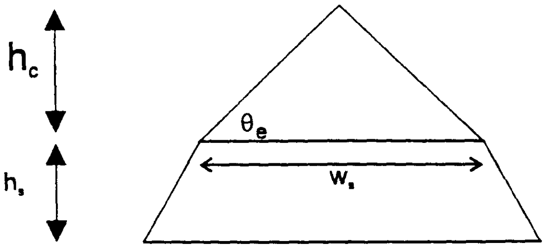

Figure 4.33 Geometrical relationships for planarization model of C.Y. Ting *et al.*[14]

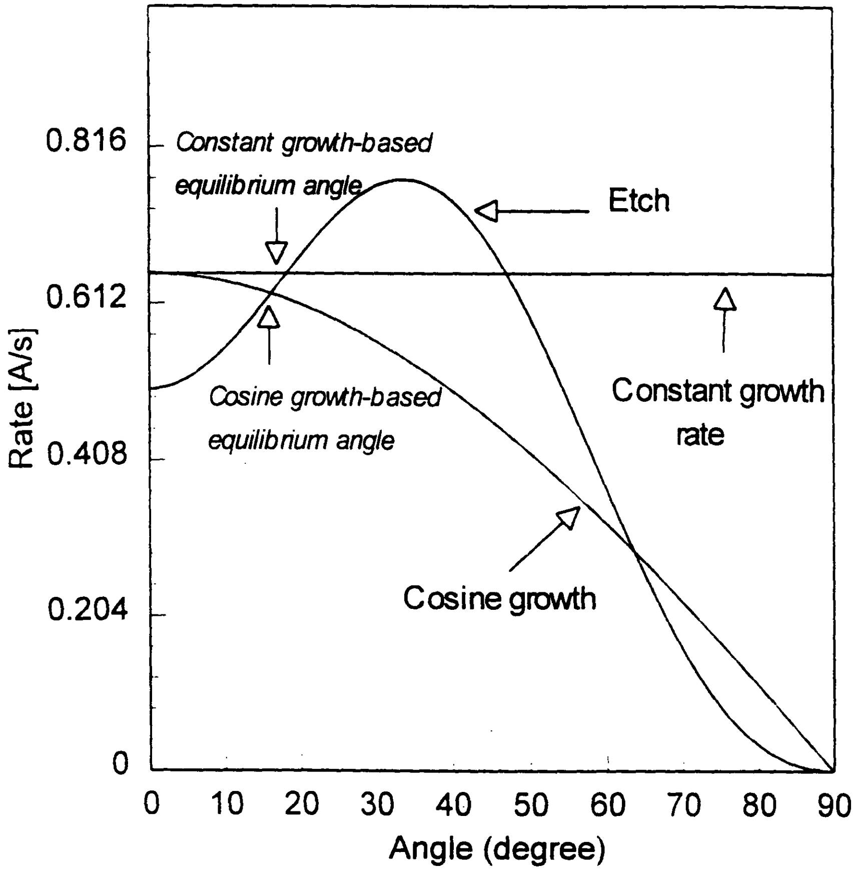

Figure 4.34 A plot illustrating the effect on equilibrium angle value when a constant growth rate is assumed.

$$h_T=h_s+\frac{1}{2}w_s\tan\theta_e \tag{4-7}$$

where h_T is the total structure height that needs to be buried. The total time, t_T, to cone burial and planarization is therefore,

$$t_T=\frac{h_T}{R_\perp} \tag{4-8}$$

Two factors are not taken into consideration by C.Y. Ting's model, however. The first is the angular dependence of film growth rate over a patterned surface. Instead, a deposition rate that is independent of the underlying surface topography is assumed for simultaneous deposition and etching. This has the effect of overestimating the equilibrium angle as shown in Figure 4.34. In addition, it is seen from the schematic in Figure 4.33 that C.Y. Ting also assumed that film growth does not take place over the angled surfaces of the step. This is true, however, only if the step angle lies in the regime where net etching dominates (see Figure 4.32). The extent of this regime will be a function of the etching behavior of the material and the deposition conditions used during planarization processing. The shape of the etch rate vs. angle curve is a function of the material that is being ion bombarded. The experimental etch rate data shown in Figure 4.29 for a number of materials[146] demonstrates the large degree of variation that exists in material etching behavior. It is possible for film growth to take place on angled surfaces for certain combinations of step angles and processing conditions. The extent of any film growth that does take place over step edges will be governed by the underlying step angle, as has been shown in Equation 4-1. The relations derived above for Ting's model therefore need to be modified in order to take additional film growth into account.

As shown in Figure 4.35, the effect of film growth over the angled surfaces is to increase the width of the underlying step. The film thickness over the angled surfaces will be related to the cosine of the underlying step angle and the deposition time. The height of the completed cone will, therefore, also be a function of the deposition time

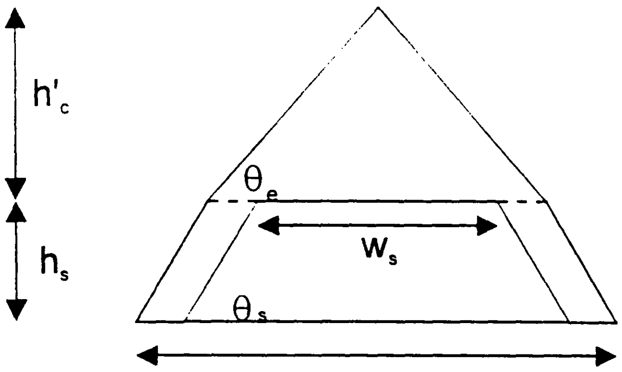

Figure 4.35 Geometrical relationships for modified planarization model which takes into account film growth over substrate steps.

$$h_c' = \frac{1}{2} \tan\theta_e \left[w_s - 2 \left(R_\perp t \cos\theta_s \right) \right] \tag{4-9}$$

Equation 4-9 shows that the height of the cone will therefore increase with deposition time. This equation, however, does not take into account the point in time at which the cone is completed and therefore stops growing; it merely shows the corresponding cone height for varying step widths. The time it takes for the cone to reach completion can also, however, be calculated from the planar deposition rate, or,

$$h_c' = R_\perp t \tag{4-10}$$

since the center of the growing cone structure remains planar until the point immediately prior to cone completion. Equating Equations 4-9 and 4-10 and solving for the time needed for cone completion, t'_c, gives

$$t_c' = \frac{1}{R_\perp} \frac{\frac{1}{2} w_s \tan\theta_e}{(1 - \cos\theta_s \tan\theta_e)} \tag{4-11}$$

The modified cone height, h'_c, can then be calculated by substituting Equation 4-11 back into Equation 4-10. Then, as before, the total time needed to achieve planarization is

$$t_T' = \frac{h_c' + h_s}{R_\perp} \tag{4-12}$$

The times required to planarize the two substrate steps shown in Figure 4.10(b) and Figure 4.11(b) were calculated for both models. Experimental values of the equilibrium angles, step widths, and step heights were used for these calculations which were obtained by measuring the features in the corresponding SEM micrographs. These values are listed in Table 4.6 along with the calculated planarization times.

C.Y. Ting's model predicts planarization times of 411 and 412 minutes, respectively, for the two different steps. For the modified model, the time needed to achieve cone burial has increased up to 68 minutes over the time previously calculated using C.Y. Ting's model. The results for the two models are also shown graphically in

Table 4.6(a) Projected planarization times calculated on the basis of C.Y. Ting *et al.*'s model

Sample ID	Total IBAD Processing time (min)	IBAD Net Deposition Rate (Å/s)[a]	Substrate Step Height h_s (Å)[a]	Substrate Step Width w_s (μm)[a]	Equilibrium Angle θ_e [a]	Cone height h_c (Å) [b]	Total height h_T (Å) [b]	Required planarization time t_T(min)[b]
120893	165	0.15	1430	2.86	9°	2265	3695	411
120993	555	0.15	1430	2.14	12°	2274	3704	412

Table 4.6(b) Projected planarization times calculated on the basis of modified planarization model

Sample ID	IBAD t (min)	IBAD Net Rate (Å/s) [a]	h_s (Å) [a]	w_s (μm) [a]	θ_e [a]	Step angle θ_s [a]	h_c (Å) [b]	h_T (Å) [b]	t_T (min) [b]
120893	165	0.15	1430	2.86	9°	39°	2583	4013	446
120993	555	0.15	1430	2.14	12°	52°	2617	4047	450
120993	"	"	"	"	"	30°	2888	4318	480

[a] Experimentally measured values
[b] Calculated values

Figure 4.36 for planarization of a 1430 Å high 52° step, (i.e., the geometry of the left hand side step in Figure 4.11(b)). In the graph, the step height difference, δ, is plotted against time. This again shows that it takes longer for onset of cone burial in the modified model. Once burial has begun, however, planarization proceeds at the same rate as C.Y. Ting's model. Data points from the IBAD planarization results presented in Section 4.3 are also plotted on the graph. It is seen that these experimental values do not match up with the predicted values.

Discussion of linear models

Both models described above are similar in that they predict similar types of linear behavior for the planarization process. In general, the time required to achieve planarization is a function of the initial step height as well as the film deposition conditions. Smaller equilibrium cone angles correspond to lower cone heights which in turn lead to lower overall film thicknesses required for planarization. These conditions do not necessarily correspond to faster processing times, however, since smaller equilibrium angles are usually achieved at the expense of lower net deposition rates.

It can be seen from the relationships for the modified model that the effect of film growth over the angled steps results in higher final cone heights since cone formation is now essentially occurring over wider steps. This results in longer processing times in order to achieve planarization. In addition, the modified model takes into account the angle of the underlying steps. As the step angle, θ_s, decreases, the increase in growth rate leads to an increase in the effective width of the step. As a result, h_c' increases which leads to longer planarization processing times. The fact that the tip of the cone in Figure 4.11(b) is not centered over the step can now be accounted for. This arises from the fact that the two step angles in the underlying step are not equal, but are measured to be 52° and 30°. This asymmetry, which is not accounted for by C.Y. Ting's model, leads to the development of the asymmetric cone.

It is important to realize that this modified model overestimates the degree of film growth that occurs on the angled surfaces. In Equation 4-9, it is assumed that the cosine growth law is active for all step angles, θ_s. In actuality, step angles that lie in the net

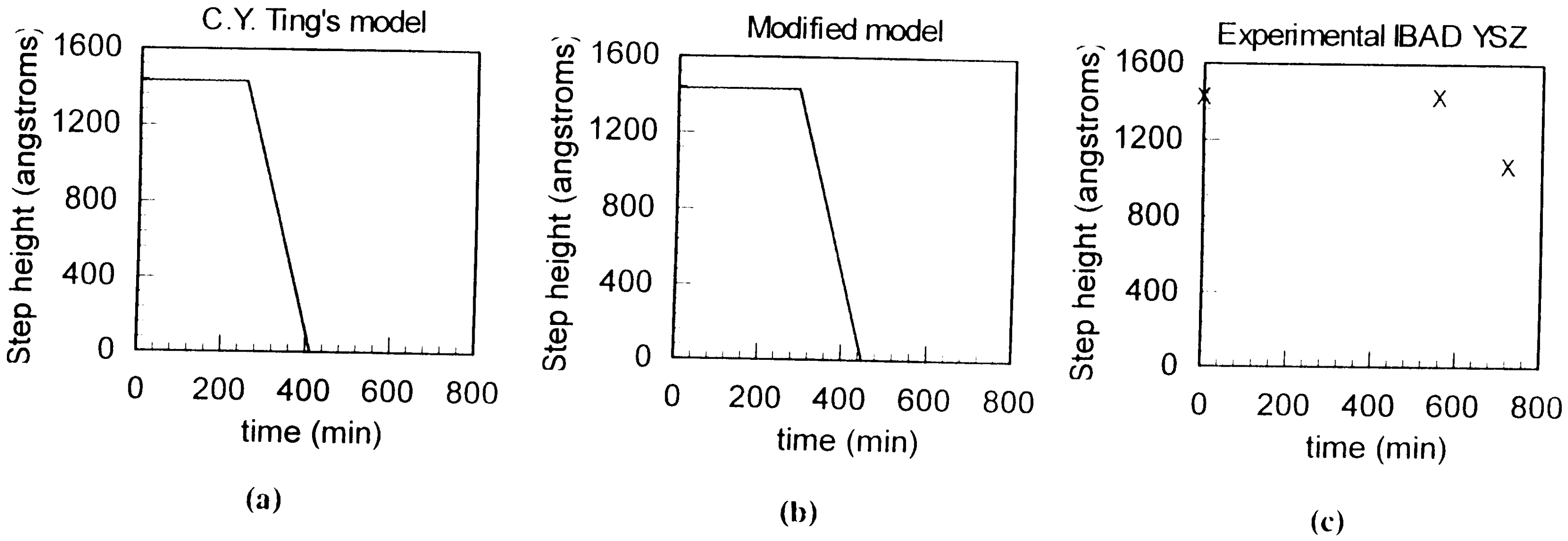

(a) **(b)** **(c)**

Figure 4.36 Planarization progress represented by variation in film step height versus processing time for: (a) C.Y. Ting's model, (b) modified model, and (c) experimental data for IBAD YSZ. Calculated/measured for a 1430 Å high, 52° substrate step and a net IBAD rate of 0.15 Å/s.

etching regime will not experience any film growth. In addition, when film growth does take place on an angled step, the cosine growth rate will be reduced to some extent due to the presence of ion etching. C.Y. Ting's model and the modified model therefore represent two extremes; no growth takes place at all on angled surfaces for the former while a cosine-type growth always occurs for the latter. The processing times that are calculated from these two models there also represent the two extremes that are possible.

Table 4.6 and Figure 4.36 show, however, that both models predict that planarization should already have been achieved for the IBAD YSZ film shown in Figure 4.11 that was processed for 555 minutes. However, measurement from the top of the cone to the lowest portion of the adjacent valley in Figure 4.9 shows that the height difference is still equal to the underlying step height. Further IBAD deposition to 720 minutes at the same deposition conditions over steps of similar widths results in only a 25% decrease in the overall step height of the film. Planarization is occurring but at a slower rate than expected. This type of nonlinear behavior is not predicted by either model.

4.5.2 Redeposition

It is clear that the planarization evolution predicted by the two linear models in the previous section does not adequately represent what is actually occurring for the IBAD YSZ films. The graph presented in Figure 4.32 for which these two linear models are based upon takes into account only bulk deposition and etching, and neglects secondary effects such as redeposition.

The SEM micrographs in Figures 4.10-4.12 for the three films deposited at 0.15 Å/s show that apart from differences in planarization, the emerging surface topography also differs from C.Y. Ting's model. Examination of the topography of these three films reveals that an extension of the cones does not intersect the top corner of the underlying substrate step. Instead, there is no clear delineation between the cones and the planar portions of the film. As seen in Figure 4.11(b) for the 555 minute film, the slope of the film surface is also not constant, but varies from ~12° to ~7° as the angled surface is traversed from the cone tip to the valley. This variation in the film slope angle and the increased film thicknesses observed in the valleys immediately adjacent to the steps bear more of a resemblance to the computer simulations developed by C.H. Ting *et al.*[15] and Bader and Lardon[12] for rf bias sputtering of planarized SiO_2 and Al films (see Figures 4.37 and 4.38) than to C.Y. Ting's construct.

The increased film thickness near the step edges can be attributed to redeposition of material sputtered from the film. Bader and Lardon explicitly took redeposition effects into account in their computer simulations while this was not done so by C.H. Ting *et al.*

Types of redeposition

Redeposition can have several origins. Material sputtered from the film can be backscattered from the plasma and redeposited. This is expected to be significant when the chamber pressure is high as is the situation for plasma based processes such as rf bias sputtering. Rough surfaces or protrusions have a particularly higher probability of receiving backscattered material. For the case of etching alone, this type of redeposition does not prevent complete etching of surface protrusions but it slows down the removal process.[147] This type of redeposition may also account for the incomplete cone eradication or burial observed by Mogami *et al.*[148] for planarized SiO_2 layers deposited by rf bias sputtering. The authors reported that planarization of 4 μm wide and 0.5 μm thick Mo lines with SiO_2 resulted in a nearly planar surface but with ~0.07-0.1 μm high cone tips. This result was found for both rf-bias sputtered SiO_2 and for etching of rf-bias sputtered SiO_2 films after cone formation had taken place. It is likely that redeposition of backscattered material led to prolonged retention of the cone tips. For the IBAD processing conditions used in this thesis research, however, the chamber pressure of 2×10^{-4} Torr is much lower than pressures typically used during plasma sputtering processes which are on the order of several to several hundred mTorr. Redeposition of backscattered material is therefore not expected to be significant.[149]

Material that is sputtered off of one angled surface can also be redeposited onto a second nearby angled surface. This is most significant when adjacent step edges are located in close proximity, as is the case with vias. This can lead to growth of overhanging material at the step edges and results in vias that are covered but are

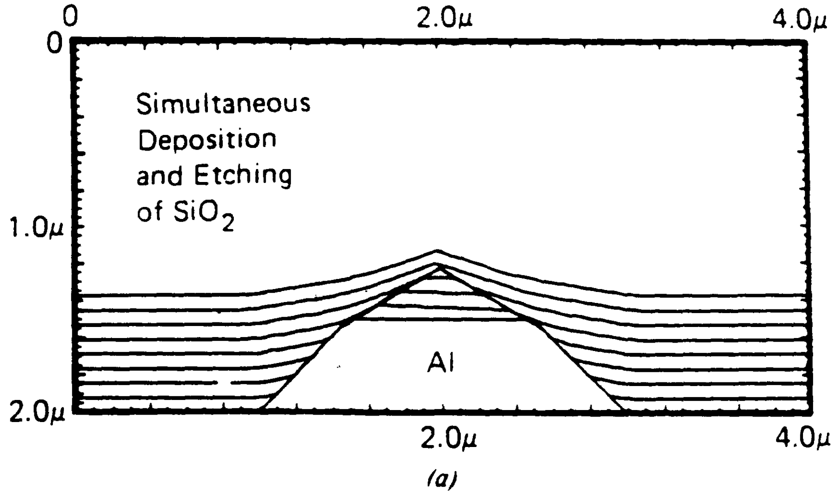

Figure 4.37 Simulated profile for SiO_2 rf-bias sputter planarization of Al interconnects (from Reference 15).

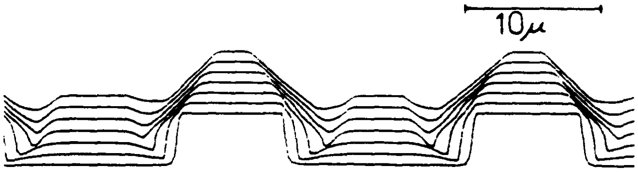

Figure 4.38 Simulated profile for Al rf-bias sputter planarization (from Reference 12).

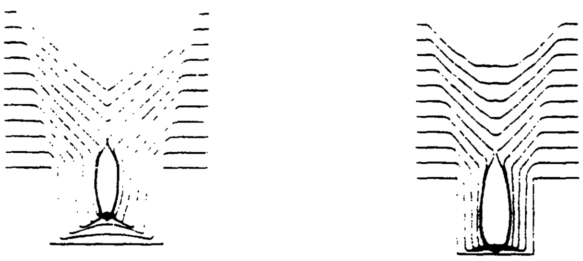

Figure 4.39 Computer simulations showing incomplete filling of vias due to redeposition and shadowing effects (from Reference 150).

incompletely filled (see Figure 4.39).[150] Again, this is not expected to be an issue here due to the relatively low aspect ratios of step height to valley width in the patterned YSZ substrates used in this study.

A third type of redeposition results from material that is sputtered from planar film regions and redeposited on adjacent non-planar surfaces, or vice-versa, i.e., material that is sputtered off the angled surfaces and redeposited in adjacent planar regions. Bader and Lardon demonstrate in their computer simulations that this type of redeposition is critical to achieving planarization. Figure 4.40 shows simulated profiles both without and with the effects of redeposition. A greater degree of progress towards planarization was achieved when redeposition effects are present. These simulated results were in agreement with experimentally obtained profiles. This third type of redeposition will be examined in a more quantitative fashion in the following section.

Quantitative assessment of redeposition

Redeposition from a planar surface onto adjacent non-planar features has been a problem associated with patterning fine features when using ion beam etching and photolithography,[151] as shown in Figure 4.41. Redeposition of material onto nearby photoresist results in an excess of undesired material being left behind. This problem is particularly severe for redeposition onto masks with vertical sidewalls. In this case, since the redeposited material is bombarded at glancing angles by the ion beam, it is not etched away and therefore remains after the photoresist has been removed.

This type of redeposition has been treated analytically[149] for emission onto sloped linear surfaces which are defined in terms of the step angle, α, and the height, H, above the surface, as shown in Figure 4.42. A cosine emission from the planar surface is assumed. Wilson *et al.*[149] have shown that the flux density integral for this situation is

$$\frac{F}{n} = \frac{F(0,l)}{n} = \frac{h\sin\alpha}{2}\int_0^l \frac{x\,dx}{[h^2 + (h\cot\alpha + x)^2]^{3/2}} \qquad (4\text{-}13)$$

where F is the redeposition flux arriving at the linear slope, n is the flux emitted from the planar region, h is the height above the planar surface, and *l* is the length over the planar

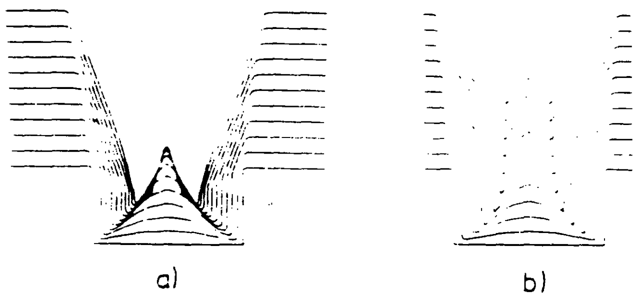

Figure 4.40 Computer simulations showing influence of redeposition on profile evolution during rf bias sputtering of Al: (a) without, and (b) with redeposition (from Reference 12).

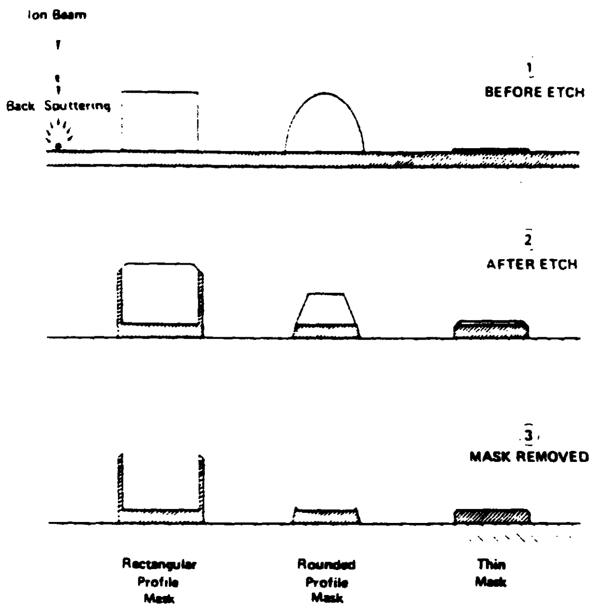

Figure 4.41 Effect of redeposition on patterning using ion beam etching and photolithography. The most severe redeposition problems are observed for rectangular masks (from Reference 151).

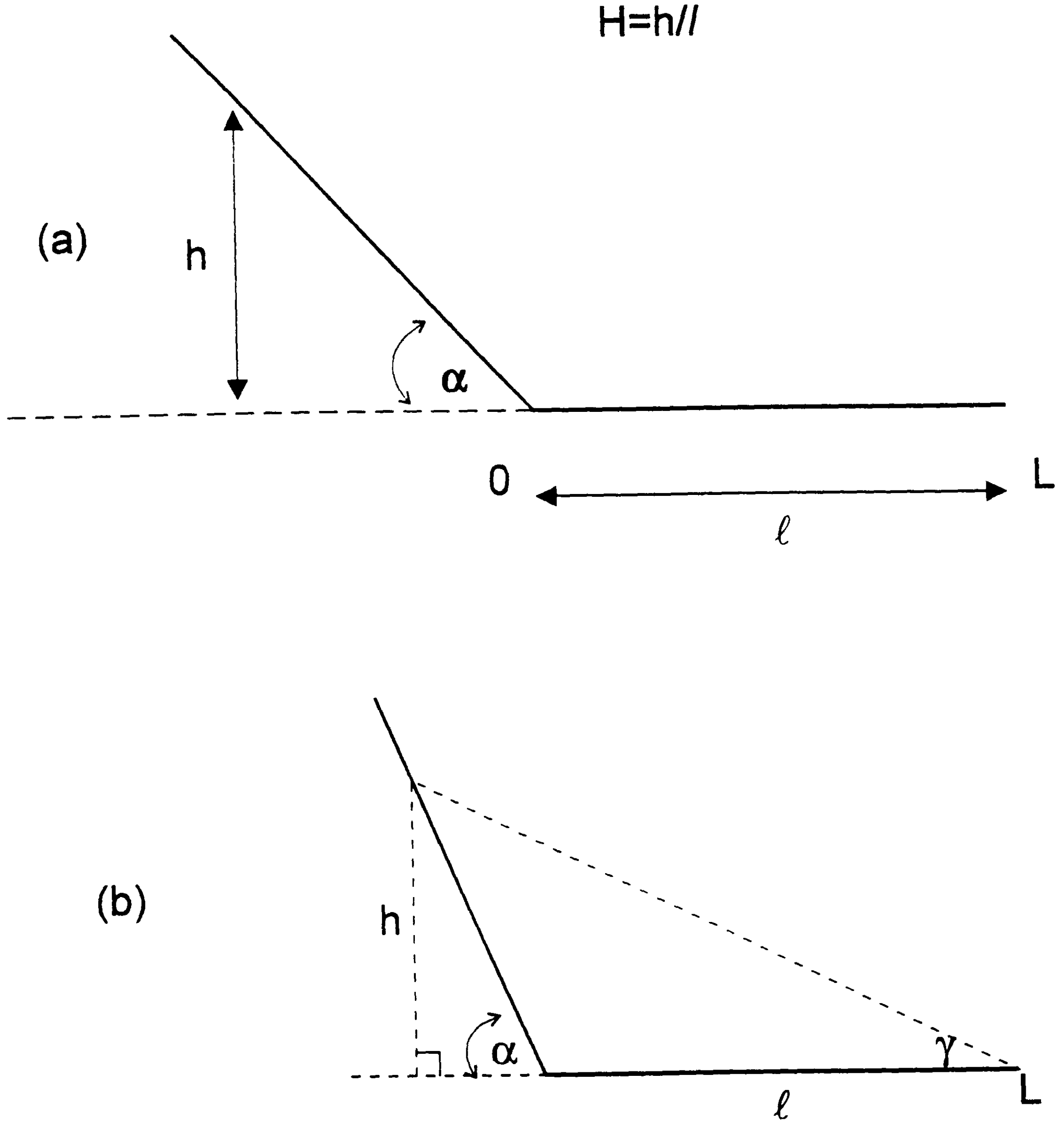

Figure 4.42 Geometrical relationships used by Wilson *et al.*[149] to derive redeposition flux equations for redeposition from a planar cosine emitter onto a linear slope of angle α: (a) for Equation 4-14; and (b) Equation 4-15.

region from which sputter emission is occurring. Integrating Equation 4-13 and transforming h into a dimensionless height of H=h/*l* gives

$$\frac{F}{n}=\frac{1}{2}\left[1-\frac{H\csc\alpha+\cos\alpha}{[H^2+(1+H\cot\alpha)^2]^{1/2}}\right]\ (H\neq 0) \qquad (4\text{-}14)$$

Figure 4.43 shows results for emission onto linear surfaces with various step angles. For each angle, the normalized redeposition flux is plotted against height above the emitter plane. It can be seen that at a given step angle, the rate of redeposition decreases with increasing height above the surface. The relative rates of redeposition, however, increase as the step angle increases.

Equation 4-14 can be rewritten to calculate deposition onto a given point above the surface on the linear slope, from a given point on the planar emitter surface, as follows

$$\frac{F}{n}=\frac{1}{2}[1-\cos(\alpha-\gamma)] \qquad (4\text{-}15)$$

where α is the step angle of the linear slope and γ is the angle of elevation from the end (L) of the emitter (see Figure 4.42(b)). This now allows redeposition rates at the base of the linear slope to be calculated by using $\gamma=0°$. Table 4.7 shows how F/n increases for increasing values of the step angle, α.

It should be noted that the normalized flux density, F/n is a dimensionless number and is proportional to the deposition/sputter rates. Actual values for the redeposition rate arriving at the linear sloped surface, R_{redep}, can therefore be calculated by setting F/n to R_{redep}/V_{source}, and substituting experimentally measured values of normal incidence etch rates for IBAD YSZ for V_{source}.

The case of redeposition from an angled surface onto adjacent planar areas was treated numerically in two dimensions by Robinson[152] as part of a study to determine the

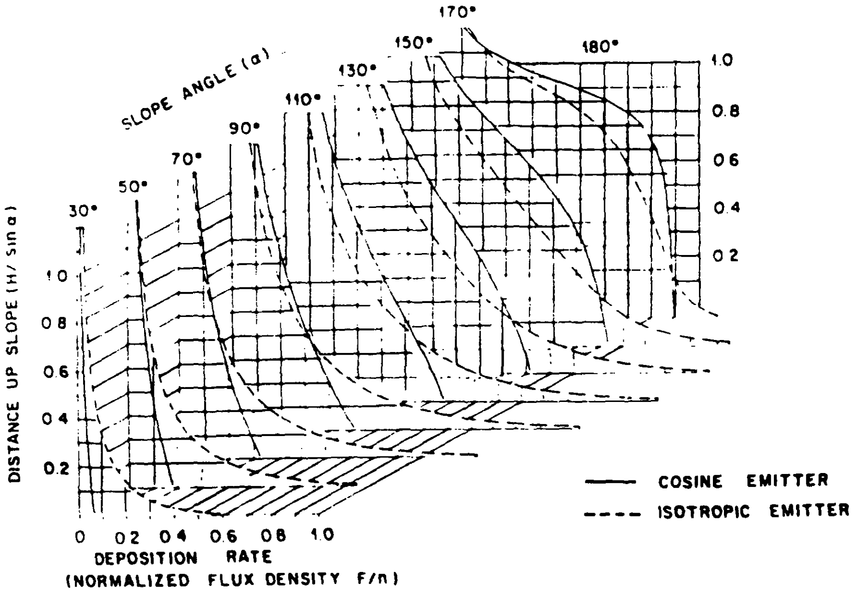

Figure 4.43 Variation of normalized redeposition flux density (F/n) as a function of distance up a linear slope and slope angle (from Reference 149).

Table 4.7 Normalized redeposition flux (F/n) due to sputtering from a planar emitter as a function of step angle (α), calculated from Equation 4-15.

Step angle α (°) of receiver plane	Normalized redeposition flux (F/n)	Redeposition Rate (Å/s) using n=0.5 Å/s
10	0.0076	0.0038
20	0.0302	0.0151
30	0.0670	0.0335
40	0.1170	0.0585
50	0.1786	0.0893
60	0.2500	0.1250
70	0.3290	0.1645
80	0.4132	0.2066
90	0.5000	0.2500

Table 4.8 Normalized redeposition flux (F/n) due to sputtering of an angled emitter, calculated as a function of step angle (β), from Equation 4-17

Step angle β of emitter plane (°)	Normalized redeposition flux (F/n)	Redeposition Rate (Å/s) using n=0.5 Å/s
10	0.0038	0.0019
20	0.0151	0.0075
30	0.0335	0.0167
40	0.0585	0.0292
50	0.0893	0.0447
60	0.1250	0.0625
70	0.1645	0.0822
80	0.2066	0.1033
90	0.2500	0.1250

redeposition rate resulting from ion bombardment of a beveled source situated on top of a planar substrate (see Figure 4.44). Assumptions for this calculation included normal incidence ion bombardment of the substrate and a cosine distribution about the local surface normal for atoms sputtered from beveled source. The geometry used to model the deposition effect is shown in Figure 4.45. The quantity y_2/h was used to define a distance away the planar surface from the source, where y_2 is the distance from the angled surface and h is the step height.

Robinson showed that the relative redeposition rate as a function of substrate position is given by

$$\frac{F}{n}=\frac{y_2\sin^2\beta}{2\pi}\int_0^L dx_1 \int_0^{\frac{h}{\sin\beta}} dy_1 y_2\left[(x_2-x_1)^2 + y_1^2\sin^2\beta+(y_2+y_1\cos\beta)^2\right]^{-2} \tag{4-16}$$

where as before, F/n refers to the normalized redeposition flux density. A numerical integration algorithm was used by Robinson to evaluate this integral since it will not generally be solvable in closed form. The variation in redeposition rate, F/n, with increasing distance away from the source, y_2/h for an underlying step angle of 45° is shown in Figure 4.46. It is seen that the redeposition rate varies up to one to two orders of magnitude and drops off rapidly with increasing distance away from the angled surface. Redeposition thus has the effect of generating a gently sloping surface.

The limit to Equation 4-16 can be obtained by changing to appropriate dimensionless variables and integrating to yield

$$\left(\frac{F}{n}\right)_{limit}=\frac{(1-\cos\beta)}{4} \tag{4-17}$$

This limit is valid for $y_2/h = 0$ which corresponds to locations immediately adjacent to the beveled surfaces and represents the highest degree of redeposition possible. Table 4.8 list values of F/n at $y_2/h = 0$ calculated for various step angle values. It is seen that the rate of redeposition increases for increasing values of the step angle, β.

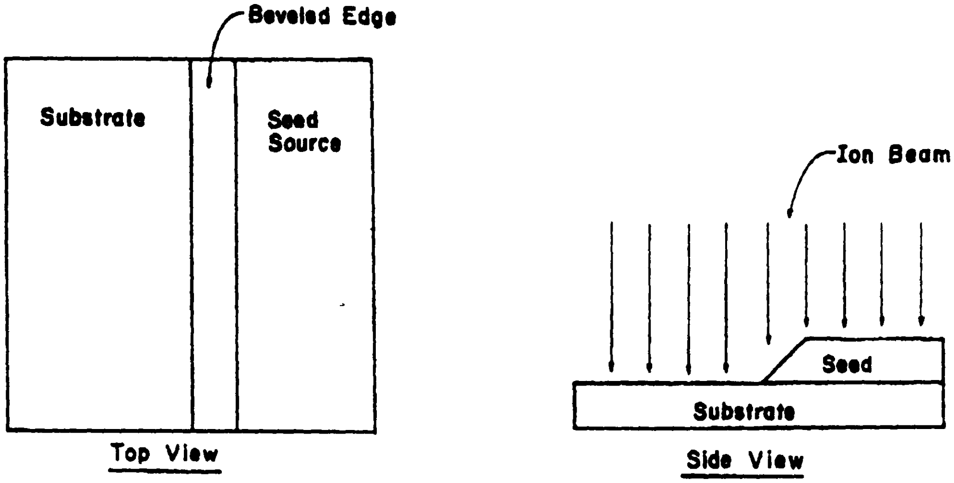

Figure 4.44 Schematic illustrating redeposition onto a planar surface as a result of sputtering of a nearby angled surface (from Reference 152).

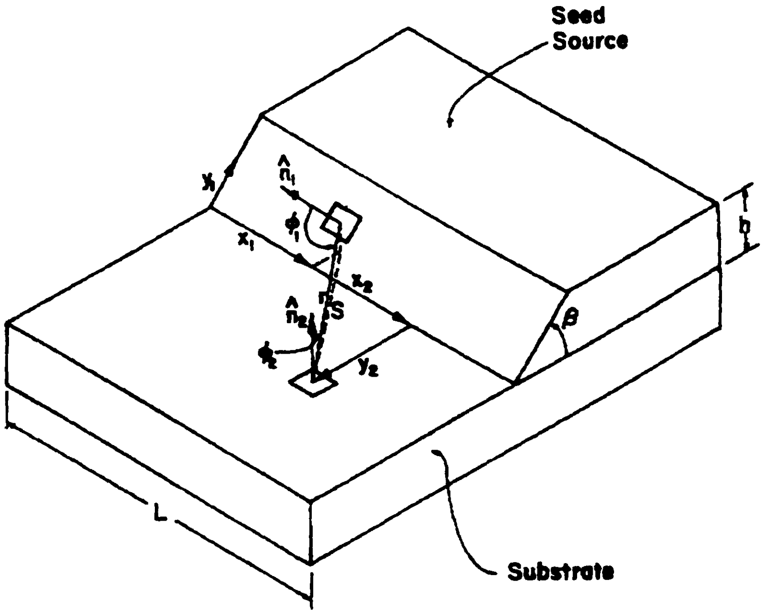

Figure 4.45 Geometry used by Robinson[152] for parameter definition for deriving relationships for redeposition flux as a function of step angle (β) and distance away from angled source.

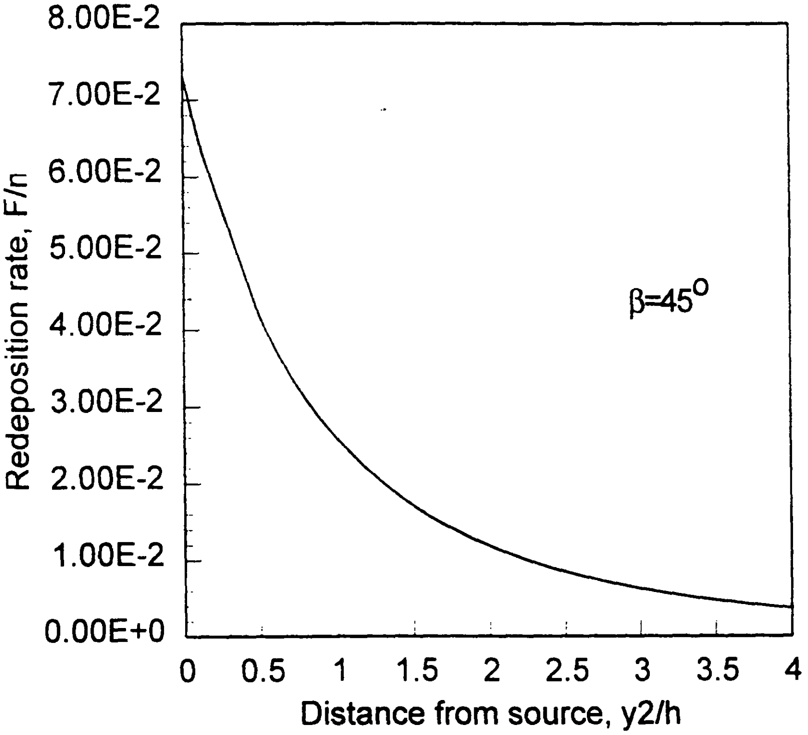

Figure 4.46 Variation in redeposition flux (F/n) as a function of distance (y_2/h) away from source based on Equation 4-16. Calculated for a step angle (β) of 45°.

For Equations 4-16 and 4-17, the value of the redeposition flux, F can be calculated by multiplying the right hand side of each equation by n, the flux emitted normal to the source plane. In this case, the value of n is proportional to the sputter yield and therefore is a function of the underlying step angle, β. The value of n(β) will generally be greater than for sputtering at normal incidence, or n(0), except at glancing angles. Using values of n(0) in Equation 4-13 will therefore allow a conservative estimate of the arriving flux at the substrate to be obtained. As discussed above, since F/n is a dimensionless number, experimentally measured values of the normal incidence sputter rate can be substituted for n(0) in order to calculate the redeposition rate.

It should be noted that a cosine sputter emission is assumed in both of these redeposition analyses. This assumption, however, may actually underestimate the degree of redeposition that can occur. The redeposition situation analyzed by Robinson involves non-normal ion incidence on a beveled source, as shown in Figure 4.44. Tsuge and Esho's work,[60] however, has shown that oblique ion incidence can result in increased forward emission, as shown in the polar plots in Figure 2.5. This type of emission pattern would enhance redeposition from a beveled source onto nearby planar features. The actual redeposition flux would then be greater than that estimated by a cosine distribution.

Tsuge and Esho also showed a departure from a cosine emission for normal incidence sputtering of oriented materials in which preferred ejection along close packed crystallographic directions was found. For sputtering of epitaxial films, this could also lead to a greater degree of redeposition from a planar surface to certain heights of adjacent non-planar features.

4.5.3 Effect of Redeposition on Net Deposition Curve

The added effect of redeposition on planarization progress can be illustrated by looking at the degree of redeposition that occurs at one point on the growing film during planarization processing. The schematic in Figure 4.47 depicts a substrate step of angle θ_s and a subsequently grown IBAD film at an angle θ_e. Redeposition from the adjacent planar film to the foot of the angled film, as indicated by the arrow in Figure 4.47, will be examined for three different deposition times.

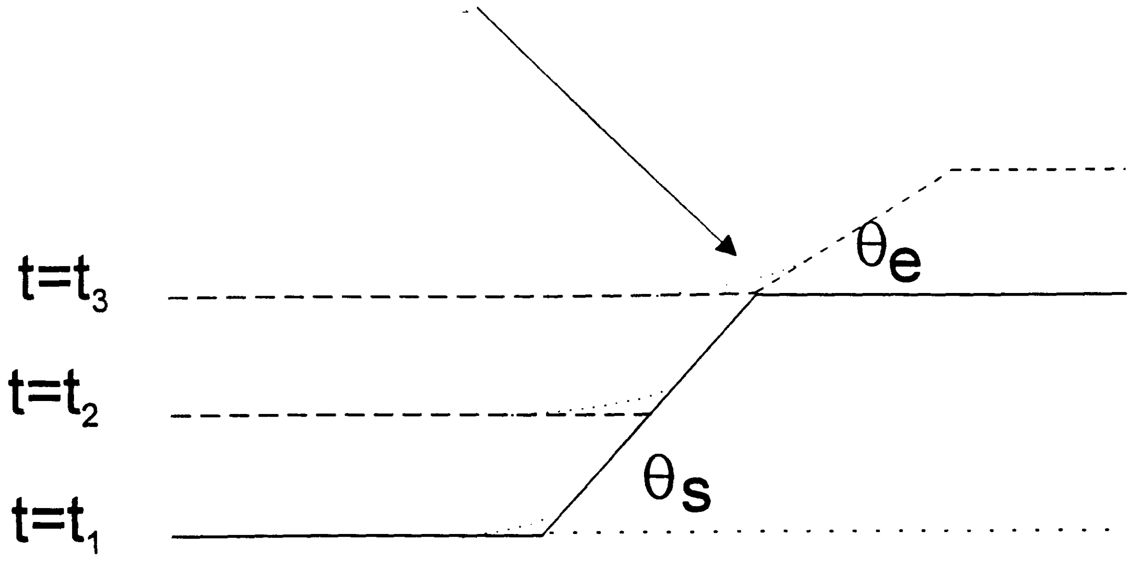

Figure 4.47 Schematic used to illustrate effect of redeposition at the base of the angled film growing at θ_e at three different times during planarization processing.

At the onset of planarization processing, an angled film will begin to form over the patterned substrate step with the equilibrium angle θ_e. Meanwhile, film growth is taking place over the planar substrate surfaces at the rate $R_{\perp(net)}$. Redeposition rates are then calculated for three different times: shortly after deposition has begun (t_1), after the thickness of the planar film has reached half of the substrate step height (t_2), and after the planar film has equaled the substrate step height (t_3). Redeposition rates at t_1 and t_2 are calculated using Equation 4-14 for a substrate step angle of 45°. The experimentally measured normal incidence IBAD YSZ sputter rate of 0.5 Å/s is used for n, while values of 1.0 and 0.5 are used for H at times t_1 and t_2, respectively. Redeposition at t_3 is calculated using Equation 4-15 for a film step angle (α) of 10° and an elevation angle (γ) of 0° (i.e., deposition at the base of the angled film). These redeposition rates are listed in Table 4.9.

It is seen that the amount of redeposition to the foot of the angled film increases as the planar film grows thicker and thus moves closer. The redeposition rate at time t_2, for instance, is over twice the rate at time t_1, and is equivalent to ~17.6% of the $R_{\perp(net)}$ rate of 0.15 Å/s. The rate of redeposition decreases after the film reaches and exceeds the substrate step height since θ_e is at a lower angle than the substrate step. This rate, however, is still a non-zero value.

The effect of redeposition on the net deposition curve can be seen in Figure 4.48. The original net curve based only on bulk deposition and etching from Figure 4.32 is plotted as curve 0. The two redeposition rates calculated at times t_1 and t_2 are superimposed on the graph. Net curves 1 and 2, respectively, take these two redeposition rates into account. It is seen that redeposition has the effect of increasing the overall growth rate and shifting the zero point of the net curve, i.e., the equilibrium angle, to higher values of θ_e'.

Once the equilibrium angle has increased to θ_e' as a result of redeposition, the original equilibrium angle θ_e at which the film was growing now no longer resides at the zero point on the new curve. Instead, θ_e now sits at some point above zero on the new net curve. Therefore films grown at the original equilibrium angle are no longer static but experience a positive net growth rate. This leads to a lower planarization rate, since

Table 4.9 Redeposition rates calculated for deposition to base of angled film depicted in Figure 4.47 at three different times during planarization processing.

	Redeposition Rate (Å/s)	% of $R_{\perp(net)}$ (= 0.15 Å/s)
$t=t_1$ ($\theta_s = 45°$)	0.0128	8.53
$t=t_2$ ($\theta_s = 45°$)	0.0264	17.6
$t=t_3$ ($\theta_e = 10°$)	0.0076	5.07

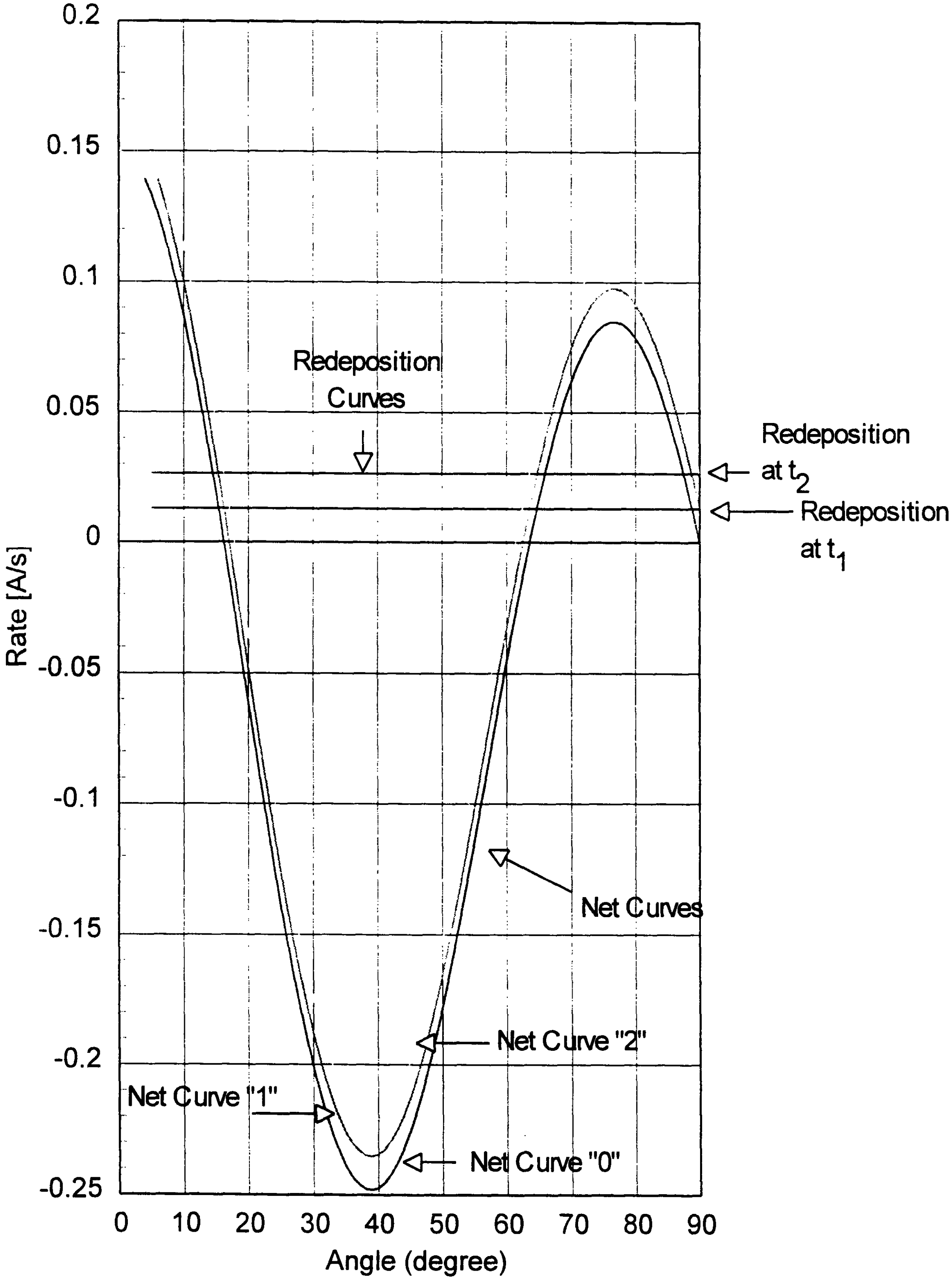

Figure 4.48 Graph showing the effect of redeposition on the net deposition curve for IBAD planarization processing.

planarization is no longer occurring at the rate $R_{\perp(net)}$, but at a rate reduced by the amount of net growth that is taking place at θ_c. This reduced planarization rate will vary with time since the redeposition rates are also varying with time, and results in a non-linear behavior with time.

This nonlinearity is enhanced by the fact that as redeposition takes place, the angle of the film will also decrease from the original angle. The degree of redeposition along the entire sloped film will be highest at the base of the film and decrease with increasing height above the surface. Thus, the highest film angle will be found at the tip of the cone where the least amount of redeposition is occurring. Increasing redeposition will cause the film angle to decrease as the film is traversed from the tip to the base. Redeposition from the angled film to the planar portion of the film will also generate a low angle sloping surface near the foot of the film, as shown previously in Figure 4.46. The net curves on Figure 4.48 show that as the film angle decreases, the overall film growth rate for that surface increases. The net planarization rate is therefore even further reduced.

Experimentally, a variation in film angle with increasing height above the surface is observed. In Figure 4.11(b), the steepest angle, 12°, is found near the tip of the cone. The angle of the sloping film away from the tip of the cone decreases by several degrees to 7° at the base and is consistent with redeposition taking place as described above. The experimental results show that after 555 minutes of IBAD processing, cone formation has occurred but with no decrease in step height. Further IBAD processing to 720 minutes results in only a ~25% decrease of the absolute step height from 1750 Å to 1300 Å while the overall film thickness increases globally. This is equivalent to an average planarization rate of ~0.045 Å/s for the time interval between 555 and 720 minutes. This is similar to the decreased rate of planarization derived from Figure 4.48 between growth on a planar surface at 0.15 Å/s and growth on a 7° angled film at 0.10 Å/s, i.e., a net planarization rate of 0.05 Å/s.

Departure from the linear planarization rates predicted by C.Y. Ting's model can now be accounted for by redeposition. Redeposition is seen to have two effects. The first is to shift the zero point on the net deposition curve to higher angles. The second is to decrease the angle of the film from the original equilibrium angle. Both effects cause an increase in the overall growth rate over the angled film surfaces and thus a corresponding decrease in the net planarization rate.

4.5.4 Summary of Planarization Process

The findings presented in this section show that consideration of etching and bulk deposition only is insufficient for accurately predicting the rate of planarization. Redeposition was found to be a significant secondary effect for the results obtained in this study. Redeposition substantially decreased the rate of planarization and prevented planarity from being achieved within reasonable processing times.

If the time dependence of θ for bulk growth and redeposition are treated using the approach used by Carter *et al.*[142] for pure etching, the time dependence of planarization can then be summarized in the following equation,

$$\frac{\partial\theta}{\partial t} = \left[-\frac{\Phi}{n}\frac{\partial S}{\partial\theta}\cos^2\theta\frac{\partial\theta}{\partial x}\right] + \left[\frac{\partial R}{\partial\theta}\cos\theta\frac{\partial\theta}{\partial x}\right] + \left[\frac{\partial F}{\partial\theta}\cos\theta\frac{\partial\theta}{\partial x}\right] \quad (4\text{-}18)$$

where R represents a generalized growth law and F represents the flux for redeposition on an angled surface, θ, from an adjacent planar source as expressed in Equation 4.13. It is seen that detailed knowledge of the dependence on angle of the sputter yield, film growth, and redeposition are needed. As mentioned earlier, this equation will not be generally solvable. Numerical solutions and computer simulations can be used, however, to generate surface profile evolution as a function of time. This will allow more accurate predictions of the time required to achieve planarization for a given set of processing conditions.

4.6 SUMMARY

In summary, the results from this research provided the first experimental demonstration of a general *in situ* epitaxial planarization technique. Ion beam assisted deposition of YSZ over patterned YSZ substrates was found to improve step coverage and planarity while achieving simultaneous growth of epitaxial YSZ. The observed planarization mechanism of cone formation and burial is largely similar to what has been previously reported in the literature for planarization via rf bias sputtering for amorphous SiO_2 and polycrystalline Al films. This demonstrates that this planarization mechanism is also applicable to single crystal-like films. However, IBAD planarization progress was also found to be retarded by the development of low angle undulating surfaces in which redeposition was found to play a significant role.

BYC films grown over IBAD-planarized surfaces using pulsed laser deposition exhibited substantial improvements in electrical properties when compared to BYC films grown over unplanarized substrates. This is an important result for HTSC multilayer device technology. BYC films deposited using sputtering were found to be inferior to PLD films, both microstructurally and electrically, suggesting that the particular BYC deposition technique and deposition conditions used for growth over these types of surfaces need to be carefully tailored.

CHAPTER 5

HETEROEPITAXIAL PLANARIZATION OF IBAD CeO_2 ON $LaAlO_3$

5.1 INTRODUCTION

The study presented in Chapter 4 demonstrated the feasibility of homoepitaxial planarization. However, working multilayer devices will consist of heteroepitaxial structures in which a lattice mismatch will exist between the planarizing layer and the underlying surface. The combined effects of lattice mismatch and macroscopic surface relief, therefore, need to be ascertained. These issues are investigated in this chapter in which the IBAD planarization process is extended to the CeO_2-$LaAlO_3$ heteroepitaxial system. The best in-plane lattice matching condition between the (100) faces for these two materials involves a mutual 45° rotation about the [001] direction. The resulting CeO_2 [110] || $LaAlO_3$ [100] orientation has a 0.9% mismatch and is similar to the lattice matching conditions observed for BYC growth on CeO_2 and YSZ. CeO_2-$LaAlO_3$ is therefore a model system with which to explore some of the issues and challenges that will be encountered with planarization of HTSC traces.

An approach similar to the one used in Chapter 4 was taken in this study. CeO_2 films were deposited using ion beam assisted deposition onto (001) $LaAlO_3$ substrates that had been patterned with a parallel groove structure. Both normal and off-normal incidence ion bombardment were examined for their planarization capabilities as well as for their effects on heteroepitaxy. Film orientation and planarization progress were studied as a function of the IBAD process parameters. The effects of the combined presence of lattice mismatch and surface topography on the ability to carry out heteroepitaxial planarization were determined.

5.2 EXPERIMENTAL PROCEDURE

5.2.1 Substrate Preparation

1/4" square $LaAlO_3$ single crystal substrates were diced with the [100] and [010] directions parallel to the substrate sides and patterned with 2-3 μm wide lines as described in Section 3.1. Some of the substrates were annealed after ion milling at 950°C in flowing O_2 (4 scfh) for 2 hours. In all deposition runs, (001) $LaAlO_3$ substrates that had not been patterned or annealed were included for use as additional references for X-ray and SEM characterization. These substrates will be referred to hereafter as as-received $LaAlO_3$ substrates.

5.2.2 CeO_2 Deposition

Two angles of ion incidence were used in this study. The orientation of the plane of the substrate surface with respect to the ion beam was varied between 90° and 45°, which are designated in this thesis as normal and off-normal incidence bombardment, respectively. Unless otherwise noted, substrates were mounted for normal incidence IBAD with the longitudinal groove direction parallel to the incoming vapor species in order to avoid shadowing. For off-normal incidence ion bombardment, several in-plane substrate orientations were studied since the grooves in the substrate experienced some degree of shadowing at any given angle from either the evaporation source or the incident ions. Substrates were therefore mounted with the grooves oriented parallel, perpendicular, and at a 45° angle to the incoming ion beam (see Figure 5.1).

The IBAD deposition system and procedures described in Section 3.2 were used for the heteroepitaxial planarization experiments. The specifics of the CeO_2 deposition were as follows. Films were deposited at temperatures of either 400°C or 600°C. Most of the IBAD CeO_2 deposition runs were preceded by a 500-1000 Å thick initial layer of evaporated CeO_2 in order to grow a layer of high quality epitaxial CeO_2 and also to prevent direct ion beam etching of the substrate. All evaporated films were deposited at 0.2 Å/s and at low pressures of $\sim 10^{-6}$ Torr (i.e. no gas flow), except as noted otherwise. IBAD deposition rates were varied between 0.2 Å/s and 1.2 Å/s. All deposition rates

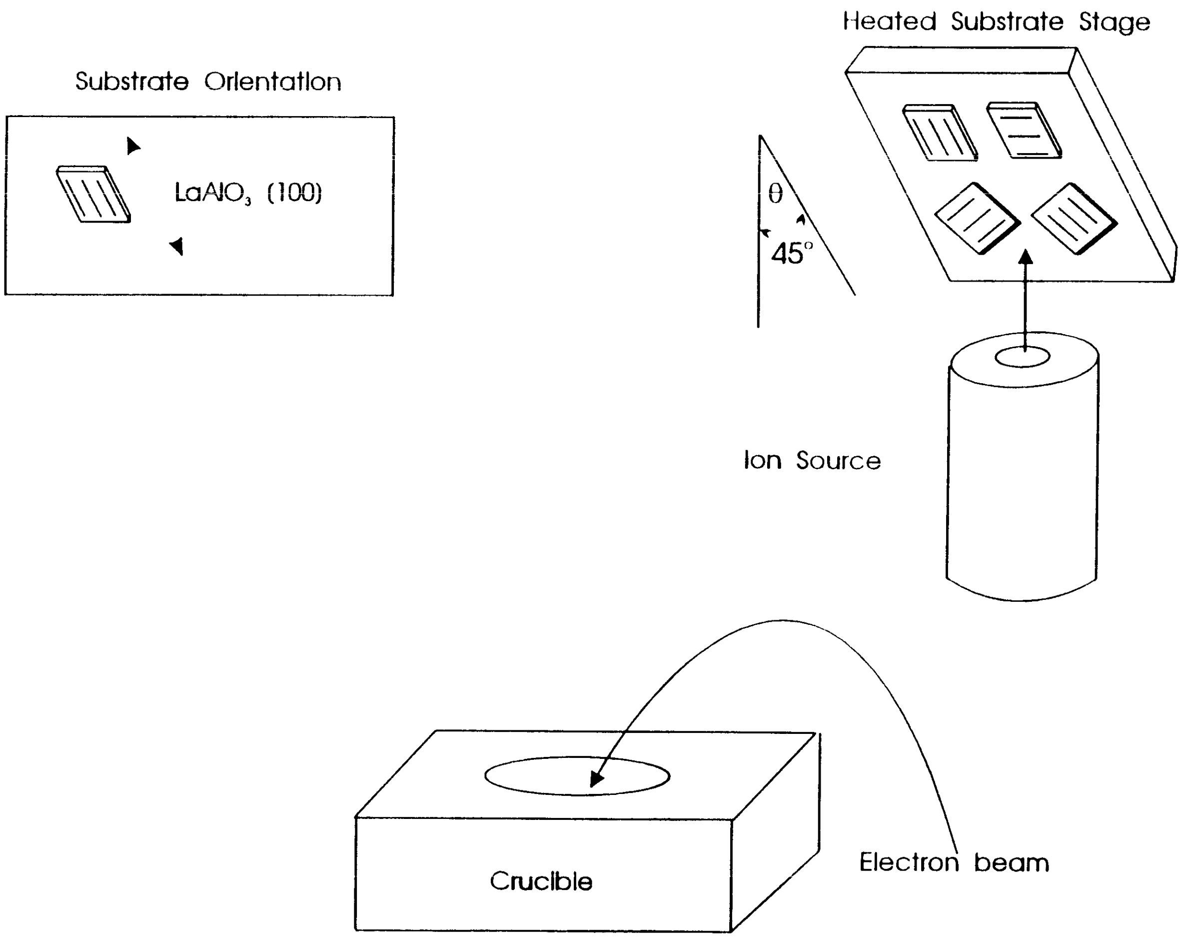

Figure 5.1 Schematic illustrating patterned substrate orientation relative to ion source and evaporation source for off-normal incidence IBAD processing.

reported in this chapter are the monitor-detected rates.

The rf ion source was operated at ion beam energies of 350 eV and 500 eV, with ion fluences between 180 μA/cm^2 and 200 μA/cm^2, neutralizer emission levels between 150-200%, and an accelerator voltage of 600 V. Typical gas flow through the ion source was ~7.5 sccm, which together with a flow of ~3.8 sccm for the PBN, gave an IBAD deposition pressure of ~2x10^{-4} Torr.

5.2.3 Characterization

Film orientation and texture were studied using X-ray diffraction, four-circle diffractometry, and X-ray pole figure measurements. Planarization progress and film microstructure were monitored using scanning electron microscopy. Further microstructural characterization of one of the normal incidence planarization samples was carried out using cross-sectional transmission electron microscopy (TEM). Sample preparation and microscopy work were performed by Dr. Paul C. McIntyre.

TEM sample preparation was carried out using a modification of the technique of Benedict *et al.*[153] as adapted by McIntyre.[10] All mechanical polishing was performed using a tripod polishing mount[83] on a Buehler polisher.[154] The specimen was first fractured to produce the cross-section of interest and a sandwich made by gluing a piece of single crystal sapphire to the top of the sample using M-Bond 610 epoxy.[155] After curing the epoxy at 140°C for 2 hours, the sandwich was polished so that the [100] $LaAlO_3$ zone axis was normal to the cross-section surface. The sandwich was then epoxied to a nickel grid with a 600 μm aperture with the cross-section to be examined face down and intersecting the center of the aperture. The entire sample was attached to the tripod polishing mount using Crystalbond[156] and the sandwich mechanically thinned from the back to a thickness of ~50 μm using a 15 μm diamond impregnated wheel and then polished using successive polishes of 9 μm, 6 μm, and 1 μm diamond paste on photographic paper. After polishing, the sample was removed from the tripod mount by dissolving the Crystalbond in acetone. The sample was then dimpled on a mechanical dimpler[157] using a texmet cloth padded tool and a 3 μm diamond slurry. After dimpling to ~5 μm thickness, the sample was ion milled to perforation in a Gatan Duomill.[158]

Milling was carried out on a liquid nitrogen cold stage with 4 keV Ar ions at an angle of 12°. High resolution TEM work was performed on a Topcon[159] 002B TEM operated at 200 kV.

5.3 EVAPORATED CeO_2 FILMS

Deposition of evaporated CeO_2 onto both patterned and as-received $LaAlO_3$ substrates was carried out. This enabled baselines to be established for film orientation, microstructure, and step coverage for the case of no ion bombardment.

5.3.1 Results

CeO_2 films evaporated at 0.2 Å/s without ion bombardment on as-received (001) $LaAlO_3$ single crystal substrates at temperatures of 400°C and 600°C grow epitaxially as determined by XRD and pole figure measurements. Typical XRD traces and pole figures for these samples are shown in Figure 5.2. The observed film-substrate relationship is CeO_2 (001) $\|$ $LaAlO_3$ (001) and CeO_2 [110] $\|$ $LaAlO_3$ [100]. CeO_2 films evaporated under the same conditions onto unannealed patterned $LaAlO_3$ substrates have a similar orientation but XRD scans also detect the presence of low intensity CeO_2 (111) and (311) peaks (see Figure 5.3(a)). CeO_2 grown over annealed patterned substrates, however, are epitaxial and exhibit only (00*l*) peaks in XRD traces (see Figure 5.3(b)).

SEM micrographs of these films shows that the evaporated CeO_2 grows in a conformal fashion, reproducing the underlying surface relief (see Figure 5.4). A difference in film microstructure is observed, however, between CeO_2 grown over milled and unmilled regions for deposition onto unannealed, patterned $LaAlO_3$ substrates. Two different columnar microstructures are obtained for deposition at 400°C in which CeO_2 grown over the milled regions possesses a coarser columnar microstructure as seen in Figures 5.4(a) and (b). At 600°C, CeO_2 deposited over the unmilled hills is dense and smooth while CeO_2 grown over the milled grooves has a more pebble-like appearance as seen in Figure 5.4(c). CeO_2 growth at 600°C on annealed patterned substrates exhibit a

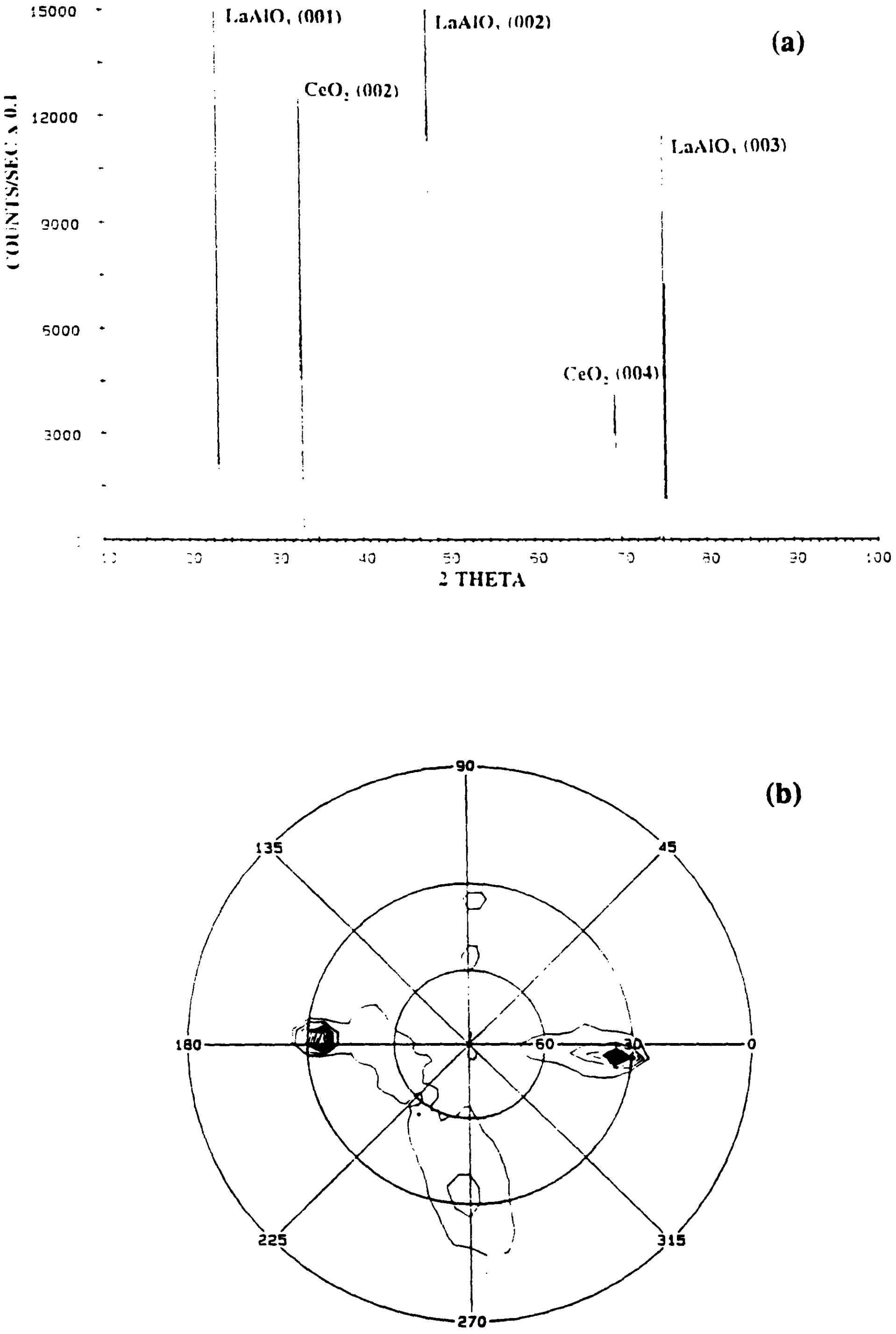

Figure 5.2 XRD scans for CeO_2 evaporated on (001) $LaAlO_3$ at 0.2 Å/s and 600°C: (a) θ/2θ scan, and (b) CeO_2 (111) pole figure.

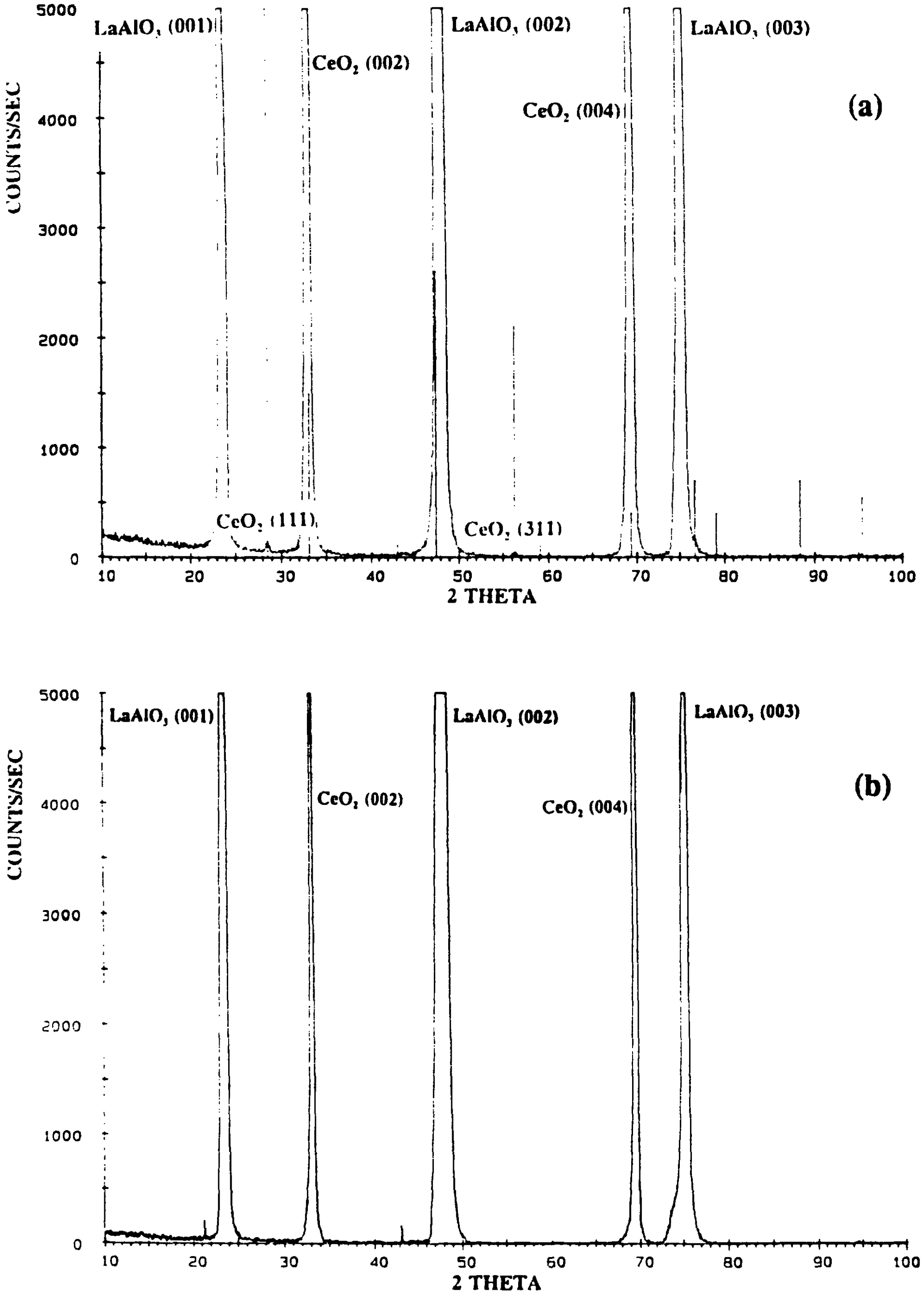

Figure 5.3 θ/2θ XRD scans for CeO_2 evaporated at 0.2 Å/s on: (a) unannealed patterned, and (b) annealed patterned (001) $LaAlO_3$ substrates.

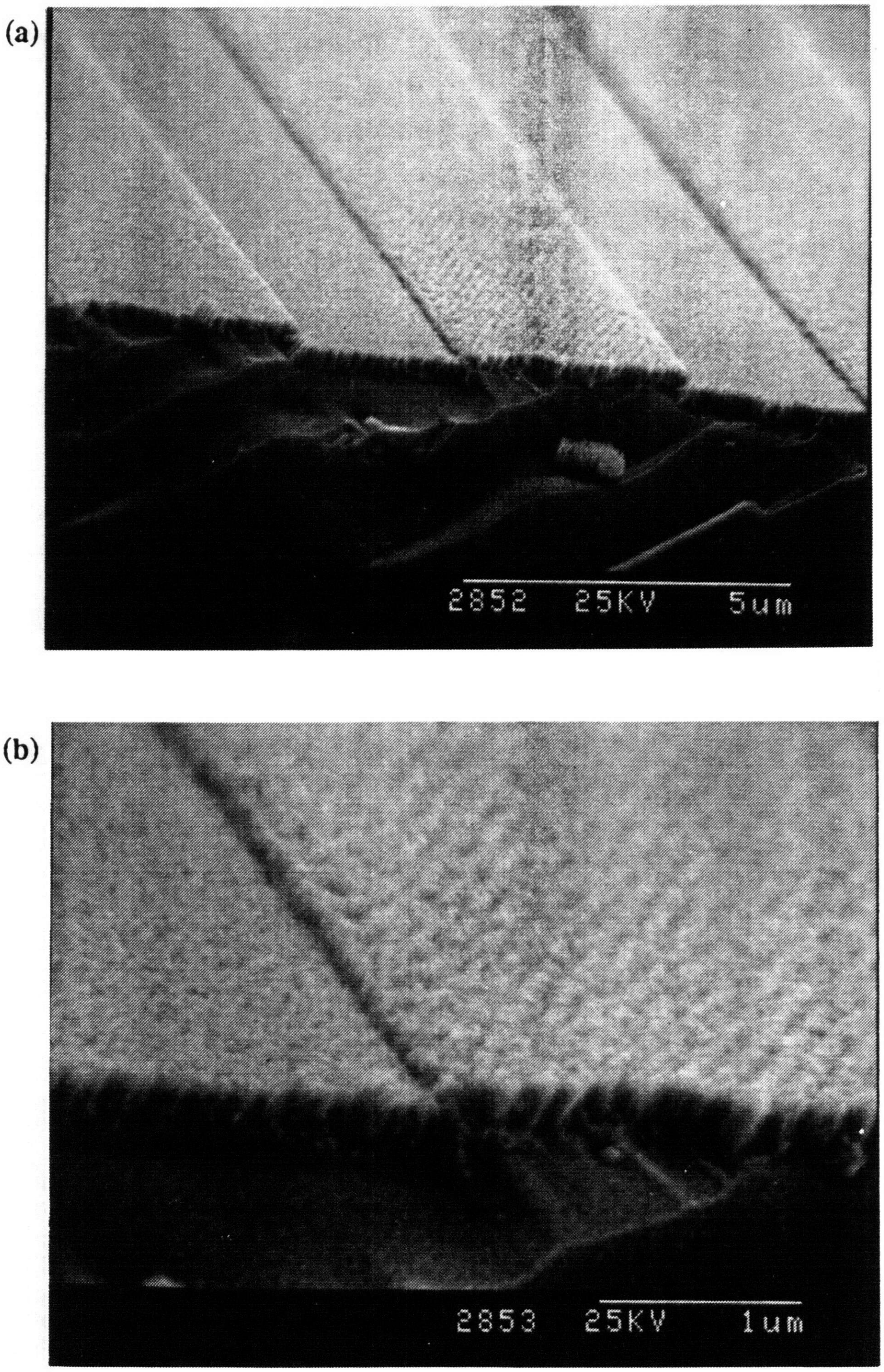

Figure 5.4 SEM micrographs of CeO_2 films evaporated on: (a) and (b) unannealed patterned $LaAlO_3$ at 400°C; (c) unannealed patterned $LaAlO_3$ at 600°C; and (d) annealed patterned $LaAlO_3$ at 600°C.

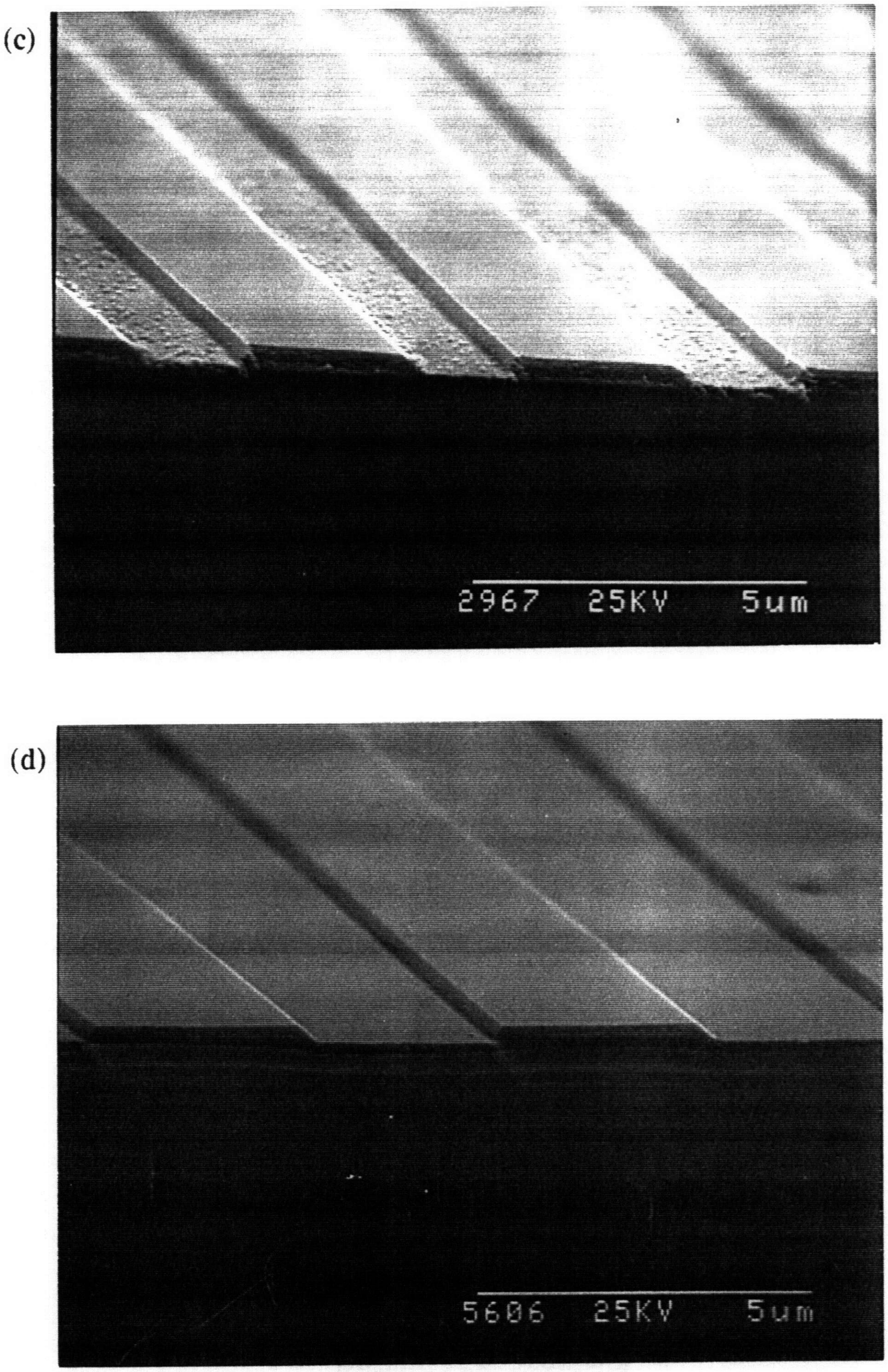

Figure 5.4 (continued).

smooth and dense microstructure that is uniform across the entire substrate as shown in Figure 5.4(d).

The effect of a faster deposition rate was examined by evaporating CeO_2 at 0.8 Å/s onto an as-received $LaAlO_3$ substrate at 600°C. The XRD $\theta/2\theta$ scans for this sample are similar to those of films deposited at 0.2 Å/s. The SEM micrograph in Figure 5.5 shows, however, that the film is not smooth but instead, possesses a densely packed columnar microstructure.

The effect of deposition pressure on evaporated CeO_2 films was also examined. 1000 Å of CeO_2 was evaporated onto an as-received $LaAlO_3$ substrate at 0.2 Å/s and 600°C while gas was flowed through the rf ion source and PBN to give a deposition pressure of $\sim 2 \times 10^{-4}$ Torr. XRD traces show no degradation in the crystalline quality of the film but SEM analysis shows that the microstructure of the film is affected. A rough, facetted microstructure is mixed in with a denser microstructure as seen in Figure 5.6. By comparison, CeO_2 films evaporated on (001) $SrTiO_3$ substrates under the same conditions exhibit a columnar microstructure as shown in Figure 5.7(a). As a reference, CeO_2 films grown on $SrTiO_3$ without gases flowing through the ion source are also columnar but appear both denser and smoother (see Figure 5.7(b)).

5.3.2 Discussion

Evaporation of CeO_2 over as-received $LaAlO_3$ substrates at 600°C results in growth of a high quality epitaxial film as shown by both XRD and SEM analysis. The observed epitaxial relationship is the one that is expected based on lowest misfit considerations and is consistent with results in the literature. The observed transition from a columnar to a dense microstructure with increasing deposition temperature is also consistent with structure zone models for evaporated films as discussed in Chapter 4.

The conformal film coverage that is obtained when CeO_2 is evaporated over patterned $LaAlO_3$ is consistent with topographical results obtained for evaporated YSZ films in Chapter 4. However, non-$(00l)$ CeO_2 peaks and a more defective microstructure are also observed only in films deposited over milled regions of unannealed patterned substrates. These can be associated with possible modifications of the $LaAlO_3$ substrate

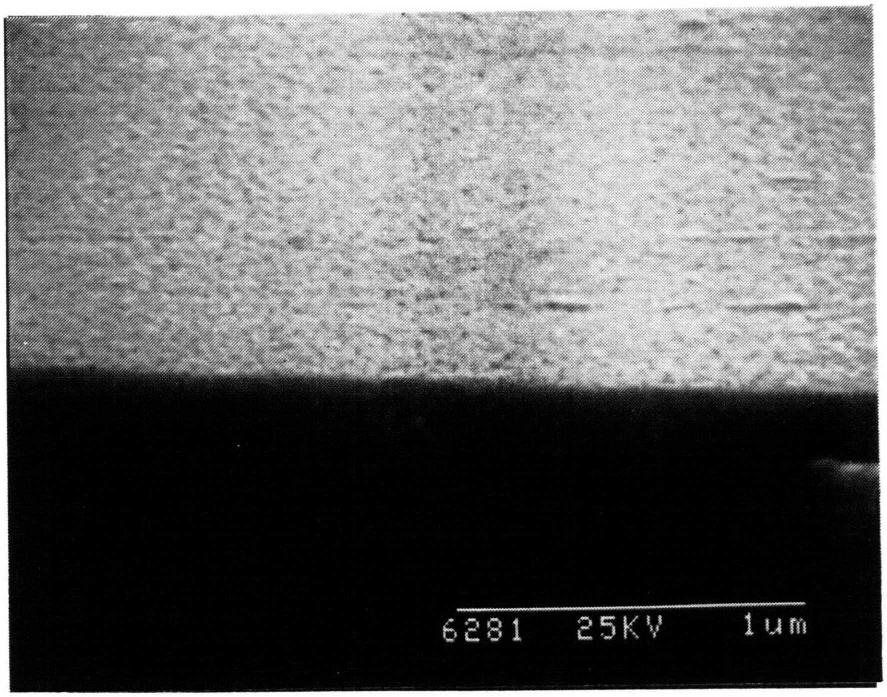

Figure 5.5 SEM micrograph of CeO_2 evaporated on as-received $LaAlO_3$ at 0.8 Å/s, 600°C, and $\sim 10^{-6}$ Torr pressure.

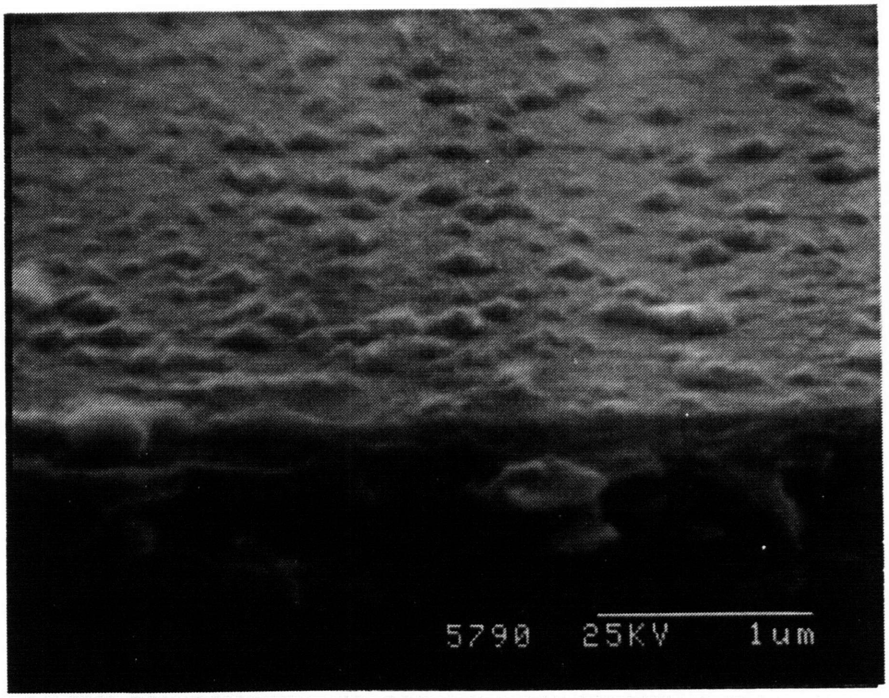

Figure 5.6 SEM micrograph of CeO_2 evaporated on as-received $LaAlO_3$ at 0.2 Å/s, 600°C, and $\sim 2x10^{-4}$ Torr pressure.

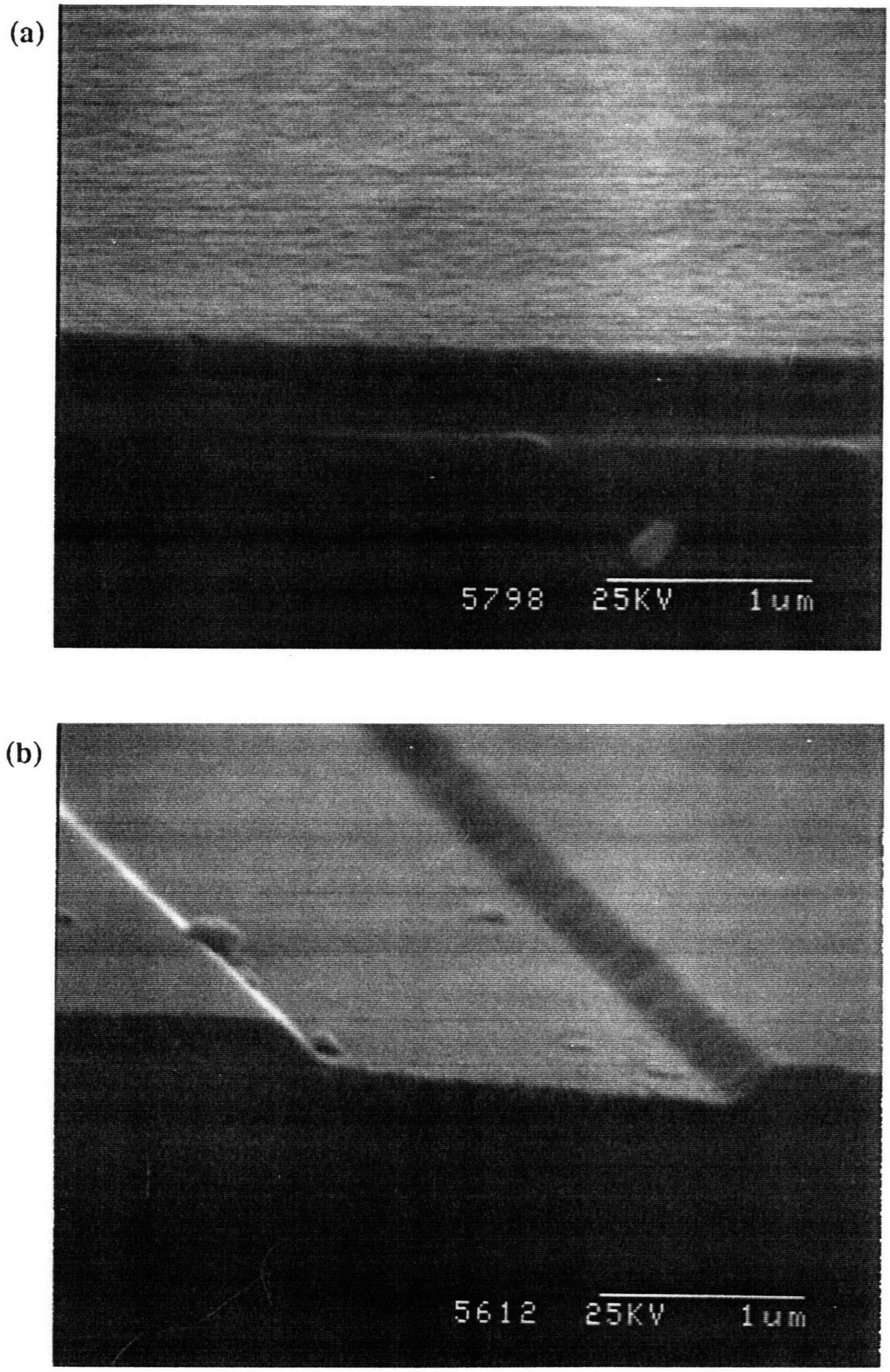

Figure 5.7 SEM micrographs of CeO_2 evaporated on (001) $SrTiO_3$ at 0.2 Å/s and: (a) ~2x10^{-4} Torr, and (b) ~10^{-6} Torr.

surface that took place during patterning of the substrate grooves. The ion energies used during the milling process are substantial enough to cause physical changes to the substrate surface such as surface lattice damage or loss of local $LaAlO_3$ stoichiometry due to preferential sputtering of one cation species over the other. The observed results are consistent with nucleation and growth of nonepitaxial CeO_2 over damaged $LaAlO_3$ since these defects are observed only for deposition over milled regions of patterned substrates. XRD and SEM results for CeO_2 growth over annealed patterned substrates demonstrate, however, that substrate surface damage sustained during ion milling can be healed through appropriate thermal treatments. It is important to obtain a uniform film microstructure over both the hills and valleys for the type of planarization processing being studied here since ion etching rates can differ quite substantially for different crystallographic orientations and microstructure.[160]

It is also seen that higher deposition rates lead to some degradation in microstructural quality of evaporated CeO_2. It is well known that high quality epitaxial film growth is favored by low deposition rates since these conditions allow enough time for the deposited species to assume the most energetically favorable sites available. As shown here, changing the evaporation rate of CeO_2 from 0.8 to 0.2 Å/s clearly results in an improvement in film microstructure.

The different microstructures observed for CeO_2 evaporated on $LaAlO_3$ at low and high pressures differ from results obtained for YSZ homoepitaxy and for CeO_2 growth on $SrTiO_3$. In the latter two cases, films grown at higher pressures consist of a coarser columnar microstructure that is consistent with structure zone model predictions as described in Chapter 4. On $LaAlO_3$, however, the formation of a second microstructure is observed by SEM. Although only (00*l*) peaks are detected in XRD scans of this film, it is still possible that the second microstructure corresponds to nonepitaxial CeO_2 that could not be detected in XRD scans due to its small volume fraction. It is clear, however, that poor vacuum conditions promote growth of degraded CeO_2 films on $LaAlO_3$. These observations again highlight the need for evaporation at low rates and under high vacuum in order to ensure high quality, defect-free films.

5.4 NORMAL INCIDENCE IBAD OF CeO_2

Normal incidence IBAD planarization experiments were carried out at 600°C. Annealed patterned substrates were used for all deposition runs. For all experiments, an initial 1000 Å thick layer of epitaxial CeO_2 was first evaporated before IBAD CeO_2 was deposited at 0.2 Å/s, 0.3 Å/s, 0.6 Å/s, 0.8 Å/s, 1.0 Å/s, and 1.2 Å/s using an ion beam energy of 500 eV and an ion fluence of 180 $\mu A/cm^2$. One experiment was also carried out at an IBAD deposition rate of 0.8 Å/s without an initial evaporated layer of CeO_2.

5.4.1 IBAD CeO_2 Film Orientation

5.4.1.1 Results

IBAD CeO_2 grown at 600°C on (001) $LaAlO_3$ are polycrystalline when deposited without an initial layer of evaporated CeO_2. XRD traces for these films show primarily weak (111), (311), and (222) peaks as seen in Figure 5.8. In contrast, IBAD CeO_2 deposited above 0.6 Å/s grows epitaxially if an initial layer of CeO_2 is first evaporated at 0.2 Å/s on the (001) $LaAlO_3$ substrate. Strong (00*l*) CeO_2 peaks can be seen in the XRD trace in Figure 5.9. X-ray pole figure results confirm epitaxial growth of the CeO_2 film (see Figure 5.9(b)). Some very weak non-(00*l*) CeO_2 reflections are also observed, however, in XRD traces of these IBAD CeO_2 films. These were detected for CeO_2 growth over both patterned and unpatterned substrates.

5.4.1.2 Discussion

Results from Chapter 4 showed that an initial layer of evaporated YSZ was not required to maintain homoepitaxial growth of IBAD YSZ. However, for the deposition conditions explored here for IBAD CeO_2 growth on $LaAlO_3$, it was necessary to first deposit a "seed" layer of high quality epitaxial CeO_2 in order to promote and maintain epitaxial growth during IBAD processing. This is consistent with the introduction of lattice mismatch. Deposition of the CeO_2 seed layer essentially allows homoepitaxial growth of IBAD CeO_2 to take place, whereas in Chapter 4, homoepitaxial growth of

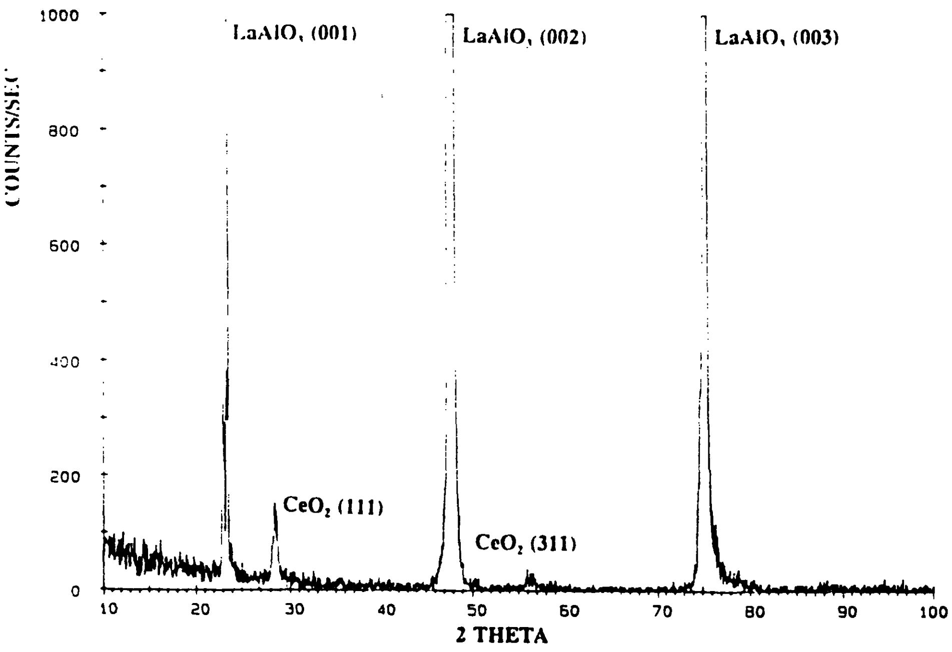

Figure 5.8 θ/2θ XRD scan of IBAD CeO$_2$ deposited on (001) LaAlO$_3$ without an initial seed layer of evaporated CeO$_2$.

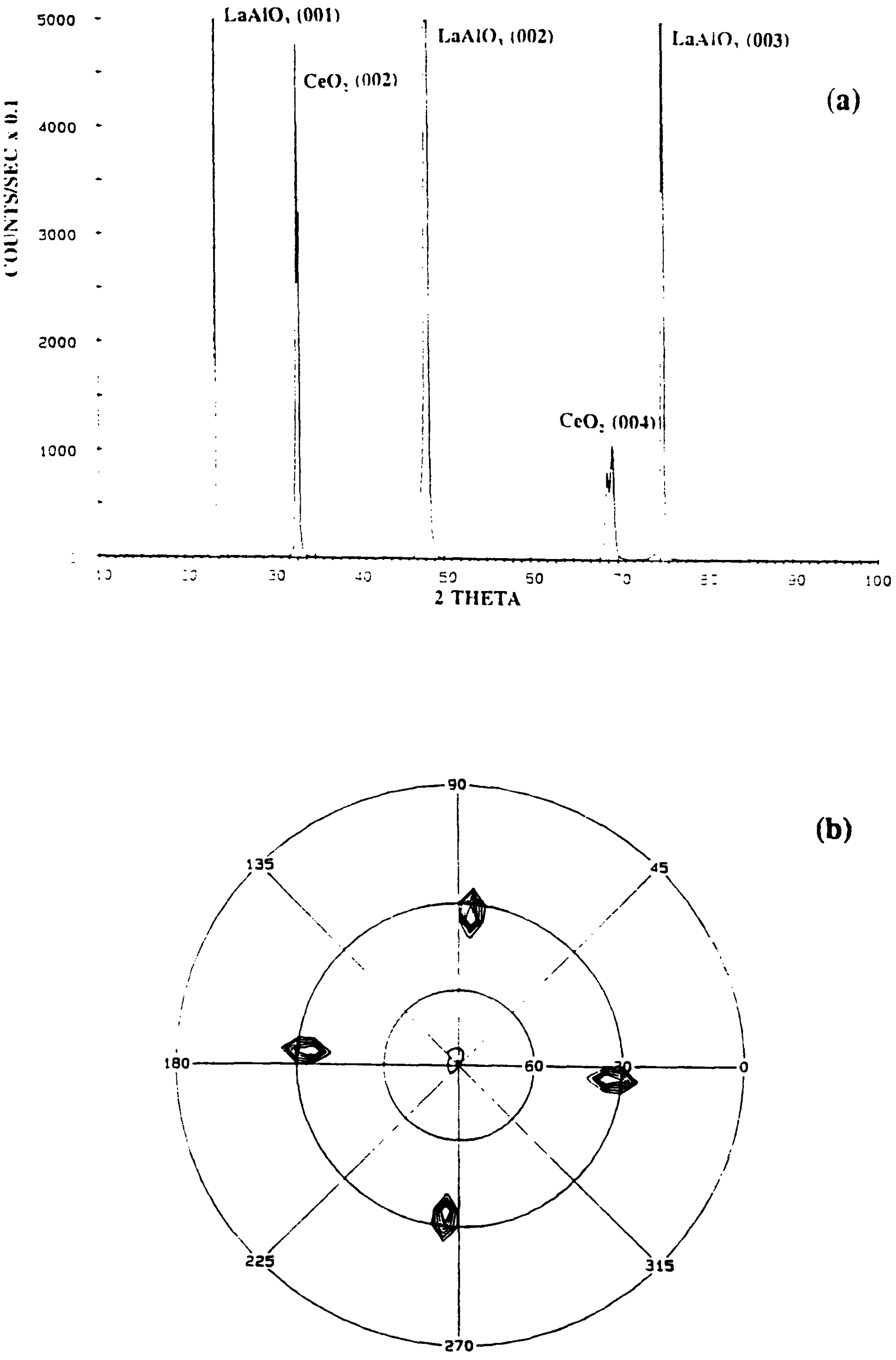

Figure 5.9 XRD scans for IBAD CeO$_2$ grown at 0.8 Å/s and 600°C on (001) LaAlO$_3$ with an initial seed layer of evaporated CeO$_2$: (a) θ/2θ scan, and (b) CeO$_2$ (111) pole figure.

IBAD YSZ took place whether or not an additional YSZ layer was present. The non-(00*l*) reflections that are observed in $\theta/2\theta$ scans of these samples are probably related to causes other than substrate surface damage since they were found for films grown over both pre-annealed and as-received substrates. This will be discussed further in upcoming sections.

Nonepitaxial IBAD growth in the absence of a seed layer may be a consequence of ion bombardment. One effect of ion bombardment is to increase the energy and hence, the surface mobility of the deposited species.[161] Enhancing the surface mobility is a well known method for improving or promoting epitaxial film growth. Common methods for achieving increased surface mobility include increasing the deposition temperature or increasing the energy of the deposited species. IBAD is therefore expected to aid in promoting epitaxy based on surface mobility considerations alone. The results obtained here, however, indicate that a competing mechanism, such as disorder introduced by the ion bombardment, may be dominating the epitaxial growth mechanism. The action of the ion beam can cause both ballistic[162] and thermal[163] interface mixing to occur, both of which can disrupt epitaxial growth. In addition, ion bombardment of the $LaAlO_3$ substrate surface during the initial stages of IBAD can cause surface damage as discussed in the previous section. This too can have an adverse effect on epitaxial film development.

Although it may be possible to find a processing window that permits epitaxial IBAD growth to occur directly over a lattice mismatched surface, a protective buffer layer is desirable for actual planarization processing. This will allow patterned BYC traces to be protected from ion bombardment. In this case, the initial evaporated layer could serve a two-fold function both as a protective buffer layer and as an epitaxial seed layer.

5.4.2 IBAD CeO_2 Microstructure

5.4.2.1 Results

The polycrystalline IBAD CeO_2 film that is obtained for growth directly on $LaAlO_3$ has a granular microstructure as shown in Figure 5.10. Epitaxial IBAD CeO_2 grown over an evaporated CeO_2 seed layer has a dense and smooth appearance when

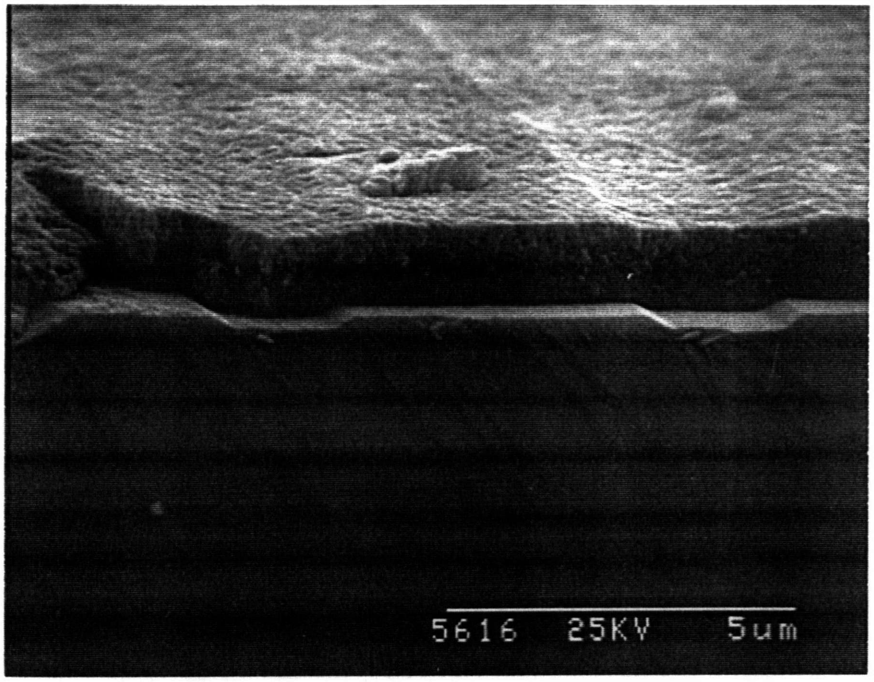

Figure 5.10 SEM micrograph of IBAD CeO_2 film grown on (001) $LaAlO_3$ without an initial seed layer of evaporated CeO_2.

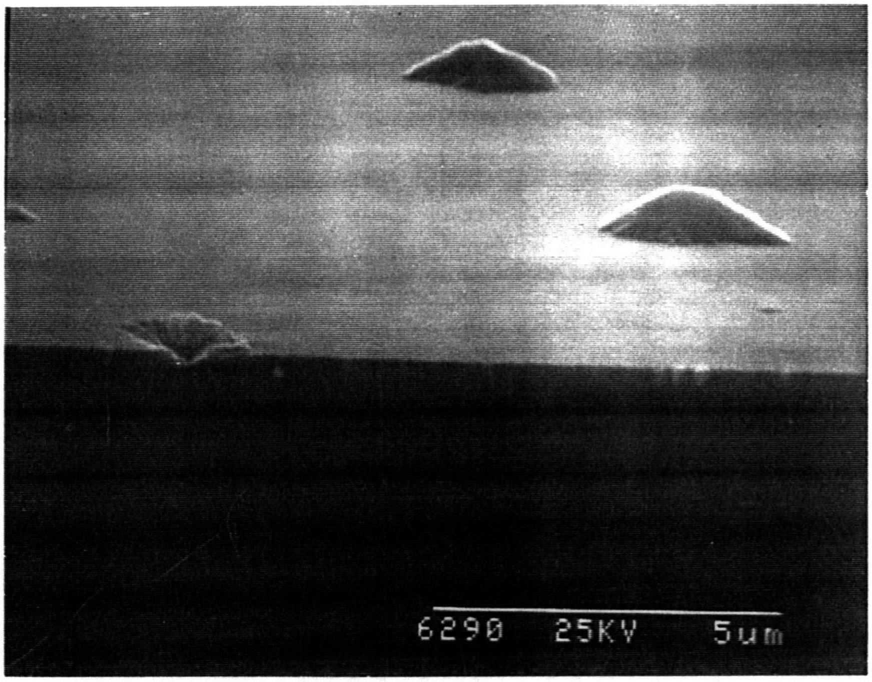

Figure 5.11 SEM micrograph of IBAD CeO_2 grown at 0.8 Å/s and 600°C on an as-received $LaAlO_3$ substrate with an initial seed layer of evaporated CeO_2.

deposited on an as-received $LaAlO_3$ substrate as seen in Figure 5.11. However, the SEM micrograph in Figure 5.11 also shows the presence of a second microstructure in the form of occasional rough protrusions. For growth over patterned substrates, a smooth dense film is obtained over planar portions of the substrate, but a rough microstructure similar to the one in Figure 5.11 is observed to be associated with the step edges as shown in Figure 5.12(a). The low magnification planview SEM micrograph in Figure 5.12(b) also shows the presence of the rough material over nonpatterned areas of the $LaAlO_3$ substrate. TEM analysis has identified this rough material as polycrystalline CeO_2.

5.4.2.2 Discussion

The differences observed in film microstructure between IBAD CeO_2 films grown directly over $LaAlO_3$ and an evaporated CeO_2 seed layer are consistent with the XRD results presented in Section 5.4.1.2. The smooth and dense microstructure of the epitaxial IBAD CeO_2 film in Figure 5.11 is similar to the one observed for epitaxial evaporated CeO_2 films grown on $LaAlO_3$. This microstructure, however, is disrupted by the presence of the polycrystalline material. The non-(00*l*) CeO_2 peaks found in $\theta/2\theta$ scans most likely correspond to this material, which is different from the non-epitaxial CeO_2 detected for growth on unannealed milled $LaAlO_3$ substrates.

SEM micrographs show that the polycrystalline CeO_2 is concentrated primarily over step edges of patterned substrates. SEM micrographs, however, also show that this material is found in films grown over as-received substrates as well as over non-grooved areas of patterned substrate. A particularly high concentration is found at the substrate corners of the patterned substrate in Figure 5.11(b). During heater block mounting, the $LaAlO_3$ substrates were pressed into the silver paste by pushing down at the substrate corners using a pair of metal tweezers which may have generated surface defects. These results suggest that non-epitaxial CeO_2 also grows preferentially over substrate surface defects. Figure 5.11 also shows that this material originates within the epitaxial microstructure and does not merely lie on top of the smooth film. More analysis on this polycrystalline material is presented in the TEM analysis given in Section 5.4.4 and the general discussion of CeO_2 microstructure in Section 5.4.6.

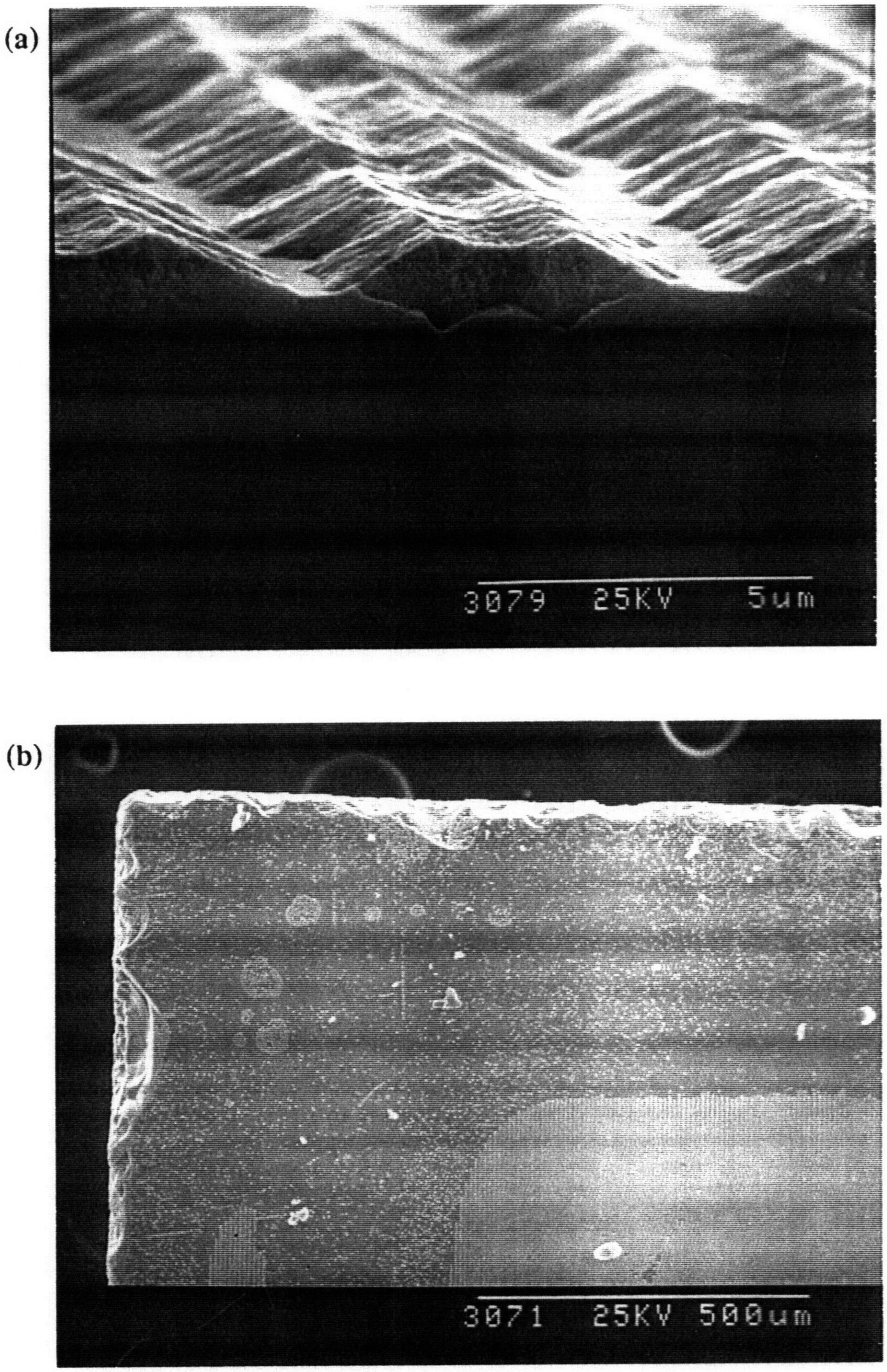

Figure 5.12 SEM micrographs of IBAD CeO_2 grown at 0.8 Å/s and 600°C on annealed, patterned $LaAlO_3$ with an evaporated CeO_2 seed layer: (a) 75° tilt, and (b) planview.

5.4.3 Topographical Evolution

5.4.3.1 Results

IBAD rates below 0.3 Å/s yield no net deposition while deposition at 0.3 Å/s results in only a thin rough conformal film (see Figure 5.13). Deposition rates from 0.8 Å/s to 1.2 Å/s yield thicker films, but the mixed microstructure mentioned above is obtained in all cases under these conditions. Figure 5.14 shows a smooth dense film interdispersed with a protruding rougher material that is concentrated over the step edges of the patterned substrate. Regions with a lower density of the rough material are also found on most of these samples. SEM micrographs show that the smooth dense films are fairly planar in these regions (see Figure 5.15). The mixed microstructure, however, tends to dominate each sample.

5.4.3.2 Discussion

These topographical results suggest that planarization via angled surface formation as observed in Chapter 4 is also possible in this materials system. However, the presence of the polycrystalline material inhibits the planarization process by preventing the ion beam from reaching the angled surfaces. This can be seen by comparing the degree of planarization in regions with different densities of the polycrystalline material (see Figures 5.12 and 5.15). Regions with a lower density of the polycrystalline CeO_2 experience etching at the angled surfaces and are more planar. In addition to inhibiting planarization, the polycrystalline material also introduces its own degree of roughness into the surface topography. The polycrystalline material appears to grow at a faster rate and therefore protrudes above the epitaxial portions of the film. This is a demonstration of the need for a uniform crystallinity and microstructure in order for planarization to take place.

5.4.4 TEM Analysis and Discussion

Cross-sectional TEM analysis was performed on an IBAD CeO_2 sample deposited at 600°C, 0.8 Å/s, 500 eV, and 180 $\mu A/cm^2$. SEM micrographs of this sample are shown in Figure 5.12. The epitaxial nature of the smooth and dense portions of this film was confirmed by cross-sectional TEM and electron diffraction analysis. Figure 5.16 is a low

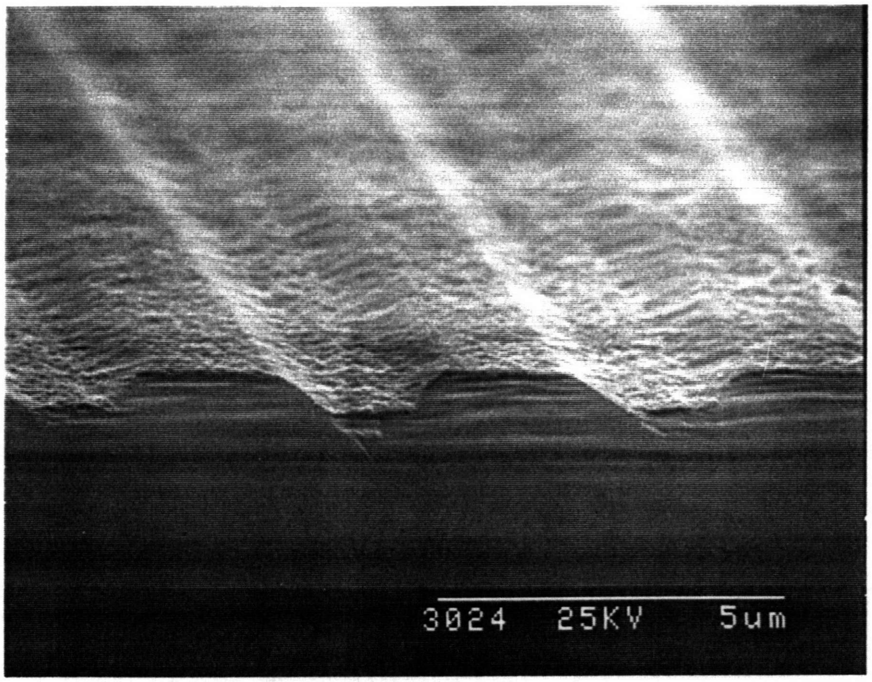

Figure 5.13 SEM micrograph of IBAD CeO_2 grown at 0.3 Å/s and 600°C on annealed patterned $LaAlO_3$ with an evaporated CeO_2 seed layer.

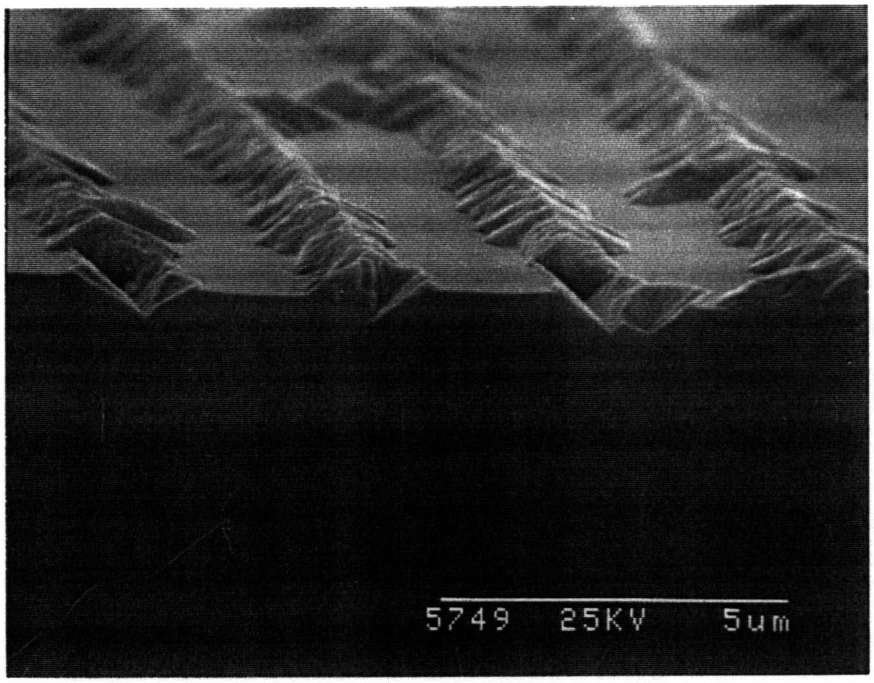

Figure 5.14 SEM micrograph of IBAD CeO_2 grown at 1.0 Å/s and 600°C on annealed patterned $LaAlO_3$ with an evaporated CeO_2 seed layer.

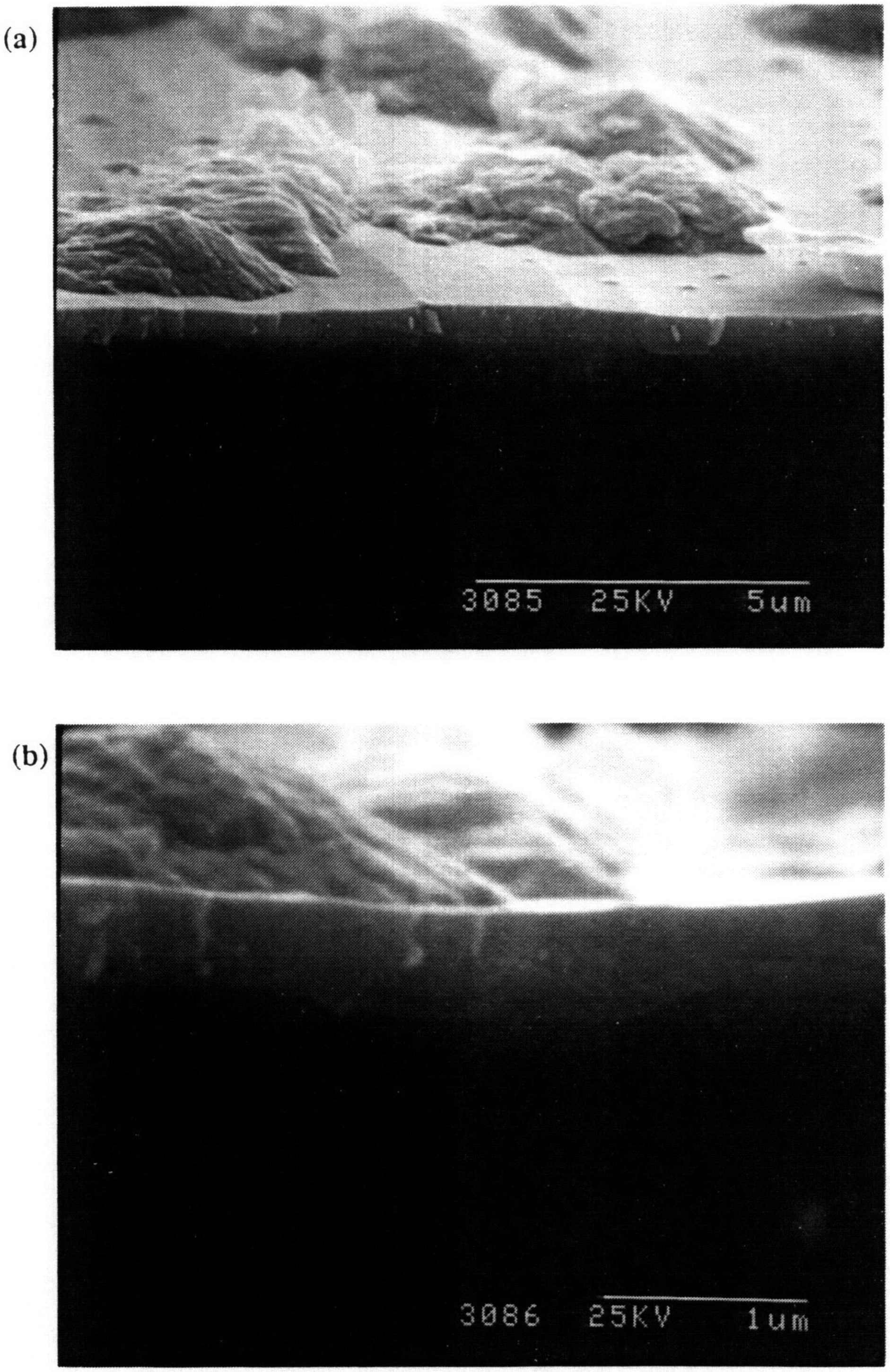

Figure 5.15 SEM micrograph of IBAD CeO_2 grown at 0.8 Å/s and 600°C on annealed patterned $LaAlO_3$ with a CeO_2 seed layer: (a) 75° tilt, (b) 90° tilt.

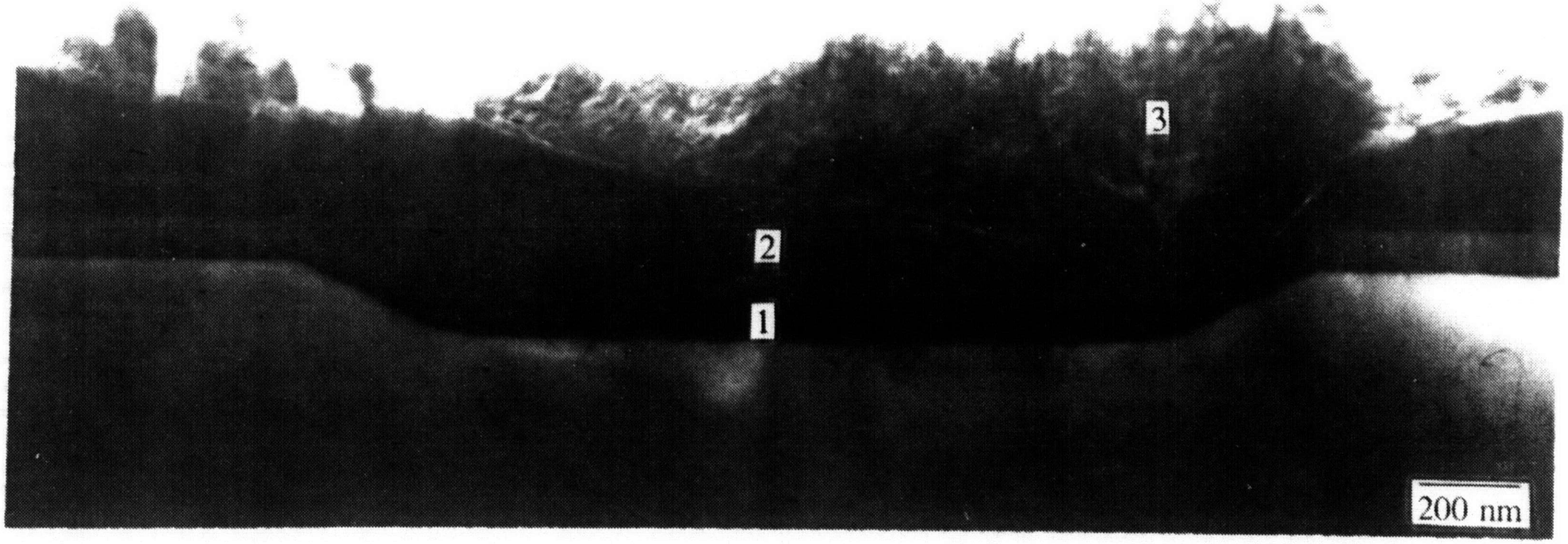

Figure 5.16 Cross-sectional TEM micrograph of sample shown in Figure 5.15 showing: (1) conformal evaporated CeO_2 seed layer, (2) epitaxial IBAD CeO_2 layer, and (3) non-epitaxial IBAD CeO_2.

magnification TEM image in which three distinct film regions can be identified. Layers "1" and "2" are both epitaxial and correspond to the evaporated and IBAD CeO_2 layers, respectively. Region "3" corresponds to the rougher microstructure observed in SEM micrographs and is non-epitaxial polycrystalline CeO_2. Crystallographic and microstructural defects are found to exist in the epitaxial CeO_2 film both over planar regions of the substrate and along the sloped sides of the groove walls. These defects are directly related to features that exist on the surface of the $LaAlO_3$ substrate.

Two types of surface relief are present in the patterned $LaAlO_3$ substrate: native steps and artificially produced grooves. The first is related to the second-order phase transformation $LaAlO_3$ undergoes at about 450°C. The transformation from the cubic phase to the rhombohedral phase upon cooling causes the formation of twins in the $LaAlO_3$.[22] Native steps can arise when the substrate detwins upon re-heating past 450°C. In addition, surface steps are generated during polishing of the substrates by the vendor due to the different mechanical properties of the $LaAlO_3$ at the twins. These surface steps are about one to two unit cells high as observed by AFM. Macro-relief consisting of ~1500 Å high steps is introduced into the $LaAlO_3$ substrates through photolithography and ion milling. TEM analysis, however, reveals that a stepped micro-relief is also associated with these patterned grooves. The sloped sides of the milled grooves are not continuous but rather, are composed of numerous ledges about one to two unit cells high in a staircase-like configuration of (001) and (100) planes.

Examination of the evaporated CeO_2 layer in Figure 5.17 reveals a difference in the growth and orientation of the film over the flat regions ("B-type") and sloped sides ("A-" and "C-types") of the patterned $LaAlO_3$. Over the "B-type" regions, (001) CeO_2 grows with the expected CeO_2 [110] || $LaAlO_3$ [100] epitaxial relationship as shown by the electron diffraction patterns. Low angle tilt boundaries and associated dislocations, however, exist in this portion of the film. These low angle tilt boundaries can be traced to individual native steps, although not all steps are associated with tilt boundaries. These numerous dislocations give the evaporated film a columnar appearance when examined at low magnifications. Over the sloped sides, however, the CeO_2 electron diffraction spots are smeared and rotated ~5° towards the slopes. The reason for this rotation can

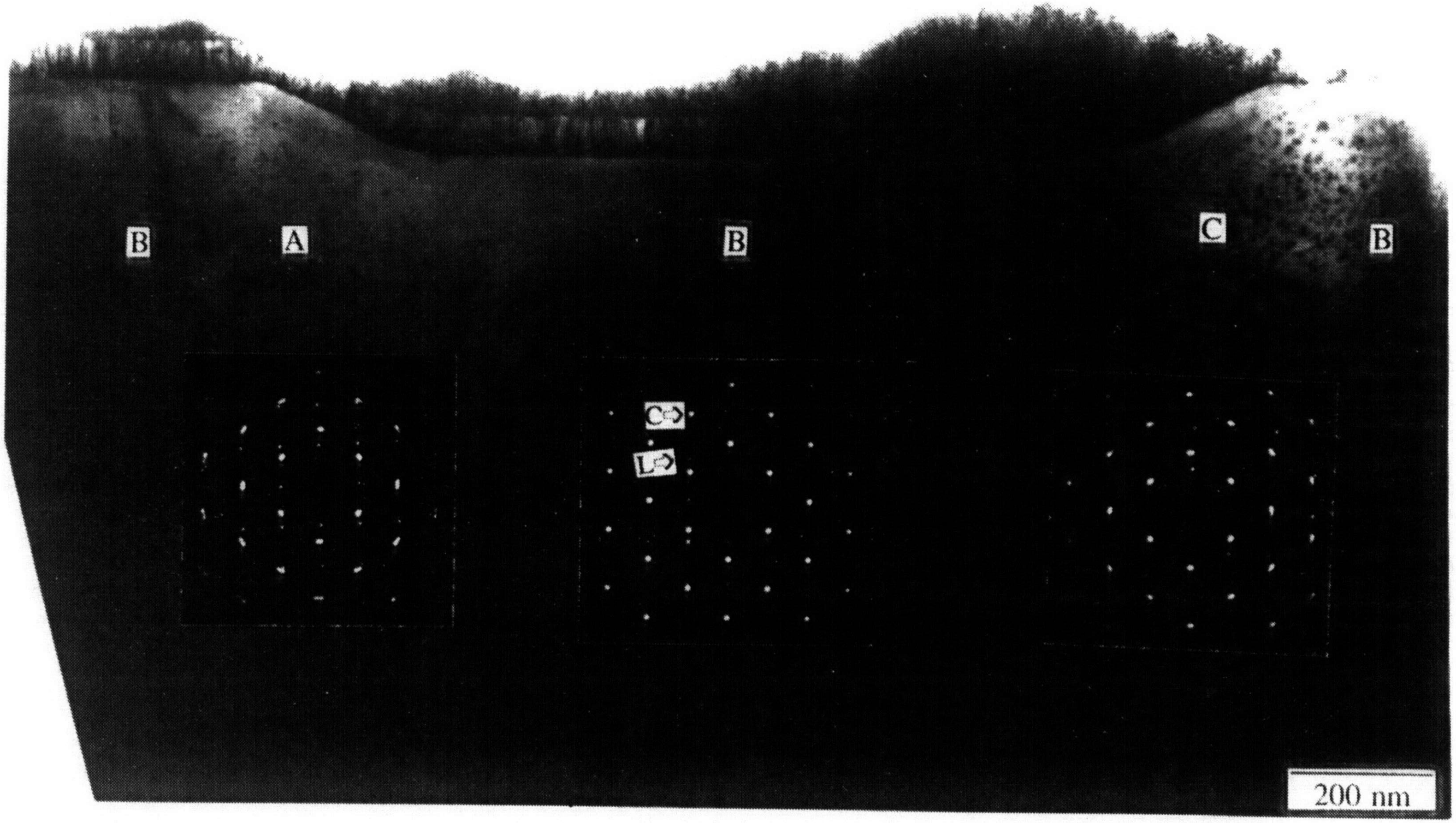

Figure 5.17 Cross-sectional TEM micrograph of a region similar to 5.16 after extensive ion thinning to reveal details of the conformal evaporated CeO_2 layer.

be seen from Figure 5.18. This high resolution TEM micrograph shows the staircase-like nature of the patterned $LaAlO_3$ slopes. The angle of the $LaAlO_3$ slope in Figure 5.18 is not constant, but varies from an average tilt of ~31° at the center to less than 20° at both the upper and lower portions. A tilt in the CeO_2 film of up to ~5° towards the slope brings relatively low index CeO_2 (112) planes parallel to the sloped surface. The (112) planes can be thought of as being made up of (111) and (001) components, as detailed in the schematic in Figure 5.19. The rotated configuration probably results in a more favorable film/substrate interface.

Both the low angle tilt boundaries found in CeO_2 over nominally flat $LaAlO_3$ and the highly incoherent $CeO_2/LaAlO_3$ interface on the slopes are a direct result of the large film-substrate lattice mismatch in the [001] direction. The lattice parameters of CeO_2 and $LaAlO_3$ are 5.41 Å and 3.79 Å, respectively. In the plane of the substrate, the lattice matching condition of (001) CeO_2 || (001) $LaAlO_3$, and [110] CeO_2 || [100] $LaAlO_3$ gives a misfit of ~0.9%. In the vertical [001] direction, however, the misfit between CeO_2 and $LaAlO_3$ is ~43% (see Figure 5.20). This mismatch produces low angle tilt boundaries in the CeO_2 film on $LaAlO_3$ native steps located in the nominally flat regions of the substrate. On the slopes, the high density of steps results in loss of coherency at the interface which results in a high concentration of tilt boundaries, dislocations, and other crystallographic defects.

The epitaxial IBAD CeO_2 layer is found to be even more highly defective than the underlying evaporated CeO_2 layer and possesses a much higher overall dislocation density. Electron diffraction patterns of the epitaxial IBAD layers are similar to those of the evaporated layer and also exhibit the same ~5° rotation over the stepped surfaces. However, the spots in the diffraction patterns are more diffuse, indicating the greater extent of crystallographic disorder.

Polycrystalline CeO_2 is found to nucleate preferentially over the stepped regions during IBAD processing. This is observed to occur over both epitaxial evaporated CeO_2 and epitaxial IBAD CeO_2. The polycrystalline material, which is more porous, grows to spread over neighboring epitaxial films. It is probable that the presence of defects in the underlying film act as preferred nucleation sites for the polycrystalline CeO_2 since the

Figure 5.18 Cross-sectional TEM image on the [100] LaAlO$_3$ zone axis of the CeO$_2$ film/substrate interface on a "C-type" step.

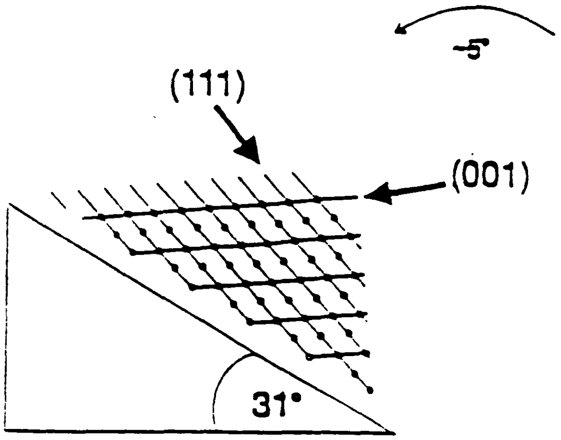

Figure 5.19 Schematic of tilt misalignment of CeO_2 deposited on a 31° "A-type" tilt in the $LaAlO_3$ substrate.

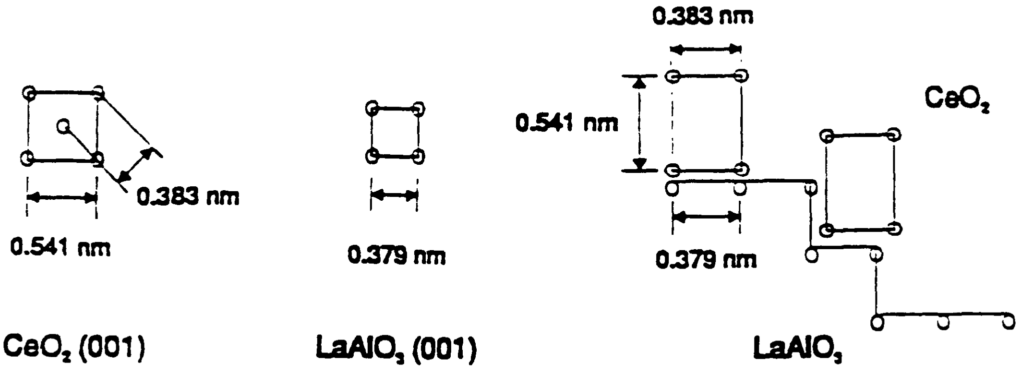

Figure 5.20 Schematic showing the (001) faces of the unit cells of $LaAlO_3$ and CeO_2, and the lattice mismatch along the [001] film and substrate axes at a unit cell high ledge in the $LaAlO_3$ substrate.

most defective areas of epitaxial CeO_2 are concentrated at the stepped edges. The deposition conditions during IBAD are most likely more conducive to nucleation of polycrystalline CeO_2 due to the disorder introduced by the ion beam and/or the higher deposition pressures. It has already been shown how evaporating CeO_2 at high pressures can lead to a more defective film microstructure.

The results of the TEM analysis suggest that the polycrystalline CeO_2 detected in SEM micrographs for IBAD film growth over as-received $LaAlO_3$ substrates may have originated over native steps in the substrate. Although the degree of film-substrate incoherency in these regions is not as severe as that found for patterned step edges, it is conceivable that the crystallographic defects can still act as preferred nucleation sites for polycrystalline CeO_2 growth. In addition, it appears that substrate surface defects themselves can act as preferred nucleation sites as well.

These results have significant and important implications on heteroepitaxial planarization for HTSC devices. The choice of dielectric interlayer materials is currently limited to those discussed in Chapter 2. Two of these materials, YSZ and CeO_2, can be lattice-matched to BYC in the plane of the film-substrate interface but are severely lattice-mismatched in the third direction. Planarization of BYC traces by either of these materials can be expected to give results similar to the results of the CeO_2-$LaAlO_3$ study. This study demonstrates that three-dimensional lattice matching is needed for device manufacturing. The presence of surface topography introduced by patterned HTSC lines forces an added constraint in lattice matching.

5.4.5 Alternative Planarization Processes Using Normal Incidence IBAD

The TEM analysis presented in the previous section highlights the need for lattice matching between BYC and the dielectric interlayer in all three dimensions in order for heteroepitaxial planarization to be successful. In the case of IBAD CeO_2 on $LaAlO_3$, the large lattice mismatch in the [001] direction resulted in a highly defective film and ultimately the nucleation and growth of unwanted polycrystalline CeO_2. One way of circumventing the problem of lattice mismatch may be to suppress the nucleation and/or growth of polycrystalline CeO_2. Two possible routes to achieving this are presented below.

One approach to suppressing nucleation and growth of polycrystalline CeO_2 is to completely separate out the deposition and etching portions of the planarization process. TEM analysis indicates that epitaxy is maintained in the evaporated CeO_2 layer despite the presence of tilt boundaries and an incoherent interface over the sloped sides. It is only during the IBAD portion of the process that the polycrystalline CeO_2 material nucleates and grows. By isolating the evaporation and etching segments, it may be possible to avoid the growth of polycrystalline CeO_2, since all deposition then takes place at optimal conditions of low pressure and low deposition rate.

A similar type of approach to planarization was discussed by C.Y. Ting *et al.*[14] and demonstrated by Mogami *et al.*[148] albeit for different reasons. A two-step rf-bias sputtering process was used by Mogami *et al.* to deposit planar SiO_2 over metal stripes. Rf bias sputtering was used to grow SiO_2 until the SiO_2 thickness over planar portions of the surface had exceeded the height of the metal stripe, at which point, partially formed cones of SiO_2 had been grown over the metal lands. The etching rate was then increased such that a net zero etching/deposition rate was obtained over planar regions of the film while net etching dominated over nonplanar features. The SiO_2 film was then processed until all protrusions had been removed, resulting in a planar film. The advantage in carrying out planarization in this manner is that the thickness of the planarizing layer can be controlled and, therefore, does not need to be a function of the height of the cone.

It is found, however, that with a two-step evaporation-etch process, the properties of the CeO_2 films at the steps tend to be inferior to films that are processed using IBAD. This was observed in one planarization experiment in which the deposition and etching segments were carried out separately. CeO_2 was evaporated at 600°C over patterned $LaAlO_3$ to a nominal thickness of 5000 Å and then etched at room temperature with an ion beam of 500 eV energy and 180 $\mu A/cm^2$ fluence for 30 minutes. Figure 5.21 shows the onset of edge moving over the angled surfaces due to etching. However, cracks are also visible in areas of the film over the step edges. These cracks are attributed to poor step coverage during evaporation which in turn caused crack generation and propagation when the sample was fractured for SEM analysis. These results indicate that a two-step

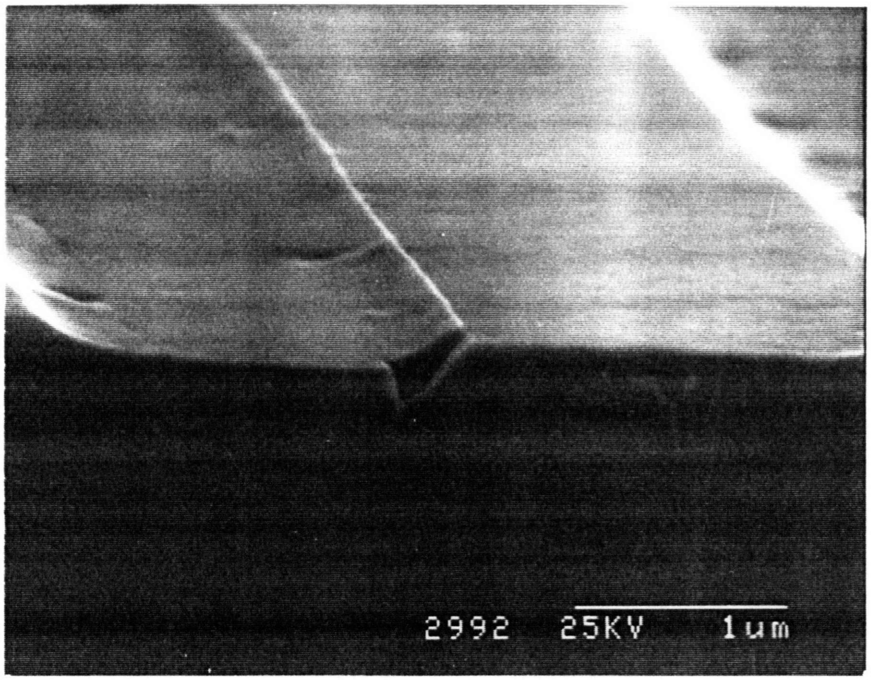

Figure 5.21 SEM micrograph of a CeO_2 film that was evaporated at 600°C over a patterned $LaAlO_3$ substrate and subsequently ion etched at room temperature.

evaporation-etching method of achieving planarization is not recommended. It is well known that evaporated films are not able to provide complete coverage over stepped surfaces.[141,15] Shadowing causes the formation of cracks or crevices in the film over the steps which cannot be filled in. However, a film deposition technique that is known to yield good step coverage, such as sputtering, can be substituted for the evaporation segment, provided that the nucleation and growth of polycrystalline CeO_2 remains suppressed. A two-step deposition-etching approach can therefore be used if the deposition method used is capable of achieving good step coverage.

The SEM and TEM results discussed in the previous section also suggest a second approach to suppressing the nucleation and growth of polycrystalline CeO_2. The fact that polycrystalline CeO_2 did not grow in certain regions of some samples indicates that there are certain conditions under which their growth can be suppressed or avoided altogether. If this processing window is found, heteroepitaxial planarization of systems such as $CeO_2/LaAlO_3$ may be possible.

Figures 5.22(a) and 5.22(b) are SEM micrographs of a CeO_2 film evaporated over a patterned $LaAlO_3$ substrate. This particular deposition run was aborted several minutes into the IBAD segment due to problems with coordinating the evaporation and etching. Thus, after evaporating the initial 1000 Å of CeO_2 at 0.2 Å/s, the film was etched by the ion beam for about one minute before evaporation also began at 1.0 Å/s. The run was then terminated after ~225 Å had been deposited with the ion beam on at 2×10^{-4} Torr. This sample therefore gives a snapshot of the IBAD planarization process several minutes after it has begun. In the SEM micrographs, the epitaxial CeO_2 film appears dense and very smooth. (The rounded features observed in these micrographs resulted from partial dewetting of the gold coating sputtered on during SEM sample preparation. This has been commonly observed in our laboratory for gold coating of extremely smooth surfaces.) However, a rough growth that is concentrated along the edges of a number of the grooves is already visible as seen in Figure 5.22(a). This rough growth appears to be similar to the polycrystalline CeO_2 that was observed previously. There are also some step edges, however, which do not exhibit this growth (see Figure 5.22(b)). It is clear from the micrographs that these edges have a shallower slope.

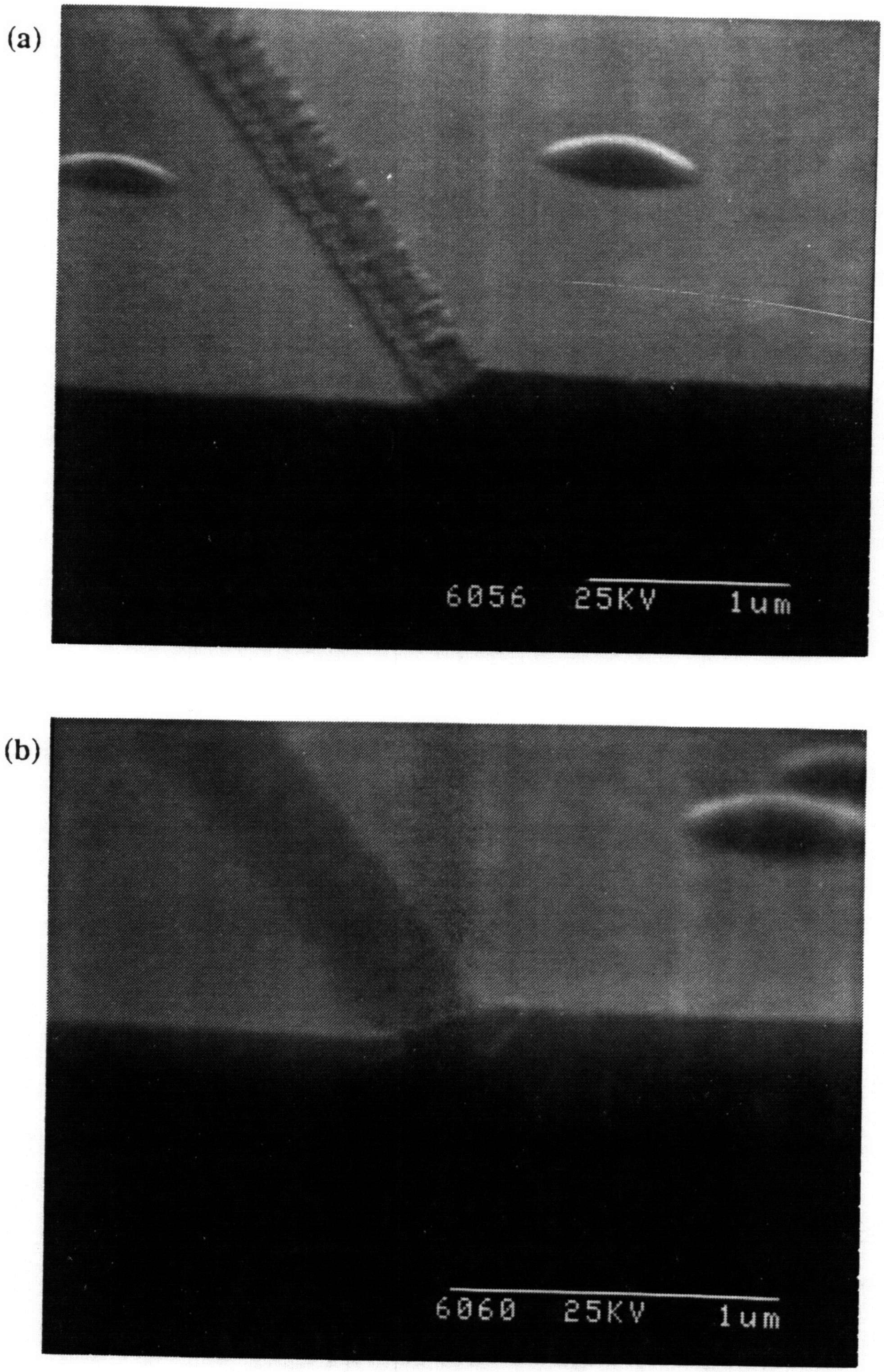

Figure 5.22 SEM micrographs of two different film/substrate steps for an aborted IBAD CeO_2 deposition run as described in text. A rough microstructure is observed at the step in (a) but not in (b).

These results, taken together with the TEM analysis in Section 5.4.4, suggest that nucleation and growth of the polycrystalline CeO_2 may possibly be suppressed for step edges with certain slope angles. In Figure 5.17, the epitaxial CeO_2 film tilts up to 5° in an effort to bring a relatively low index (112) film plane into contact with the substrate surface. The average slope of this particular step is ~31°, and since the angle between a (100) and (112) plane is 35.26°, the tilt required to bring the (112) plane into contact at the interface is nearly 5°. Since the slope of the sidewall varies continually along its entire length, the "instantaneous" slope at each point varies. This accounts for the range of tilts observed in the film, and therefore, the smearing of the diffraction spots. However, if a step edge has a slope angle that coincides exactly with a ($11l$) low index plane, that may allow less defective epitaxial CeO_2 to grow, which in turn may permit IBAD CeO_2 to grow without nucleating polycrystalline material. This would require stringent control over the angle of the step edges, which was not carried out during patterning of the $LaAlO_3$ substrates used in this study. If this turns out to be correct, strict control over patterning of BYC lines with the correct slope angles would then be needed in order for heteroepitaxial planarization to succeed. This may prove to be extremely difficult and may not be practical for large scale device fabrication.

It should be emphasized that although processing methods might exist which allow the lattice mismatch problem of the type encountered here to be circumvented, they are not ideal solutions. Crystallographic defects, such as low angle tilt boundaries and dislocations will still exist due to mismatch at surface steps, and it is very likely these defects will have a detrimental effect on the quality of a BYC overlayer.

5.4.6 General Discussion on CeO_2 Microstructure and Substrate Steps

The results from this study show that the growth of epitaxial CeO_2 on $LaAlO_3$ is very sensitive to deposition and substrate surface conditions. TEM analysis shows that even at the best conditions of low deposition rate and low pressure, defects are introduced in the CeO_2 film upon growth over native substrate surface steps. Deposition conditions during IBAD are much less favorable to high quality film growth in which the primary differences are higher deposition pressures and the action of the ion beam. Studies on the individual effects of these changes show that both cause degradation in CeO_2 film quality. Higher deposition pressures results in the nucleation and growth of polycrystalline CeO_2. It is possible that these polycrystalline particles formed over native substrate steps. It is also seen that the action of the ion beam is capable of completely disrupting epitaxial growth in the absence of a seed layer. Even when heteroepitaxial IBAD growth takes place, the resulting film is highly defective as shown by TEM analysis of epitaxial IBAD CeO_2. The deposition conditions that exist during IBAD result in a highly nonequilibrium film growth process. The presence of native steps as well as substrate surface damage then become significant as IBAD appears to enhance the effect of the CeO_2-$LaAlO_3$ mismatch.

5.5 OFF-NORMAL INCIDENCE IBAD OF CeO_2

All off-normal IBAD planarization experiments were carried out at 400°C on unannealed, patterned $LaAlO_3$ substrates. An initial 500 Å thick layer of CeO_2 was first evaporated on all samples. Unless otherwise noted, both evaporation and IBAD processing took place at a block angle of 45° at 0.2 Å/s. Ion beam parameters of 350 eV and 184-200 $\mu A/cm^2$ were used for all runs.

5.5.1 Topographical Evolution

5.5.1.1 Results

Figures 5.23(a)-(d) are SEM micrographs of IBAD CeO_2 films deposited with grooves oriented parallel, perpendicular, and at a 45° in-plane orientation with respect to the ion beam. Arrows indicate the projection in the plane of the film of the incoming ion beam direction. Figure 5.24 shows two other films deposited with grooves oriented perpendicular to the ion beam. Midway through this deposition run, the first sample (see Figure 5.24(a)) was removed and the stainless steel block to which the substrates were attached was rotated 180°. IBAD was then continued with the ion beam attacking from the opposite direction.

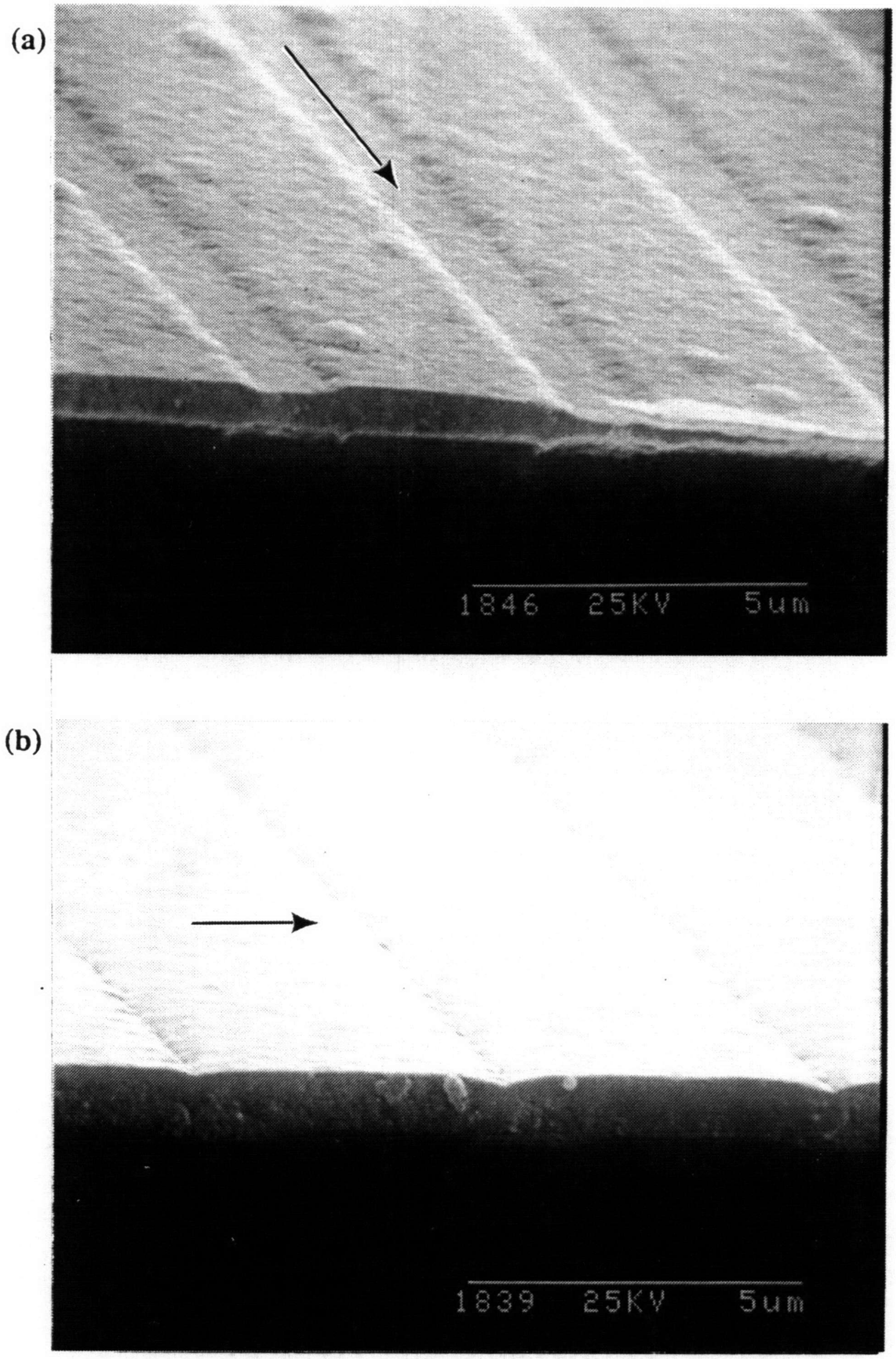

Figure 5.23 SEM micrographs for off-normal incidence IBAD CeO_2 films grown on patterned $LaAlO_3$ at 0.2 Å/s and 400°C. Ion beam directions relative to substrate grooves were: (a) parallel, (b) orthogonal, (c) and (d) at a 45° in-plane orientation, as indicated.

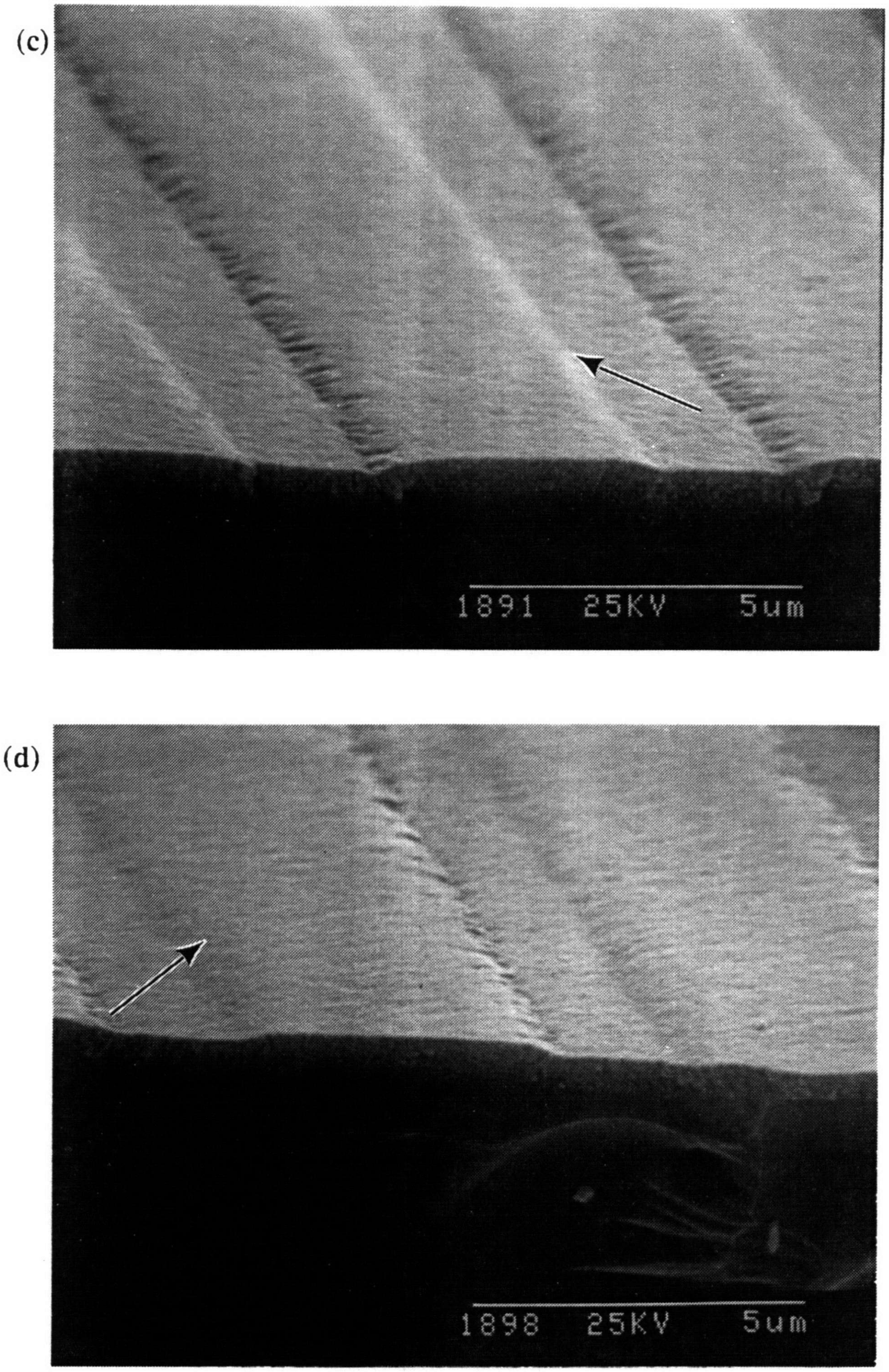

Figure 5.23 (continued).

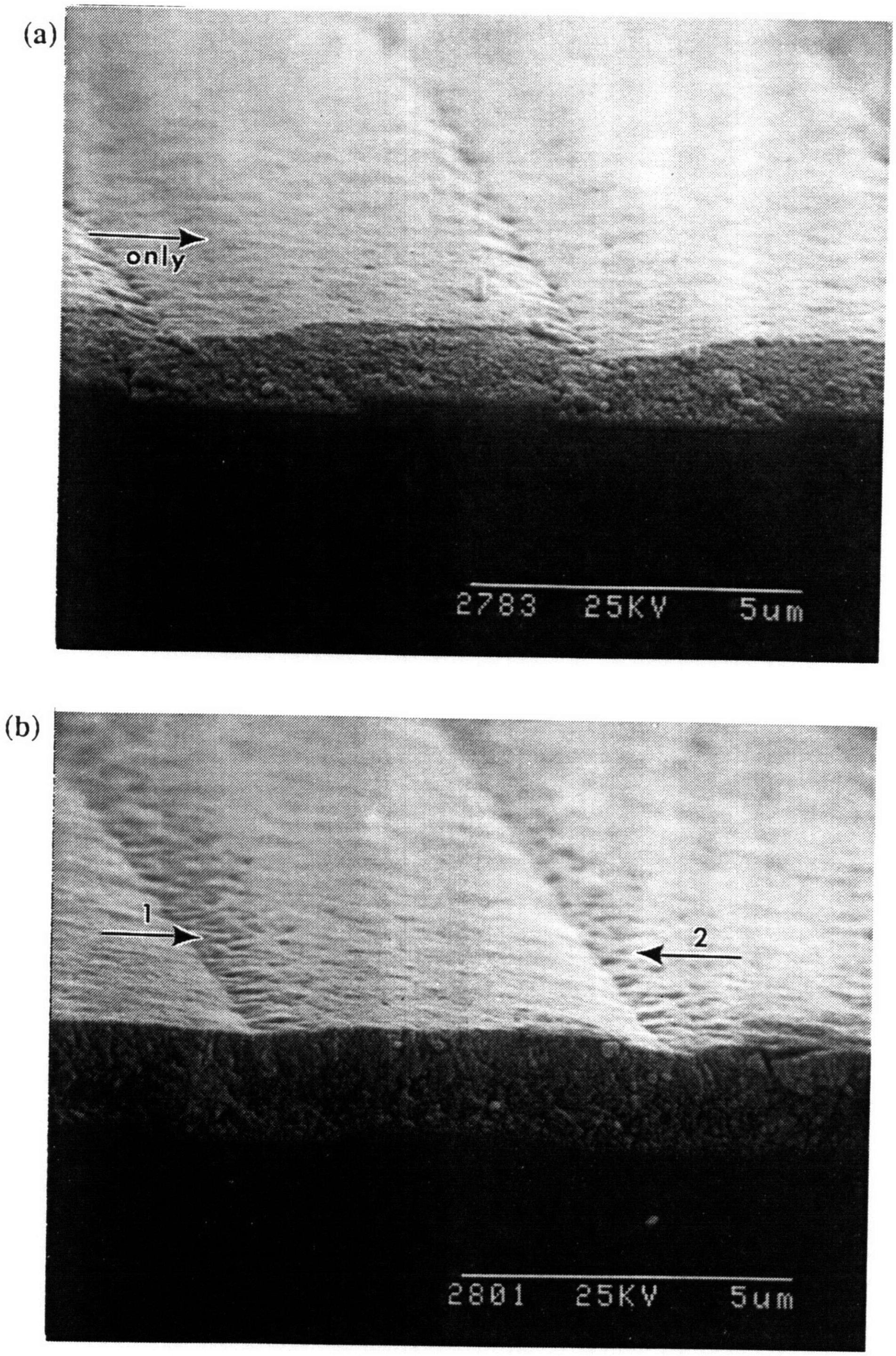

Figure 5.24 Off-normal incidence IBAD CeO_2 grown on patterned $LaAlO_3$ at 0.2 Å/s and 400°C with ion beam direction orthogonal to substrate grooves: (a) sample processed with ion beam attacking from left hand side only, and (b) sample processed first with the ion beam from the left hand side and then switched to the right hand side about halfway through deposition.

Good step coverage is achieved by IBAD films deposited over substrates oriented with grooves parallel to the ion beam. However, full planarization is not achieved. Figure 5.23(a) shows that the underlying substrate hill-and-valley structure is reflected in the overlying film. Substrates oriented with grooves orthogonal to the ion beam, however, show substantial improvement towards planarization. In figure 5.23(b), the 1 μm thick film uniformly covers the surface and fills in the ~1800 Å deep and 1.5 μm wide grooves, leaving only a narrow ~1800 Å deep dip. This dip is located over the substrate grooves close to the step edges facing away from the ion beam. The same dip morphology is observed for the two-part experiment in which the block was rotated 180° midway through deposition. SEM micrographs, however, show that the dip is now located above the center of the groove. Figures 5.23(c) and (d) for films oriented 45° in-plane to the beam show a topography similar to those films placed with grooves orthogonal to the ion beam.

5.5.1.2 Discussion

Planarization results were found to depend to a large extent on the orientation of the grooves with respect to the ion beam. Similar topographical results were observed by Cuomo *et al.*[164] and Harper *et al.*[133] for step coverage studies using off-normal ion beam assisted deposition of SiO_2. The goal in these studies was not planarization, however, but to improve poor step coverage obtained when using vapor deposition. Improved step coverage was obtained when ion beam bombardment was orthogonal to the patterned substrate features (see Figure 5.25) but a nonplanar surface remained. The authors attributed the improvement in step coverage solely to the removal of overhanging atoms at the upper step corners by the ion beam. This eliminated shadowing of the vapor stream at the step edges by overhanging film. It was also found that better coverage was obtained over the step edges facing away from the ion beam due to the greater ease by which overhanging atoms could be forward sputtered away.

From the results for off-normal IBAD of CeO_2 on $LaAlO_3$, it is clear that planarization is taking place by more than just removal of overhanging atoms, since such a mechanism should yield only improved step coverage. It is also clear that the

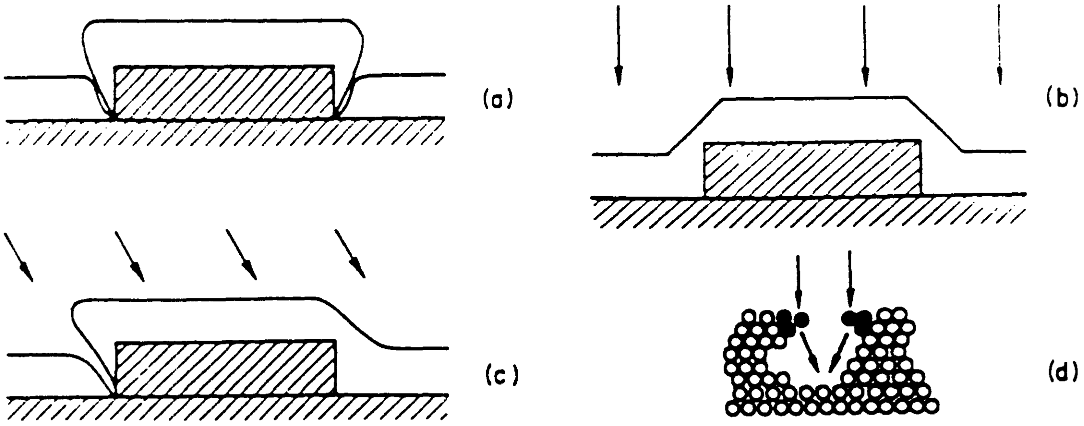

Figure 5.25 Schematics illustrating step coverages obtained with: (a) film deposition without ion bombardment; (b) deposition with normal incidence ion bombardment; and (c) deposition with off-normal incidence ion bombardment. (d) shows avoidance of void formation via forward sputtering.

controlling planarization mechanism for off-normal ion bombardment differs from the mechanism active in planarization techniques based on normal incidence ion bombardment. The results obtained here for ion bombardment at 45° are consistent with a planarization mechanism of forward sputtering and redeposition. Off-normal ion incidence results in increased emission in the forward direction as illustrated by Tsuge and Esho[60] in their polar plots. When the ion beam is parallel to the groove direction, forward sputtering and redeposition also occur in a parallel direction and material tends not to be redeposited towards the sides. Hence, the overall topography is maintained and planarization does not proceed to completion. On the other hand, when the ion beam is oriented perpendicular to the groove direction, redeposition of forward sputtered material fills in the grooves. Step edges facing away from the ion beam, however, are always shadowed from the beam. Initially, these shadowed regions do not contribute forward sputtered and redeposited material which results in the formation of a dip located near each shadowed step edge. As the film grows thicker, shadowing from the ion beam becomes less severe, but the dip remains. This can be related to the angle of the film at the dip, which is extremely small when taken with respect to the incoming ion beam. Little etching occurs at these glancing angles and again there is no sputtered material available for redeposition.

Figures 5.24(a) and (b) of the specimens from the two-part experiment show that these substrates have wider grooves than the substrates in Figure 5.23(b). It is seen that thicker films are required to provide the same degree of film coverage for wider grooves. Therefore, Figure 5.24(a) can be considered a "snapshot" of Figure 5.23(b) at an earlier stage in the deposition. It is also seen that IBAD processing from both sides of the groove direction does not eliminate formation of the dip. After the first half of deposition, the groove is not yet completely filled in. When the ion attack is shifted to the other side, glancing incidence etching is now experienced by the sloping portion of the film over the center of the groove which results in repositioning of the final location of the dip. Additional IBAD processing from different angles may be needed to achieve elimination of the dip.

Figures 5.23(c) and (d) show that the ion beam need not necessarily be orthogonal to the groove direction for this planarization mechanism to dominate. Ion etching at a 45° in-plane angle still permits material to be forward sputtered and redeposited in the groove. This mechanism is therefore active as long as the beam is not parallel to the groove direction.

5.5.2 Film Orientation

5.5.2.1 Results

XRD traces show that all of the films deposited at 45° are preferentially (001) oriented although some weak (111) and (311) peaks are also detected. A typical $\theta/2\theta$ scan is shown in Figure 5.26. X-ray pole figure measurements (see Figure 5.27) show the presence of two separate in-plane orientations. The CeO_2 [110] || $LaAlO_3$ [100] epitaxial orientation, is found in all films. For films processed with the substrate grooves oriented either parallel or perpendicular to the ion beam, a second in-plane orientation is detected 45° away, i.e. CeO_2 [100] || $LaAlO_3$ [100]. Samples with grooves located at a 45° in-plane orientation to the ion beam have a second in-plane orientation that is very close to, but does not coincide exactly with the epitaxial relationship.

A 1000 Å thick YSZ capping layer was evaporated at 0.2 Å/s and 600°C on one of these IBAD CeO_2 films in order to ascertain the in-plane orientation of only the IBAD CeO_2 film. $\theta/2\theta$ scans show that the YSZ film is preferentially (001) oriented. Pole figure measurements of the YSZ layer were inconclusive due to diffraction interference from the CeO_2 film. Four-circle diffractometry ϕ-scans were performed on this sample at Los Alamos National Laboratory on a Siemens D5000 diffractometer at 50 kV and 40 mA. These scans detected only one in-plane orientation for both the YSZ and CeO_2 layers which correspond to the epitaxial in-plane orientation, as seen in Figure 5.28.

IBAD CeO_2 was also deposited on a standard $LaAlO_3$ single crystal substrate under the same conditions and to similar film thicknesses as the samples described above, but without the initial layer of evaporated CeO_2. The XRD trace in Figure 5.29 shows that this film is preferentially (001) oriented but with relatively significant (111) and (311) components as well. Overall peak intensities are about an order of magnitude lower than samples processed with the initial seed layer. The pole figure and β-scan measurements

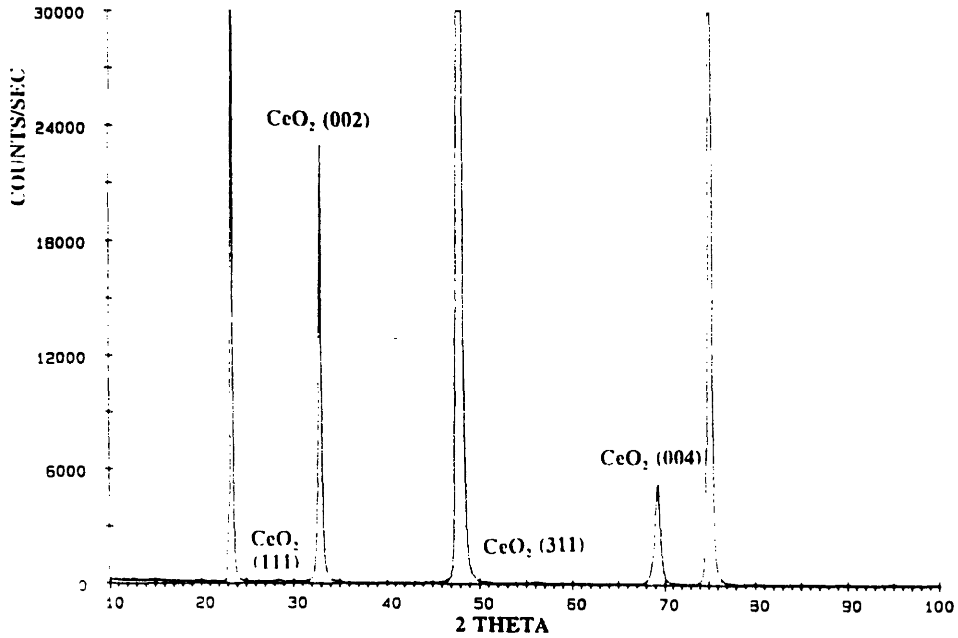

Figure 5.26 Typical θ/2θ XRD scan for off-normal incidence IBAD CeO_2 films grown on patterned (001) $LaAlO_3$.

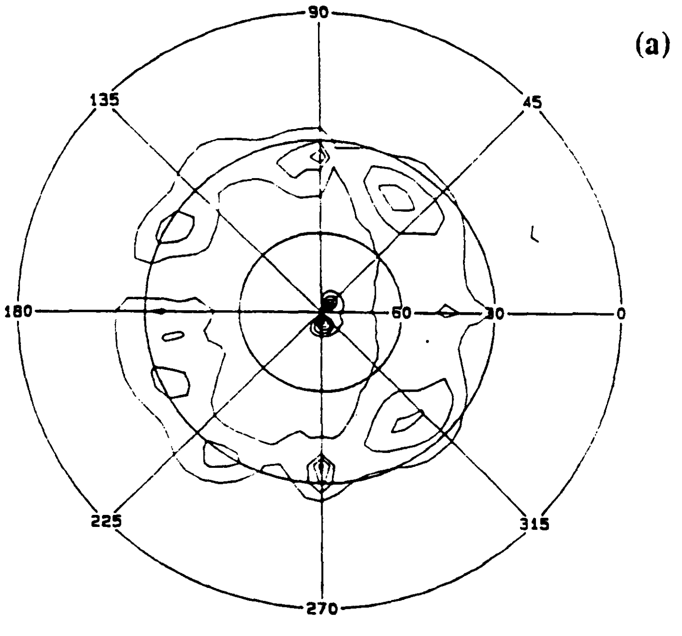

Figure 5.27 X-ray pole figures and β-scans of CeO_2 (111) for off-normal incidence IBAD of CeO_2 on $LaAlO_3$ at: (a) orthogonal, (b) parallel, and (c) 45° in-plane directions.

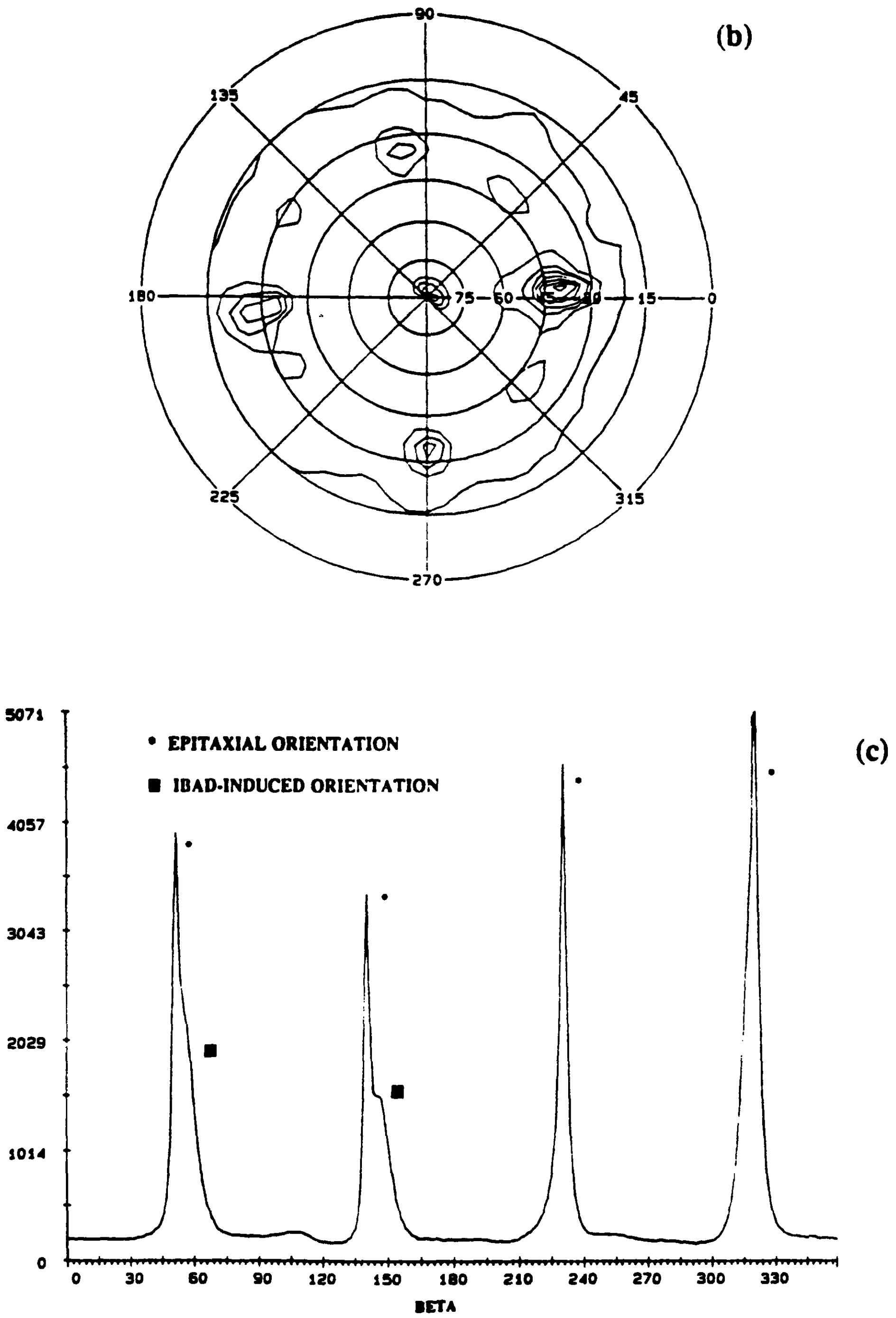

Figure 5.27 (continued).

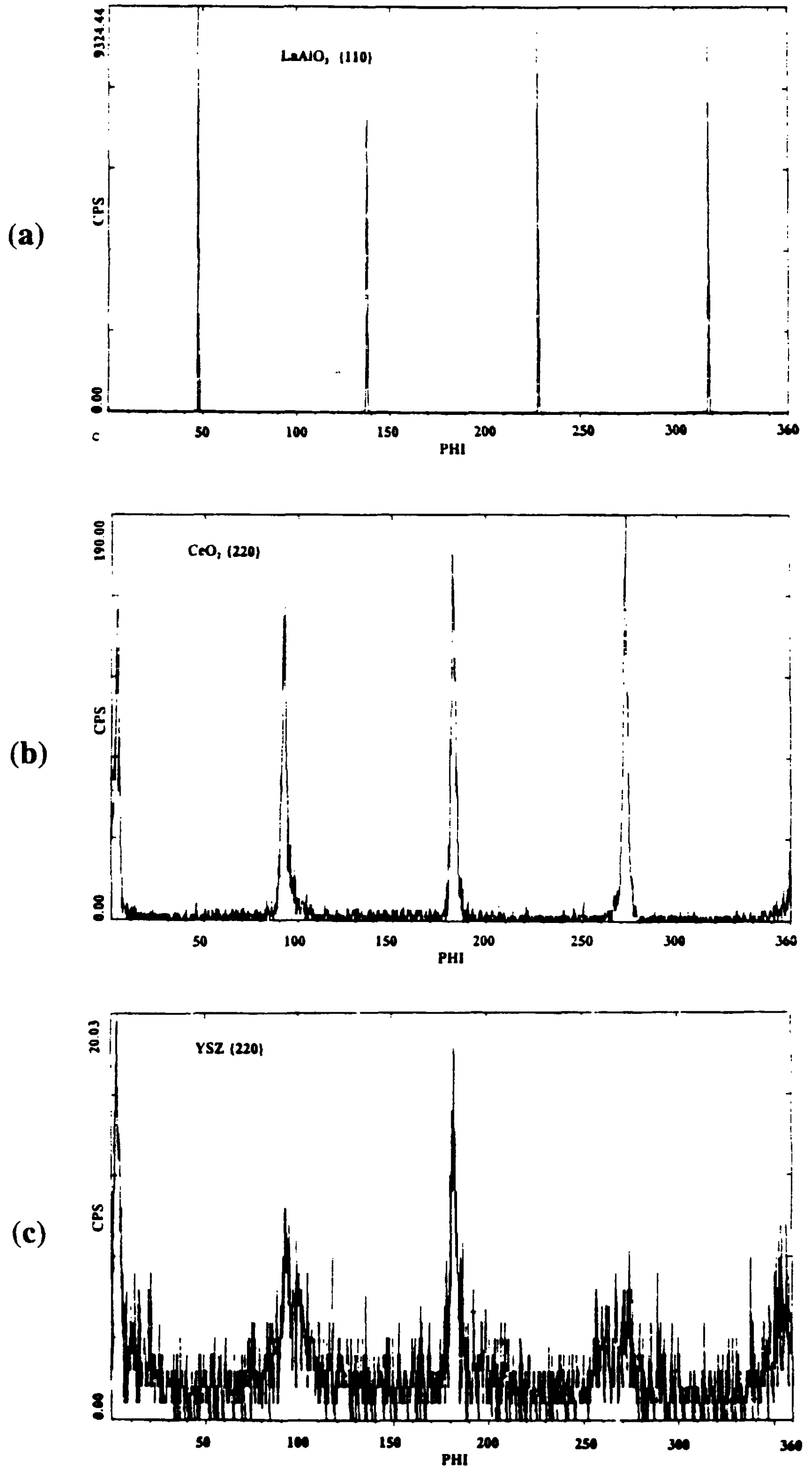

Figure 5.28 Four-circle ϕ-scan of YSZ capping layer evaporated on an off-normal IBAD CeO_2 film similar to those in Figure 5.26 showing epitaxial growth of underlying CeO_2.

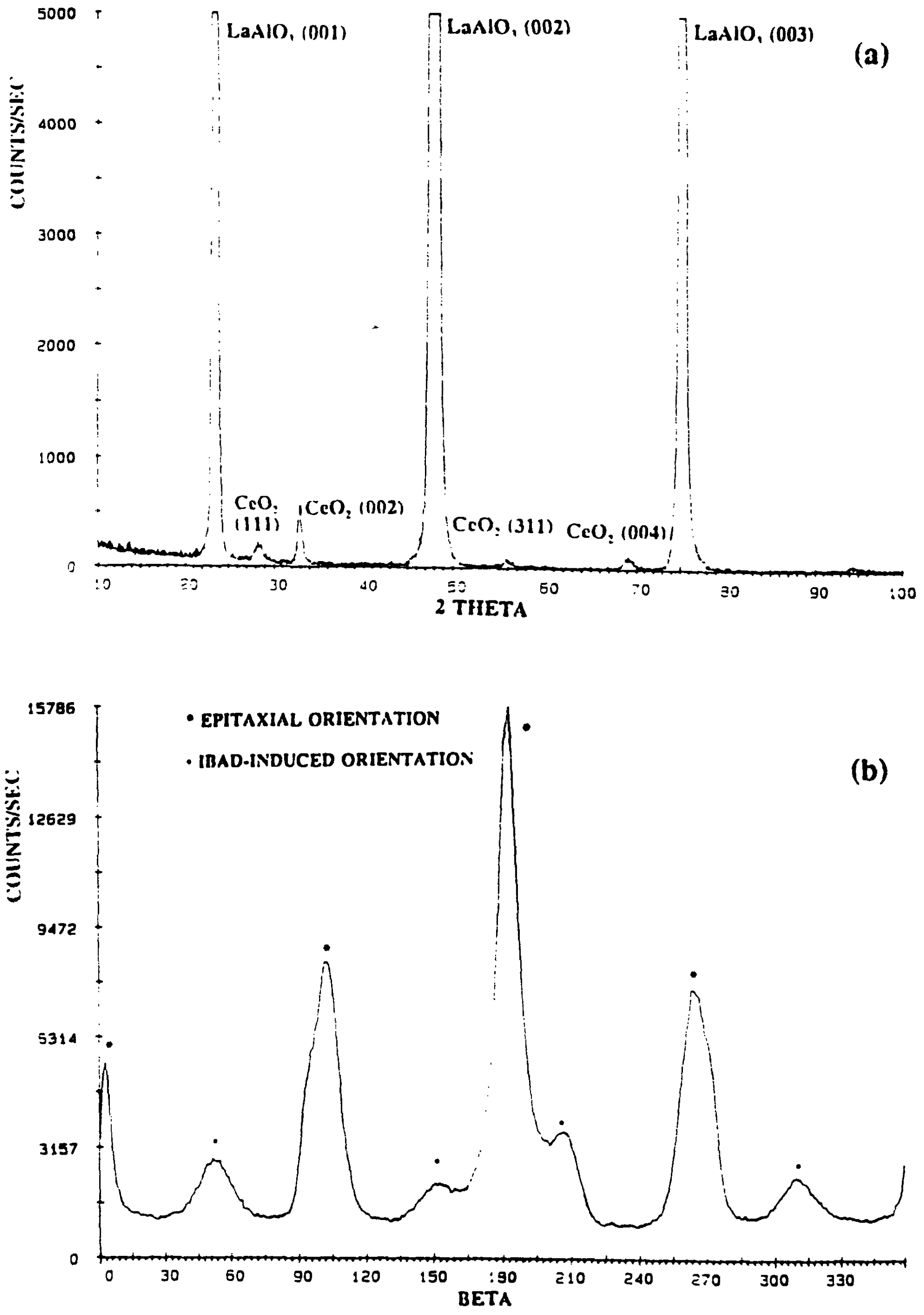

Figure 5.29 Various XRD scans for off-normal incidence IBAD CeO$_2$ deposited on (001) LaAlO$_3$ without an evaporated CeO$_2$ seed layer: (a) θ/2θ scan, (b) CeO$_2$ (111) β-scan, and (c) CeO$_2$ (111) pole figure.

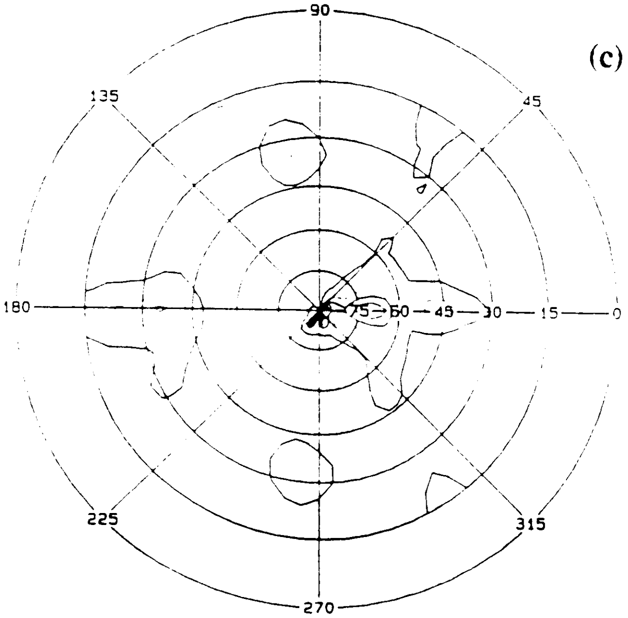

Figure 5.29 (continued).

in Figure 5.29 indicate the presence of two in-plane orientations, one of which is the epitaxial orientation. The second orientation is again located 45° away.

5.5.2.2 Discussion

For all films, the first in-plane orientation is the epitaxial relationship between CeO_2 and $LaAlO_3$. The XRD results indicate that both the initial 500 Å of evaporated CeO_2 and the IBAD CeO_2 layer contribute to this orientation. The second in-plane orientation results from the subsequent IBAD CeO_2 film and is consistent with a CeO_2 [110] channeling direction facing the ion beam as has been observed for similar deposition conditions for IBAD ZrO_2 films on amorphous substrates.[96]

It is seen that the detected intensities in the ϕ-scan in Figure 5.28 are much lower than those observed in pole figure β-scans. This may be due to instrumental differences between the two diffractometers used for these measurements. The four circle diffractometer used here has an X-ray tube source while the pole figure diffractometer used a rotating anode source. The results obtained from the two instruments suggest that the epitaxial in-plane orientation is dominant even in the IBAD CeO_2 layer while the IBAD-induced orientation is much weaker such that it is not detected in the ϕ-scans. It is difficult to ascertain the relative amounts of each orientation in this sample, however, since the detected epitaxial in-plane orientation comprises diffraction from both the evaporated and IBAD CeO_2 films.

The XRD results for IBAD CeO_2 grown directly over $LaAlO_3$ confirm that for samples processed with the initial seed layer, the majority of the CeO_2 (002) peak intensity is due to the initial epitaxial CeO_2 layer. The β-scan in Figure 5.29(b) shows that even without an evaporated seed layer, the epitaxial orientation is more intense than the IBAD-induced orientation. A volume fraction of ~20% can be estimated for the IBAD-induced in-plane orientation using the most intense peak for each in-plane orientation in Figure 5.29(b).

The lower XRD intensities of the specimen deposited with IBAD only are comparable to biaxially aligned CeO_2 films deposited with IBAD on amorphous substrates in which typical (002) peak intensities have the same order of magnitude.[165] IBAD CeO_2

films grown directly on $LaAlO_3$, however, have narrower rocking curves than their counterparts grown on amorphous substrates. In addition, the in-plane alignments of both of the in-plane orientations are also superior to those of films grown on amorphous substrates.

From these results, it is clear that the orientation of the IBAD film is primarily a function of the orientation of the underlying substrate or film. The IBAD deposition parameters however, clearly exert an influence on the in-plane orientation independent of the substrate orientation. This is clearly seen in the samples processed with a 45° in-plane groove orientation. Although the substrates were mounted in this orientation in order to promote an in-plane IBAD orientation commensurate with the epitaxial layer underneath, the substrates were misoriented just enough from the ion beam so that the second orientation still does not match the epitaxial layer, as shown by the β-scan in Figure 5.26. Therefore, even an underlying in-plane film orientation very close to the in-plane orientation induced by ion assist does not influence the IBAD-induced orientational development.

IBAD results for biaxially aligned films grown on amorphous substrates show that in order for biaxial alignment to occur, sufficient polycrystalline nucleation needs to occur initially. A growth extinction mechanism can then prevail in which grains of a certain out-of-plane orientation are favored to grow and eventually dominate. The action of the ion beam then produces in-plane texture by leaving behind only the grains that crystallographically channel the ion beam. Since CeO_2 and $LaAlO_3$ are lattice matched to each other, the CeO_2 growth is already biased (001). The weak (111) and (311) peaks detected in XRD scans suggest that the effects of the ion beam may be disruptive enough so that some polycrystalline nucleation and growth still take place. The (001) out-of-plane orientation still dominates, however, but the film ends up with an in-plane orientation partially dictated by the ion beam parameters. The natural (001) domination may be the reason these films possess superior crystallographic alignment to the biaxially aligned films. The presence of an epitaxial CeO_2 seed layer may also be beneficial since the most intense non-(00*l*) peaks were obtained for IBAD CeO_2 grown directly over $LaAlO_3$. It is clear, however, that the epitaxial in-plane orientation is dominant despite the effects of the ion beam.

5.6 SUMMARY

5.6.1 Normal Incidence IBAD

Epitaxial growth of IBAD CeO_2 on as (001) $LaAlO_3$ was maintained only in the presence of a seed layer of epitaxial evaporated CeO_2. The presence of the seed layer essentially permitted homoepitaxial growth of IBAD CeO_2 to take place.

Planarization via the cone formation mechanism was not achieved due to the formation of a mixed microstructure of epitaxial and polycrystalline CeO_2. The polycrystalline CeO_2, which was found to nucleate preferentially over step edges during IBAD processing, prevented the ion beam from etching at the angled surfaces of the epitaxial portions of the CeO_2 film and, therefore, inhibited the planarization process. Regions which possessed a lower density of the polycrystalline material exhibited etching of angled surfaces and a greater degree of planarity.

The formation of the polycrystalline material resulted from the large lattice mismatch that exists between the [001] directions of CeO_2 and $LaAlO_3$. The high density of microsteps in patterned step edges in the $LaAlO_3$ substrate surface led to a highly incoherent interface between the substrate and evaporated CeO_2 films. The ensuing crystallographic defects in the evaporated film apparently acted as preferred nucleation sites for the formation of polycrystalline CeO_2.

The effect of the large lattice mismatch between CeO_2 and $LaAlO_3$ was also evident for film growth over nominally flat $LaAlO_3$. SEM also detected the growth of polycrystalline CeO_2 for these films. The presence of native steps in the substrate led to the formation of numerous tilt boundaries in subsequently evaporated CeO_2 films some of which may have become preferential nucleation sites for polycrystalline CeO_2.

The results from this study show that the presence of microsteps in the substrate surface are significant and can have an adverse impact on epitaxial film growth for materials that are not properly lattice matched. Although CeO_2 and $LaAlO_3$ can be lattice matched in two dimensions through a mutual rotation of their (100) faces, the introduction of both macroscopic and microscopic surface relief causes the formation of crystallographic defects due to the large mismatch in the [001] direction. These results demonstrate that lattice matching is needed in all three dimensions between materials used in epitaxial multilayer devices.

5.6.2 Off-normal Incidence IBAD

It was found that off-normal incidence IBAD of films that are lattice-matched to the underlying substrate resulted in multiple in-plane orientations. The epitaxial in-plane orientation was found to dominate, but the effect of the ion beam also induced a small amount of material that was biaxially aligned with the direction of the incoming ion beam.

It is therefore seen that this technique of biaxial planarization is more appropriate to deposition of non-lattice matched materials. The technological implications are similar to those for deposition of biaxially aligned films on amorphous substrates. The in-plane orientation can be tailored such that the in-plane orientation of subsequently grown BYC layers can be specified. Near complete planarization is achieved when the ion beam direction is not parallel to the groove direction The degree of planarization achieved in this manner may be sufficient to allow BYC films to be grown without developing weak-links. Actual devices, however, will have a surface topography that will be more complicated than sets of parallel lines. Complete planarization therefore cannot be achieved with ion beam bombardment from one direction only. This problem can be overcome by rotating the sample during IBAD to achieve planarization before capping the film off with a layer deposited with the ion beam set at one direction to induce the proper biaxial alignment.

CHAPTER 6

MgO FILM GROWTH

6.1 INTRODUCTION

MgO is an attractive candidate dielectric interlayer material for HTSC devices. The ability to grow highly oriented or epitaxial MgO thin films over BYC would be invaluable due mainly to the fact that MgO has the lowest dielectric constant of all dielectric materials that are lattice-matched to BYC (~10).[19] MgO also has reasonable dielectric loss tangent values and good thermal expansion properties relative to BYC.[19] However, MgO also has the largest lattice mismatch with respect to BYC (~-10% for MgO growth on BYC) among candidate dielectric materials. In this chapter, epitaxial growth of MgO films deposited using off-axis rf magnetron sputtering over single crystal $SrTiO_3$ and $LaAlO_3$ substrates is examined. The lattice mismatches between MgO, and $SrTiO_3$ and $LaAlO_3$ are -7.9% and -11%, respectively, which fall on either side of the MgO-BYC lattice mismatch. It may be possible to develop a process for depositing high quality MgO buffer layers on BYC by understanding the mechanisms through which MgO grows on these substrates. In addition, single crystal $SrTiO_3$ and $LaAlO_3$ possess much more ideal surfaces for studying MgO film growth than BYC films which will introduce less ambiguity in interpretation of results.

6.2 BACKGROUND

MgO is a strongly ionic material with a high melting point of ~2800°C. MgO has a lattice constant of 4.213 Å and has the rock-salt crystal structure. In crystalline materials, low energy surfaces generally correspond to those with low Miller indices (i.e. closest packing and large interplanar spacing). Additional constraints that apply to ionic systems include electrical neutrality and the absence of a net dipole moment.[166] In rock-salt crystal structures, both the (100) and (110) planes are neutral while the (111) plane is polar. For MgO, the (100) surface has a lower surface energy than the (110) plane[166] and is expected to be the preferred thin film orientation based on minimum surface energy considerations. The polar nature of (111) MgO, on the other hand, causes it to be unstable for macroscopic crystals.

Growth of MgO thin films has been widely studied due to the large number of potential applications. In addition to HTSC devices, MgO can also be used for epitaxial oxide growth on GaAs, as buffer layers in devices involving ferroelectric films, and as barrier layers for low temperature superconducting junction devices. MgO has a high secondary electron emission coefficient which has also prompted interest in its use in plasma display panels. Furthermore, its refractory properties may allow MgO to be used as a refractory coating material.

Methods that have been used for physically depositing MgO include electron-beam (e-beam) evaporation, sputtering, and pulsed laser deposition. Aboelfotah carried out a series of studies using e-beam evaporation to grow MgO thin films on glass,[167] single crystal Ag films,[168.169] and single crystal alkali halide substrates.[170.171] Reflection high energy electron diffraction (RHEED) was used *in situ* to study film growth and orientation development. On amorphous substrates, it was found that an initial random crystal structure yielded to a [111] preferred orientation after reaching a film thickness of 500 Å. On (001) and (111) oriented single crystal Ag films, deposition below 150°C yielded (111) wire texture and (111) epitaxial films, respectively. At higher temperatures, (100) oriented MgO was obtained on both types of Ag films. Since the (100) orientation has similar lattice mismatches with both (001) and (111) Ag, this result suggested that the energetically favored (100) orientation was obtained when deposition temperatures were high enough to ensure adequate surface mobilities. However, a (111) wire texture began to emerge at film thicknesses of 500 Å which completely dominated the film by 4000 Å.

For growth on alkali halide substrates of (001) LiF, NaCl, and KCl, which have lattice mismatches to MgO of +3%, -25%, and -33%, respectively, it was found that the minimum substrate temperature required to obtain epitaxial MgO increased with increasing lattice misfit. It was also found that the maximum thickness to which epitaxy could be obtained for a given deposition temperature decreased with increasing misfit. This maximum thickness could be increased by increasing the deposition temperature. The in-plane orientation of MgO deteriorated beyond this thickness on LiF while a (110) wire texture developed on NaCl and KCl.

Aboelfotah also examined the roles of oxygen, water vapor, and post-annealing on the development of MgO films using infrared spectroscopy (IR) and RHEED. Introduction of 99.99% oxygen at pressures of 10^{-5}-10^{-4} Torr during deposition produced no changes in the film orientations. IR revealed the presence of hydroxyl groups in the films, that presumably had been picked up from residual water vapor in the vacuum system, since films deposited at faster deposition rates and higher temperatures possessed a lower hydroxyl group concentration. Only films deposited at the highest rates and deposition temperatures exhibited a dissolution of the <111> orientation and development of some <100> orientation upon annealing in dry nitrogen. This suggested that the presence of residual gases such as water vapor may inhibit surface diffusion since the (100) orientation is the most energetically favored.

Several other groups have also used e-beam evaporation to deposit MgO thin films.[172-177] Yadavalli *et al.*[172] were able to obtain epitaxial single crystal MgO films on V, Nb, and sapphire substrates at deposition temperatures as low as 140K up to 1300K. It was observed that a minimum growth temperature of 200K was required to prevent poor quality crystal from forming on the surface. The authors explained these results by using results from an earlier study[173] that suggested fast surface diffusion of alkali halides on neutral planes allowed epitaxial growth of ionic materials to be achieved at temperatures as low as $\sim 0.1T_m$, where T_m is the absolute melting point of the material being deposited. This threshold is much lower than what is generally required for metals ($3T_m/8$) and semiconductors ($0.55T_m$).

Berezin *et al.*[174,175] were able to grow 1200 Å thick epitaxial (001) MgO on R-plane sapphire $(1\bar{1}02)$ using e-beam evaporation. Subsequently evaporated BYC films had a T_c of 88.5K and J_c of 1 x 10^6A/cm^2 at 77K which was an indication of the high quality of the MgO buffer layer. Although Berezin *et al.* did not notice any dependence of epitaxial growth on the oxygen partial pressure during deposition, they make a reference to amorphous films being obtained for too high of a p_{O2}.

Reichelt[176] was able to evaporate up to 8000Å of epitaxial MgO on a LiF film evaporated onto appropriately oriented NaCl single crystal substrates. It was found that in order for single crystal MgO films to be obtained, the LiF layer needed to be deposited as a single crystal. Rakotomiraho *et al.*[177] used reactive evaporation to grow MgO films up to 5 μm thick onto amorphous pure fused quartz surfaces at 400°C. No discernable XRD peaks could be detected for films under 1 μm thick while a preferential <111> orientation was found for films over 1 μm thick.

A number of groups have used rf-sputtering to deposit MgO thin films on NbN[44,48] and semiconductors,[45-47] primarily for low temperature superconducting device fabrication studies. MgO is preferred as a dielectric over native oxides due to its large bandgap. Shoji[44] found that on NbN, room temperature deposition resulted in amorphous films. Thakoor *et al.*[48] give no structural information but report that high quality pin-hole free layers were obtained. Tonuchi *et al.*[47] were able to grow epitaxial MgO on Si, GaAs, InP, and GaSb at deposition temperatures of 300°C, although the surface morphology of the MgO grown on InP turned out to be rough. The quality of the ultrathin (5-600Å) MgO layers was measured by the orientation of an NbN overlayer since NbN is known to grow epitaxially on MgO. However, epitaxial NbN was also obtained on a 10 Å thick MgO film grown on thermally oxidized SiO_2. The authors attributed the orientation of the MgO layer to either natural orientation or graphoepitaxy that may have resulted from "structural surface deformation" introduced during sputter cleaning of the substrate surface. Unfortunately, no further information is given on this phenomenon. Baba *et al.*[45] found MgO to grow with a preferred (100) orientation on glass and Si substrates that were not "subjected to any control." When substrate bias was applied, however, a (110) orientation emerged. Ishiguro *et al.*[46] grew MgO on (100) Si at 170°C. It was found that the initial 40 Å was amorphous but that any film grown beyond that was polycrystalline with a strongly preferred (100) orientation.

Vuoristo *et al.*[177,178] also used rf sputtering to coat polished surfaces of metal with 2.7 - 4.5 μm of MgO at temperatures between 220°C and 450°C. The final crystal structures were found to be independent of substrate material except in the case of Cu due to substrate-film interactions. XRD patterns showed a preferentially (100) oriented structure with some (110) material detected at lower sputtering pressures and higher temperatures. No (111) orientation was detected. SEM micrographs also disclosed a columnar microstructure which became denser with higher temperatures and lower pressures.

Sakuta *et al.*[180] were able to deposit MgO at 350°C by using pressure controlled reactive rf magnetron sputtering in a 50% Ar - 50% O_2 atmosphere onto both amorphous and epitaxial BYC films. XRD and RHEED were used in structural analysis of the films. The MgO films were oriented randomly when grown on amorphous BYC but oriented parallel to the surface when grown on epitaxial BYC. Although higher quality MgO could be grown in a pure Ar atmosphere, O_2 was required to protect the superconducting properties of the BYC.

Reactive ion-beam sputtering has also been used to grow MgO films.[181,43] Hebard *et al.*[181] obtained polycrystalline MgO on a variety of substrates at room temperature with no evidence of any amorphous material. Chow *et al.*[43] were able to grow epitaxial MgO on Si and sapphire substrates at temperatures between 500°C and 700°C. Chow *et al.* point out that although there is a fairly large mismatch of 6-12% between MgO and sapphire for the orientations they observe, structural symmetry between the film and substrate may be a more important factor than lattice matching for obtaining oriented films.

More recently, pulsed laser deposition (PLD) has been used to grow MgO films. The interest in this work has been primarily for potential HTSC applications. Epitaxial MgO has been obtained on Si[54] and other lattice-matched substrates.[21] Growth on silicon was found to be sensitive to both substrate surface and deposition conditions. It was found that removing the native oxide from the Si substrate surface and terminating it with a hydrogen layer was crucial to obtaining high quality MgO. In addition, an optimal p_{O2} of 0.005 mTorr was found. Using either higher or lower oxygen pressures resulted in degradation of epitaxial quality. The relationship between MgO and Si was found to be a coincident site lattice rather than direct matching.

In summary, the results reported in the literature suggest that growth of high quality oriented or epitaxial MgO is highly dependent on the conditions of the underlying substrate surface. MgO film growth is also sensitive to deposition conditions. (100) appears to be the preferred orientation for MgO films in the absence of lattice-matching, particularly for films deposited by sputtering, although the (110) orientation was also observed in several instances. Results obtained from e-beam evaporated films, however, do not follow this trend. In addition to exhibiting a preferred <111> orientation, a deterioration in film orientation with increasing film thickness is also observed. This may be due in part to differences in surface mobilities of the deposited species. Sputtered species generally are much more energetic than evaporated species (10 eV versus 0.1 eV).[182] The resultant increase in surface mobility may allow the MgO film to adopt a more energetically favorable orientation.

Although the deterioration in MgO orientation with increasing film thickness has been observed only for film growth using evaporation, it is nevertheless of concern. Dielectric interlayers in HTSC devices will need to be 1-2 μm thick. A change in dielectric film orientation cannot be tolerated during device fabrication.

6.3 EXPERIMENTAL PROCEDURE

6.3.1 Substrate Preparation

Substrates used in this study were (100) and (110) oriented single crystal $SrTiO_3$ and $LaAlO_3$. In addition, $LaAlO_3$ substrates that had been treated to modify the substrate surfaces were used. (100) $LaAlO_3$ substrates were blanket ion milled at 500 eV for 30 minutes using the procedures described in Section 3.1.3. Some of these substrates were subsequently annealed at 950°C in flowing oxygen for 2 hours.

Vicinally polished (100) $LaAlO_3$ substrates were also used for MgO deposition. As-received nominally flat (100) $LaAlO_3$ substrates were polished several degrees off from the [100] axis towards the [001] direction using a Buehler[154] polishing wheel and a tripod sample holder originally designed for TEM sample preparation. The tripod mount has three legs whose heights can be adjusted independently which allows polishing a substrate at any desired angle.

The substrate surface was first ground flat at the desired angle using a 15μm diamond impregnated wheel and water as the lubricant. The surface was then polished to an optical finish using successive polishes of 9μm, 3μm, and 1μm diamond paste on photographic paper using kerosene lubricant. A final polish was applied using SYTON[83] colloidal silica. The substrates were then cleaned by first ultrasonicating in basic water (ph~9) to remove the colloidal silica and then in acetone and methyl alcohol. The substrates were then heat treated at 950°C for 2 hours in flowing oxygen at 4 scfh to generate steps in the surface.

6.3.2 Deposition Procedure

MgO films were deposited using the procedures described in Section 3.3.3. Films were grown at temperatures between 200°C and 700°C. The composition of the sputtering gas was varied between 10 and 20% oxygen, while the sputtering pressure was varied between 2.5 and 5.5 mTorr. Unless otherwise mentioned, nominal film deposition thicknesses were ~1800 Å.

6.3.3 Film Characterization

Film orientation was characterized using X-ray and four-circle diffractometry. Film microstructure was examined using SEM and AFM. AFM was also used to characterize substrate surfaces.

6.4 RESULTS

6.4.1 MgO Deposition on $SrTiO_3$

MgO thin films were deposited on (100) $SrTiO_3$ single crystal substrates at deposition temperatures between 200°C and 700°C at a sputtering pressure of 2.5 mTorr with 20% O_2 by flow. In addition, for deposition runs at 435°C, a sputtering pressure of 2.5 mTorr was used with the flow of oxygen varied between 10% and 20%. MgO was also deposited on (110) oriented $SrTiO_3$ at 300°C and 500°C with 20% O_2 at 2.5 mTorr.

6.4.1.1 MgO Film Orientation

MgO thin films grown on (100) $SrTiO_3$ at all deposition temperatures and conditions explored possess a (100) orientation as determined by $\theta/2\theta$ XRD. Table 6.1 is a summary for films deposited at 20% O_2 and 2.5 mTorr. FWHM values from rocking curve measurements of the MgO (200) peak range from 0.9° to 1.1°. Four circle diffractometry ϕ scans reveal an in-plane orientation of MgO [001] $\parallel$ $SrTiO_3$ [001], or "cube on cube" growth throughout this temperature range. Typical $\theta/2\theta$ XRD and ϕ scans are shown in Figure 6.1. On (110) $SrTiO_3$, MgO grows with a (110) film orientation at both 300°C and 500°C (see Figure 6.2). Four circle diffractometry ϕ scans also measure an in-plane orientation in the film parallel to that of the substrate (see Figure 6.2(b)). XRD results for (110) MgO films are also summarized in Table 6.1.

6.4.1.2 MgO Film Microstructure

The following SEM microstructural results are for MgO films deposited with 20% O_2 at 2.5 mTorr on (100) $SrTiO_3$. At deposition temperatures above 435°C, MgO films display a smooth and dense microstructure as observed by SEM (see Figure 6.3(a)). A deterioration in the microstructure begins to occur below 435°C, however. Figure 6.3(b) shows the emergence at 400°C of a facetted plate-like microstructure mixed with the smooth and dense material. The number density of the "plates" increases with decreasing deposition temperature and dominates the microstructure by 200°C (see Figures 6.3(c) and

Table 6.1 XRD data for MgO deposited on (100) and (110) $SrTiO_3$ at 20% O_2 and 2.5 mTorr

T (°C)	MgO/(100) $SrTiO_3$ (200) Intensity (cps)	MgO/(100) $SrTiO_3$ (200) Rocking Curve FWHM	MgO/(110) $SrTiO_3$ (220) Intensity (cps)	MgO/(110) $SrTiO_3$ (220) Rocking Curve FWHM
200°C	85,000	0.95°		
300°C	149,000	1.04°	2,500	1.41°
400°C	164,000	0.98°		
500°C	155,000	0.90°	113,000	0.903°
600°C	128,000	0.91°		
700°C	95,000	1.070°		

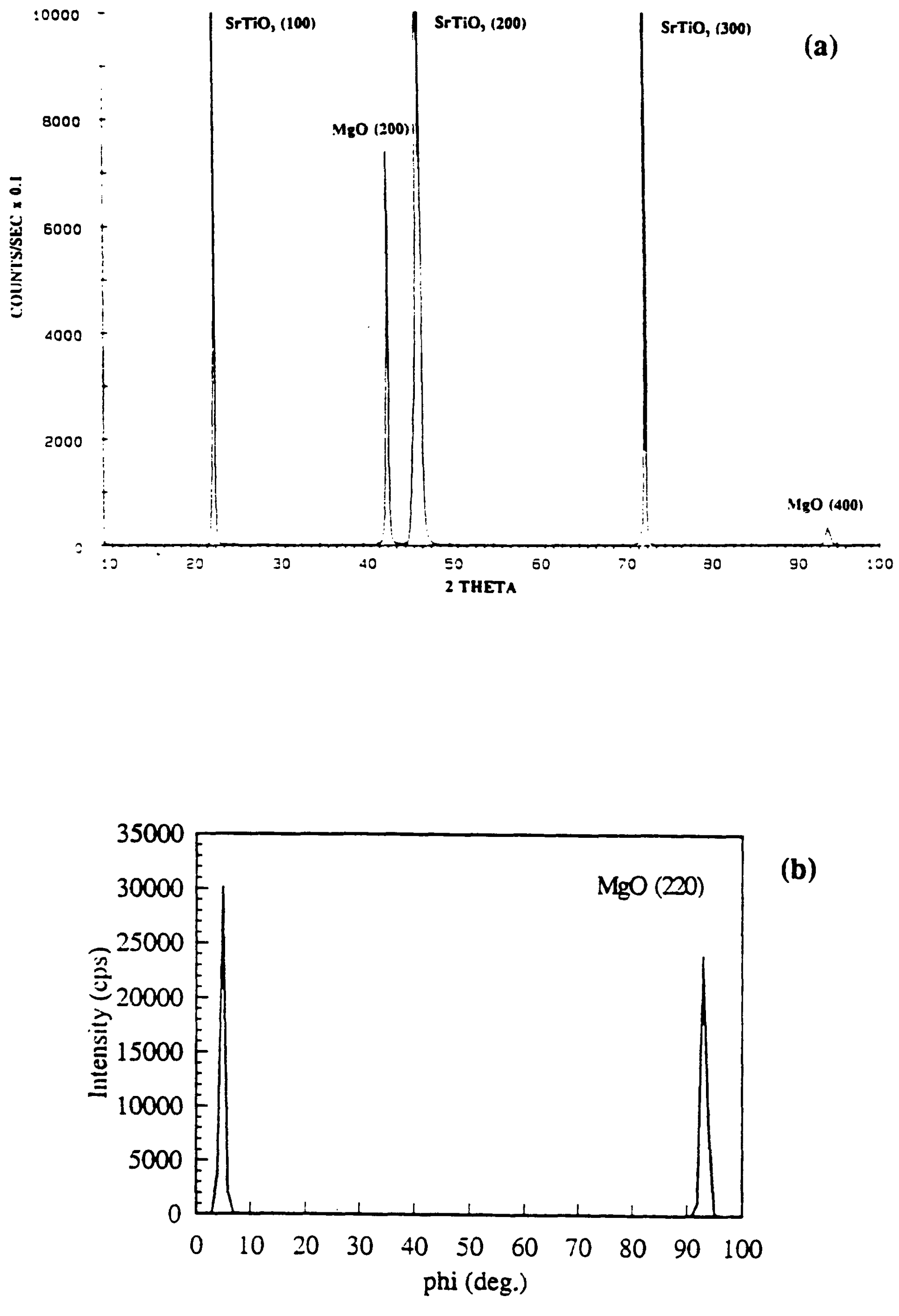

MgO [100] || $SrTiO_3$ [100]

Figure 6.1 XRD scans for MgO film sputtered on (100) $SrTiO_3$ at 600°C, 2.5 mTorr, and 20% O_2: (a) $\theta/2\theta$ scan, and (b) four-circle ϕ-scan at $\chi=45°$.

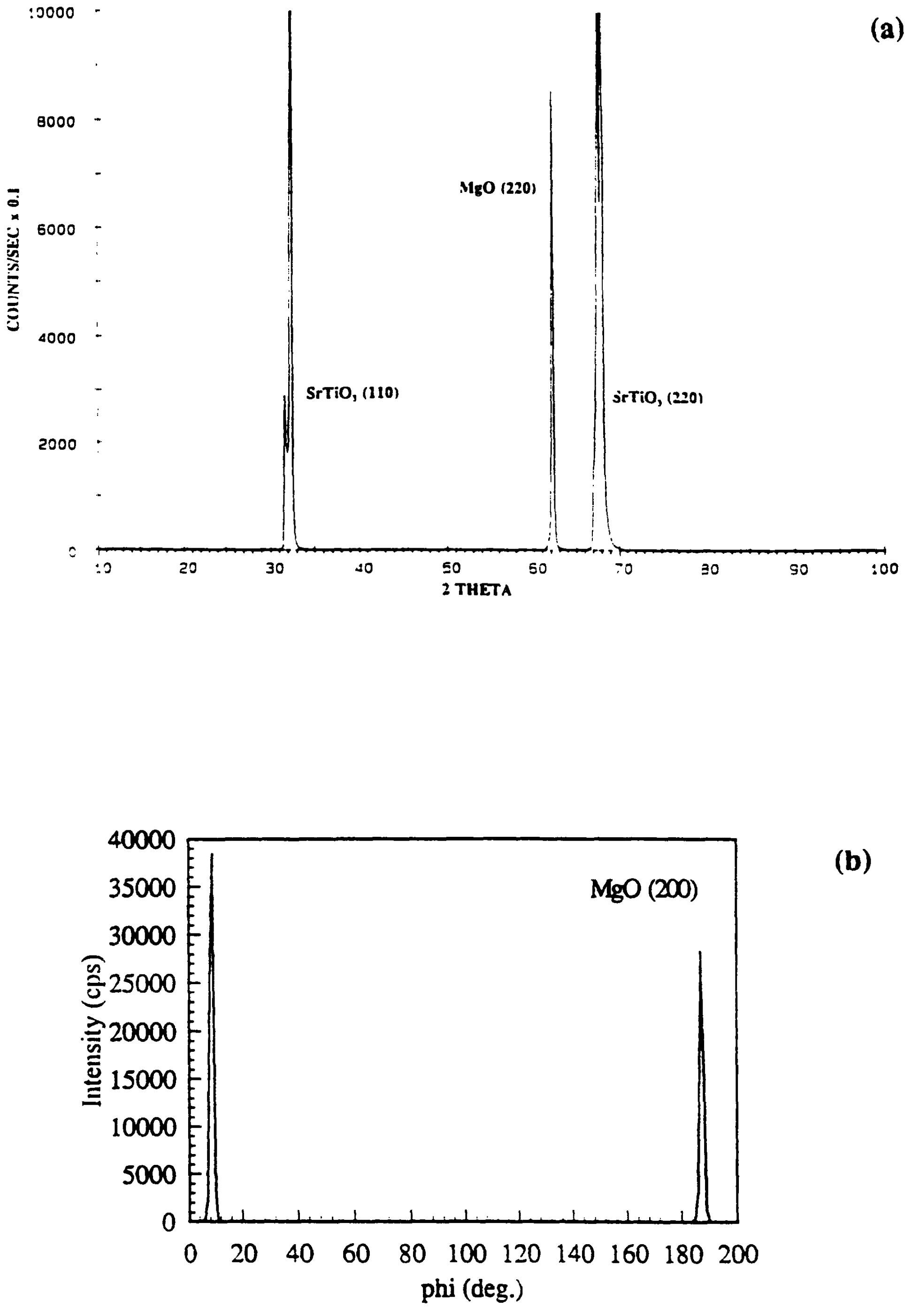

MgO [110] || SrTiO$_3$ [110]

Figure 6.2 XRD scans for MgO sputtered on (110) SrTiO$_3$ at 500°C, 2.5 mTorr, and 20% O_2: (a) $\theta/2\theta$ scan, and (b) four-circle ϕ-scan at $\chi=45°$.

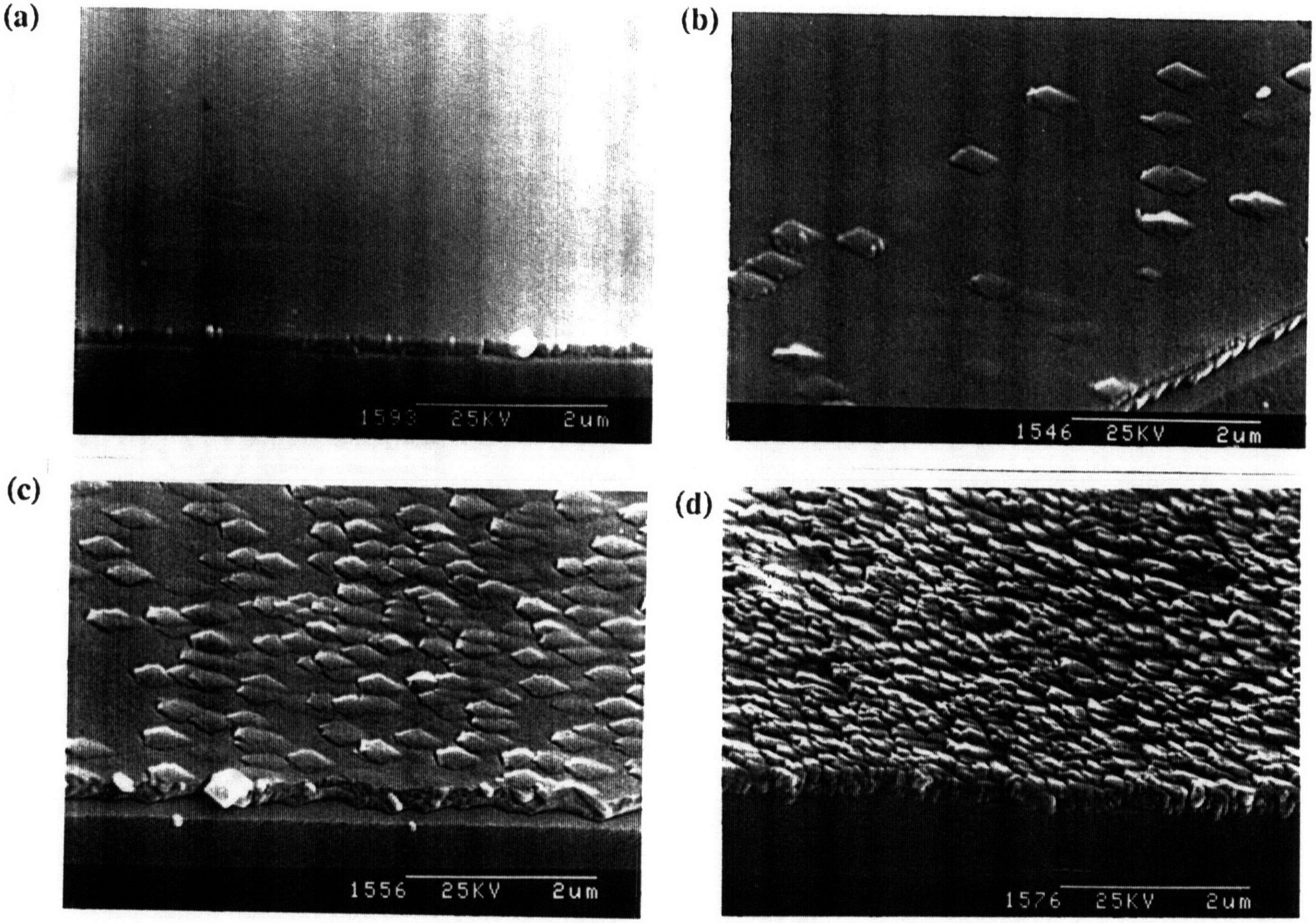

Figure 6.3 SEM micrographs for MgO sputtered on (100) $SrTiO_3$ at 2.5 mTorr, 20% O_2, and: (a) 700°C, (b) 400°C, (c) 300°C, and (d) 200°C.

(d)). The "plates" appear to be oriented with respect to each other. The film density is also observed to decrease with decreasing temperature. Thicker films were obtained at lower temperatures as determined by cross-sectional SEM measurements. The same nominal amount of material, however, was deposited at all temperatures as measured by the quartz crystal thickness monitor.

A similar trend in microstructure was observed for MgO films sputtered on (110) $SrTiO_3$. The films are smooth and dense appearance when grown at 500°C but have a rougher surface when deposited at 300°C (see Figures 6.4(a) and (b)).

The surface roughness of (100) MgO films deposited above 435°C on (100) $SrTiO_3$ was measured by AFM. Figure 6.5 is an AFM micrograph of a MgO film sputtered at 500°C, 2.5 mTorr, and 10% O_2. The mean roughness of this film over a 4.96 μm^2 area was measured to be 0.25 nm.

6.4.2. $LaAlO_3$ Substrate Surface Characterization

As-received, ion milled, and vicinally polished (100) $LaAlO_3$ substrates were examined using AFM and/or optical microscopy. All substrates were cleaned with solvents as described in Section 3.2.1.5 prior to examination or substrate treatment.

Twins that are present in the $LaAlO_3$ substrates can be observed by optical microscopy. In Figure 6.6, the lines running parallel and at a 45° angle to the side of the substrate are (100)/(010) and (110)-type twins, respectively.

Figures 6.7(a) and (b) are AFM micrographs of an as-received substrate. The edges of the micrographs are oriented parallel to the substrate sides and hence the $LaAlO_3$ [010] and [001] directions. Rows of steps running parallel to these directions are clearly visible. The height of these steps is on the order of the $LaAlO_3$ unit cell spacing. As shown in Figure 6.7(a), the step frequency is ~6-7/μm. A change in row direction can also be seen in the lower left hand corner of Figure 6.7(a). The two different row directions appear to correspond to the two types of substrate twins that are observed in the optical microscope.

An absence of steps is detected in ion milled $LaAlO_3$ substrates. Figure 6.8(a) is an AFM micrograph of a substrate that had been milled for a total of 30 minutes at 500

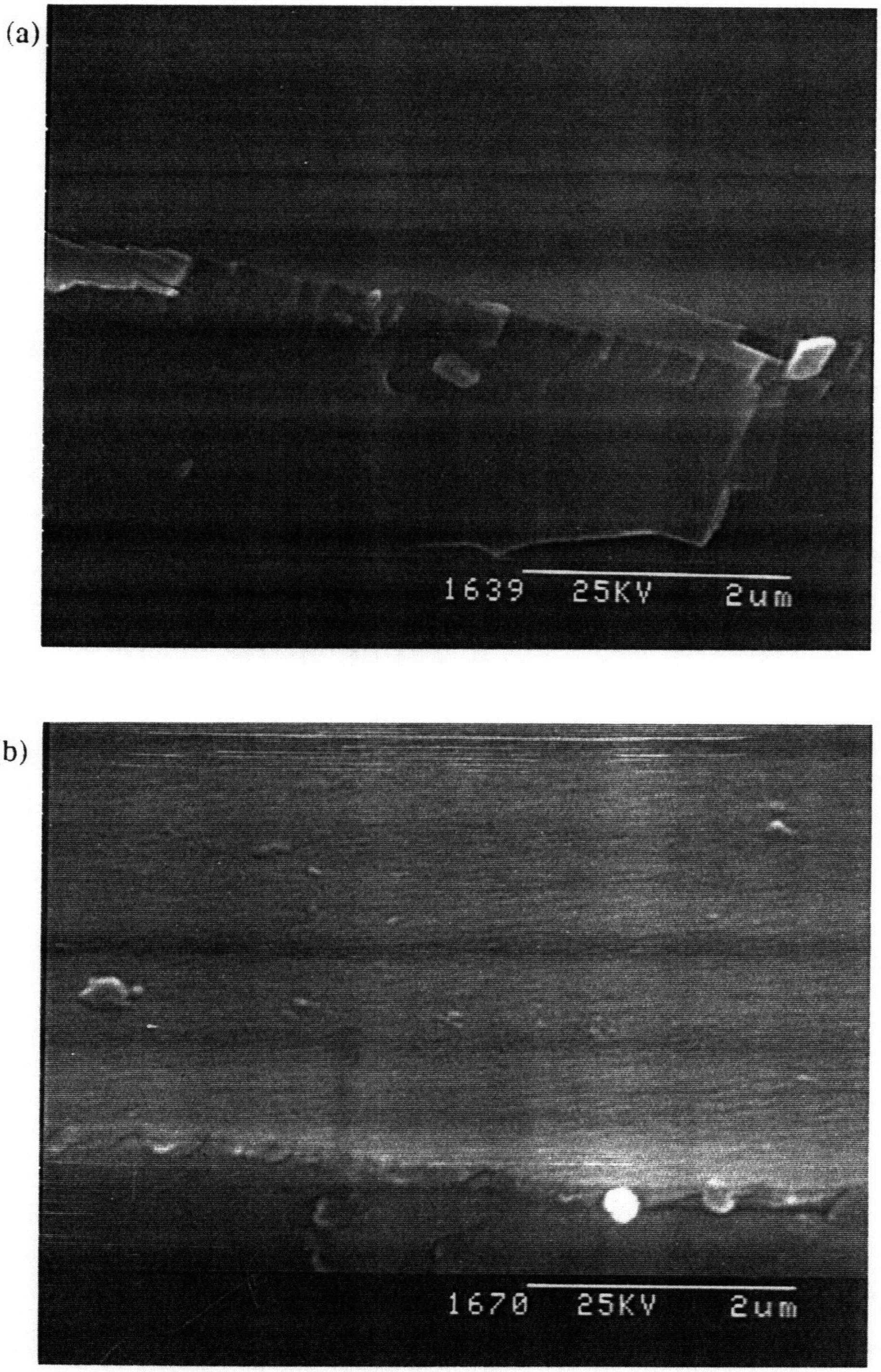

Figure 6.4 SEM micrographs for MgO sputtered on (110) $SrTiO_3$ at 2.5 mTorr, 20% O_2, and (a) 500°C, and (b) 300°C.

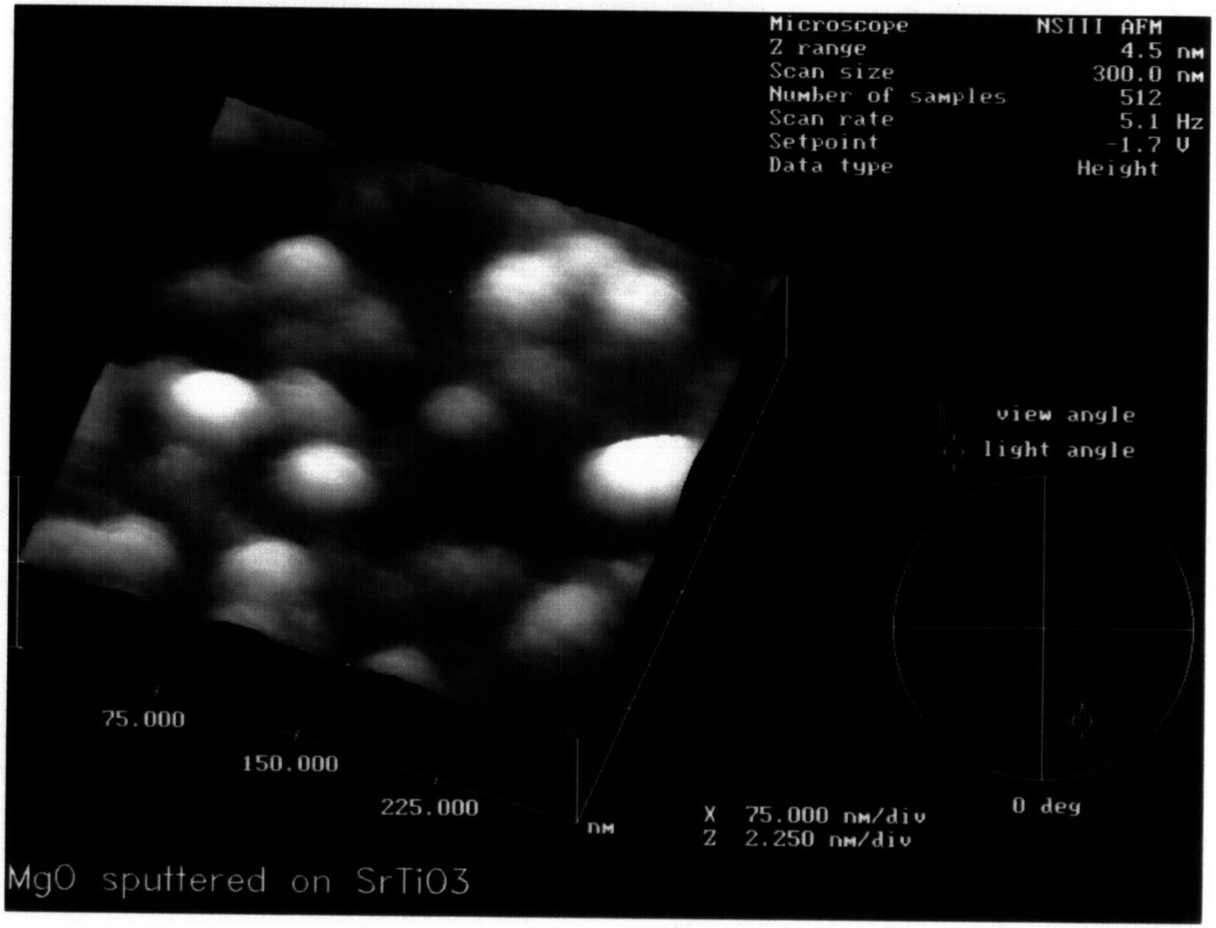

Microscope	NSIII AFM
Z range	4.5 nm
Scan size	300.0 nm
Number of samples	512
Scan rate	5.1 Hz
Setpoint	-1.7 V
Data type	Height

X 75.000 nm/div
Z 2.250 nm/div

Figure 6.5 AFM micrograph of MgO sputtered on (100) $SrTiO_3$ at 500°C, 10% O_2, and 2.5 mTorr. Mean roughness over 25 μm^2 area is 0.25 nm.

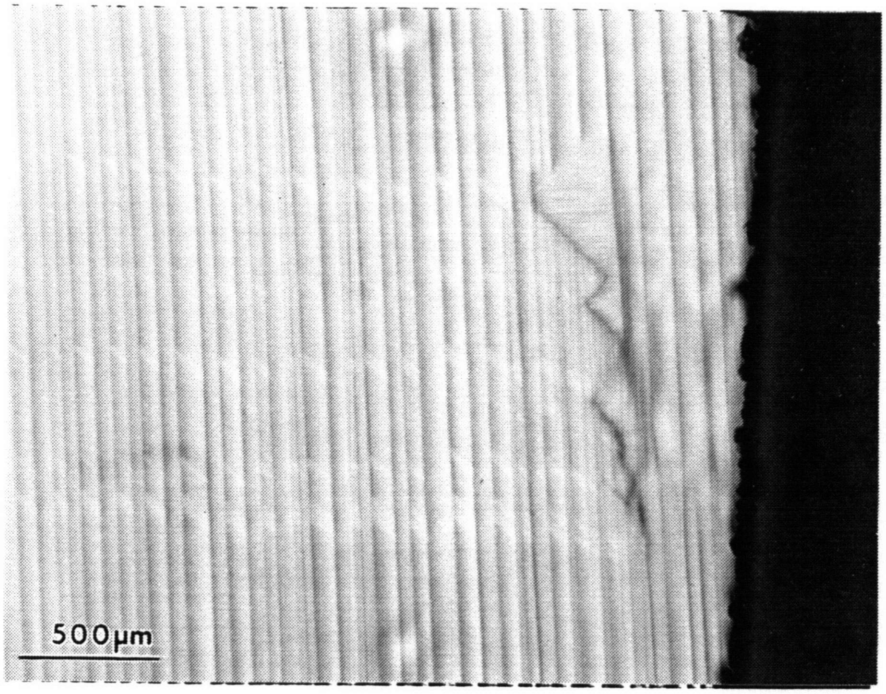

Figure 6.6 Optical micrograph of twinned (100) $LaAlO_3$ substrate.

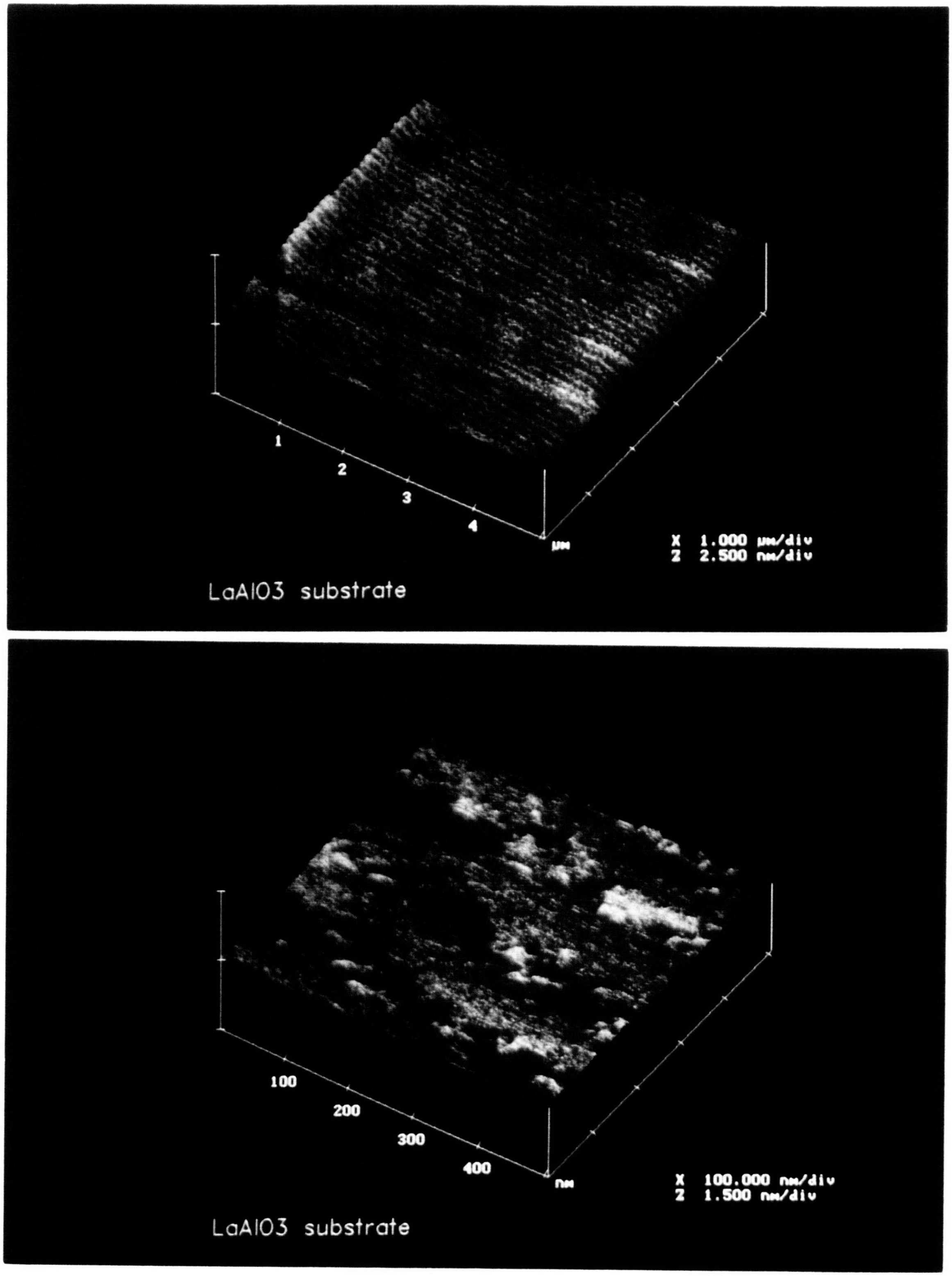

Figure 6.7 AFM micrographs of (100) $LaAlO_3$ substrate showing presence of substrate steps.

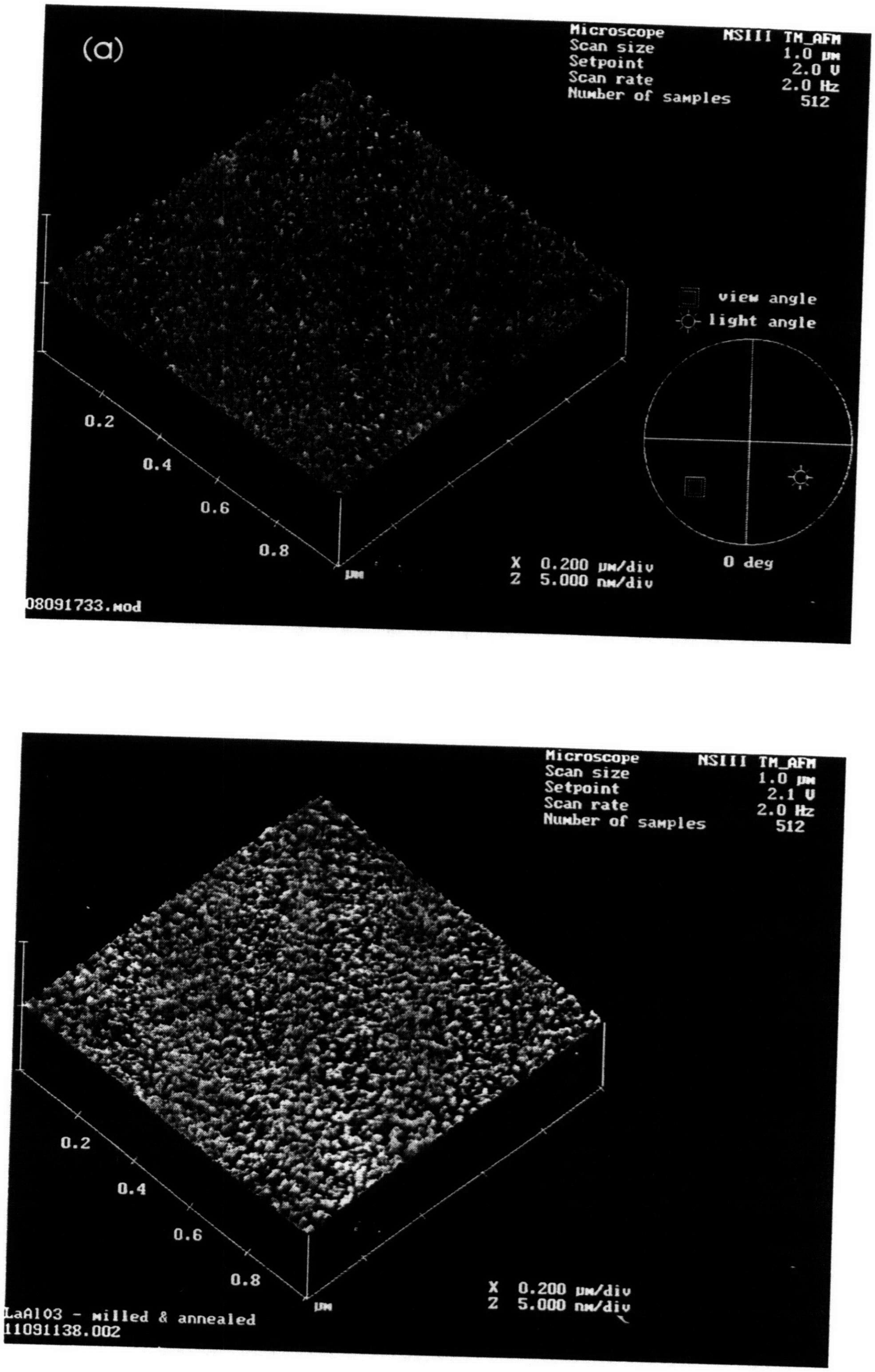

Figure 6.8 AFM micrograph of (100) $LaAlO_3$ substrate surface: (a) after ion milling for 30 minutes at 500 eV, and (b) after ion milling and subsequent annealing at 950°C in flowing O_2 for 2 hours.

eV. The rows of steps have been replaced by a surface consisting of small cones. Subsequent annealing at 950°C does not substantially alter the surface as seen in Figure 6.8(b).

6.4.3 MgO Deposition on As-received $LaAlO_3$ Substrates

6.4.3.1 MgO Film Orientation

Unless otherwise noted, all results presented below are for films deposited between 200°C and 700°C at a sputtering pressure of ~2.5 mTorr and an oxygen composition of 20%. A nominal thickness of ~1800 Å was deposited on all substrates as measured *in situ* by the quartz crystal rate monitor. The orientation of MgO films grown on (100) $LaAlO_3$ was found to vary between a (100) orientation and a mixed (100)/(110) orientation. Although the majority of the films are (100) oriented, a variation in the quality of this orientation was also observed. No (111) orientation was detected in any of the films. The results for these two categories will be presented below separately.

MgO films with a (100) orientation were grown on (100) $LaAlO_3$ at deposition temperatures between 200°C and 600°C. A summary of the best XRD results obtained at each temperature is shown in Table 6.2. FWHM values of the MgO (200) rocking curves range from 1.41° to 2.51°. ϕ-scans show that these films are also in-plane oriented with MgO [001] $\|$ $LaAlO_3$ [001]. Typical $\theta/2\theta$ and ϕ-scans are shown in Figure 6.9.

MgO was found to grow, however, either with depressed (*h*00) peak intensities or with a mixed (100)/(110) orientation at temperatures between 300°C and 700°C, an example of which is shown in the XRD trace in Figure 6.10. Overall MgO XRD intensities from these films are much weaker than those of the highly (100) oriented films. The FWHM values from the (200) rocking curve for these films are also typically 0.5° to several degrees broader. Although the absolute intensity of the MgO (220) peak is low in all cases ($\leq$ 200 cps), the relative intensity of the (220) peak becomes quite large when taken with respect to the depressed intensities of the (200) peaks.

Table 6.3 is a summary of XRD results obtained for multiple deposition runs at 500°C and is an example of the inconsistency observed for film orientation. A variation in the FWHM value of the MgO (200) rocking curve is observed, as well as a large

Table 6.2 XRD data for MgO deposited on (100) and (110) $LaAlO_3$ at 20% O_2 and 2.5 mTorr

T (°C)	MgO/(100) $LaAlO_3$ (200) Intensity (cps)	MgO/(100) $LaAlO_3$ (200) Rocking Curve FWHM	MgO/(110) $LaAlO_3$ Main Peak Intensity (cps)	MgO/(110) $LaAlO_3$ Main Peak Rocking Curve FWHM
200°C	12,780	2.51°		
300°C	45,000	1.41°	(220): 2,500	(220): 3.93°
400°C	48,000	1.45°		
500°C	29,000	1.60°	(200): 2,000	(200): 2.29°
600°C	6,500	1.69°		
700°C	800	~2°		

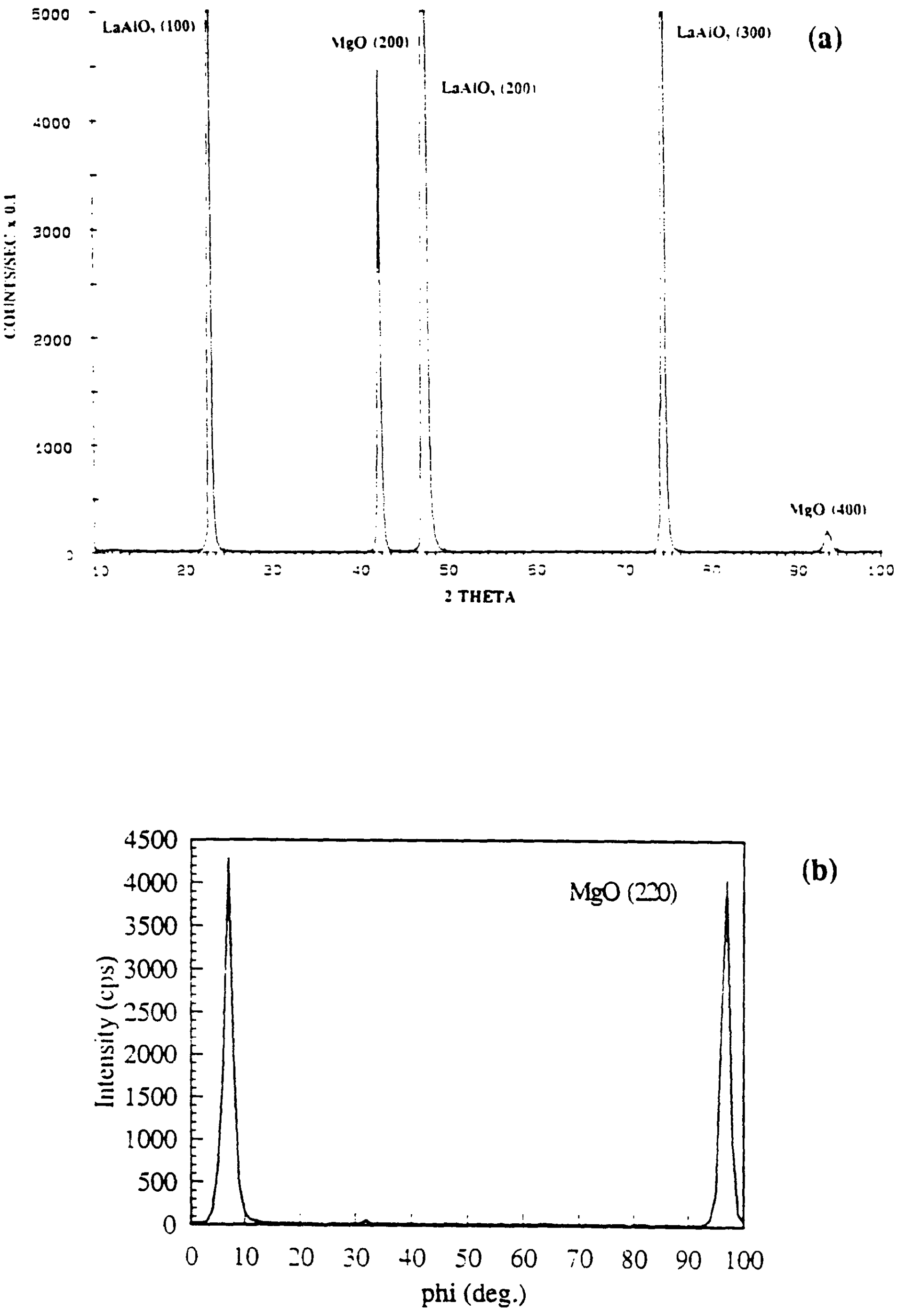

MgO [100] || $LaAlO_3$ [100]

Figure 6.9 XRD scans for MgO sputtered on (100) $LaAlO_3$ at 300°C, 2.5 mTorr, and 20% O_2: (a) $\theta/2\theta$ scan, and (b) four-circle ϕ-scan at $\chi=45°$.

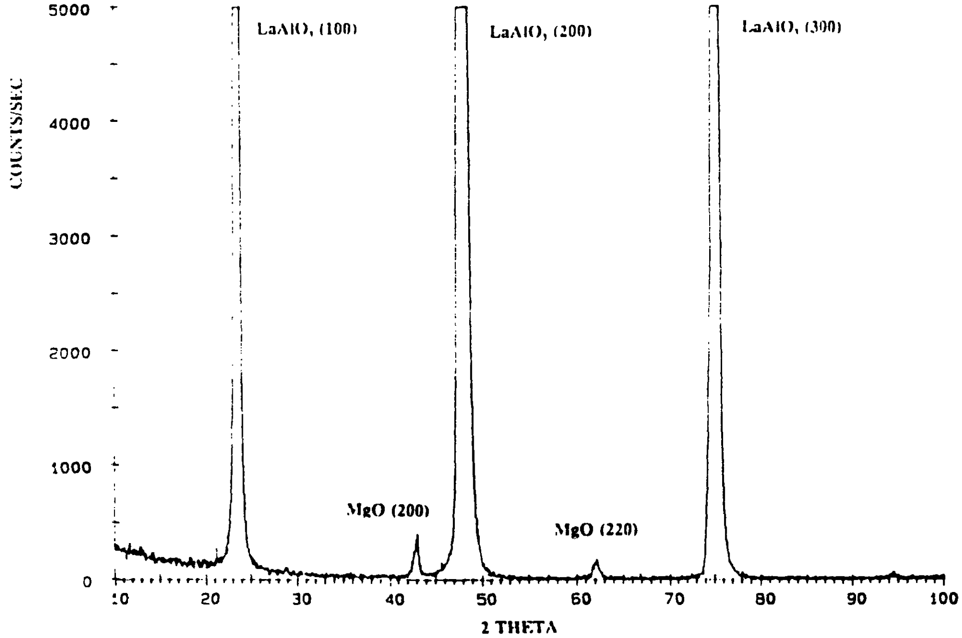

Figure 6.10 θ/2θ XRD scan of MgO sputtered on (100) $LaAlO_3$ at 700°C, 2.5 mTorr, and 20% O_2.

Table 6.3 XRD data of multiple deposition runs of MgO deposited on (100) $LaAlO_3$ at 500°C, 20% O_2, and 2.5 mTorr.

ID#	MgO (200) Intensity (cps)	MgO (220) Intensity (cps)	MgO (200) Rocking Curve FWHM	Observed microstructure
010	27,000	----	1.33°	Facetted
030	1,450	~50	2.29°	Mixed
032a	10.500	----	1.72°	Mixed
032b	700	*	3.55°	Mixed
046	1,100	----	2.36°	Mixed

variation in the intensity of the MgO (200) peak even though the same nominal amount of material was sputter deposited on all samples. Typically the rocking curves become broader as MgO (200) peak intensities decrease.

MgO was also deposited on (110) $LaAlO_3$ substrates at 300°C and 500°C. At 300°C, MgO grows with a (110) preferred orientation (see Figure 6.11(a)). The FWHM values of the MgO (220) rocking curve is 2.29°. At 500°C, MgO grows with a (100) preferred orientation (see Figure 6.11(b)) with a FWHM value of 3.93° for the MgO (200) rocking curve.

ϕ-scans show that the (110) MgO film grown at 300°C is oriented parallel to the underlying substrate. The (100) film deposited at 500°C has an in-plane orientation of MgO [001] $\parallel$ $LaAlO_3$ [001] and MgO [010] $\parallel$ $LaAlO_3$ [110] (see Figure 6.12).

6.4.3.2 MgO Film Microstructure

A variation in film microstructure was also observed for MgO grown on (100) $LaAlO_3$. Films with a strong (100) preferred orientation possess a facetted plate-like microstructure that is reminiscent of MgO grown on $SrTiO_3$ at lower deposition temperatures, but with smaller "plates" (see Figure 6.13(a)). This facetted microstructure is present at all deposition temperatures. MgO films that are less strongly (100) oriented also have a plate-like microstructure, but the plates are not as pronounced and are mixed with a columnar microstructure (see Figure 6.13(b)). Films with a mixed orientation have a columnar microstructure as seen in Figure 6.14.

The plates in the MgO films are often observed to be aligned in parallel rows as seen in Figure 6.13. SEM micrographs of thinner films show this effect to be particularly pronounced. Figure 6.15 are SEM micrographs for MgO films deposited to a nominal thickness of 400 Å at 400°C. Small grains in the film are aligned in parallel rows. The directions of the rows themselves are observed to vary. Higher magnification images show that the microstructure appears to consist of facetted particles set within a denser phase. AFM micrographs in Figure 6.16 for this sample reveal a similar film microstructure.

Two different microstructures are also observed for MgO deposited on (110)

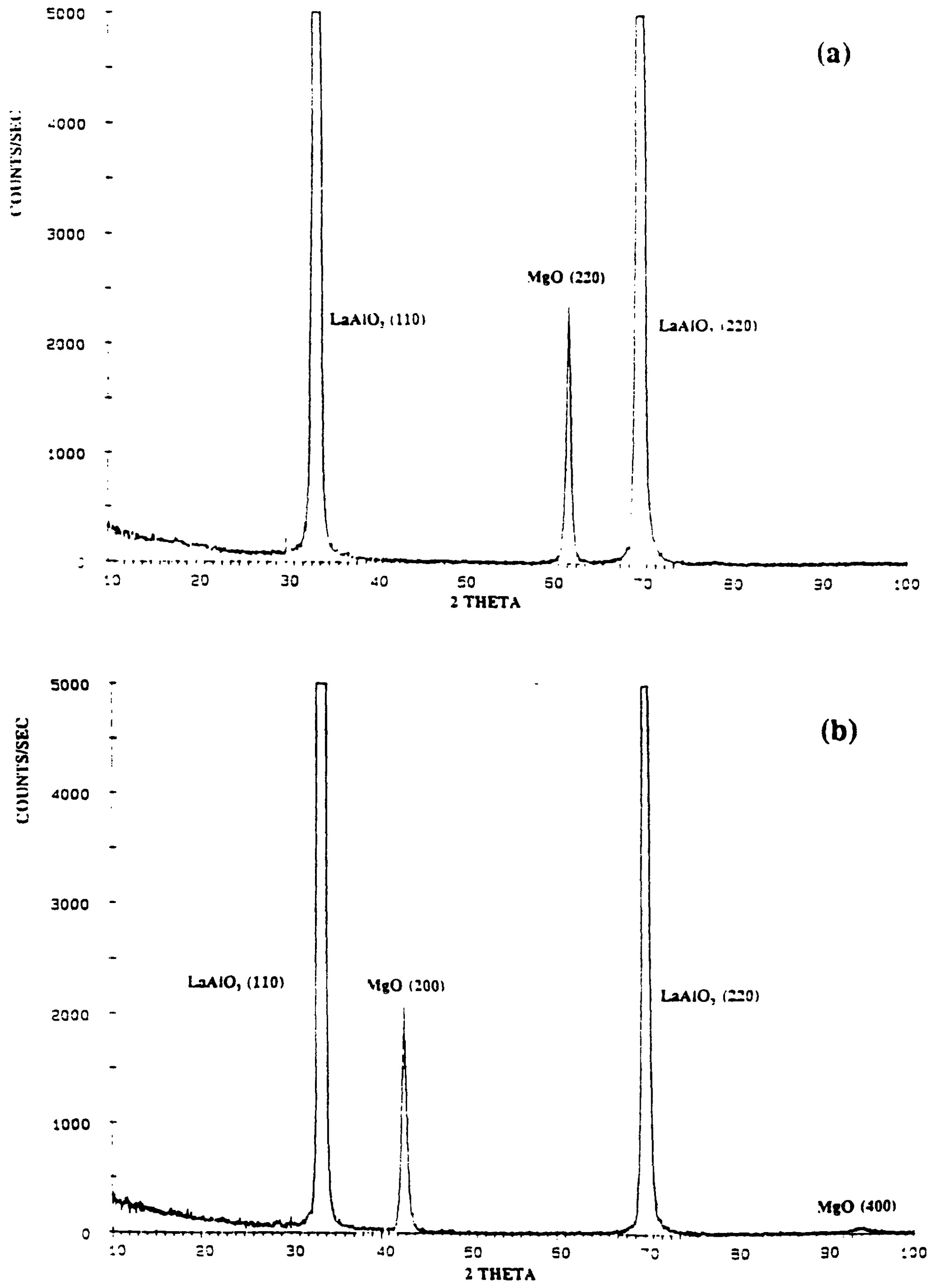

Figure 6.11 θ/2θ scans for MgO films sputtered on (110) LaAlO$_3$ at: (a) 300°C, and (b) 500°C.

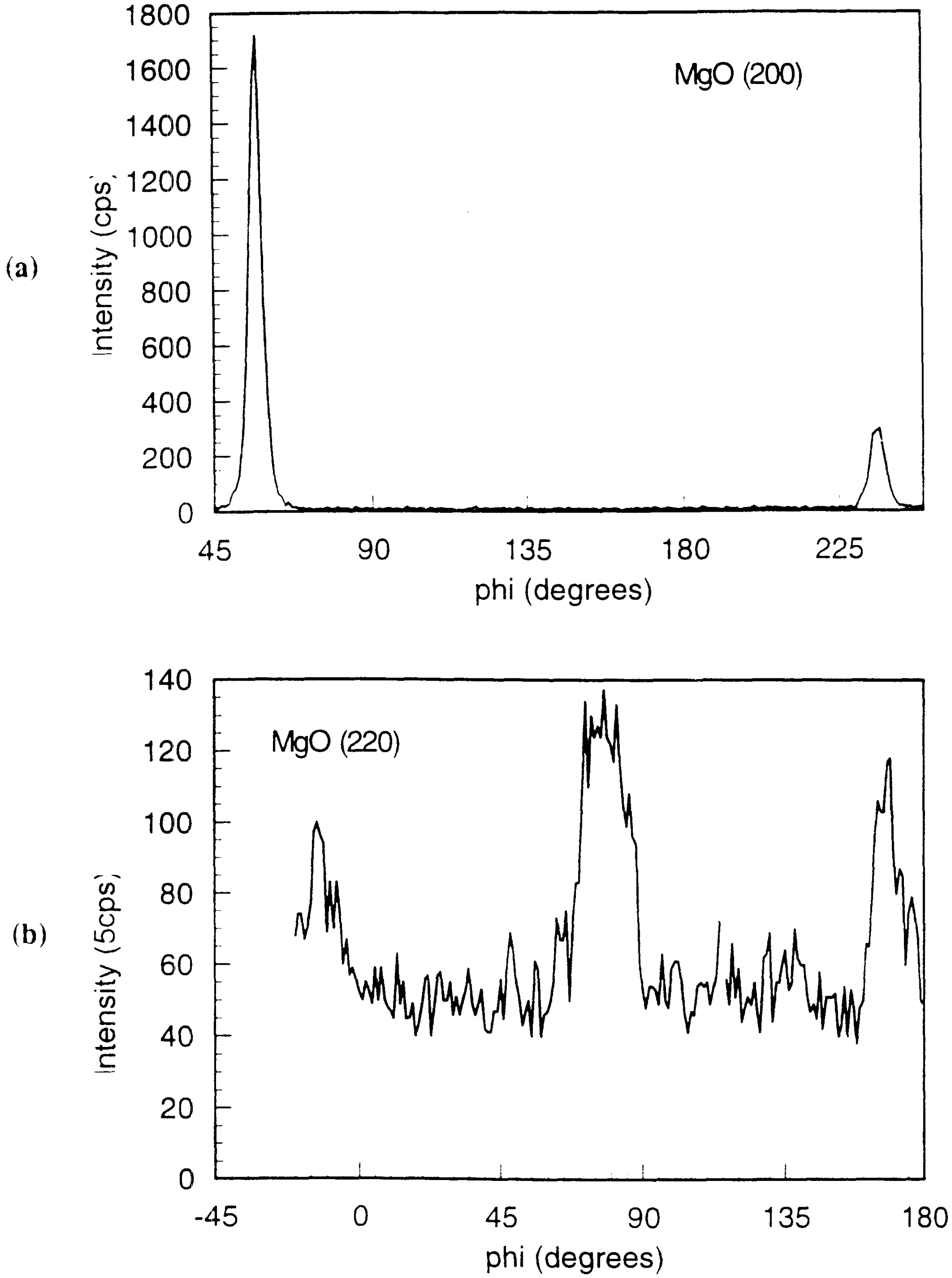

Figure 6.12 Four-circle ϕ-scans at χ=45° of MgO films sputtered on (110) $LaAlO_3$ at: (a) 300°C, and (b) 500°C.

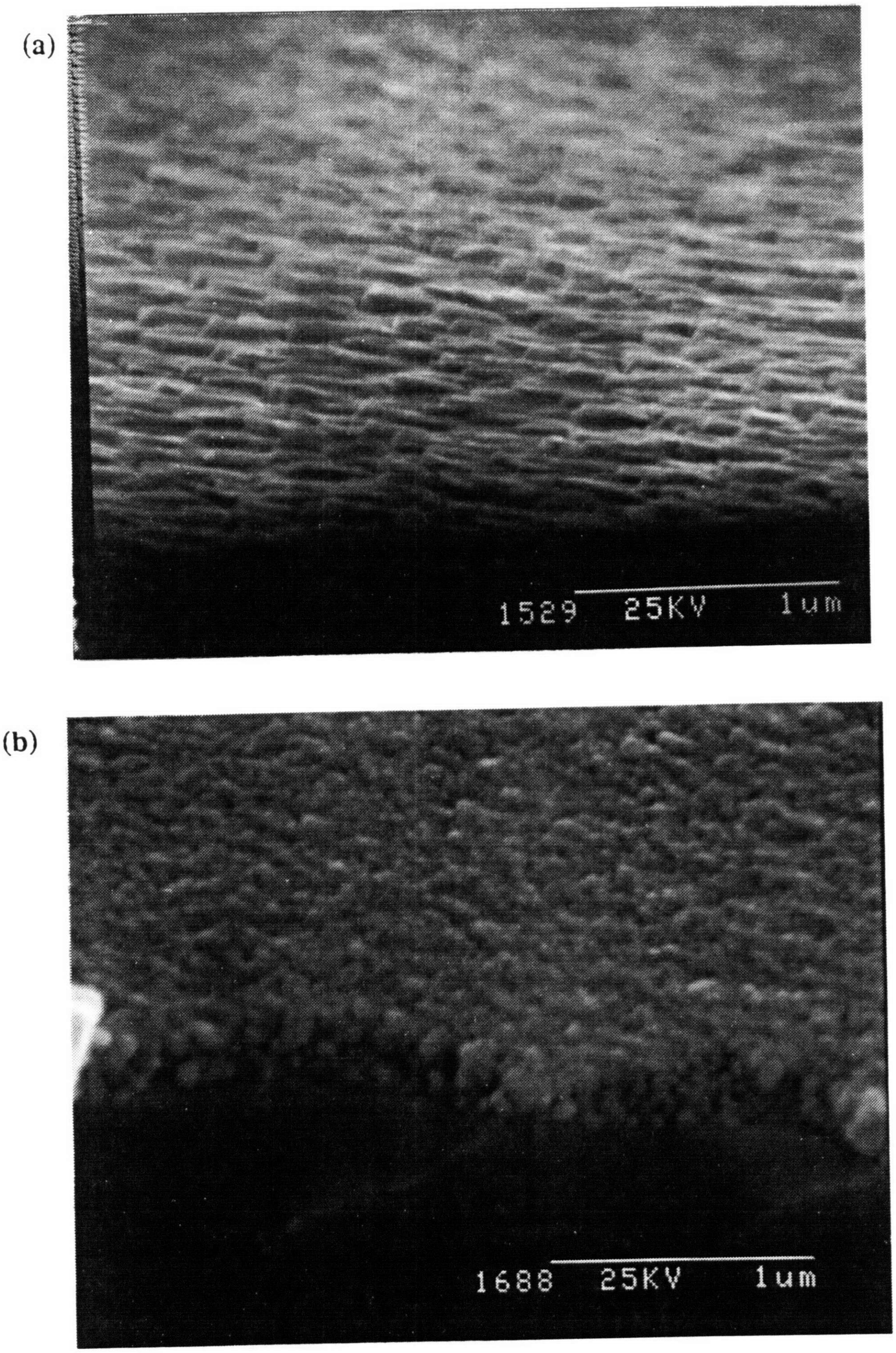

Figure 6.13 SEM micrographs of MgO sputtered on (100) $LaAlO_3$ at 500°C, 2.5 mTorr, and 20% O_2.

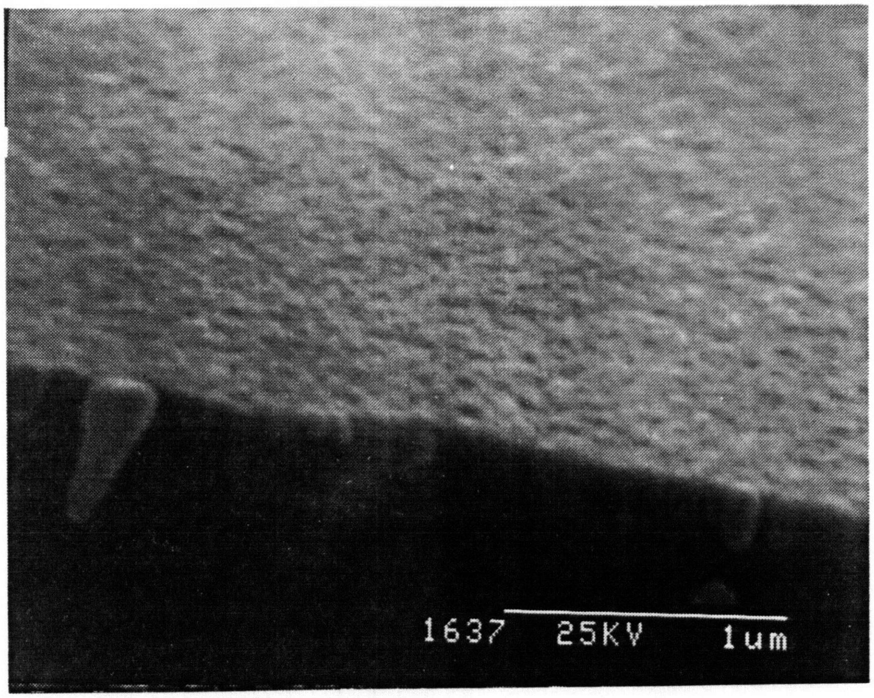

Figure 6.14 SEM micrograph of MgO sputtered on (100) $LaAlO_3$ at 700°C, 2.5 mTorr, and 20% O_2.

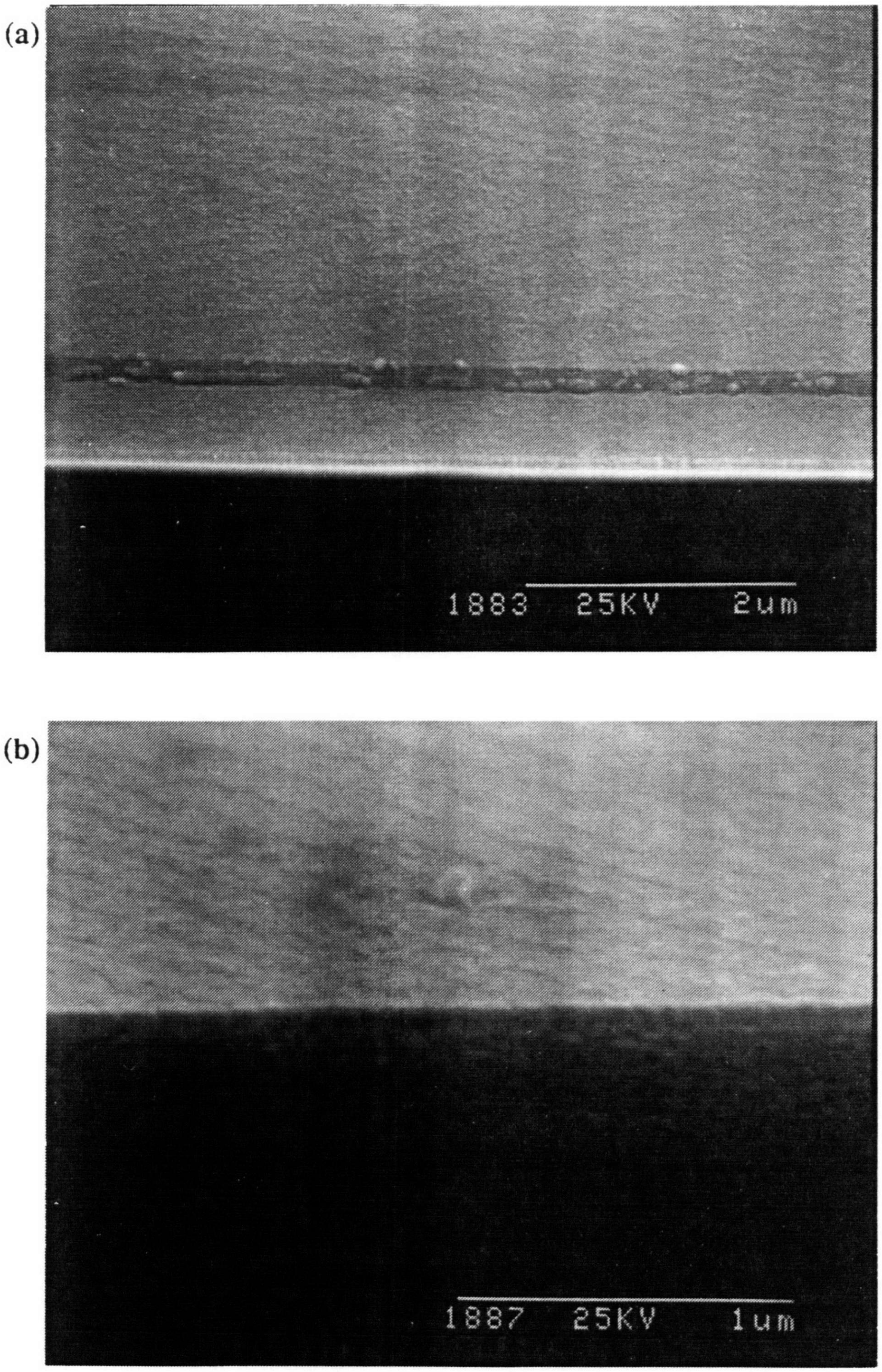

Figure 6.15 SEM micrographs of MgO sputtered to a nominal thickness of 400 Å on (100) $LaAlO_3$ at 400°C, 2.5 mTorr, and 20% O_2.

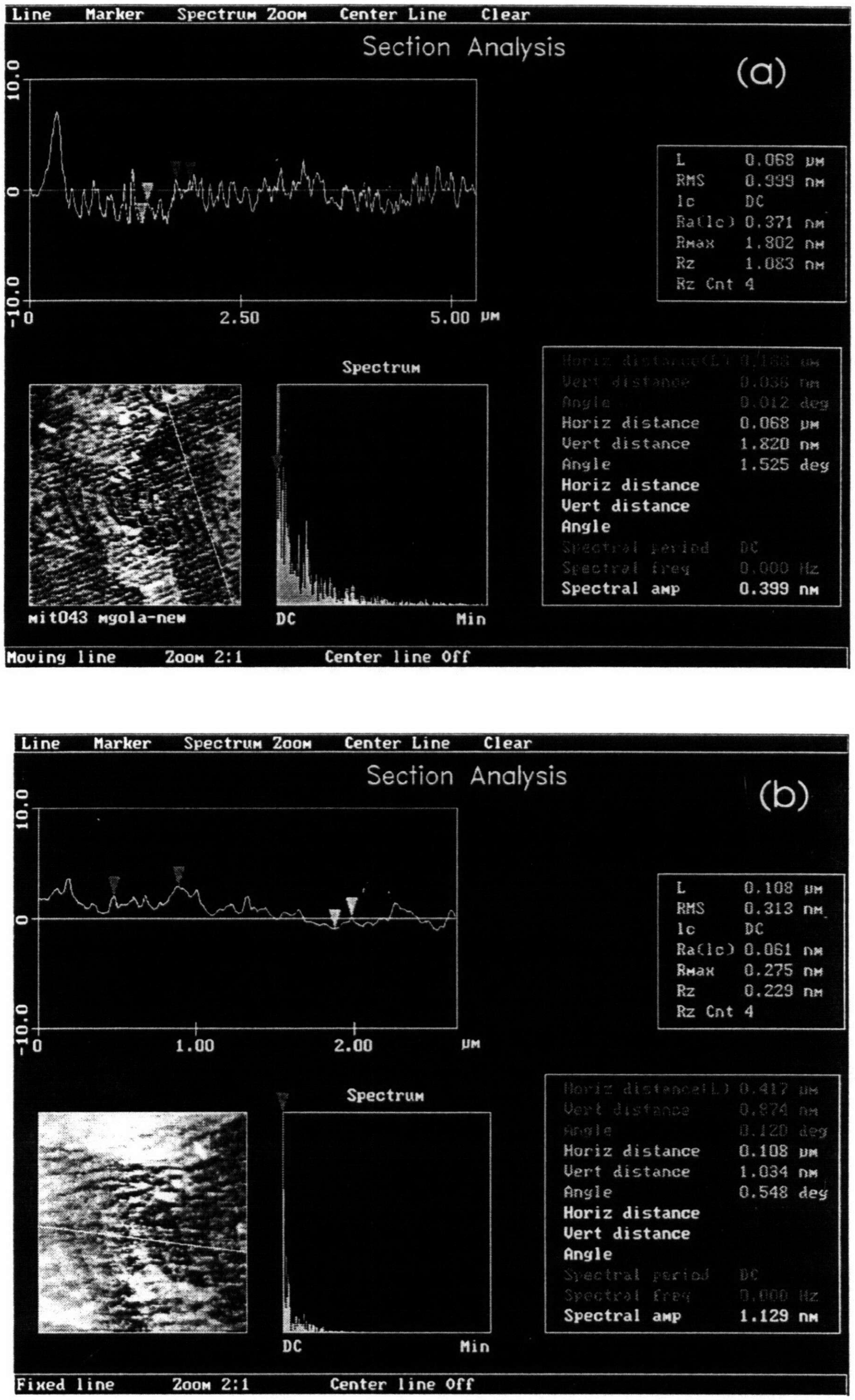

```
L         0.068 µm
RMS       0.999 nm
lc        DC
Ra(lc)    0.371 nm
Rmax      1.802 nm
Rz        1.083 nm
Rz Cnt 4
```

```
Horiz distance(L)  0.188 µm
Vert distance      0.036 nm
Angle              0.012 deg
Horiz distance     0.068 µm
Vert distance      1.820 nm
Angle              1.525 deg
Horiz distance
Vert distance
Angle
Spectral period    DC
Spectral freq      0.000 Hz
Spectral amp       0.399 nm
```

```
L         0.108 µm
RMS       0.313 nm
lc        DC
Ra(lc)    0.061 nm
Rmax      0.275 nm
Rz        0.229 nm
Rz Cnt 4
```

```
Horiz distance(L)  0.417 µm
Vert distance      0.874 nm
Angle              0.120 deg
Horiz distance     0.108 µm
Vert distance      1.034 nm
Angle              0.548 deg
Horiz distance
Vert distance
Angle
Spectral period    DC
Spectral freq      0.000 Hz
Spectral amp       1.129 nm
```

Figure 6.16 AFM micrographs of the MgO film shown in Figure 6.15 revealing features similar to those observed by SEM.

$LaAlO_3$. At 300°C, the (110) oriented film has a porous, columnar microstructure (see Figure 6.17(a)). For deposition at 500°C, the (100) oriented film has a somewhat denser and more plate-like appearance, as seen in Figure 6.17(b).

6.4.4 MgO Deposition on Treated $LaAlO_3$ Substrates

MgO was also grown at 500°C on $LaAlO_3$ substrates that had been blanket ion milled. Deposition on an unannealed milled substrate results in a largely amorphous film as shown by XRD (see Figure 6.18(a)). MgO deposited on an annealed milled substrate was slightly more crystalline with a preferred (100) orientation. The XRD trace in Figure 6.18(b), however, shows that the (200) peak is relatively weak. The microstructure of the two films are similar; both films are rough but are neither highly facetted nor highly columnar, as seen in Figures 6.19(a) and (b).

MgO was also deposited at 300°C onto a vicinally polished and annealed (100) $LaAlO_3$ substrate. AFM scans of the substrate surface prior to film deposition revealed a fairly featureless surface. XRD scans show that the MgO film is preferentially (110) oriented (see Figure 6.20). Subsequent ϕ-scans show that the film has an in-plane orientation of MgO [001] $\|$ $LaAlO_3$ [001] and MgO [110] $\|$ $LaAlO_3$ [010]. The SEM micrograph in Figure 6.21 for this sample shows a dense columnar microstructure.

6.5 DISCUSSION

6.5.1 MgO Deposition on $SrTiO_3$

MgO films grow epitaxially on (100) $SrTiO_3$ single crystal substrates when deposited above 435°C at all deposition conditions explored. The measured cube-on-cube in-plane alignment is the expected orientation based on minimum lattice misfit considerations and is consistent with observations reported in the literature.[21] Both SEM and AFM analysis confirm the microstructural quality of these films. The measured mean roughness of 0.25 nm for a film grown at 500°C is comparable to the measured roughnesses of ~0.1-0.2 nm for bare, as-received (100) $SrTiO_3$ substrates. Thus, such a

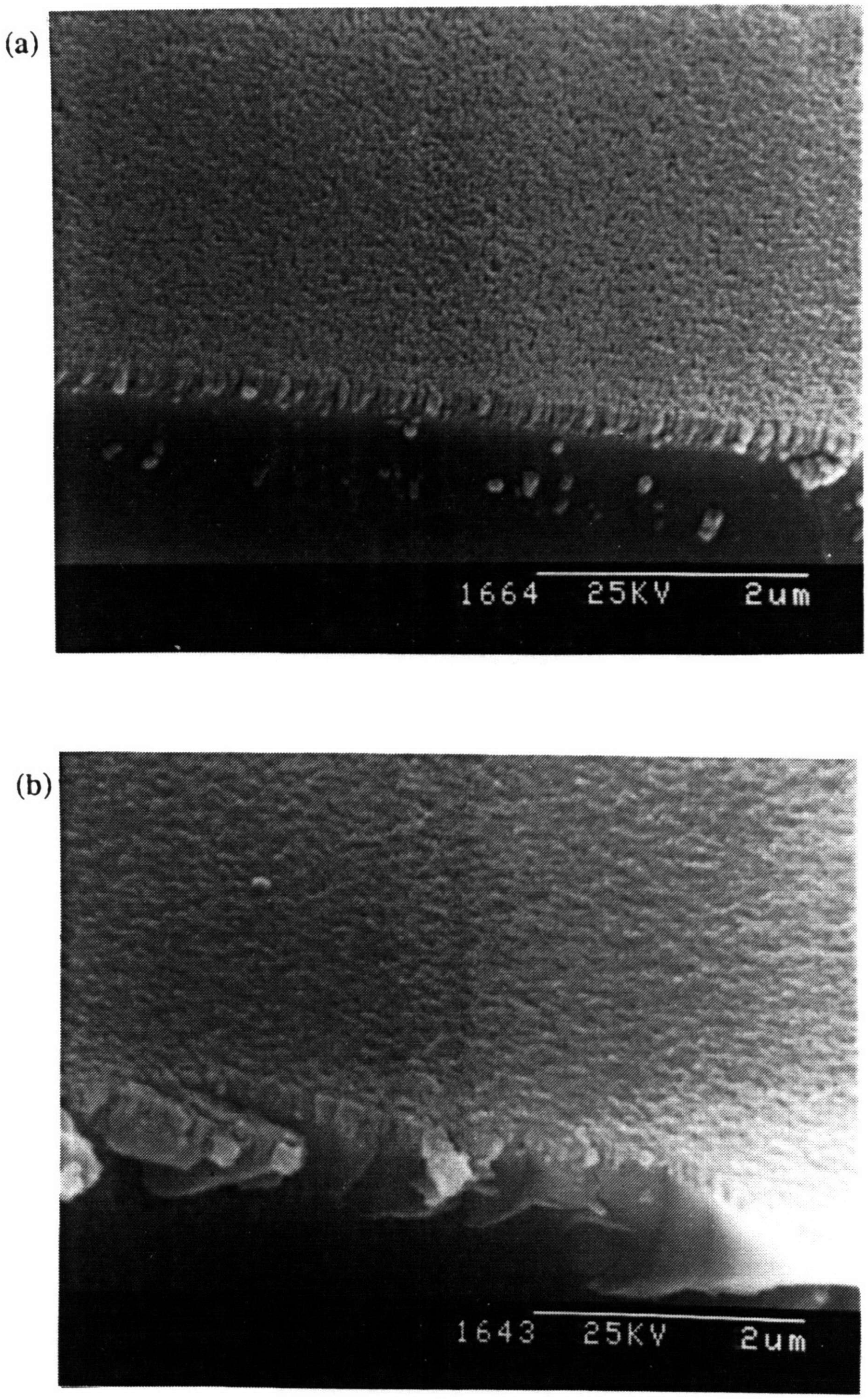

Figure 6.17 SEM micrographs of MgO films sputtered on (110) $LaAlO_3$ at 2.5 mTorr, 20% O_2, and: (a) 300°C, and (b) 500°C.

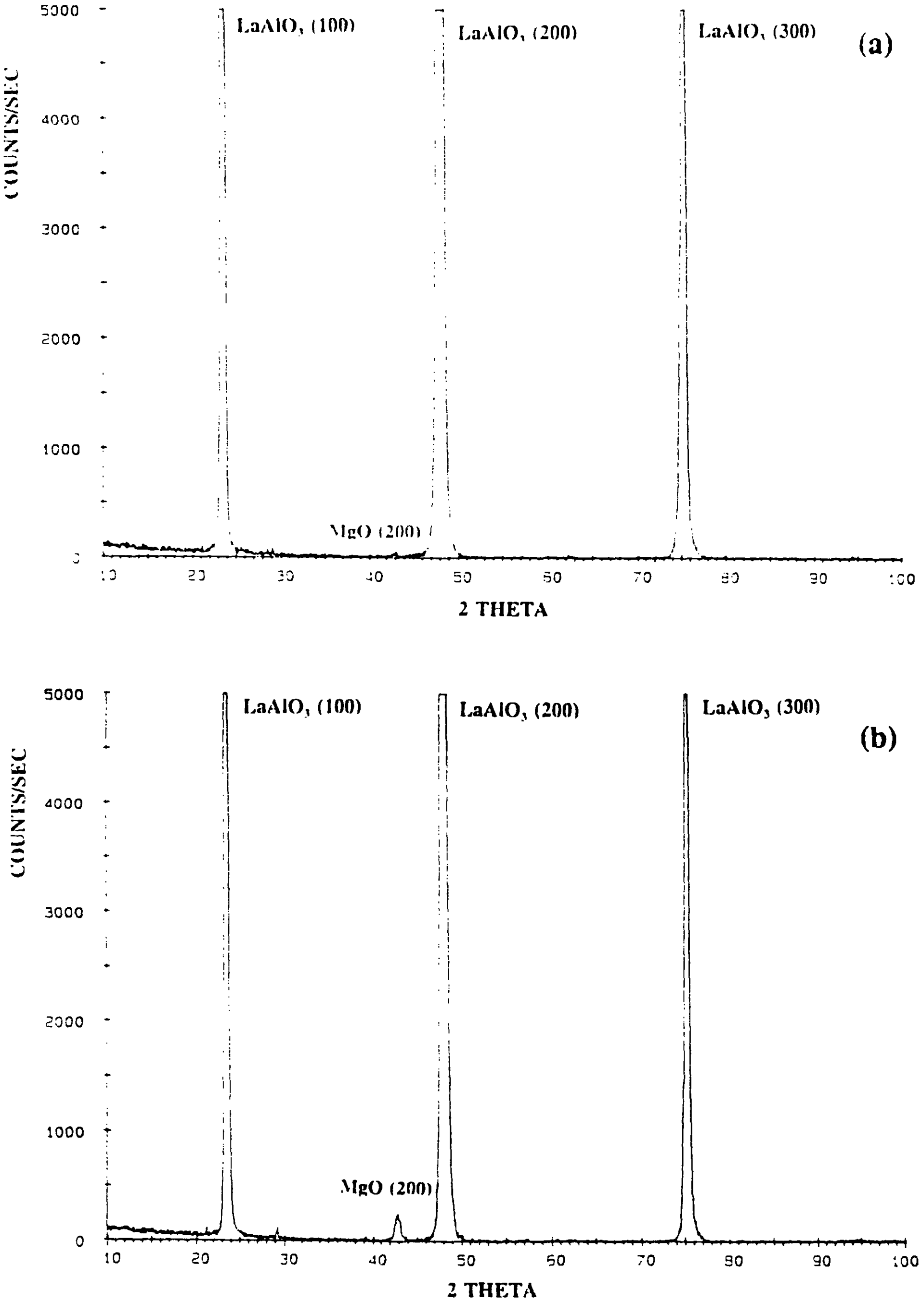

Figure 6.18 θ/2θ XRD scans for MgO sputtered at 500°C on (100) LaAlO$_3$ substrates that were: (a) ion milled for 30 minutes at 500 eV, and (b) ion milled substrates that were subsequently annealed at 950°C for 2 hours in flowing O$_2$.

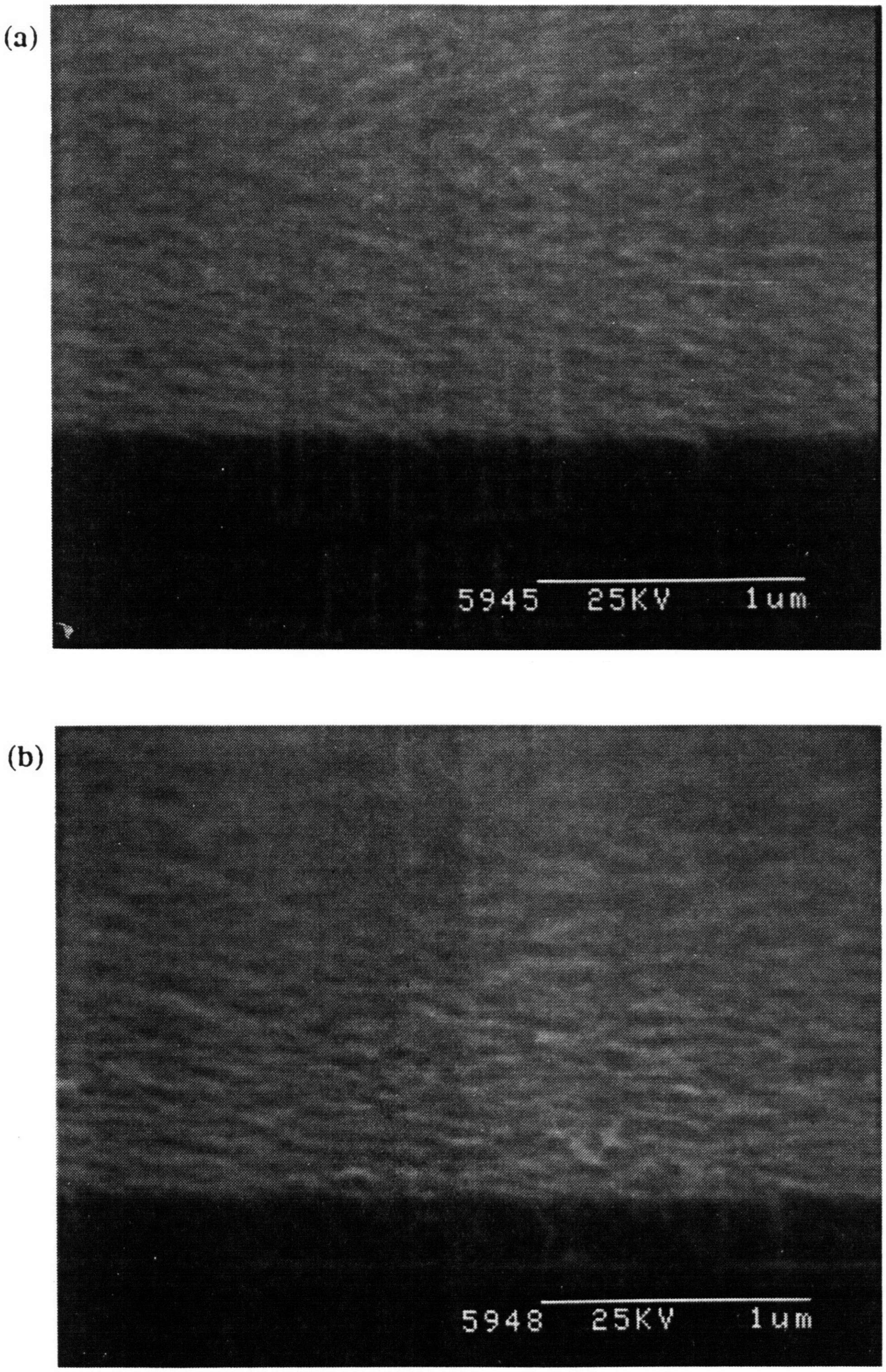

Figure 6.19 SEM micrographs of MgO films described in Figure 6.18 grown on: (a) ion milled $LaAlO_3$ substrate, and (b) annealed, ion milled $LaAlO_3$ substrate.

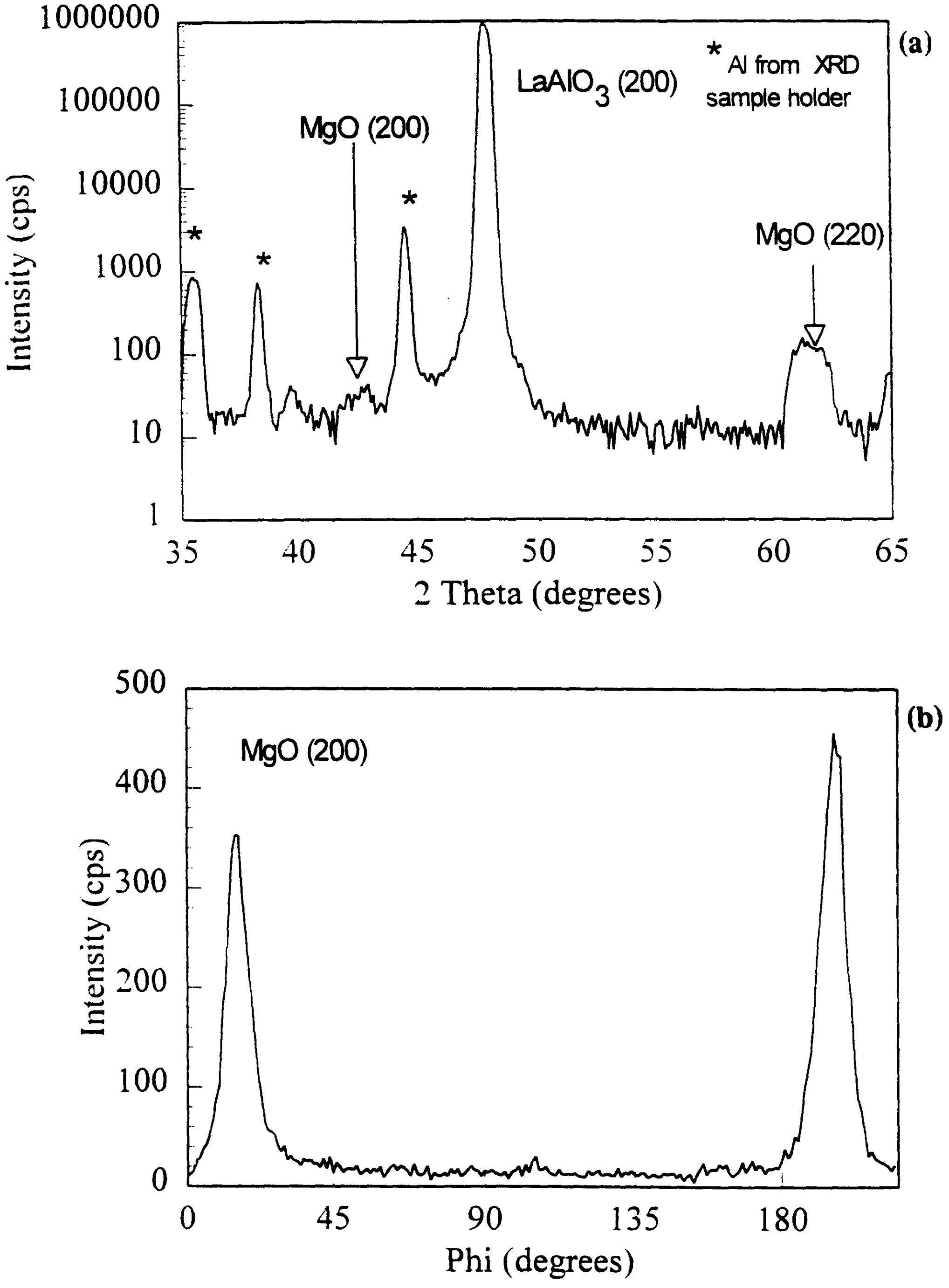

Figure 6.20 XRD scans of MgO film sputtered at 300°C on vicinally polished (100) LaAlO$_3$: (a) $\theta/2\theta$ scan, and (b) ϕ-scan of MgO (200) at χ=45°.

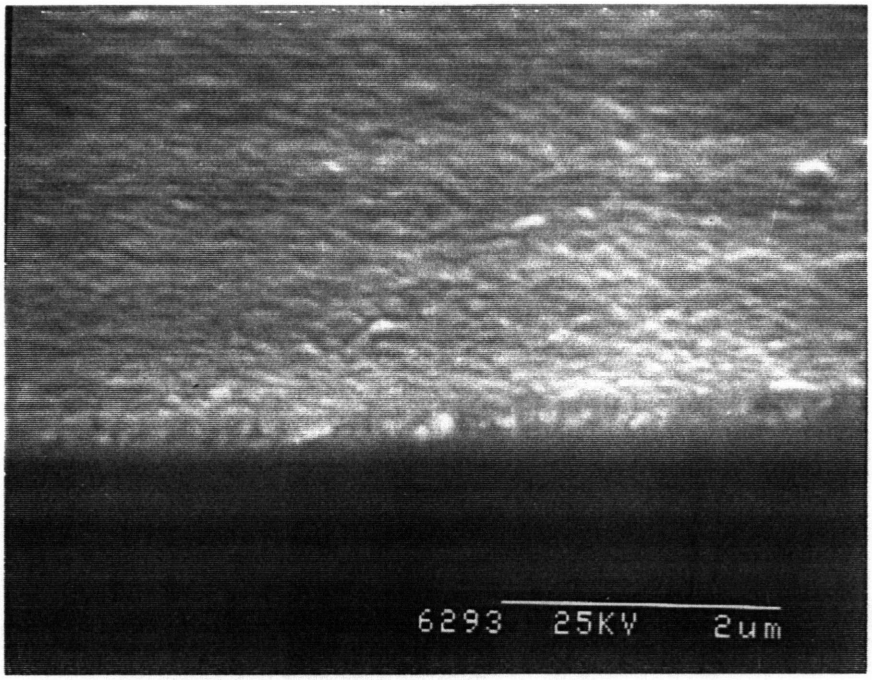

Figure 6.21 SEM micrograph of MgO film sputtered at 300°C on vicinally polished (100) $LaAlO_3$.

film should be suitable for use in epitaxial multilayer deposition.

The changes observed in MgO microstructure with decreasing deposition temperature is consistent with relative changes in MgO film nucleation and growth. Although changes in the ratio of nucleation to growth rates with temperature cannot in general be predicted a priori, the increasingly facetted appearance of the (100) MgO film with lower deposition temperature suggests a higher degree of nucleation at lower temperatures. As the deposition temperature is increased, growth is observed to become favored over nucleation. In this case, it is seen that the 7.9% lattice mismatch is low enough so that film growth is not impeded. This results in the formation of a smooth and uniform microstructure. Very little variation in the crystalline quality of these films was observed by X-ray $\theta/2\theta$ and rocking curve scans despite the observed microstructural variations.

MgO was also sputtered deposited on (110) oriented $SrTiO_3$ to further determine if the (100) orientation was truly an epitaxial one. As discussed in the introduction, the (100) orientation is expected to be naturally favored because of its low surface energy. The results obtained for (110) MgO film growth on (110) $SrTiO_3$ substrates indicate that the underlying $SrTiO_3$ substrate orientation does indeed influence the orientation of the MgO films. Four-circle diffractometry ϕ-scans show that (110) MgO films are oriented parallel to the underlying (110) $SrTiO_3$ substrate. The microstructural results for these films as revealed by SEM show the same trend that was observed for (100) MgO films.

6.5.2 MgO Deposition on $LaAlO_3$

Both the XRD and SEM results for highly oriented (100) MgO films on (100) $LaAlO_3$ are analogous to the results obtained for MgO growth on (100) $SrTiO_3$. The films are in-plane aligned in a cube-on-cube fashion with respect to the underlying substrate although the observed XRD intensities are about an order of magnitude lower and the MgO (200) rocking curves are up to ~1.5° broader. The facetted MgO microstructure is also similar to that of MgO growth on $SrTiO_3$ at deposition temperatures below 435°C, except that in the case of $LaAlO_3$, it is retained at higher deposition temperatures.

The variation in properties of MgO films deposited on $LaAlO_3$, however, indicates that an aspect of film growth related to the substrate is not being adequately controlled as seen by the XRD data presented in Table 6.3. In several instances, deposition on multiple $LaAlO_3$ substrates in the same run produced films with very different properties (i.e. one film would be strongly (100) oriented while another one would have a mixed (100)/(110) orientation). The microstructure of the films can also be related to their orientation. Highly (100) oriented films on $LaAlO_3$ have regularly shaped plate-like particles that are oriented with respect to each other which in itself suggests the presence of an in-plane orientation that is confirmed by ϕ-scan measurements. Less highly oriented (100) MgO films have a mixed facetted and columnar microstructure. Films with a mixed (100) and (110) orientation possess a columnar microstructure.

These differences are even more clearly manifested for MgO deposition on (110) oriented $LaAlO_3$ single crystal substrates. In contrast to results obtained for deposition on (110) $SrTiO_3$, MgO film orientation on $LaAlO_3$ is found to be temperature dependent. MgO deposited at 300°C is (110) oriented while MgO grown at 500°C is (100) oriented. Although both films have a single in-plane orientation that is related to the underlying substrate, it is clear that the film-substrate orientation here is different from the epitaxial relationship between MgO and $SrTiO_3$. The two different film microstructures obtained for growth on (110) $LaAlO_3$ are also consistent with observations for MgO film growth on (100) $LaAlO_3$. (100) oriented films have a facetted microstructure while (110) films are columnar.

Deposition of MgO onto modified (100) $LaAlO_3$ surfaces also results in decreased (100) film orientation. MgO deposited on both unannealed and annealed milled $LaAlO_3$ substrates are very weakly (100). Growth over vicinally polished (100) substrates yields (110) oriented MgO films instead. Clearly, modification of the $LaAlO_3$ substrate surface affects the quality of subsequently deposited MgO films.

As previously discussed in Chapter 5, $LaAlO_3$ is a perovskite-like material that is rhombohedral at room temperature and undergoes a second order phase transition somewhere between 400°C and 500°C[22] to a high temperature cubic phase. The single crystal substrates used in this study were cut from boules grown by the Czochralski method and therefore have been cooled through this phase transition which results in substantial twinning. The actual twin density varies from boule to boule, and also in substrates cut from different regions of a single boule.

AFM studies show the existence of surface steps whose height is about one unit cell spacing on bare $LaAlO_3$ substrates. This is consistent with cross-sectional TEM observations in Chapter 5 where native steps were observed in $LaAlO_3$. As mentioned previously, steps can be generated at the substrate surface during polishing due to the presence of the twins. The variation in density and character of twins present in $LaAlO_3$ substrates allows for the presence of steps that may be oriented in a number of ways on the surface. It is also possible that the nature of these steps changes as the substrate is heated during deposition runs above 400°C and goes through the phase transition. Additional steps may also arise as the substrate de-twins when heated through the transition temperature.

As shown previously in Figure 6.7(a), rows of $LaAlO_3$ surface steps with a frequency of ~6-7 per μm are observed. Examination of the SEM micrograph in Figure 6.13(a) for a (100) MgO film deposited on (100) $LaAlO_3$ at 500°C reveals a similar pitch in the terraced, facetted rows of plates, and suggests that the film is nucleating along these steps. Since the mismatch between MgO and $LaAlO_3$ is high, the presence of these steps may provide preferred nucleation sites that help to reinforce oriented growth.

The SEM and AFM micrographs is Figures 6.15 and 6.16 for films deposited to a nominal thickness of 400 Å show enhanced surface relief that appears to be a reflection of the underlying substrate surface features. The presence of parallel rows in the microstructure are clearly visible. Figure 6.16(a) also shows a change in direction of the rows that is similar to features observed on bare substrates. These results also suggest preferential nucleation of MgO at the substrate steps.

Preferential nucleation at steps is commonly observed both for oriented and non-oriented films as previously discussed in Chapter 2. In the case of oriented film growth over amorphous or non-lattice matched substrates, orientation is attributed to graphoepitaxy. However, steps have also been found to aid oriented film growth in systems where the lattice mismatch is high. Work carried out at Cornell on BYC film growth over highly stepped MgO substrates demonstrated that highly oriented c-axis BYC films could be grown despite the large lattice mismatch.

The film microstructures observed for MgO grown on $LaAlO_3$ can be classified into three types as described in Table 6.4. The first, designated as "facetted," is a highly facetted, plate-like microstructure such as that shown in Figure 6.13(a). The second type, designated as "mixed," consists of a mixture of facetted and columnar microstructures, an example of which is shown in Figure 6.13(b). The third, called "columnar," is a wholly columnar microstructure as shown in Figure 6.14.

Figure 6.22 is a graph representing the XRD data listed in Tables 6.2 and 6.3 for MgO films deposited on (100) $LaAlO_3$. The MgO (200) peak intensity for each film is plotted against the FWHM of the MgO (200) rocking curve. Each data point is represented by a letter designating the microstructure observed for that film. It is seen that films with high XRD intensity and narrow rocking curves possess the facetted microstructure, while the mixed microstructure is associated with films that possess lower intensities and broader rocking curves.

A frequency of ~6-7 rows of facets per μm similar to that in Figure 6.13(a) is observed for all the films marked "facetted" on Figure 6.22. In films with a mixed microstructure, the rows of less pronounced facets also have a similar spacing but no regularity in the arrangement of the columnar microstructure is observed.

It is seen that facetted films are obtained only when the MgO films are highly (100) oriented. In all cases, the similarity in facet row spacing with the step spacing on $LaAlO_3$ substrates suggests that the underlying substrate is influencing film growth. The facets in films with a mixed microstructure exhibit a similar spacing, which again suggests the influence of the substrate. However, the reduced facet population along with the presence of a columnar microstructure also suggests a difference in the underlying substrate surface.

If MgO is nucleating preferentially at native steps on $LaAlO_3$ substrates, then the degree of oriented growth for each film then depends entirely on the step characteristics of the underlying substrate. The presence of parallel rows of steps could nucleation and growth of MgO towards a highly oriented film. On the other hand, if fewer steps are

Table 6.4 Classification of microstructures observed for MgO films sputtered on $LaAlO_3$ substrates

Classification	Description	Example
"Facetted"	Highly facetted, plate-like microstructure	Figure 6.13(a)
"Mixed"	Mixture of facetted and columnar microstructures; facets tend to be less pronounced than those observed in "facetted" microstructure	Figure 6.13(b)
"Columnar"	Columnar microstructure	Figure 6.14

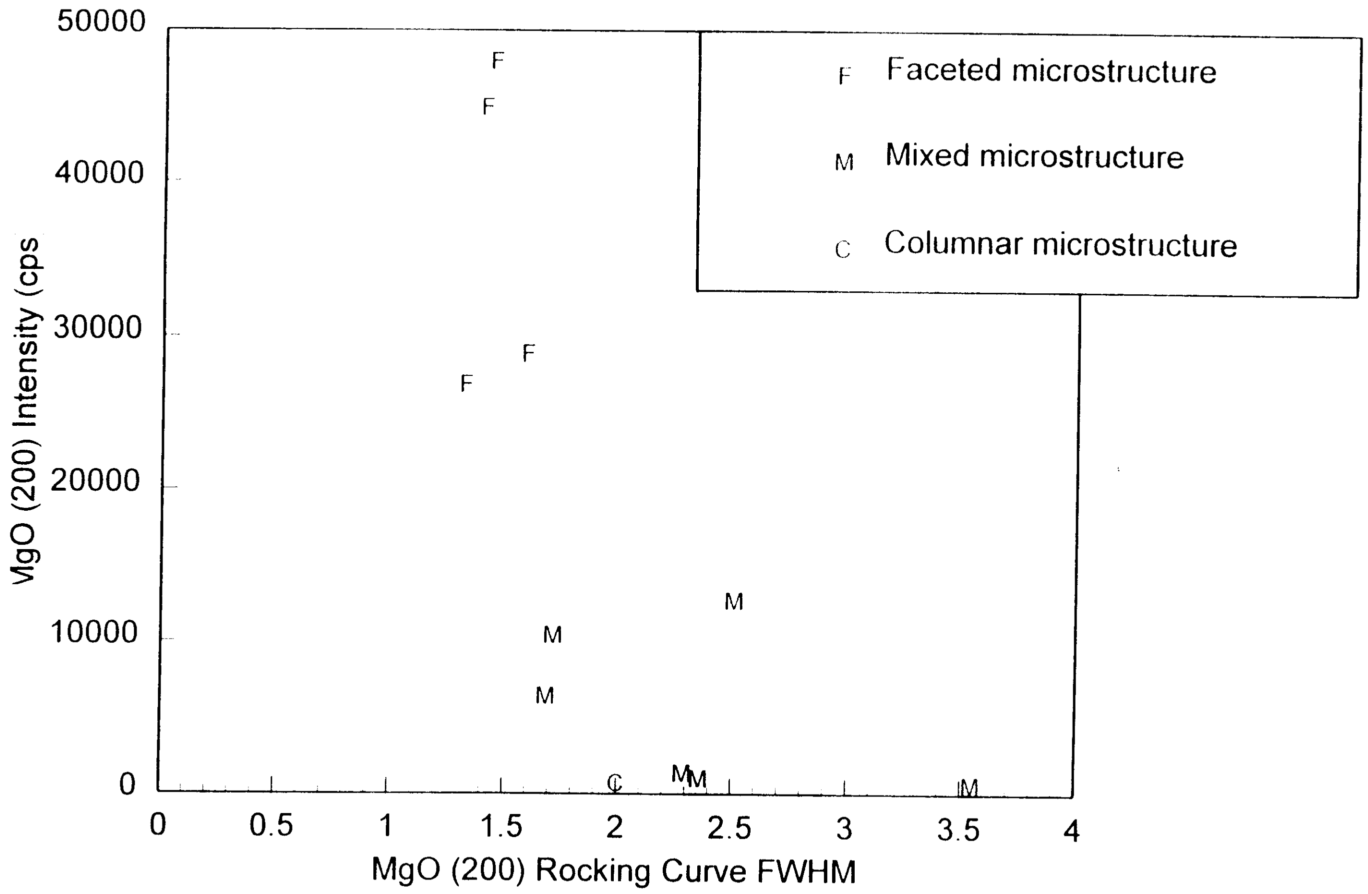

Figure 6.22 MgO (200) XRD peak intensity plotted against MgO (200) rocking curve FWHM for MgO films deposited on $LaAlO_3$ as listed in Tables 6.2 and 6.3. The microstructure observed for each film is noted.

present in the substrate, there is then a less of a driving force towards nucleation and growth of an oriented film. Thus, variations in step nature and density could account for the variation in quality of MgO films grown on $LaAlO_3$.

The results obtained for MgO deposition onto treated $LaAlO_3$ substrate surfaces are consistent with modification of surface step density. For instance, ion milling eliminates the stepped surface of the $LaAlO_3$ substrate as shown in Figure 6.8. XRD scans show that MgO grown over this surface is largely amorphous. It was seen previously in Chapter 5 that ion-milled $LaAlO_3$ surfaces could not support high quality epitaxial CeO_2 growth due to surface damage. Annealing the substrates permitted the necessary healing to take place and allowed growth of high quality epitaxial CeO_2 films to take place. In this case, however, annealing the milled substrate results in only a small improvement in MgO film crystallinity. AFM shows that annealed milled substrates are still devoid of steps. These results tend to support the fact that surface steps are needed to permit oriented film growth to take place.

MgO was also deposited on the vicinally polished and annealed $LaAlO_3$ substrate. The vicinal polishing and annealing processes were carried out in order to artificially create a highly stepped surface. AFM analysis for this substrate did not reveal the presence of significant surface features. It is probable that the 950°C annealing temperature that was used was not high enough to generate surface steps. The MgO film deposited on this substrate was the only one grown over a (100) oriented substrate to exhibit a relatively strong (110) orientation. MgO [110] is not well lattice-matched to $LaAlO_3$ <100>. Multiples of MgO [110] and $LaAlO_3$ [100] spacings, however, do result in a 4.8% mismatch, which is less than half of the mismatch between <100> directions for the two materials. Examination of the (110) and (100) planes for MgO and $LaAlO_3$, respectively, however, shows that the number of coincident atoms is low.

These observations suggest that the driving force for growth of the (100) orientation may only be slightly greater than that for (110) MgO for deposition on $LaAlO_3$. Highly oriented (100) growth appears to be aided by the presence of surface steps. These films evince strong row-like features in their microstructure that are similar to step patterns in the underlying substrate. The lattice mismatch for cube-on-cube growth may be high enough so that it can take place only in the presence of properly oriented steps. These steps act to reinforce epitaxy. The difference between MgO growth on $SrTiO_3$ and $LaAlO_3$ is most likely a function of the lattice mismatch. On $LaAlO_3$, growth at high temperatures is still impeded due to the larger mismatch and it is more favorable for an oriented film to develop via frequent nucleation events rather than extensive growth. This results in the retention of the facetted microstructure even at higher deposition temperatures.

On the other hand, the columns observed for (110) MgO films do not appear to exhibit any regularity in arrangement, which suggests that nucleation and growth of this orientation does not depend on the presence of surface steps. It also appears that for growth on (100) $LaAlO_3$, this orientation is favored at higher deposition temperatures. This is also consistent with the results for growth on (110) $LaAlO_3$ in which non-parallel film growth of obtained only at higher temperatures. This indicates that cube-on-cube type growth may not be the most energetically favored for MgO films deposited on $LaAlO_3$.

6.6 SUMMARY

It was found that two different film growth mechanisms are active in the growth of MgO on $SrTiO_3$ and $LaAlO_3$. Growth of MgO on $SrTiO_3$ is epitaxial while growth of oriented MgO on $LaAlO_3$ depends on the nature of the substrate surface and deposition conditions. The difference is attributed to the different lattice mismatches. The mismatch between MgO and $LaAlO_3$ is large enough such that cube-on-cube growth needs to take place in the presence of oriented native steps in the substrate, which bias film growth and help to reinforce epitaxy. Modification of $LaAlO_3$ surface steps was found to reduce the degree of (100) MgO film growth.

MgO films have been used successfully in the past in HTSC devices, but only in conjunction with a $SrTiO_3$ buffer layer. The presence of $SrTiO_3$ permits growth of high quality epitaxial MgO similar to the results in this study. $SrTiO_3$, however, cannot be used in many HTSC devices because of its high dielectric constant. Recent trends in HTSC device processing have been moving away from use of MgO films due to problems with maintaining the desired (100) orientation.

From this study, the implications for high quality MgO film growth directly on BYC films are not promising. BYC has a 9.2% mismatch to MgO, which falls in between that of $SrTiO_3$ and $LaAlO_3$. This mismatch may be large enough such that MgO film growth becomes exceedingly sensitive to the surface of the BYC films. Since BYC film surfaces are not as smooth as optically polished single crystal substrates, this could result in growth of misoriented MgO. In addition, it was found that even for the most highly oriented MgO films grown on $LaAlO_3$, the resulting film surfaces were quite rough. These would also not be ideal for epitaxial multilayer applications.

It may be possible to reproducibly grow higher quality MgO films on $LaAlO_3$ if a deposition method could be found which relied more on growth than nucleation. Rapid growth and fewer nucleation events could lead to few misoriented grains. This was demonstrated recently in comparing BYC film growth over step edges patterned in $LaAlO_3$ substrate by using metal-organic deposition (MOD) and pulsed laser deposition (PLD). The higher ratio of growth to nucleation rates in MOD processing led to the formation of a single a-axis grain over each step edge, while the higher nucleation rate in PLD resulted in a mixture of numerous smaller a- and c-axis domains over the step edge. A similar film fabrication process might prove promising for MgO film growth.

CHAPTER 7

CONCLUSIONS AND FUTURE WORK

7.1 CONCLUSIONS

The goal of this thesis research was to investigate methods for growing high quality epitaxial, planar, dielectric thin films for multilayer HTSC device applications. Both epitaxial planarization processing and epitaxial film growth were examined in the context of HTSC devices. It was found that the presence of surface relief, such as that generated by device fabrication, as well as the existence of microsteps, both within patterned features and in the form of native steps in the substrate, affected epitaxial film growth and epitaxial planarization. The specific conclusions drawn from this research are as follows:

(1) Homoepitaxial planarization using normal incidence ion beam assisted deposition of YSZ films over patterned YSZ substrates was successfully demonstrated. IBAD conditions were found in which epitaxial growth of YSZ was maintained. The planarization mechanism relied on the variation of film etch rate with ion incidence angle and involved formation of angled surfaces over patterned features that became buried by the faster net film growth that took place over planar regions. This is similar to the model proposed by C.Y. Ting *et al.*[14] for amorphous SiO_2 films. Redeposition of sputtered film during the planarization process, however, retarded the rate of planarization and led to the formation of low angle gently undulating surfaces.

(2) Epitaxial BYC films were successfully deposited using pulsed laser deposition over

IBAD-planarized YSZ surfaces. $T_c(0)$ values above 85K and J_c values of up to 7×10^5 A/cm^2 were measured for these films. SEM analysis showed these films to be continuous. In contrast, BYC deposited over unplanarized surfaces did not become superconducting for measurements down to 25K and exhibited poor step coverage.

(3) Heteroepitaxial growth of normal incidence IBAD CeO_2 over $LaAlO_3$ substrates was successful when an initial seed layer of high quality epitaxial CeO_2 was first evaporated onto the substrate. This essentially allowed homoepitaxial CeO_2 film growth to take place. A trend towards planarization was observed for IBAD CeO_2 deposition over patterned $LaAlO_3$ substrates. However preferential growth of polycrystalline CeO_2 over underlying patterned step edges inhibited the planarization process by preventing the ion beam from reaching the epitaxial CeO_2 angled surfaces. This was a direct result of the large lattice mismatch that existed between (001) CeO_2 and (001) $LaAlO_3$ in the [001] direction. Although epitaxy between the two materials was maintained in the evaporated seed layer, the mismatch led to the formation of tilt boundaries over substrate native steps and a complete loss of coherency over the patterned substrate step edges which themselves were composed of microsteps. These defects apparently acted as preferential nucleation sites for the polycrystalline phase.

(4) A different planarization mechanism was found to be operative for off-normal IBAD planarization of CeO_2 over patterned $LaAlO_3$. At an ion incidence angle of 45°, a mechanism of forward sputtering and redeposition permitted patterned surface features oriented orthogonally to the ion beam to be planarized. (001) out-of-plane texture was maintained for the CeO_2 film, but two in-plane orientations were detected in all films. In all cases, the dominant one was the epitaxial orientation for CeO_2 grown on $LaAlO_3$. A second orientation was aligned with the direction of the ion beam and is similar to the biaxial film orientation that is obtained when using IBAD to deposit films over amorphous substrates.

(5) MgO films deposited on $SrTiO_3$ and $LaAlO_3$ single crystal substrates using off-axis

rf magnetron sputtering were found to grow via two different mechanisms. At temperatures above 435°C, MgO was found to grow epitaxially on both (100) and (110) $SrTiO_3$. On (100) $LaAlO_3$, however, a large variation in MgO orientation was observed which was related to the density and character of native steps present in the substrate. The presence of the steps appeared to act as preferential nucleation sites and may have served to reinforce oriented growth. Removal of the steps through ion milling resulted in subsequent growth of weakly oriented MgO films.

7.2 IMPLICATIONS

(1) The results from the IBAD YSZ study demonstrate the feasibility of epitaxial planarization technology. Epitaxial planarization is vital, not only for HTSC device applications, but for the fabrication of any multilayer epitaxial device structure. It is important to note that the IBAD planarization process is a general one which has the potential to be extended to any material. This is in contrast to epitaxial planarization processes being studied for compound semiconductors which involve phenomena such as selective regrowth and are, therefore, highly materials dependent.

(2) The results from the CeO_2-$LaAlO_3$ heteroepitaxial planarization study point out the importance of lattice matching. For actual device applications, materials need to be lattice matched in all three dimensions rather than only in the plane of the film as is commonly considered. Patterning films into device structures introduces a new constraint in lattice matching conditions.

(3) The presence of microsteps on the order of unit cell spacings can have a significant effect on epitaxial development as seen in both the CeO_2-$LaAlO_3$ and MgO-$LaAlO_3$ studies. Poor lattice matching in the former case led to the formation of crystallographic defects over native substrate surface steps. In the latter case, the presence of properly oriented steps appeared to aid in overcoming the large lattice

mismatch and reinforce oriented growth. Therefore it is seen that steps on the order of unit cell spacings can have both beneficial and detrimental effects to epitaxial film development.

The results from this research also demonstrate the differences between studying a model system and actual technological applications of the results from such a study. The IBAD YSZ planarization study showed that epitaxial planarization is a feasible process. However, application of the process to a heteroepitaxial system of the type that might be found in working devices showed how departures from model systems can lead to additional complications. In this case, the additional constraint of three-dimensional lattice matching for heteroepitaxial planarization processing was highlighted.

7.3 SUGGESTIONS FOR FUTURE WORK

Several of the issues raised in the course of this thesis research warrant continued investigation. IBAD has been found to an effective method of planarizing films. It was shown, however, that knowledge of both the etching and growth behavior of the IBAD films with respect to the angle of incidence was needed in order to more accurately predict and understand the topographical evolution that took place during planarization processing. Detailed determination of the etch rate vs. angle curve for IBAD YSZ would therefore be beneficial to establishing optimal processing parameters for planarization.

The results from the IBAD YSZ study show that a slight degree of disorder is being introduced into the epitaxial YSZ films. This is most likely a consequence of ion bombardment. Although subsequently deposited BYC films were shown to posses good electrical characteristics, the small degree of crystallographic disorder present in the underlying YSZ film was also reflected in the BYC films. It is possible that cumulative disorder in the course of IBAD processing of multiple dielectric layers in a single device can occur. Thus BYC films deposited at a later point in the fabrication process may be more crystallographically disordered than films deposited at an earlier point. It may be possible to reduce or minimize this disorder by reducing the ion beam energies used. Examination of the ion beam energies and fluences used in planarization should be undertaken to ascertain if it is possible to achieve planarization at lower energies without reducing processing efficiency.

Film misorientation associated with the patterned step edges was also detected in a few of the samples in the YSZ homoepitaxial planarization study. Since lattice mismatch is not present in this system, it should be determined how the presence of macrosteps themselves can affect epitaxial growth. The fact that the anomalous rocking curves were observed for only some samples suggest that the IBAD processing conditions used may also play a role. Cross-sectional TEM analysis of these samples may be needed to understand the origin of this misorientation.

The effect of a large lattice mismatch was found to have negative consequences for heteroepitaxial planarization efforts in planarizing patterned $LaAlO_3$ substrates with CeO_2 films. To aid in further understanding the role of lattice mismatch, heteroepitaxial planarization of two materials that exhibit cube-on-cube growth, such as CeO_2-YSZ, should be studied. Such a system possesses identical lattice mismatches in all three dimensions and would therefore also be representative of an actual device situation. It can then be seen whether or not a smaller lattice mismatch can be tolerated in heteroepitaxial planarization processing.

As was discussed in Chapter 5, it may also be possible to overcome the problems presented by the large CeO_2-$LaAlO_3$ mismatch which would be beneficial from a technological point of view. Alternative processing methods that could avoid or suppress growth of the polycrystalline phase should be examined. These include two-part deposition-etching processes and use of a deposition method other than e-beam evaporation. It may also be possible to adjust IBAD conditions, e.g. relative rates of deposition versus etching, so that growth of the epitaxial phase is favored over the polycrystalline phase.

The presence of native steps in $LaAlO_3$ substrates were found to introduce an uncontrolled variable in studying oriented MgO film growth. In the work presented in this thesis, the steps appeared to act as preferred nucleation sites. However, the variation in character and density of native substrate steps did not allow a controlled study to be carried out. It would therefore be of interest to pursue studies in which substrate steps could be introduced in a controlled manner. Use of vicinally polished substrates is one potentially useful method in which the effect of both the orientation and height of substrate steps could then be examined. The use of more than one type of substrate material could also provide insight into the relative effect of substrate steps on oriented film growth in systems with different lattice mismatches.

It is also possible certain film deposition methods are more sensitive to the presence of these steps than others. Use of a film deposition method that favors a higher rate of growth than nucleation may prevent growth of unoriented MgO. More reproducible results might be obtained if nucleation could occur preferentially at the steps followed by rapid film growth. Investigation of an *ex situ* chemical method such as metal-organic deposition may allow such a process to take place.

BIBLIOGRAPHY

1. B. Oh, R.H. Koch, W.J. Gallagher, R.P. Robertazzi, and W. Eidelloth, Appl. Phys. Lett. **59**, 123 (1991).

2. A.H. Miklich, J.J. Kingston, F.C. Wellstood, J. Clarke, M.S. Colclough, K. Char, and G. Zaharchuk, Appl. Phys. Lett. **59**, 988 (1991).

3. F.C. Wellstood, J.J. Kingston, and J. Clarke, J. Appl. Phys. **75**, 683 (1994).

4. R.H. Ono, MRS Bull. **17** [8], 34 (1992).

5. C.L. Jia, B. Kabius, K. Urban, K. Herrman, G.J. Cui, J. Schubert, W. Zander, A.I. Braginski, and C. Heiden, Physica C **175**, 545 (1991).

6. C.L. Jia, B. Kabius, K. Urban, K. Herrmann, J. Schubert, W. Zander, and A.I Braginski, Physica C **196**, 211 (1992).

7. D. Dimos, P. Chaudhari, and J. Mannhart, Phys. Rev. B **41**, 4038 (1990).

8. M.J. Cima, private communication.

9. R.R. Tummala, R.W. Keyes, W.D. Grobman, and S. Kapur, in Microelectronics Packaging Handbook, edited by R.R. Tummala and E.J. Rymaszewski (Van Nostrand Reinhold, New York, 1989).

10. P.C. McIntyre, Sc.D. Thesis (Department of Materials Science and Engineering, M.I.T., 1993).

11. T.H. Geballe, Mater. Res. Soc. Symp. Proc. **341**, 3 (1994).

12. H.P. Bader and M.A. Lardon, J. Vac. Sci. Technol. A **3**, 2167 (1985).

13. Y. Homma and S. Tsunekawa, J. Electrochem. Soc. **132**, 1466 (1985).

14. C.Y. Ting, V.J. Vivalda, and H.G. Schaefer, J. Vac. Sci. Technol. **15**, 1105 (1978).

15. C.H. Ting and A.J. Neureuther, Solid State Technol. **25** 115 (1982).

16. S.K. Ghandi, VLSI Fabrication Principles (John Wiley and Sons, New York, 1983), pp. 582-585.

17. e.g. N. Misawa, T. Ohba, and H. Yagi, MRS Bull. **19** [8], 63 (1994).

18. e.g. M. Gailhanou, C. Labourie, J.L. Lievin, A. Perales, M. Lambert, F. Poingt, and D. Sigogne, Appl. Phys. Lett. **58**, 796 (1991); A. Tate, Y. Ohmori, and M. Kobayashi, J. Crystal Growth **89**, 360 (1988); F.S. Turco, S. Simhony, K. Kash, D.M. Hwang, R.S.

Ravi, E. Kapon, and M.C. Tamargo, J. Crystal Growth **104**, 766 (1990).

19. E.A. Giess, R.L. Sandstrom, W.J. Gallagher, A. Gupta, S.L. Shinde, R.F. Cook, E.I. Cooper, E.J.M. O'Sullivan, J.M. Roldan, A.P. Segmuller, and J. Angilello, IBM J. Res. Develop. **34**, 916 (1990).

20. T. Inoue, Y. Yamamoto, S. Koyama, S. Suzuki, and Y. Ueda, Appl. Phys. Lett. **56**, 1332 (1990).

21. X.D. Wu, L. Luo, R.E. Muenchausen, K.N. Springer, and S. Foltyn, Appl. Phys. Lett. **60**, 1381 (1992).

22. G.W. Berkstresser, A.J. Valentino, and C.D. Brandle, J. Crystal Growth **109**, 467 (1991).

23. G. Koren, A. Gupta, E.A. Giess, A. Segmuller, and R.B. Laibowitz, Appl. Phys. Lett. **54**, 1054 (1989).

24. J.M. Phillips, M.P. Siegal, C.L. Perry, and J.H. Marshall, IEEE Trans. Magn. **27**, 1006 (1991).

25. M.J. Cima, J.S. Schneider, S.C. Peterson, and W. Coblenz, Appl. Phys. Lett. **53**, 710 (1988).

26. X.D. Wu, R.C. Dye, R.E. Muenchausen, S.R. Foltyn, M. Maley, A.D. Rollett, A.R. Garcia, and N.S. Nogar, Appl. Phys. Lett. **58**, 2165 (1991).

27. L.P. Lee, K. Char, M.S. Colclough, and G. Zaharchuk, Appl. Phys. Lett. **59**, 3051 (1991).

28. M.J. Burns, K. Char, B.F. Cole, W.S. Ruby, and S.A. Sachtjen, Appl. Phys. Lett. **62**, 1435 (1993).

29. L.A. Tietz, C.B. Carter, D.K. Lathrop, S.E. Russek, R.A. Buhrman, and J.R. Michael, J. Mater. Res. **4**, 1072 (1989).

30. S.-T. Lee, S. Chen, L.S. Hung, and G. Braunstein, Appl. Phys. Lett. **55**, 286 (1989).

31. R. Ramesh, D.M. Hwang, J.B. Barner, L. Nazar, T.S. Ravi, A. Inam, B. Dutta, X.D. Wu, and T. Venkatesan, J. Mater. Res. **5**, 704 (1990).

32. R. Ramesh, D.M. Hwang, T.S. Ravi, A. Inam, J.B. Barner, L. Nazar, C.Y. Chen, B. Dutta, and T. Venkatesan, Appl. Phys. Lett. **56**, 2243 (1990).

33. D.M. Hwang, T.S. Ravi, R. Ramesh, S.-W. Chan, C.Y. Chen, L. Nazar, X.D. Wu, A. Inam, and T. Venkatesan, Appl. Phys. Lett. **57**, 1690 (1990).

34. M.G. Norton, S.R. Summerfelt, and C.B. Carter, Appl. Phys. Lett. **56**, 2246 (1990).

35. B.H. Moeckly, S.E. Russek, D.K. Lathrop, R.A. Buhrman, J. Li, and J.W. Mayer, Appl. Phys. Lett. **57**, 1687 (1990).

36. B.H. Moeckly, S.E. Russek, D.K. Lathrop, R.A. Buhrman, M.G. Norton, and C.B. Carter, Appl. Phys. Lett. **57**, 2951 (1990).

37. B.H. Moeckly, D.K. Lathrop, S.E. Russek, R.A. Buhrman, M.G. Norton, and C.B. Carter, IEEE Trans. Magn. **27**, 1017 (1991).

38. M.G. Norton and C.B. Carter, J. Crystal Growth **110**, 641 (1991).

39. M.G. Norton, B.H. Moeckly, C.B. Carter, and R.A. Buhrman, J. Crystal Growth **114**, 258 (1991).

40. M.G. Norton and C.B. Carter, Scanning Microscopy **6**, 385 (1992).

41. S.K. Streiffer, B.M. Lairson, and J.C. Bravman, Appl. Phys. Lett. **57**, 2501 (1990).

42. D.K. Fork and G.B. Anderson, Appl. Phys. Lett. **63**, 1029 (1993).

43. A.F. Chow, S.H. Rou, D.J. Lichtenwalner, O. Auciello, and A.I. Kingon, Mater. Res. Soc. Symp. Proc. **268**, 253 (1992).

44. A. Shoji, M. Aoyagi, S. Kosaka, F. Shinoki, and H. Hayakawa, Appl. Phys. Lett. **46**, 1098 (1985).

45. S. Baba, S. Kinbara, T. Kajiwara, and K. Watanabe, Thin Solid Films **164**,169 (1988).

46. T. Ishiguro, K. Matsushima, and K. Masasaki, J. Appl. Phys. **73**, 1151 (1993).

47. M. Tonuchi, Y. Sakaguchi, and T. Kobayashi, J. Appl. Phys. **62**, 961 (1987).

48. S. Thakoor, H.G. Leduc, J.A. Stern, A.P. Thakoor, and S.K. Khanna, J. Vac. Sci. Technol. A **5**, 1721 (1987).

49. T. Inoue, T. Ohsuna, L. Luo, X.D. Wu, C.J. Maggiore, Y. Yamamoto, Y. Sakurai, and J.H. Chang, Appl. Phys. Lett. **59**, 3604 (1993).

50. D.K. Fork, S.M. Garrison, M. Hawley, and T.H. Geballe, J. Mater. Res. **7**, 1641 (1992).

51. S.M. Garrison, N. Newman, B.F. Cole, K. Char, and R.W. Barton, Appl. Phys. Lett. **58**, 2168 (1991).

52. D.K. Fork, D.B. Fenner, G.A.N. Connell, J.M. Phillips, and T.H. Geballe, Appl. Phys. Lett. **57**, 1137 (1990).

53. D.K. Fork, D.B. Fenner, R.W. Barton, J.M. Phillips, G.A.N. Connell, J.B. Boyce, and

T.H. Geballe, Appl. Phys. Lett. **57**, 1161 (1990).

54. D.K. Fork, F.A. Ponce, J.C. Tramontana, and T.H. Geballe, Appl. Phys. Lett. **58**, 2294 (1991).

55. K. Char, M.S. Colclough, S.M. Garrison, N. Newman, and G. Zaharchuk, Appl. Phys. Lett. **59**, 733 (1991).

56. K. Char, M.S. Colclough, L.P. Lee, and G. Zaharchuk, Appl. Phys. Lett. **59**, 2177 (1991).

57. J. Clarke, Sci. Am. August, 46 (1994).

58. J.L. Vossen, J. Vac. Sci. Techno. **11**, 875 (1974).

59. G. Wehner, J. Appl. Phys. **30** 1762 (1971).

60. H. Tsuge and S. Esho, J. Appl. Phys. **52**, 4391 (1981).

61. T.N. Kennedy, J. Vac. Sci. Technol. **13**, 1135 (1976).

62. D.W. Pashley, in Epitaxial Growth, Part A, edited by J.W. Matthews (Academic Press, New York, 1975), p. 1-27.

63. L. Royer, Bull. Soc. Fr. Mineral. Crist. **51**, 7 (1928).

64. P.S. Peercy, E.G. Bauer, B.W. Dodson, E.J. Ehrlich, L.C. Feldman, C.P. Flynn, M.W. Geis, J.P. Harbison, R.J. Matyi, P.M. Petroff, J.M. Phillips, G.B. Stringfellow, and A. Zangwill, J. Mater. Res. **5**, 852 (1990).

65. K.N. Tu, J.W. Mayer, and L.C. Feldman, Electronic Thin Film Science (Macmillan Publishing Co., New York, 1992) pp. 157-167.

66. E. Bauer, Z. Kristallogr. **110**, 372 (1958).

67. M.H. Grabow and G.H. Gilmer, Surface Sci. **194**, 333 (1988).

68. R. Bruinsma and A. Zangwill, Europhys. Lett. **4**, 729 (1987).

69. H.I. Smith, M.W. Geis, C.V. Thompson, and H.A. Atwater, J. Crystal Growth **63**, 527 (1983).

70. E.I. Givargizov, Oriented Crystallization on Amorphous Substrates (Plenum Press, New York, 1991).

71. H.I. Smith and D.C. Flanders, Appl. Phys. Lett. **32**, 349 (1978).

72. D.C. Flanders, D.C. Shaver, and H.I. Smith, Appl. Phys. Lett. **32**, 597 (1978).

73. T. Osaka and Y. Kasukabe, J. Crystal Growth **73**, 10 (1985).

74. T. Yonehara, H.I. Smith, C.V. Thompson, and J.E. Palmer **45**, 631 (1984).

75. C.V. Thompson and H.I. Smith, Appl. Phys. Lett. **44**, 63 (1984).

76. G.A. Bassett, Phil. Mag. **3**, 1042 (1958).

77. T. Osaka, T. Kawana, T. Nojima, and K. Heinemann, J. Crystal Growth **61**, 509 (1983).

78. T. Osaka, Y. Kasukabe, and H. Nakamura, **69**, 149 (1984).

79. P.W. Tasker and D.M. Duffy, Surface Sci. **137**, 91 (1984).

80. Ceres Corp., Billerica, MA.

81. Applied Technology Enterprises, Irmo SC.

82. Commercial Crystal Laboratories, Inc., Naples, FL.

83. South Bay Technology, Inc., San Clemente, CA.

84. Kimberly-Clark Corp., Roswell, GA.

85. A.C. Westerheim Ph.D. Thesis (Department of Materials Science and Engineering, M.I. T., 1992), pp. 159-160.

87. SPI Supplies, West Chester, PA.

87. Shipley Co., Marlborough, MA.

88. Headway Research Inc., Garland, TX.

89. Karl Suss, Waterbury Center, VT.

90. CD30 photoresist developer; Shipley Co., Marlborough, MA.

91. Oxford Plasma Technology, U.K.

92. Wakefield Engineering Inc., Wakefield, MA.

93. J.J. McNally, in Handbook of Plasma Processing Technology, edited by S.M. Rossnagel, J.. Cuomo, and W.D. Westbook (Noyes Publications, Park Ridge, NJ, 1990), p. 473-476.

94. S. Zhu, D.H. Lowndes, J.D. Budai, and D.P. Norton, Appl. Phys. Lett. **65**, 2012 (1994).

95. P.J. Martin and R.P. Netterfield, in Handbook of Ion Beam Processing Technology, edited

by J.J. Cuomo, S.M. Rossnagel, and H.R. Kaufman (Noyes Publications, Park Ridge, NJ 1989), p. 373.

96. N. Sonnenberg, A.S. Longo, M.J. Cima, B.P. Chang, K.G. Ressler, P.C. McIntyre, and Y.P. Liu, J. Appl. Phys. **74**, 1027 (1993).

97. K.G. Ressler, N. Sonnenberg, and M.J. Cima, Mater. Res. Soc. Symp. Proc. **316**, 953 (1993).

98. N. Sonnenberg, K.G. Ressler, P.C. McIntyre, and M.J. Cima, Mater. Res. Soc. Symp. Proc. **341**, 183 (1994).

99. K.G. Ressler, N. Sonnenberg, P.C. McIntyre, and M.J. Cima, presented at High-T_c Superconductivity - Materials and Applications, MRS Fall Meeting, 1994.

100. Y. Iijima, N. Tanaba, and O. Kohno, 4th International Symposium on Superconductivity, Oct. 14-17, 1991 Tokyo, Japan.

101. L.S. Yu, J.M.E. Harper, J.J. Cuomo, and D.A. Smith, Appl. Phys. Lett. **47**, 932 (1985).

102. Temescal, Berkeley, CA.

103. Ion Tech, Inc., Ft. Collins, CO.

104. Sycon Instruments, Syracuse, NY.

105. Union Carbide, Advanced Ceramics, Cleveland, OH.

106. Omega Engineering, Inc., Stamford, CT.

107. Tosoh Corp., Tokyo, Japan.

108. Aldrich Chemical Co., Milwaukee, WI

109. S.M. Rossnagel and J.J. Cuomo, AIP Conf. Proc. **165**, 106 (1988).

110. R.L. Sandstrom, W.J. Gallagher, T.R. Dinger, R.H. Koch, R.B. Laibowitz, A.W. Kleinsasser, R.J. Gambino, B. Bumble, and M.F. Chisolm, Appl. Phys. Lett. **53**, 444 (1988).

111. C.B. Eom, J.Z. Sun, K. Yamamoto, A.F. Marshall, K.E. Luther, T. Geballe, and S.S. Laderman, Appl. Phys. Lett. **55**, 595 (1989).

112. A.E. Lee, C.E. Platt, J.F. Burch, R.W. Simon, J.P. Goral, and M.M. Al-Jassim, Appl. Phys. Lett. **57**, 2019 (1990).

113. Balzers, Hudson, NH.

114. US Inc., Campbell, CA.

115. Advanced Energy Industries, Ft. Collins, CO.

116. MKS Instruments, Inc., Burlington, MA.

117. Tateho, Japan.

118. R. Robertazzi, Ph.D Thesis, Cornell University.

119. Inficon, Leybold-Heraeus, Syracuse, NY.

120. The Kanthal Corp., Hallstahammer, Sweden.

121. Huber, Rimsting, Germany.

122. Rigaku/USA, Danvers, MA.

123. Hitachi Instruments Inc., Japan

124. Digital Instruments, Inc., Santa Barbara, CA.

125. Olympus Optical Co., Ltd., Japan.

126. PLD courtesy of J.Z. Sun, IBM T.J. Watson Research Center, Yorktown Hts., NY.

127. Off-axis dc sputtering courtesy of P.L. Broussard, Naval Research Laboratory, Washington, D.C.

128. Inverted cylindrical magnetron sputtering courtesy of L.H. Allen, Naval Research Laboratory, Washington, D.C.

129. Mech-El Industries, Inc., Woburn, MA.

130. Dektak 8000; Veeco Instruments, Inc., Santa Barbara, CA.

131. Energy Beam Sciences, Agawam, MA.

132. J.M.E. Harper, G.R. Proto, and P.D. Hoh, J. Vac. Sci. Technol. **18**, 156 (1981).

133. J.M.E. Harper, J.J. Cuomo, R.J. Gambino, and H.R. Kaufman, in Ion Bombardment Modification of Surfaces: Fundamentals and Applications, eds. O. Auciello and R. Kelly (Elsevier, New York, 1984), 127.

134. J.M.E. Harper, J.J. Cuomo, R.J. Gambino, and H.R. Kaufman, Nucl. Instrum. and Methods **B7/8**, 886 (1985).

135. B.A. Movchan and A.V. Demchisin, Phys. Met. Metallogr. **28**, 83 (1969).

136. J.A. Thornton, Ann. Rev. Mater. Sci. **7**, 293 (1977).

137. Physical Vapor Deposition, ed. R.J. Hill (Temescal, Berkeley CA 1986), p. 49.

138. E. Kay and S.M. Rossnagel, in Handbook of Ion Beam Processing Technology, edited by J.J. Cuomo, S.M. Rossnagel, and H.R. Kaufman (Noyes Publications, Park Ridge, NJ, 1989), p.175.

139. K.-H. Muller, in Handbook of Ion Beam Processing Technology, edited by J.J. Cuomo, S.M. Rossnagel, and H.R. Kaufman (Noyes Publications, Park Ridge, NJ, 1989), p. 249.

140. J.J. Cuomo, S.M. Rossnagel, and H.R. Kaufman, in Handbood of Ion Beam Processing Technology, edited by J.J. Cuomo, S.M. Rossnagel, and H.R. Kaufman (Noyes Publications, Park Ridge, NJ, 1989), p. 1.

141. I.A. Blech, Thin Solid Films **6**, 113 (1970).

142. G. Carter, J.S. Colligon, and M.J. Nobes, J. Mater. Sci. **6**, 115 (1971).

143. C. Catana, J.S. Colligon, and G. Carter, J. Mater. Sci. **7**, 47 (1972).

144. T. Ishitani, M. Kato, and R. Shimizu, J. Mater. Sci. **9**, 505 (1974).

145. I.W. Rangelow, J. Vac. Sci. Technol. A **1**, 410 (1983).

146. S. Somekh, J. Vac. Sci. Technol. **13**, 1003 (1976).

147. S.M. Rossnagel and R.S. Robinson, J. Vac. Sci. Technol. A **1**, 426 (1983).

148. T. Mogami, M. Morimoto, H. Okabayashi, and E. Nagasawa, J. Vac. Sci. Technol. B **3**, 857 (1985).

149. I.H. Wilson, J. Belson, and O. Auciello, in Ion Bombardment Modification of Surfaces: Fundamentals and Applications, eds. O. Auciello and R. Kelly (Elsevier, New York, 1984), pp. 250-265.

150. H.P. Bader and M.A. Lardon, J. Vac. Sci. Technol. B **4**, 833 (1986).

151. R.E. Lee, J. Vac. Sci. Technol. **16**, 164 (1979).

152. R.S. Robinson, Ph.D. Thesis (Department of Physics, Colorado State Univeristy, 1979), pp. 129-145.

153. J.F. Benedict, S.J. Klepeis, W.G. Vandygrift, and R. Anderson, Electron Microscopy Soc. Am. Bull. **19** [11], 74 (1989).

154. Ecomet IV; Buehler Ltd., Lake Bluff, IL.

155. M-Bond 610; Measurements Group, Inc., Raleigh, NC.

156. Aremco Products, Inc., Ossining, NY.

157. VCR D500i dimpler; VCR Group, Inc., South San Francisco, CA.

158. Gatan, Warrendale, PA.

159. 002B TEM

160. B. Chapman, Glow Discharge Processes, (John Wiley & Sons, Inc., New York, NY 1980).

161. *ibid*, p. 203.

162. C.R. Guarnieri, private communication.

163. G. Hubler, presented at Beam-Solid Interations for Materials Synthesis, 1994 Fall MRS Symposia.

164. J.J. Cuomo, R.E. Gegenwarth, J.M.E. Harper, and G.R. Proto, IBM Tech. Discl. Bull. **25**, 1681 (1982).

165. N. Sonnenberg, private communication.

166. P.W. Tasker, Adv. Ceram. **10**, 176 (1984).

167. M.O. Aboelfotah, Appl. Phys. Lett. **24**, 347 (1974).

168. M.O. Aboelfotah, J. Vac. Sci. Technol. **12**, 67 (1975).

169. M.O. Aboelfotah, Thin Solid Films **33**, 373 (1976).

170. M.O. Aboelfotah, J. Appl. Phys. **49**, 2770 (1978).

171. M.O. Aboelfotah, Thin Solid Films **58**, 175 (1979).

172. S. Yadavalli, M.H. Yang, and C.P. Flynn, Phys. Rev. B **41**, 7691 (1990).

173. R. Du and C.P. Flynn, J. Phys. Condens. Matter **2**, 1335 (1990).

174. A.B. Berezin, C.W. Yuan, and A.L. deLozanne, Appl. Phys. Lett. **57**, 90 (1990).

175. A.B. Berezin, C.W. Yuan, A.D. deLozanne, S.M. Garrison, and R.W. Barton, IEEE Trans. Magn. **27**, 970 (1991).

176. K. Reichelt, J. Crystal Growth **19**, 258 (1973).

177. A. Rakotomiraho, E. Charles, and A. Boyer, J. Mater. Sci. **21**, 2124 (1986).

178. P. Vuoristo, T. Mantyla, and P. Kettunen, J. Vac. Sci. Technol. A **4**, 2932 (1986).

179. P. Vuoristo, T. Mantyla, and P. Kettunen, Vacuum **42**, 1001 (1991).

180. K. Sakuta, K. Asano, T. Awaji, S. Hashiguchi, and T. Kobayoshi, Jpn. J. Appl. Phys. **29**, 1668 (1990).

181. A.H. Hebard, A.T. Fiory, S. Nakahara, and R.H. Eick, Appl. Phys. Lett. **48**, 520 (1986).

182. E. McClanahan and N. Laegreid in Topics in Applied Physics: Sputtering by Particle Bombardment **64**, edited by R. Behrisch and K. Wittmaack (Springer-Verlag, Berlin Heidelberg, 1991), p. 341.